A CODED-MASK IMAGER
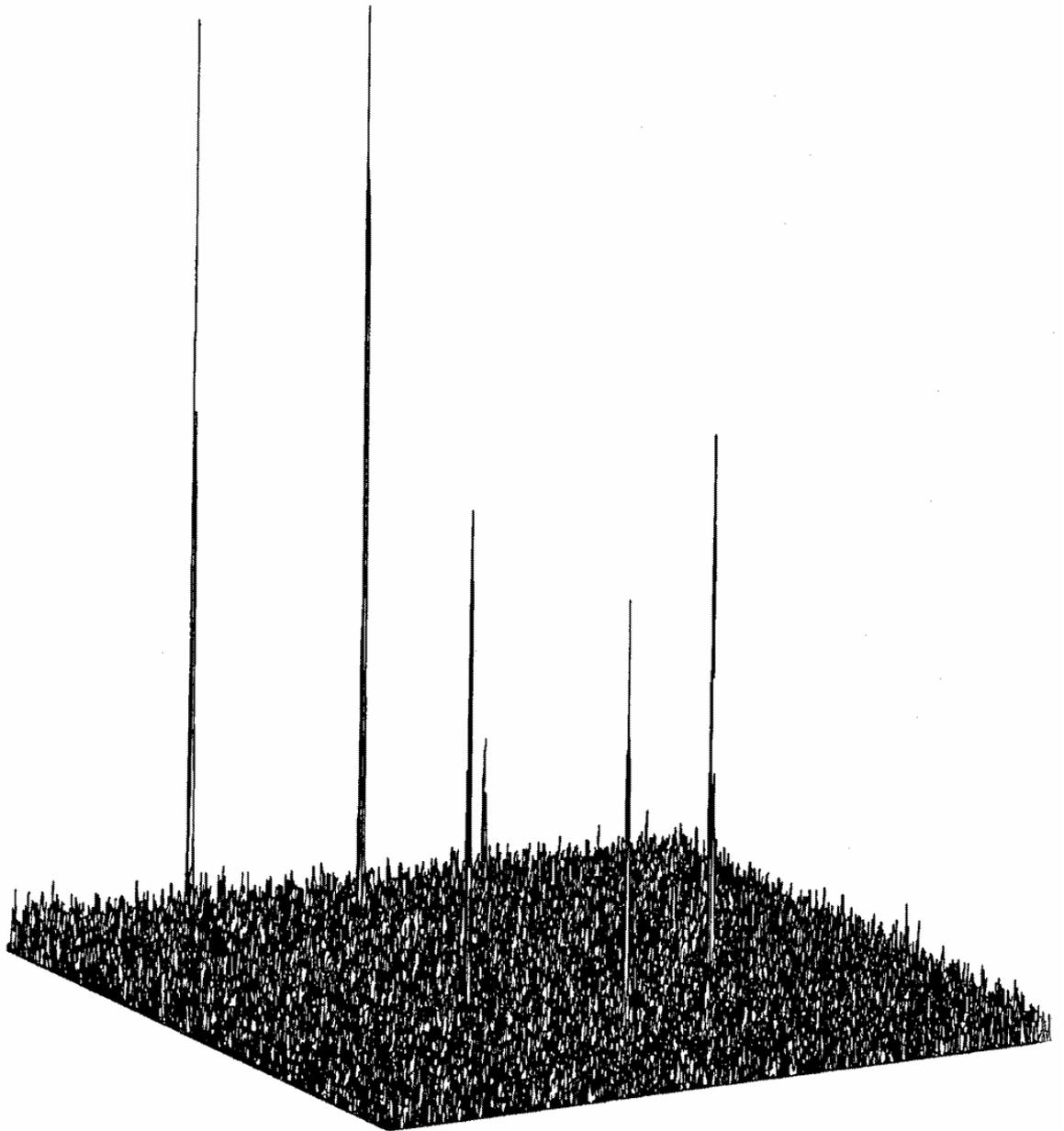# AS MONITOR OF
GALACTIC X-RAY SOURCES

Jean in 't Zand

A Coded-Mask Imager as Monitor of Galactic X-Ray Sources

Een Schaduwmaskercamera als Monitor van Galactische Röntgen-bronnen

(MET EEN SAMENVATTING IN HET NEDERLANDS)

PROEFSCHRIFT

TER VERKRIJGING VAN DE GRAAD VAN DOCTOR AAN DE RIJKS-
SUNIVERSITEIT TE UTRECHT, OP GEZAG VAN DE RECTOR MAG-
NIFICUS PROF. J.A. VAN GINKEL, INGEVOLGE HET BESLUIT VAN
HET COLLEGE VAN DECANEN IN HET OPENBAAR TE VERDEDI-
GEN OP WOENSDAG 14 OKTOBER 1992 TE 12.45 UUR

DOOR

Johannes Joseph Marie in 't Zand

GEBOREN OP 13 OKTOBER 1960 TE BUNDE

Contents

Abbreviations and acronyms

AC	–	Anti Coincidence
ADC	–	Analog-to-Digital Converter or Accretion Disk Corona
AGN	–	Active Galactic Nucleus
ASM	–	All-Sky Monitor
BASUB	–	BAckground SUBtraction on detector
BHC	–	Black Hole Candidate
CDMS	–	Command and Data Managing System
COMIS	–	COded-Mask Imaging Spectrometer
CPU	–	Central Processing Unit
CV	–	Cataclysmic Variable
FFT	–	Fast Fourier Transform
FOV	–	Field Of View
FWHM	–	Full-Width at Half Maximum
FWZR	–	Full-Width to Zero Response
GC	–	Galactic Center
HEXE	–	High-Energy X-ray Experiment
HLD	–	High-Level Discriminator
HMXB	–	High-Mass X-ray Binary
IFC	–	In-Flight Calibration
IKI	–	Russian abbreviation for the Space Research Institute in Moscow
IROS	–	Iterative Removal Of Sources
LLD	–	Low-Level Discriminator
LMC	–	Large Magellanic Cloud
LMXB	–	Low-Mass X-ray Binary
LTF	–	Live-Time Fraction
MEM	–	Maximum Entropy Method
MES	–	Mask Element Size
MIF	–	MInor telemetry Frame
NM	–	Normal Mode
NS	–	Neutron Star
PSF	–	Point-Spread Function
QPO	–	Quasi-Periodic Oscillations
RM1/5	–	Rate Meter 1 through 5
RMC	–	Rotation-Modulation Collimator
SAA	–	South-Atlantic Anomaly
SLA	–	Source Location Accuracy
SNR	–	Signal-to-Noise Ratio
SRON	–	Space Research Organization of the Netherlands
SS	–	Star Sensor
SWA	–	Simplified Weight Averaging of detector subsections
TTM	–	Russian abbreviation for shadow mask telescope, used as alternative name for COMIS
URA	–	Uniformly-Redundant Array
WA	–	Weight Averaging of detector subsections
WD	–	White Dwarf
XB	–	X-ray Binary

Summary

This thesis concerns subjects from the development, calibration and scientific output of the *COMIS* instrument, which was launched in 1987 as part of the *Röntgen* observatory in the *Kvant* module of the manned space station *Mir*. *COMIS* is a collaborative effort between the SRON-Laboratory for Space Research Utrecht (the Netherlands), the University of Birmingham (United Kingdom) and the Space Research Institute in Moscow (Russia). It brings into practice coded-mask imaging in X-ray astronomy (at photon energies between 2 and 30 keV). Due to the wide field of view (16×16 square degrees) and an angular resolution of $2'$, the instrument is capable of studying simultaneously several X-ray sources that are within the observed sky. Thus, it can monitor the behavior of persistent sources as well as watch the sky for unexpected events such as short outbursts of otherwise undetectable sources (e.g. transient sources).

Chapter 1 gives a general introduction to the physics and characteristics of bright galactic X-ray sources, a discussion of the contribution that coded mask imaging devices can provide to the understanding of these sources and a motivation of the research discussed in this thesis.

A coded-mask imaging device basically consists of three components: the mask plate (and the pattern of holes in it), the detector and the reconstruction hard- and software. In part I of this thesis the development considerations and calibration of these components are discussed for the *COMIS* instrument. This starts in chapter 2 with an overview on all the instruments of the *Röntgen* observatory, indicating the scientific role of *COMIS* within the observatory. In chapter 3, the concept of coded-mask imaging is introduced; an account is provided of the requirements to the pattern of mask holes, the capabilities of the detector and the reconstruction algorithm, to arrive at an optimum imaging performance. In chapter 4 the development considerations and implementation of the mask and detector hardware of *COMIS* are discussed that determine the scientific capability of the instrument. The applied reconstruction hard- and software are presented in chapter 5; new algorithms are put forward to suppress Poisson noise (this algorithm specifically concerns the mask-detector configuration as applied in coded-mask systems like *COMIS*) and to deal with imperfections in the imaging capability of the detector. These algorithms potentially improve the statistical quality of the data several times. Finally, in chapter 6, pre- and in-flight calibration items of *COMIS* are discussed, as performed by the author, that are crucial in the scientific analysis of the data, e.g. the spectral response, the point-spread function and the dead times of the detector.

Part II deals with scientific results obtained with *COMIS* by the author. Apart from the scientific relevance, these results indicate the potential of observations with a wide-field coded-mask imaging device. At first, in chapter 7, an overview is given of the monitor results of *COMIS* on 65 point sources, detected between October 1988 and February 1992. *COMIS* has observed in this period the X-ray sky for about a total of 150 hours, of which 80% in 1989. The top-priority target in this period was the galactic bulge, to which 20% of the exposure time was dedicated. Four of the sources detected are transients, that had not been detected previously with other instruments. Furthermore, fourteen burst events were observed which could be attributed to persistent X-ray sources within the galactic bulge.

Three of the new transient sources are situated within a few degrees of the galactic center. Two of these were seen to burst more than once. KS1732−273 and KS1741−293 are weak transients, with a peak intensity less than 30 mCrab. They are discussed separately in chapter 8.

In chapter 9 the observed spectral variability of the X-ray transient GS2023+338 is discussed. This bright transient and best galactic black hole candidate is shown to exhibit in essence variability in two spectral components which are superposed on a power-law spectrum with a constant index: a low-energy absorption whose variability decays with time and a Compton-reflected component whose relative magnitude decays with time. The decay observed in both components is probably due to a clean-up of environmental material by accretion.

In conclusion, it is shown that wide-field coded-mask imaging is a valuable tool to monitor the X-ray sky. Its capability conveniently fills the gap between all-sky monitors and narrow-field instruments. On the one hand it compares to an all-sky monitor by the potential of quicker localization of short events and on the other hand it enables the simultaneous study of more than one strong X-ray source. The term 'selected-sky monitor' well characterizes such an instrument. The results stress the importance of monitoring the X-ray sky with similar instruments, e.g. the wide-field cameras currently developed at SRON-Utrecht for use aboard the *Satellite per Astronomia a raggi X (SAX)*, an Italian-Dutch X-ray observatory which is due for launch in 1994.

Chapter 1

Introduction

1.1 Advent of X-ray astronomy

Prior to 1962 it was generally thought that celestial sources outside the solar system radiate the same proportion of their bolometric luminosity in X-rays as the sun does (about 10^{-7}). It therefore came as a surprise when in that year, during a tentative observation of the moon, the first extra-solar X-ray source was detected in the constellation of Scorpius (Sco X-1, Giacconi *et al.* 1962) at the sensitivity level of the early X-ray detectors ($\sim 10^{-7}$ erg s^{-1}cm^{-2} in $1-10$ keV). Assuming that Sco X-1 is a nearby star, it would emit X-rays at a rate 10^7 to 10^8 greater than the sun[1]! This discovery initiated a decade of rocket and balloon-borne X-ray measurements of the sky and substantial theoretical effort to explain the source of the high X-ray emission in Sco X-1 and in other subsequently discovered strong celestial X-ray emitters. A major breakthrough occurred in 1972 when space-borne measurements with the first X-ray satellite *Uhuru* showed signs of orbital motion in Cen X-3 (Schreier *et al.* 1972). This confirmed the suspicion that many such X-ray sources originate in galactic close binary star systems in which mass is transferred from a 'normal' star to a collapsed star; the mass in-fall into the deep gravitation well of the collapsed star serves to power the energetic X-radiation. In a few other sources the X-rays were found to originate from synchrotron emission in the nebulae of young supernova remnants. Although the physical nature of these sources has since been firmly established, many questions remain to be answered. These questions predominantly concern the evolutionary history and present status of these binary systems. In practice this means that basic system parameters need to be determined, e.g. masses and dimensions. Since the nineteen sixties a large effort has been made to accomplish this.

Space-borne observational work[2] started off in the early seventies with the main purpose to make an archive of celestial X-ray sources and their X-ray characteristics (with satellites such as *Uhuru*, *Ariel-V* and *HEAO-1*). In the next decade, more sensitive instrumentation was launched into space (e.g. *Einstein*, *EXOSAT*, *Ginga*) which permitted a more careful temporal and spectral study of X-ray sources. These studies contributed considerably to the understanding of the environment of X-ray sources and often provided the necessary data to obtain the basic parameters of such close binary star systems. This thesis describes the application of a novel observing technique, coded-mask wide-field imaging, which is specifically relevant to the investigation of variability in bright X-ray sources, particularly those sources which are bright for only a short time (several seconds to weeks).

The following chapter introduces the reader to the main physical aspects of high-luminosity compact galactic X-ray sources and to the observational techniques applied for studying the variability of these sources on time scales of several seconds to weeks.

---

[1] In 1966 the optical counterpart of Sco X-1 was discovered (Sandage *et al.* 1966, Johnson & Stephenson 1966). It was found that this object emitted 1000 times more power at X-ray wavelengths than at optical wavelengths.

[2] For a review of X-ray astronomy missions, see Bradt *et al.* 1992.

1.2   Bright compact galactic X-ray sources

Many galactic objects emit X-radiation but the range in luminosity is large, from $\sim 10^{27}$ erg s^{-1} for weak coronal emission to $\sim 10^{38}$ erg s^{-1} for the strongest accretion-driven binaries. The latter category of sources is of primary interest in this thesis and the subsequent discussion will focus on these sources.

A binary star system may contain a collapsed star, which is the end-product of stellar evolution. This can either be a white dwarf (WD), neutron star (NS) or black hole (BH). If, by some mechanism, mass is transferred from the 'normal' companion star to the collapsed component, this matter will fall into a deep gravitation well and potential energy is transformed into kinetic and thermal energy. The energy-transformation is highly efficient: for a NS the energy produced is equivalent to about 10% of the rest mass of the in-falling matter. This energy may again be transformed into radiation, with typical wavelengths in the X-ray regime. The precise mechanisms at work in the transformation of energy and the resulting characteristics of the radiated energy depend on the specific physical circumstances in the binary as a whole and on the characteristics of the individual components, e.g. the masses $M_{\rm x}$ and $M_{\rm c}$ of the collapsed object and companion star respectively, the mechanism responsible for the mass loss of the companion star, the mass accretion rate $\dot{M}_{\rm x}$ of the collapsed object, the nature of the collapsed object, the magnetic field strength B of the collapsed object, the rotation periods ($P_{\rm x}$ and $P_{\rm c}$) and the orbital period $P_{\rm orb}$. These parameters are set by the evolutionary history of the binary system.

The luminosity of these binaries depends in particular on $\dot{M}_{\rm x}$ and the radius of the collapsed object ($R_{\rm x}$). A simple estimate for the power W of the liberated potential energy can be inferred from

$$W \quad = \quad \frac{G\,M_{\rm x}\,\dot{M}_{\rm x}}{R_{\rm x}} \tag{1.1}$$

A typical mass accretion rate is $\dot{M}_{\rm x} \approx 10^{-8}$ M$_\odot$yr^{-1} (Savonije 1983), resulting in roughly $W = 10^{38}$ erg/s for a NS and 10^{35} erg/s for a WD. If all this energy were thermally radiated with a single temperature at the collapsed object's surface, the maximum of the black body distribution would lie at 7 and 0.04 keV respectively. Therefore, it is expected that binaries containing a WD have a substantially lower hard X-ray luminosity[3] than those containing a NS or BH. Because of this, binaries with the latter types of collapsed objects are generally called X-ray binaries (XBs). A recent overview of these systems was given by White (1989). Two types of XBs are distinguished, depending on the nature of the companion star:

HIGH-MASS X-RAY BINARIES (HMXBs). The companion star has a mass of $\gtrsim 10$M$_\odot$ and an early spectral type (earlier than $\sim$B2). It looses matter predominantly through a wind −the accretion is then designated as 'wind driven'− although in some cases incipient Roche-lobe overflow is suspected. There is indirect evidence for the presence of an accretion disk in some systems. HMXBs are generally young ($\lesssim 10^7$ yr) and if the collapsed object is a NS it may possess a magnetic field strong enough ($\sim 10^{12}$ G) to funnel the mass accretion along the field lines to the magnetic poles. If the magnetic and rotation axes are not co-aligned, the X-radiation beam may periodically sweep through the line of sight, thus creating a pulsating signal to the observer. The ratio of optical to X-ray flux of HMXBs is $\lesssim 1$, while the X-ray spectrum is hard (typical $kT \gtrsim 15$ keV).

The group may further be subdivided in two groups (each comprising about half of the HMXBs): super-giant X-ray binaries (the companion is of luminosity class I-II) and Be X-ray binaries (class III-IV).

LOW-MASS X-RAY BINARIES (LMXBs). In these systems the companion star has a mass of $\lesssim\ 2$M$_\odot$, is of a late spectral type and looses matter through Roche-lobe overflow. These

---

[3]HARD X-radiation is here defined as radiation with photon energies between 1 and 10 keV.

systems are generally old and the magnetic field of a possible NS is weak ($B \sim 10^8 - 10^9$ G). Due to the high angular momentum of the transferred matter, an accretion disk is formed; the accretion is designated as 'disk driven'. This accretion disk forms a buffer in the mass transfer. To this date, no pulsars have been found among LMXBs, most probably due to their low magnetic field. The X-radiation dominates the optical luminosity ($L_{\mathrm{x}}/L_{\mathrm{opt}} \sim 350$ on average). In fact, the optical radiation of the companion star may be so weak that the optical radiation observed is dominated by reprocessed X-radiation from the accretion disk and by X-ray heating of the companion star. Luminous LMXBs located in the galactic bulge have not yet been identified with optical counterparts, owing to the strong interstellar absorption in that direction. For those that have an identified counterpart, the optical spectrum is often a-typical for a main-sequence star. The X-ray spectrum is relatively soft (typical $kT \lesssim 15$ keV).

The above-mentioned groups are rather well defined. Only a few XBs (e.g. GX1+4, 4U1626-67, H2259+035 and Her X-1) are difficult to classify, because they show characteristics of both groups. Van Paradijs (1991) lists 44 HMXBs and 43 LMXBs that have been identified with optical counterparts. Other luminous X-ray sources have also been classified on the basis of their analogy with those optically identified. The total amount of known XBs is 124.

The X-ray intensity of XBs is often persistent, suggesting a continuous mass transfer. Some sources, however, "turn on" their X-ray flux for only a short time. These are transient sources, in the sense that their X-ray luminosity remains most of the time below the detection threshold of the X-ray detectors. This phenomenon is basically attributed to an irregular mass transfer rate. The observational aspects of transient sources are discussed in 1.3.6.

The luminosity arising from in-falling matter on a collapsed object has an upper limit. If the mass transfer gives rise to so much radiation that the radiation pressure balances the gravitational attraction, no accretion is possible anymore. A simple estimate (i.e. employing spherical symmetry) for the upper limit to the X-ray luminosity and the corresponding mass accretion rate is obtained by balancing the gravitational force and the radiation pressure due to Thompson scattering by hydrogen atoms and is called the Eddington limit:

$$L_{\mathrm{edd}} \quad = \quad 1.3 \times 10^{38} \frac{M_{\mathrm{x}}}{\mathrm{M}_{\odot}} \ \mathrm{erg/s}; \quad \dot{M}_{\mathrm{edd}} = 10^{-8} \ \frac{M_{\mathrm{x}}}{\mathrm{M}_{\odot}} \ \mathrm{M}_{\odot}/\mathrm{yr} \qquad (1.2)$$

A couple of X-ray characteristics of XBs are clear indicators for the NS nature of the collapsed object. These include bursts and pulsations (see 1.3). However, such characteristics are in many cases not found and the nature of the collapsed component remains uncertain. Till now, six XBs are suspected to contain a BH, on the basis of lower limits to the collapsed object's mass. Theory predicts that collapsed objects more massive than 3 $\mathrm{M}_{\odot}$ will collapse to form a BH. Objects with lower mass limits in excess of this value are designated as BH candidates (BHC); the candidacy refers to the fact that the theory is not fully secure regarding the existence of BHs. The lower mass limits for these six BHCs have been obtained by the measurement of the radial velocity curve of Doppler-shifted optical spectral lines (i.e. shifted due to the orbital motion of the companion star) and application of Kepler's third law.

Binaries with a WD as collapsed object were first recognized in the optical band and are called CAT-ACLYSMIC VARIABLES (CV). Typical for most of these binaries is that they show outburst behavior in their optical lightcurves. These outbursts may be either single or quasi-periodic events, possible causes comprise thermonuclear runaway in the grown envelope of the WD, irregular accretion rates or accretion disk instabilities. Several subclasses have been recognized (see e.g. Córdova & Mason 1983), including classical novae, dwarf novae and recurrent novae. Most of the CVs emit X-rays at a level of $< 10^{33}$ ergs/s (0.1-4 keV) during quiescence.

Table 1.1: Types of XB Variability in order of time scale

Name	Type[a]	Time scale s	On-Time s	Suggested Origin
Rapid variability	A	$\lesssim 10^{-1} - \gtrsim 10^3$	–	Instabilities in accretion
QPO	Q	$10^{-2} - 10^2$	–	Beat of rotation and revolution or accretion disk instability
Pulsation	P	$10^{-2} - 10^3$	–	NS rotation
Type II Burst	A	$10^1 - 10^3$	$10^0 - 10^3$	Accretion instabilities
Type I Burst	A	$10^3 - \gtrsim 10^5$	$10^0 - 10^2$	Thermonuclear flash
Orbital modulation	P	$10^3 - 10^7$	–	Revolution of binary components or matter
Hard transient behavior	A/P	$10^6 - 10^8$	10^6	Irregular wind and/or eccentric orbit
(Ultra-)Soft transient behavior	A	$\gtrsim 10^7$	10^6	Unstable accretion
Fast transient behavior[b]	A	?	$10^2 - 10^4$	Magnetic surface activity
Long-term cycles	A/P	$10^6 - \gtrsim 10^8$	–	Precession or companion variability

[a] Type of signal: P = periodic, A = a-periodic, Q = quasi-periodic.
[b] This type of variability does not apply to XBs, but to stars of late spectral type.

1.3 The variability of bright galactic X-ray sources

The X-ray flux of compact galactic sources often is very variable. Several types of variability have been recognized, based on observational characteristics (i.e. the appearance of the lightcurve and sometimes its Fourier spectrum). The relation between these various types of variability and the underlying physical processes is reasonably understood, although certainly not completely. The designation of the various types is summarized in Table 1.1. In the following section they will be described in some detail.

1.3.1 Rapid variability

Aperiodic X-ray rapid variability or 'flickering' (see e.g. Van der Klis 1989 or Makishima 1988) is seen in members of all types of XBs (as well as in other types of emitters). The most prominent flickering sources are Cyg X-1 and Cir X-1. Rapid variability is characterized by a power-density spectrum of the time series which follows a power law within a restricted range of frequencies: $P(\nu) = A \nu^{-q}$, where ν is the frequency, q the power-law slope and A a normalization constant. Observed power-law slopes lie roughly between 1 and 2 and are, for each source, independent of the X-ray energy considered (except for Cyg X-1, see e.g. Miyamoto & Kitamoto 1989). The lower limit to the frequency range of the power-law spectrum has for a few sources been detected at ~ 0.1 Hz, but the LMXB cases in particular do not show a flattening of the power-density spectrum down to ~ 1 mHz (which is the detection limit).

The amplitude of the rapid variability, expressed in integrated fractional rms variation within 2–250 mHz, varies between a few percents to $\gtrsim 20\%$. Characteristic for LMXB cases is that the amplitude increases with photon energy and with persistent X-ray luminosity.

The physical origin for rapid variability has not been firmly established yet. However, a model

has been proposed for the rapid variability of Cyg X-1, which includes the random accretion of clumps of matter with different sizes onto the collapsed object (Miyamoto & Kitamoto 1989). Each accreted clump gives rise to a 'shot' in the X-ray intensity, which shows spectral hardening with time and thus results in a phase lag in the variability between two different photon-energy ranges.

1.3.2 Orbital modulations

Measured P_{orb}'s (from X-ray as well as optical data) range from 0.19 to 235 hr for the LMXBs (Parmar & White 1988) and from 1.4 to several hundred days for the HMXBs (Stella *et al.* 1986). The difference in P_{orb} between both groups is clearly related to the different size of the companion stars. The X-ray orbital modulation is either found in a periodic Doppler shift of pulse arrival times (see e.g. Rappaport & Joss 1983) or a periodic modulation of the X-ray flux.

Some ~ 30 XBs show orbital modulation in their X-ray flux due to eclipses. The shape of the X-ray lightcurve is determined by the geometry of the X-ray emitting region and that of the eclipsing object(s). The potential X-ray emitting regions include the surface of the collapsed object, an accretion disk and an accretion disk corona (ADC, this term refers to both coronae and winds surrounding the accretion disk, the X-rays observed originate from the accretion disk and the NS and are subsequently scattered by the ADC). Eclipses may arise from the companion star and/or an accretion disk rim.

Eclipses seen in HMXBs are mostly caused by the companion star. The (OB) companion in a bright HMXB is usually large with respect to the distance between both components, therefore the probability of an eclipse is larger than in LMXBs. The X-ray lightcurves often show additional structure, due to density variations of wind material in the line of sight (see e.g. White 1989).

In LMXBs the geometry is more complicated because of the presence of an accretion disk. Two types of modulation are typical for LMXBs: dips and smooth (quasi-sinusoidal) variations (see e.g. Parmar & White 1988). The dips (a reduction of X-ray flux for a time which is short with respect to P_{orbit}) are due to a combination of a small X-ray emitting area (i.e. the inner accretion disk or the surface of a NS) and a structured accretion disk rim. The presence of dips is very sensitive to the inclination angle. Smooth periodical X-ray variations can be modelled by an ADC as the X-ray emitter (the central X-ray source being obscured by an accretion disk) which is periodically eclipsed by the companion or a local thickening of the accretion disk rim.

1.3.3 Pulsations

Some 40-50 X-ray pulsars have been found to this date, with pulse periods between 0.033 and 835 s. About half of these are identified with HMXBs, on the basis of an identification with an optical counterpart (see Van Paradijs 1991), the rest is either situated in a supernova remnant or a CV system or is not yet classified (the latter group probably consists of HMXBs with no optical counterpart).

XB pulsar periods provide a powerful tool to describe the XB's parameters (see e.g. Rappaport & Joss 1983). If Doppler shifts from orbital motion are detected in pulse arrival times (from the collapsed object) as well as in optical spectral lines (from the companion star) and eclipses are seen, one may infer the inclination angle, M_{c}, M_{x} and R_{c}, when applying reasonable assumptions on the binary's geometry. Van Paradijs (1989) lists seven cases of NS mass estimates thus obtained (including one radio pulsar). Remarkably, these are all consistent with a single mass of $M_{\mathrm{x}} = 1.4 \pm 0.2$ M$_\odot$ but it should be noted that the uncertainties in the mass determinations are sometimes quite large.

Worth mentioning is the potential of period-derivative studies: due to the transfer of angular momentum to the NS in XBs, the NS is often spun-up. This is expected if the rotation sense of the NS is the same as that of the orbital motion. The efficiency of angular momentum transfer is high if the companion looses mass through Roche lobe overflow, via an accretion disk. Characteristic for many HMXBs, however, is that the companion looses matter via a radiatively-driven wind. This

degrades the transfer of angular momentum and the pulse period history may show erratic changes. Erratic changes ('glitches') may also arise from changes in the internal structure of the NS.

1.3.4   Bursts

X-ray bursts pertain to flux increases that last for only a very short time. The typical rise time is $\sim 1 - 10$ s and the decay time ranges from seconds to minutes. Two types of bursts have been recognized (Hoffman *et al.* 1978): Type I and Type II bursts. Type I bursts are characterized by a spectral softening during decay. The intervals between these bursts vary from 4 minutes to more than a day. It is generally accepted that such bursts are caused by thermonuclear flashes on a NS surface, induced by the build-up of temperature and pressure in a nuclear fuel reservoir of Hydrogen and Helium. Studies of Type I bursts provide a valuable test for constraining the equation of state of NS matter, since the bursts reflect physical conditions on the NS surface, which in turn relate to the average mass density of the NS.

Currently almost 40 Type-I burst sources have been identified (for a relatively recent list, see Damen 1990). Most of these sources show a persistent X-ray flux as well, usually with a soft spectrum ($kT \sim 5$ keV), and are concentrated on the sky towards the galactic center. None of the bursters detected so far show X-ray pulsations. These two characteristics clearly demonstrate the association of burst sources with the LMXBs. Slightly over 10 sources have been proven to be LMXBs through identification of an optical counterpart.

Type II bursts show no spectral softening during decay and have bursts intervals 2 to 3 orders of magnitude shorter than Type I bursts. Type II bursts have till now only been found in one single source, the 'rapid burster' (X1730-333), and are thought to result from instabilities in an accretion disk.

1.3.5   QPO and their relation to spectral variability

Quasi-periodic oscillations (QPO), as found in LMXBs (see e.g. Van der Klis 1989), are defined as broad symmetric peaks in the power spectrum of a time series of the intensity. The centroid frequency is between 5 and 60 Hz, the peak width is roughly half the centroid frequency and the rms-amplitude lies between 1 and 10% of the total intensity. The data are always found to be too noisy to 'see' QPO directly in the X-ray lightcurve itself. Van der Klis lists 8 bright LMXB QPO sources. Slower QPO, with frequencies down to a factor of $\sim 10^3$ less, have been found in a few cases of HMXBs and BHCs.

The QPO behavior in LMXBs seems related to their spectral behavior (Hasinger & Van der Klis 1989). In the subclass of so-called 'Z-sources' (the 'Z' refers to the pattern traced out by the source in color-color or color-intensity diagrams), three spectral states are recognized with each a different QPO signature. In the hard spectral state high-frequency QPO (20-45 Hz) occur, which have been suggested to be due to the interaction of clumps of material, in Keplerian motion around the NS, with the magnetic field of the NS ('beat-frequency modulated accretion', Alpar & Shaham 1985 and Lamb *et al.* 1985). In a softer state, 6 Hz QPO emerge which are thought to originate in resonances within the accretion flow (Lamb 1989). Recent observations of Cyg X-2 (Hasinger *et al.* 1990) indicate that the changes of spectral state and QPO behavior might be due to a varying mass accretion rate which influences the thickness of the accretion disk and its interaction with the magnetosphere.

1.3.6   Transient behavior

Van Paradijs & Verbunt (1984) define transient sources (in short 'transients') as sources that emit the bulk of their X-ray emission in rather well-defined events, which last for at least a few days, during which the X-ray luminosity increases by at least a factor of 10. In contrast to these (slow) transients, so-called 'fast transients' are known (sometimes called 'high-latitude transients'), whose on-state lasts typically three orders of magnitude shorter. This difference in transient time scale points at totally different physical processes.

Slow transient sources during outburst show many similarities with persistently bright XBs in their major characteristic features, such as pulsations or bursts. In fact, the same classification scheme of low- and high-mass XBs can be applied; the equivalent designations are 'hard' ($kT \gtrsim 15$ keV) and 'soft transients' ($kT \lesssim 15$ keV) respectively. The important difference between persistent and transient sources is the stability of the mass accretion or transfer.

Non-steady accretion in HARD X-ray transients is mostly attributed to a combination of irregular winds from a fast rotating Be star and the motion of a NS in an eccentric orbit ($e \sim 0.1 - 0.5$, see e.g. Priedhorsky & Holt 1987). These two properties provide an environment for irregular mass accretion, which is sometimes correlated with $P_{\rm orb}$. Many hard transients show flux levels at quiescence of about a factor 10 lower than during outburst (sometimes this factor is more than 100), which indicates a low-level accretion flow from the companion's wind. Recently, Koyama *et al.* (1990) have discovered 7 new probable Be XBs, concentrated in the sky in the Scutum region. These discoveries are important, since they imply that the galactic population of Be XBs is large (> 1000), which is supported from an evolutionary point of view (Rappaport & Van den Heuvel 1982).

The accretion in SOFT transients is thought to be due to either an intermittent flow through the inner Lagrangian point or continuous Roche lobe overflow mediated by an accretion disk in which material is stored until it is released by an instability. The occurrence of soft transients with a peak X-ray luminosity exceeding 10^{37} erg/s is estimated at ~ 6 yr^{-1} (Van Paradijs & Verbunt 1984). The observed rise time lies between 2 and 10 days, while the typical e-folding decay time is ~ 1 month. The associated optical lightcurve, if observed, always decays slower than the X-ray lightcurve, with a decay time ~ 2 times longer (Van Paradijs 1983). The optical emission is due to reprocessed X-rays in an accretion disk; during decay, the black-body temperature of the disk decreases and a larger fraction of the total disk luminosity emerges in the visual region of the spectrum. Observed recurrence times, which are sometimes inferred from outbursts in only the optical band, range from 0.5 till 50 years. It has been suggested by White *et al.* (1984) that mass accretion may become unstable if its rate is less than $\sim 5 \times 10^{-10}$ M$_\odot$yr^{-1}, which applies to soft transients. This would imply that no persistent LMXBs with a luminosity below a few times 10^{36} erg/s do exist; this seems supported by the available observational data. Finally it has been noted that soft transients are similar to dwarf novae, the difference between both being essentially the nature of the collapsed object (NS versus WD). The list provided by Van Paradijs (1991) (see also Bradt & McClintock 1983), covering 20 years of space-borne X-ray studies, lists 19 bright galactic LMXB transients (of which 13 have been optically identified).

Besides (slow) hard and soft X-ray transients a third group has been recognized: that of the ULTRA-SOFT X-ray transients. These are thought to contain a BH instead of a NS. The X-ray spectrum then only comprises the soft accretion-disk-originated emission; the (harder) thermal bremsstrahlung component of the spectrum, otherwise apparent from the regions near to a NS, is missing.

We note that the above classification of slow transients is not strict. This is illustrated by the case of GS2023+338, a transient which flared in 1989 in the constellation of Cygnus (see e.g. chapter 9): despite its hard X-ray spectrum, the optical counterpart was shown to be of a late spectral type and the compact object a BHC.

Fast transients in general presumably have a completely different origin than the slow transients. This is indicated by those that have been found in two surveys: one through *Ariel-V* data (Pye & McHardy 1983) and the other through *HEAO-1* data (Connors *et al.* 1986). Together these surveys revealed 35 fast transient events, with on-states lasting between 60 s and 93 h. The number-flux relations of both surveys are consistent with a homogeneous spatial distribution, suggesting a nearby ($\lesssim 100$ pc) or an extra-galactic origin. The frequency of the events is expected to be at least $\gtrsim 10^4$ yr^{-1} above 1 mCrab[4] (2–20 keV). The identification of these events with known sources of radiation proved to be difficult due to the bad positional accuracies of both surveys. Some of the *Ariel-V*

---

[4]One Crab unit is a common intensity unit in astrophysical applications, it refers to the ratio of the intensity of the source and the intensity of the Crab source, as measured with the same type of detector; the Crab source has a flux of 1.0 mJy at 5.5 keV or 2.4×10^{-8} erg s^{-1}cm^{-2} in the 2–10 keV band or 3.5×10^{-8} erg s^{-1}cm^{-2} in the 2–30 keV band.

events were attributed by Pye & McHardy to RS CVn systems (these are thought to exhibit high coronal activity) while Connors *et al.* found some of the events in the *HEAO-1* survey to be hard flares from dMe-dKe stars. It remains essentially an open question what objects are responsible for fast transient events and a monitoring device with high positional accuracy is needed to answer this question.

1.3.7   Long term cycles in XBs

Priedhorsky & Holt (1987) have given an overview of long-term cycles in X-radiation variation (i.e. cycles longer than P_{orb}) of XBs. Different time scales and underlying physical mechanisms apply to HMXBs and LMXBs.

Among HMXBs (excluding Be XBs, see 1.3.6), long term cycles in X-radiation have been found for about 10 sources. The cycle period (with various degrees of coherence), P_{long}, ranges from 5.6 to ~ 165 d, a factor of 5 to 60 larger than P_{orb}. The modulation depth varies between sources from 10 to 100%. The explanation is sought in precession of either an accretion disk or a NS.

Among LMXBs, long-term cycles may arise from variations in the mass transfer rate (although the evidence for this is circumstantial). Amplitudes range up to 100% and time scales are in the order of a year, which is much longer than P_{orb}. The evidence for a periodic nature is not so strong as in HMXBs. There are indications that long-term cycles among LMXBs are only present in medium-luminosity sources (i.e. a luminosity less than 10^{37} erg s^{-1}) which often show bursting activity. In several sources the long time scale lightcurve is sawtooth-shaped, i.e. a sharp rise (extending to ~ 0.2 cycles) followed by a gradual decay.

1.4   Instrumentation for the study of transients and bursters

The previous section summarized the types of X-ray variability seen in bright galactic sources and the relevance that timing measurements have on developing physical models for these objects. Of particular interest in this thesis are studies on time scales from seconds to weeks, concentrating on transient and bursting behavior, resulting from either irregularities in the mass accretion rate onto a collapsed object or flaring activity on a neutron or late-type star.

The population of burst and transient sources, i.e. their number-flux relation, has remained rather unclear. Up till now ~ 40 slow transients have been recognized (Van Paradijs 1991), both hard and (ultra-)soft transients. These transients are mostly bright ($\gtrsim 100$ mCrab), relatively little is known about weak transients. Furthermore, ~ 40 burst sources are known (Damen 1990) and ~ 35 fast transients. Presumably many of the short-duration events from these type of sources have been missed all together. In any case, the fast transients that have been detected are often located with a bad accuracy. One may ask what type of instrument is needed to fill this lack of information.

The classical instrument which is intended for research in part of the above-mentioned field, is the all-sky monitor (ASM). Conventional ASMs are operative in the 2-10 keV range and intended as an alarm device for the onset of slow and bright transients (providing the requirement to observe the transient with a more sensitive instrument) and as a monitoring device for the long-term variability of bright X-ray sources. The ASM instrument is typically either a scanning slit collimator, a rotation modulation collimator or a pinhole camera (see e.g. Holt & Priedhorsky 1987 and Priedhorsky & Holt 1987). Typical characteristics of these instruments are a sensitivity of ~ 100 mCrab in one day of observation, an angular resolution of the order of degrees and a duty cycle (i.e. the fraction of time that each sky position is covered) between 10^{-4} and 10^{-2}. Three successful ASMs have flown up till 1992[5]. The most sensitive ASM was that on board the *Ginga* satellite (Tsunemi *et al.* 1989), which scanned every day, during 20 minutes, a $360° \times 45°$ region of the sky, observing each sky location for typically 7 s at a 5σ detection threshold of ~ 50 mCrab (2–30 keV) at an angular

---

[5]We do not address here successful ASMs operating at photon energies above ~ 15 keV, e.g. *BATSE* on the *Compton* observatory and *Watch* on the *Granat* observatory.

resolution of 1°. Other (non-scanning) types of ASMs are studied (e.g. Holt & Priedhorsky) that watch the complete sky simultaneously with similar sensitivities, slightly better angular resolutions and higher duty cycles.

It is clear that ASMs fall short in the other fields of interest mentioned above, i.e. monitoring burst activity and weak or short transient behavior. This is mainly due to the small duty cycle of conventional ASMs. This point is illustrated by the fact that much of the knowledge in these fields has not been acquired from ASM data, but by fortunate pointed observations with higher-sensitivity instruments. Furthermore, the location accuracy of ASMs is insufficient to locate events without the help of other instruments. However, the requirement of large sky coverage, inherent to ASMs, remains mandatory for observing burst and short transient events, since these events take place unexpectedly.

Further characteristics of the burst and weak transient sources may be utilized to put constraints on the definition of an optimum instrument for their study. Most importantly, one may ask whether it is essential that the WHOLE sky should be monitored. The answer is negative regarding the XBs and slow transients: they are mainly located along the galactic plane (see e.g. Van Paradijs 1991). Bursters are even more concentrated, towards the galactic center (see e.g. Damen 1990). Therefore, to make a study of these sources it is most efficient to concentrate the observations on this part of the sky. The situation is different for the fast transients, with their isotropic sky distribution. However, an instrument with a somewhat limited sky coverage could still make a worthwhile contribution to the study of these sources, provided that the source location accuracy is better than 1 arcminute, to enable identification with counterparts in other spectral regimes.

Given the above requirements, a good alternative to an ASM is a wide-field coded-mask camera. This instrument principally has the potential of a higher duty cycle and angular resolution, and indirectly provides better sensitivity and temporal resolution. Coded-mask cameras are particularly suited for monitoring selected parts of the sky, such as for instance the galactic center and galactic plane regions. Their use on the galactic center is specifically worthwhile since they do not suffer from source-confusion problems, in contrast to conventional ASMs. One could designate a coded-mask camera as 'selected-sky monitor'. It compares to an ASM (as defined by Holt & Priedhorsky 1987) by stressing temporal and angular resolution at the expense of sky coverage.

1.5 Motivation of the research discussed in this thesis

The SRON-Laboratory for Space Research in Utrecht, in collaboration with the School of Physics and Space Research of the University of Birmingham (UK) and on invitation by the Space Research Institute (IKI) of Moscow in 1981, has developed and built an X-ray wide-field coded-mask camera, to be part of an X-ray observatory on the Soviet manned space station *Mir*. The scientific aims of the utilization of this instrument, called the COded-Mask Imaging Spectrometer (*COMIS*[6]), have been described briefly in the previous section, i.e. the monitoring of X-ray sources (particularly transients and bursters) situated in the galactic bulge and plane. The complete X-ray observatory was launched and coupled to *Mir* (in the *Kvant* module) in April 1987. Since then, it has completed a large number of observations on an intermittent basis.

COMIS is the first WIDE-FIELD coded-mask camera ever launched[7]. Therefore, it also serves as an important pilot experiment regarding the 'hands-on' data handling for such a type of instrument. This is non-trivial: the direct output of a coded-mask camera is not an image of the sky. To arrive at such an image, the raw data needs to be decoded. Computer hardware and software for this decoding process constitute essential parts of the instrument. These parts are not incorporated in the space segment but are located on earth at each of the collaborating institutes. Since the

---

[6]The instrument is in the literature mostly referred to as *TTM*, which is the Russian abbreviation for shadow mask camera. This name will also be used in part II of this thesis.

[7]i.e. with a field of view in excess of 10×10 square degrees. In 1985, the *XRT* coded mask camera was launched with *Spacelab-2* on an eight day long mission (Skinner *et al.* 1987). It had a field of view of 6×6 square degrees and its optical design was different to that of *COMIS*.

instrument is a non-direct imaging device, it is strictly speaking better to name it 'imager' rather than 'camera'. However, since the latter term is more common in the literature, 'camera' is used throughout this thesis.

An important part of the operations of such an instrument is the in-flight performance verification of the space-based as well as ground-based parts. This includes the optimization of the decoding software and the in-flight calibration of the detector and its electronics. For *COMIS*, this task has been handled by the author; the results are treated in part I of this thesis. They provide a fruitful reference to the handling of coded-mask imaging data for future projects carrying similar instruments. Two such cameras are at this date being build by SRON (Jager *et al.* 1989), and will become part of the *SAX* observatory, which is due for launch in 1994. The experience obtained with *COMIS*, both on hardware and software issues, is extensively used in the development of the *SAX* wide-field cameras.

In the second part of this thesis astrophysical results of *COMIS* are highlighted. This includes an overview of the data obtained in the period Oct. 1988–Feb. 1992, a presentation and discussion of the archive obtained from *COMIS*-data on most of the observed X-ray sources, specific results on transients and particularly on the bright X-ray transient GS2023+338.

Some final remarks:

- Unfortunately *COMIS* did not yield a database as large as was originally envisaged. Therefore, the results are as yet meager for population studies of transients and bursters. Instead, the author has emphasized in this thesis the presentation of the problems related to coded-mask imaging in practice, i.e. the decoding process and calibration-items that are particularly important for coded-mask imaging. The potential of coded-mask camera observations for future population studies of transients and bursters can, nevertheless, be convincingly demonstrated.

- Chapters 1 to 4 form an introduction to the remainder of this thesis. Chapter 4 was written in collaboration with W.A. Mels. The investigations discussed in chapters 5 to 7 have been carried out by the author in collaboration with several persons at the SRON-Laboratory for Space Research Utrecht: J.A.M. Bleeker (Chs. 6 and 7), A.C. Brinkman (Ch. 2), J.J. Blom (Ch. 7), J. Heise (Chs. 5 and 7), R. Jager (Chs. 5 and 7), W.A. Mels (Chs. 6) and J.J. Schuurmans (Ch. 5). Chapter 8 has been published in *Advances in Space Research* and chapter 9 is accepted for publication in *Astronomy & Astrophysics*. The investigations discussed in these two chapters were carried out by the author in collaboration with a number of co-authors who are mentioned on the chapter title pages.

References

Alpar, M.A., Shaham, J.: 1985, *Nature* **316**, 239

Bradt, H.V.D., McClintock, J.E.: 1983, *Ann. Rev. Astron. Astrophys.* **21**, 13

Bradt, H.V.D., Ohashi, T., Pounds, K.A.: 1992, to appear in *Ann. Rev. Astron. Astrophys.***30**

Connors, A., Serlemitsos, P.J., Swank, J.H.: 1986, *Astrophys. J.* **303**, 769

Córdova, F.A., Mason, K.O.: 1983, in "*Accretion-Driven Stellar X-ray Sources*", eds. E.P.J. van den Heuvel and W.H.G. Lewin (Cambridge: Cambridge University Press), 147

Damen, E.: 1990, Ph.D. Thesis (University of Amsterdam)

Giacconi, R., Hursky, H., Paolini, F.R., Rossi, B.B.: 1962, *Phys. Rev. Lett.* **9**, 439

Hasinger, G., Van der Klis, M.: 1989, *Astron. Astrophys.* **225**, 79

Hasinger, G., Van der Klis, M., Ebisawa, K., Dotani, T., Mitsuda, K.: 1990, *Astron. Astrophys.* **235**, 131

Hoffman, J.A., Marshall, H.L., Lewin, W.H.G.: 1978, *Nature* **271**, 630

Holt, S.S., Priedhorsky, W.: 1987, *Sp. Sc. Rev.* **45**, 269

Jager, R., in 't Zand, J.J.M., Schuurmans, J.J., Heise, J., Mels, W.A., Brinkman, A.C.: 1989, *SPIE Proc. Ser.* **1159**, 2

Johnson, H.M., Stephenson, C.B.: 1966, *Astrophys. J. Lett.* **146**, 602

Koyama, K., Kawada, M., Kunieda, H., Tawara, Y., Takeuchi, Y., Yamauchi, S.: 1990, *Nature* **343**, 148

Lamb, F.K., Shibazaki, N., Alpar, M.A., Shaham, J.: 1985, *Nature* **317**, 681

Lamb, F.K.: 1989, in ”*Proc. 23rd ESLAB Symp. on Two Topics in X-Ray Astronomy*”, eds. J. Hunt and B. Battrick (Noordwijk: ESA SP-296), 215

Makishima, K.: 1988, in ”*Proc. Int. Symp. on Physics of Neutron Stars and Black Holes*”, ed. Y. Tanaka (Tokyo: Universal Academy Press), 175

Miyamoto, S., Kitamoto, S.: 1989, *Nature* **342**, 773

Parmar, A.N., White, N.E.: 1988, *Memoria S. A. It.* **59**, 147

Priedhorsky, W.C., Holt, S.S.: 1987, *Sp. Sc. Rev.* **45**, 291

Pye, J.P., McHardy, I.M.: 1983, *Mon. Not. R. Astron. Soc.* **205**, 875

Rappaport, S.A., Van den Heuvel, E.P.J.: 1982, in ”*Be-stars*” (IAU-Symp. No. 96), eds. M. Jaschek and H.-G. Groth (Dordrecht: Reidel), 327

Rappaport, S.A., Joss, P.C.: 1983, in ”*Accretion-Driven Stellar X-ray Sources*”, eds. E.P.J. van den Heuvel and W.H.G. Lewin (Cambridge: Cambridge University Press), 1

Sandage, A.R., Osmer, P., Giacconi, R., *et al.*: 1966, *Astrophys. J.* **146**, 316

Savonije, G.J.: 1983, in ”*Accretion-Driven Stellar X-ray Sources*”, eds. E.P.J. van den Heuvel and W.H.G. Lewin (Cambridge: Cambridge University Press), 343

Schreier, E., Levinson, R., Gursky, H. *et al.*: 1972, *Astrophys. J. Lett.* **172**, L79

Skinner, G.K., Willmore, A.P., Eyles, C.J. *et al.*: 1987, *Nature* **330**, 544

Stella, L., White, N.E., Rosner, R.: 1986, *Astrophys. J.* **308**, 669

Tsunemi, H., Kitamoto, S., Manabe, M., Miyamoto, S., Yamashita, K., Nakagawa, M.: 1989, *Pub. Astron. Soc. Japan* **41**, 391

Van der Klis, M.: 1989, *Ann. Rev. Astron. Astrophys.* **27**, 517

Van Paradijs, J.: 1983, in ”*Accretion-Driven Stellar X-ray Sources*”, eds. E.P.J. van den Heuvel and W.H.G. Lewin (Cambridge: Cambridge University Press), 189

Van Paradijs, J.: 1989, in ”*Proc. Workshop on Timing Neutron Stars*”, eds. H. Ögelman and E.P.J. van den Heuvel, NATO ASI Series No. C262 (Dordrecht: Kluwer Academic Publishers), 191

Van Paradijs, J.: 1991, in ”*Neutron Stars: Theory and Observation*”, eds. J. Ventura and D. Pines (Dordrecht: Kluwer Academic Publishers), 245

Van Paradijs, J., Verbunt, F.: 1984, in ”*High Energy Transients in Astrophysics*”, ed. S.E. Woosley (New York: American Institute of Physics), 49

White, N.E., Kaluzienski, J.L., Swank, J.H.: 1984, in ”*High Energy Transients in Astrophysics*”, ed. S.E. Woosley (New York: American Institute of Physics), 31

White, N.E.: 1989, *Astron. Astrophys. Rev.* **1**, 85

Part I

COMIS/TTM
Instrument Description
&
Calibration

.
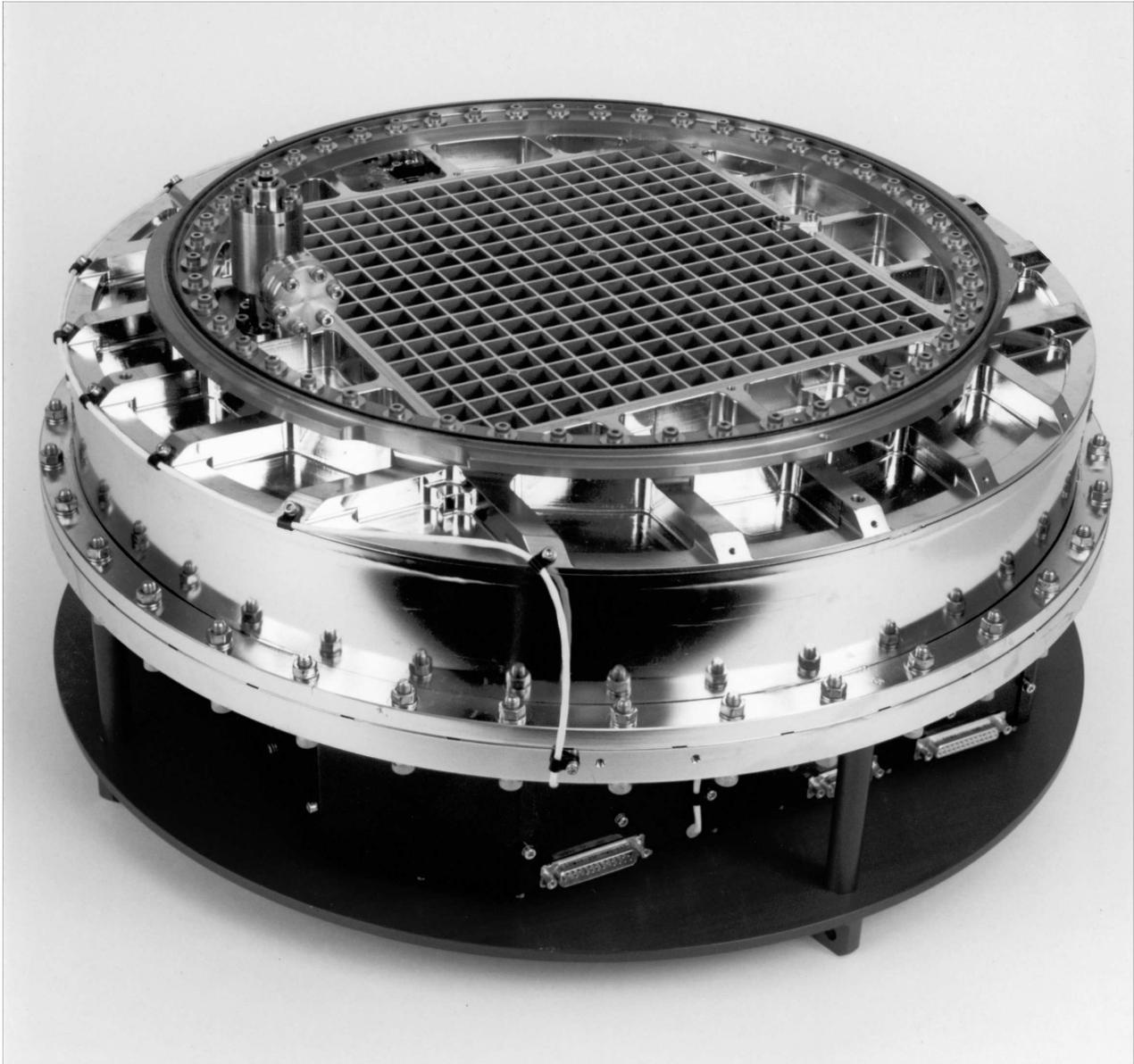
Photograph of the COMIS *detector (top) and its electronics (bottom). Clearly visible is the support structure grid in front of the entrance window (see Chapter 4).*

Chapter 2

The *Mir-Kvant* module and the *Röntgen* observatory

The ***Mir-Kvant*** module and the ***Röntgen*** observatory

Abstract – An overview is given of the four X-ray instruments that are contained in the *Röntgen* observatory, indicating the scientific role of *COMIS* (the subject of this thesis) within the observatory. Furthermore, the basic principles of operations of *Röntgen* are discussed as well as a short history of observations.

2.1 Introduction

In the early 1980's the Space Research Institute (IKI) in Moscow took the initiative to develop and build a scientific module with astrophysical experiments, to be attached to the *Saljut-7* manned space station. A collaboration was formed with institutes from four west-European countries (the Netherlands, United Kingdom, Germany and Switzerland) and the European Space Agency. This resulted in five experiments. Four of these cover the medium and high X-ray regime part of the electromagnetic spectrum between 2 and 800 keV. This group of experiments was given the name 'Röntgen observatory'. The fifth experiment, *GLAZAR*, measures at UV wavelengths.

In reality, the scientific module was attached to the first of a new generation of space stations, *Mir*, and given the name *Kvant*. Docking of the module took place on April 12th 1987, about one year after the launch of *Mir*. Fig. 2.1 shows the general layout of *Kvant* in cutaway.

2.2 The *Röntgen* observatory

The ***Röntgen*** observatory

2.2.1 Payload description

All four X-ray instruments of the *Röntgen* observatory are rigidly fixed to *Kvant* and point towards the same point in the sky. In order to move from one target to another, the entire space station has to be re-oriented. This is accomplished by the use of gyroscopic flywheels. *Kvant* is provided with 6 of these, two in each of three mutually perpendicular planes. To supply the necessary amount of electric power to the gyros, a third blanket of solar cells was installed.

The X-ray instruments cover X-ray energies between 2 and 800 keV (or wavelengths between 1.6×10^{-2} and 6.2 Å). Each of the instruments covers a complementary part of this range, except for *SIRENE-2* (see below). In the following, a brief description of each instrument is given:

1. *COMIS* (COded Mask Imaging Spectrometer, Brinkman *et al.* 1985) has a useful energy range of 2-30 keV, with a spectral resolution of 18% full-width at half-maximum (FWHM) at 6 keV. It is the only imaging instrument of the observatory with a wide field of view (FOV) of 7.8×7.8
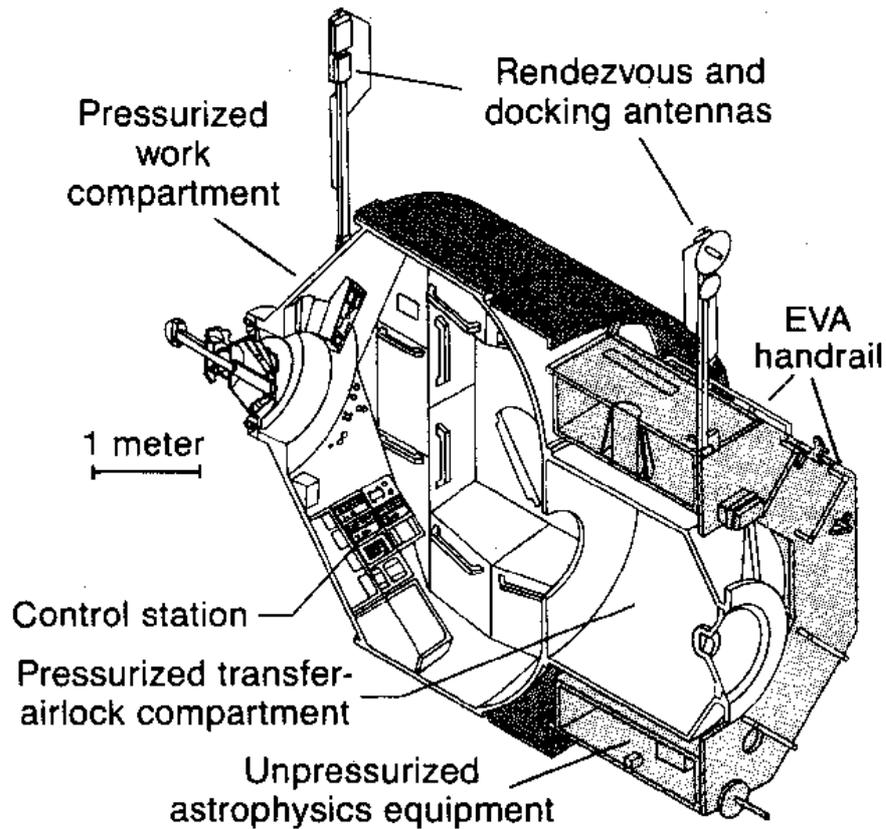
Figure 2.1: General layout of the *Kvant* module in cutaway (from Beatty 1987)

square degrees (FWHM of the collecting area) and an angular resolution of $2'$. The detector (a proportional counter) has a geometric area of 655 cm^2. The data-packing provides a time resolution of 1.0 s. Furthermore, the *COMIS* instrument block includes a star sensor that provides the pointing information for all instruments of the observatory. *COMIS* was built by the SRON-Laboratory for Space Research in Utrecht (the Netherlands) and the School of Physics and Space Research of the University of Birmingham (UK). The design and the analysis of data of this instrument is the subject of this thesis.

2. *HEXE* (High Energy X-Ray Experiment, see Reppin *et al.* 1985) is a joint project of the Max Planck Institut für Extraterrestrische Physik at Garching and the University of Tübingen (Germany). It is a follow-up in a series of *HEXE* detectors that have flown in balloon flights. It consists of a 750 cm^2 geometric area NaI/CsI phoswich detector that operates at X-ray energies of 15-200 keV with an energy resolution of 30% (FWHM) at 60 keV (Mony *et al.* 1989). Its FOV is defined by two honeycomb shaped collimators, each with a 1.6×1.6 square degrees FOV (FWHM). Each collimator can be tilted by $2°3$ to allow for a measurement of the background at 2 minute intervals. The instrument can be used at time resolutions of 0.3 or 25 ms; the latter is used most frequently.

3. *SIRENE-2*, a high pressure gas scintillation proportional counter (GSPC), has a useful sensitivity in the same energy range as *COMIS* and partly *HEXE*: 2-100 keV. It was built by ESA at ESTEC in Noordwijk (the Netherlands) (Smith 1985). Its spectral resolution is better than the other two instruments, e.g. 10.5% (FWHM) at 6 keV. This is coupled to an effective area of 170 cm^2 at 6 keV. Two telemetry modes provide a time resolution of 1.25 and 2.50 ms. The FOV is $2°3$ FWHM.

4. *Pulsar X-1* is the Soviet contribution to the payload of the *Röntgen* observatory, built at the Space Research Institute (IKI) in Moscow (Sunyaev *et al.* 1987). It is sensitive to X-ray energies from 50 to 800 keV, the X-ray photons are detected with four 20 cm diameter NaI/CsI phoswich

detectors. The FOV is 3° FWHM and the time resolution 5 to 10 s.
Both *SIRENE-2* and *Pulsar X-1* depend for background measurements on the rocking mode of the space station (see 2.2.2).

The *Röntgen* observatory is furthermore equipped with the 'Burs' system, that takes care of the telemetry control and allocation to all X-ray instruments, and 'Spectr-3', an on-board quick-look facility to monitor the time-variability of the X-ray fluxes detected in the experiments. Finally, a power-supply filter block is present.

2.2.2   Some basic principles of operations

Mir's orbit is about 350 km above the earth at an inclination angle of 57°. Several items associated with this orbit have impact on the programming of observations with *Röntgen*:

- During the $1\frac{1}{2}$ hour orbit, the station may cross the South Atlantic Anomaly (SAA). All X-ray experiments are then turned off to prevent damage by high fluxes of energetic particles and photons, present in this magnetic belt.

- Ground contact is only available during a limited part of the orbit, either with a ground station in the former USSR or with a communications ship.

- Observations are usually done in day light, to acquire enough power from the solar panels. Furthermore, the orientation of the *Mir* in space must ensure an optimal orientation of the solar panels with respect to the sun.

The precise constraints that determine the observation's programming are not publicly available; however, practical experience during the first three years of operations (based on the data of 128 operational days of *COMIS*) has shown that:

- The effective useful observing time per orbit can be as high as half an hour; on average it amounts to 20 minutes.

- Out of 16 orbits per day, at most 7 to 8 are used for operating *Röntgen*, the average is about 4 to 5 orbits per observing day.

- Due to the multi-purpose use of the manned station, interference with *Röntgen* observations is likely. This can result in prolonged periods of inactivity of *Röntgen*.

As discussed above, the *Pulsar X-1* and *SIRENE-2* experiments can only do a background measurement by slewing the entire station, so that both instruments will be pointed away from the X-ray source being studied. Therefore, the 'rocking' mode has been introduced. In this mode the station is rocked at time intervals of 4 minutes between two attitudes 4 to 12° apart. One attitude coincides with the position of the target X-ray source to enable the measurement of the flux of that source (plus background), the other attitude enables a background measurement on "empty" sky. The typical slewing time between the two attitudes is 100 s. The rocking mode is only used when observations with *Pulsar X-1* or *SIRENE-2* have priority, the mode is inconvenient for *COMIS* and *HEXE*. In practice about one out of five observations is done in rocking mode.

2.3   Short history of *Röntgen* operations, up to February 1992

Short history of **Röntgen** operations, up to February 1992

Operations with the X-ray instruments aboard *Kvant* started in June 1987. Within a short time it was clear that two of them did not function properly. *COMIS* and *SIRENE-2* encountered problems with the high-voltage control, ie. the detector gas gain was found to be unstable, thus deteriorating the spectral resolution of the instruments. The problems with *COMIS* became more serious by the end of August 1987 when no scientific data could be extracted anymore from this instrument.
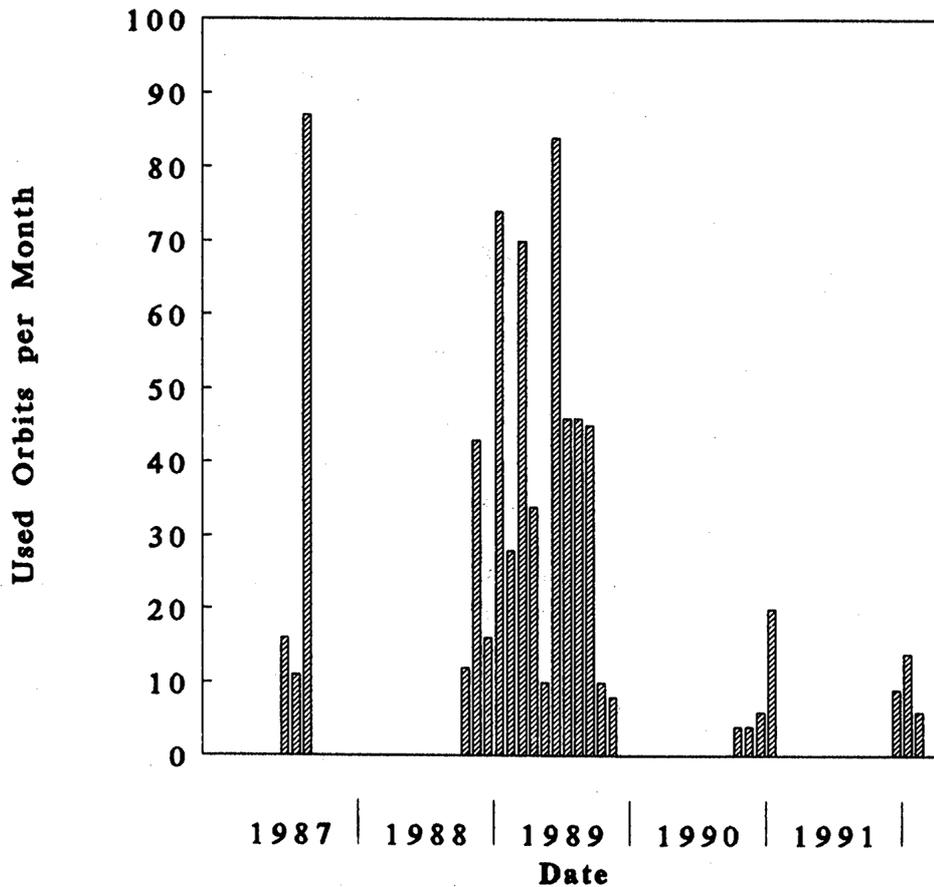
Figure 2.2: Histogram of observation frequency of *COMIS* through almost 5 years of operation (updated to February 1992)

The problem with *COMIS* could be traced to the malfunctioning of a single electronic component (the high-voltage converter). Despite the fact that *COMIS* was not built to be repaired in-flight, the Soviets offered to carry out an exchange with the flight spare detector during an extra vehicular activity (EVA). Thus a repair program was initiated that involved refurbishing and testing the spare flight detector in Utrecht, the design of repair tools in Utrecht, the construction of these tools in Birmingham, the set-up of repair procedures at the cosmonaut training center in Moscow and the training of the cosmonauts aboard *Mir* for the necessary EVA-procedures. A first repair attempt was made on June 30th 1988, but could not be completed. This was achieved during a second EVA on October 20th. Observations started the next day and showed the repair to be a complete success.

Unfortunately, the star sensor experienced also a malfunction, in March 1988. A repair attempt on October 20th failed. Although the *Mir* station was better stabilized than anticipated and *COMIS* could act as a substitute star sensor most of the time, working at X-ray instead of visual wavelengths, the absence of the star-sensor data complicated the X-ray analysis considerably. In particular, if no accurate pointing information can be provided by *COMIS* (when there are less then two X-ray sources detected), the uncertainty in the response of the other instruments is large.

During all this time *HEXE* and *Pulsar X-1* functioned without much trouble.

In November 1989, observations with *Kvant* were stopped temporarily because the *Mir* station was reconfigured with two additional modules, *Kvant-2* and *Kristall*. The on-board activity associated with this change of the station's configuration lasted almost a full year. An attempt was done in October 1990 to restart the observations again. However, it was soon recognized that slewing the revised station cost too much energy: instead of only using the gyroscopic flywheels, rockets were necessary to aid the re-orientation of the station. This situation was solved in about a years time

and operations started again on a reasonably regular basis early 1992. In Fig 2.2 the observation frequency of *COMIS* since launch is presented.

References

Beatty, J.K.: 1987, *Sky & Telescope* **74**, 599

Brinkman, A.C., Dam, J., Mels, W.A., Skinner, G.K., Willmore, A.P: 1985, in "*Proc. Non Thermal and Very High Temperature Phenomena in X-Ray Astronomy*", eds. G.C. Perola and M. Salvati (Roma: Università "La Sapienza"), 263

Mony, B., Kendziorra, E., Maisack, M. *et al.*: 1989, in "*Proc. 23rd ESLAB Symp. on Two Topics in X-Ray Astronomy*", eds. J. Hunt and B. Battrick (Noordwijk: ESA SP-296), 541

Reppin, C., Pietsch., W., Trümper, J., Kendziorra, E., Staubert, R.: 1985, in "*Proc. Non Thermal and Very High Temperature Phenomena in X-Ray Astronomy*", eds. G.C. Perola and M. Salvati (Roma: Università "La Sapienza"), 279

Smith, A.: 1985, in "*Proc. Non Thermal and Very High Temperature Phenomena in X-Ray Astronomy*", eds. G.C. Perola and M. Salvati (Roma: Università "La Sapienza"), 271

Sunyaev, R., Kaniovsky, A., Efremov, V. *et al.*: 1987, *Nature* **330**, 227

Chapter 3

X-ray wide-field camera imaging concept

Abstract – The concept of coded-mask imaging, as applied to X-ray wide-field imaging, is reviewed. The three principal components of a coded-mask imager (mask, detector and reconstruction) are discussed and requirements are introduced to arrive at an optimum imaging capability.

3.1 Introduction: multiplexing techniques as alternative to focusing techniques

In the energy range under consideration (2−30 keV) it is only partly possible to make use of traditional methods to image the sky. Focusing of X-rays is technically feasible for photon energies up to about 10 keV through grazing incidence reflection (Aschenbach 1985). This method can provide a very good angular resolution, i.e. down to $0.5''$ which is the value proposed for AXAF (van Speybroeck 1987). The sensitivity is optimized through the use of nested grazing incidence mirrors. The field of view (FOV) is limited by the grazing incidence to about $1°$, but can be enlarged by using a special configuration of the mirrors ('Lobster-eye' telescopes, Aschenbach 1985).

An alternative class of imaging techniques employs straight line ray optics that offer the opportunity to image at higher photon energies and over larger FOV's. These techniques have one common signature: the direction of the incoming rays is, before detection, encoded; the image of the sky has to be reconstructed by decoding the observation afterwards. It is apparent that this method of producing sky images is a two-step procedure, in contrast to the direct or one-step imaging procedure of focusing techniques. These alternative techniques are referred to as MULTIPLEXING techniques.

Multiplexing techniques can be divided in two classes: those based on TEMPORAL multiplexing and those on SPATIAL multiplexing (Caroli *et al.* 1987). A straightforward example of temporal multiplexing is the scanning collimator: when the direction of a collimator is moved across a part of the sky which contains an X-ray point source, the number of counts per second that is detected as a function of time has a triangular shape. The position of the maximum of the triangle is set by the position of the source along the scanning direction and the height of the triangle is set by the flux of the source. A second scan along another direction completes the two-dimensional position determination of the source. More scans may be necessary if the source is extended or when there are more sources in the FOV of the collimator. The Large Area Counter (LAC) of the Japanese X-ray satellite *Ginga* (Makino *et al.* 1987 and Turner *et al.* 1989) is a recent example of an instrument employing a collimator. Another obvious example of time multiplexing is the covering of an X-ray source by the moving moon.

A more complex but popular device that is based on time multiplexing was introduced by Mertz (1968) and further described by Schnopper *et al.* (1968): the rotation modulation collimator (RMC). RMCs are often used as all-sky monitor. Several RMCs have flown, for instance in *Ariel-V* (Sanford

23

1975), *SAS-3* (Mayer 1972) and *Hakucho* (Kondo *et al.* 1981) and in several balloon experiments (see e.g. Theinhardt *et al.* 1984). The most recent example is the *Granat* observatory which carries 4 RMCs (Brandt *et al.* 1990). In its basic form an RMC has the disadvantage of being insensitive to short term (with respect to the rotation period of the aperture) fluctuations of X-ray intensity, because the temporal information must be used for reconstructing the position of sources. However, techniques to circumvent this problem have been developed (Lund 1985).

Temporal multiplexing techniques in principle do not need a position-sensitive detector, contrary to spatial multiplexing techniques. Spatial multiplexing techniques can be divided in two subclasses: in the first subclass two or more collimator grids, widely separated, are placed in front of a detector, and in the second subclass one or more arrays of opaque and transparent elements are placed there. Instruments of the former class are called 'Fourier transform imagers' (Makishima *et al.* 1978 and Palmer & Prince 1987). These instruments record a number of components of the Fourier transform of the observed sky, and the observed sky can be reconstructed by inverse Fourier transform in a way that is common in radio astronomy ('CLEAN' algorithm).

Instruments of the second subclass are called 'coded-mask systems'. *COMIS* belongs to this subclass. In the following chapter, a short review is given on the imaging concept of coded-mask systems, dealing separately with each important component of such a system. This includes requirements to arrive at an optimum imaging capability of the whole system.

3.2   Basic concept of coded-mask imaging

A coded-mask camera, intended to image the sky in the photon energy band E_1 to E_2, basically consists of:

- a coded mask, i.e. a plate with areas that are transparent or opaque to photons in the energy range E_1 to E_2. The transparent and opaque areas, or shortly 'mask elements', all have an equal size and are distributed in a pre-determined pattern, which is placed on a regular grid. The form of a mask element may be arbitrary.

- a position-sensitive detector, whose spatial resolution is sufficiently matched to the mask-pattern grid size and which is sensitive to photons with energies between E_1 and E_2.

The principle of the camera is straightforward (Fig. 3.1): photons from a certain direction in the sky project the mask on the detector; this projection has the same coding as the mask pattern, but is shifted relative to the central position over a distance uniquely correspondent to the direction of the photons. The detector accumulates the sum of a number of shifted mask patterns. Each shift encodes the position and its strength encodes the intensity of the sky at that position. It is clear that each part of the detector may detect photons incident from any position within the observed sky. After a certain illumination period, the accumulated detector image may be decoded to a sky image by determining the strength of EVERY possible shifted mask pattern.

Proper performance of a coded-mask camera requires that every sky position is encoded on the detector in a unique way. This can be stated in terms of the autocorrelation function of the mask pattern: this should consist of a single peak and flat side-lobes. This puts demands on the type of mask pattern and on the way its (shifted) projections are detected.

An important difference to direct-imaging systems is the fact that Poisson noise from any source in the observed sky is, in principle, induced at ANY other position in the reconstructed sky.

The imaging quality of the camera is determined by the type of mask pattern, the optical design of the camera, the spatial response of the detector and the decoding (or reconstruction) method. These items will be discussed in the remainder of this chapter.

3.3   Mask pattern

In view of the imaging quality, one would want the mask pattern to satisfy the following conditions:
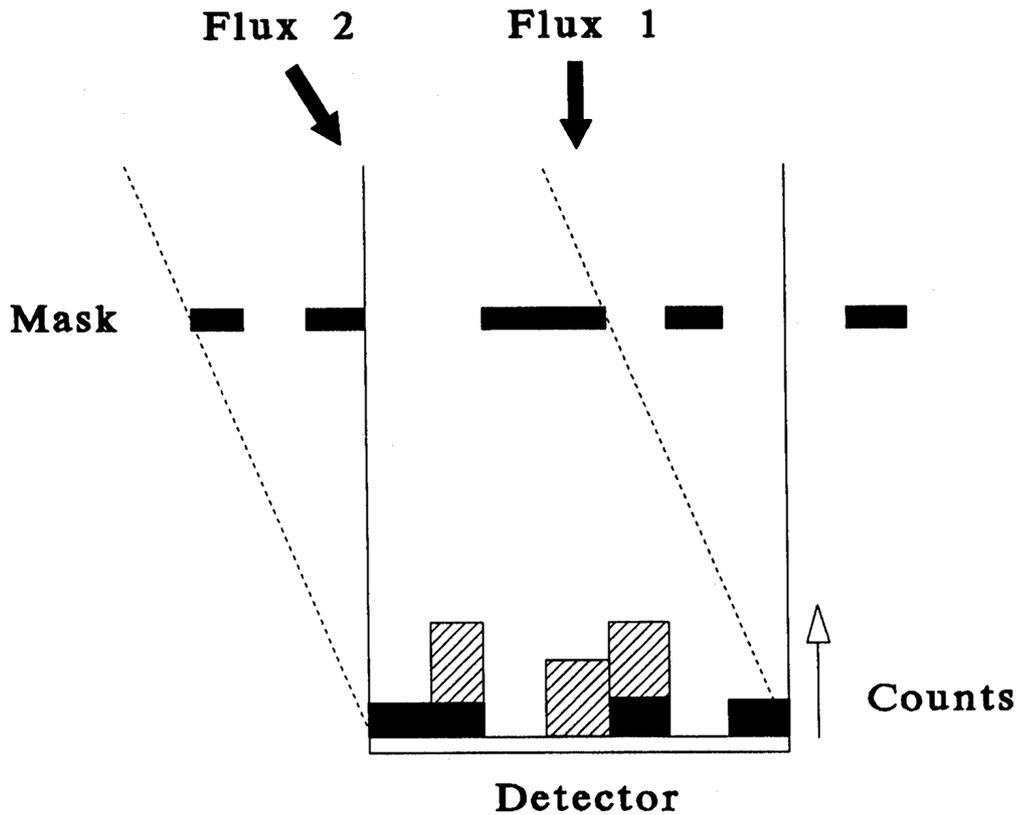
Figure 3.1: Basic concept of coded-mask imaging. Two point sources illuminate a position-sensitive detector through a mask. The detector thus records two projections of the mask pattern. The shift of each projection encodes the position of the corresponding point source in the sky; the 'strength' of each projection encodes the intensity of the point source

1) the autocorrelation function of the mask pattern should be a single peak with perfectly flat side-lobes;
2) the signal-to-noise ratio of a coded sky source should be optimum.

In the early days of multiplex imaging, two types of mask patterns were proposed: a pattern of Fresnel zones (Mertz & Young 1961) and the random pinhole pattern (Dicke 1968 and Ables 1968). While a camera with a Fresnel zone plate was never applied in X-ray astronomy (except for solar studies in the early 1970's), concepts based on the random pinhole pattern have. The random pinhole pattern was proposed as an extension of a pinhole camera. The pinhole camera has ideal imaging properties with respect to the first condition (in fact it is a direct-imaging system), but delivers a poor signal-to-noise ratio, since the sensitive area is severely restricted by the size of the pinhole. The sensitivity may be increased by enlarging the pinhole, but at the expense of angular resolution. The idea behind the random pinhole camera is to increase the open area of the plate, while preserving the angular resolution, by placing many duplicate pinholes at random in the plate. The random character is necessary to meet the first condition as closely as possible.

Both Fresnel zone and random pinhole mask patterns are not ideal with respect to the first condition, the patterns possess autocorrelation functions whose sidelobes are not perfectly flat. Later work concentrated on finding patterns, based on the idea of the random pinhole pattern, that do have flat side-lobes. Ideal patterns were found that are based on cyclic difference sets (Gunson & Polychronopulos 1976).

A cyclic difference set D, characterized by the parameters n, k and z, is a collection of k integer numbers $\{I_1, I_2, ..., I_k\}$ with values $0 \leq I_i < n$, such that for any $J \neq 0 \pmod{n}$ the congruence

$I_i - I_j = J \pmod{n}$ has exactly z solution pairs (I_i, I_j) within D (Baumert 1971). An example of a cyclic difference set D with $n = 7$, $k = 4$ and $z = 2$ is the collection $\{0, 1, 2, 4\}$. Cyclic difference sets can be represented by a binary sequence a_i $(i = 0, ..., n-1)$ with $a_i = 1$ if i is a member of D and $a_i = 0$ otherwise. In the above example a_i is given by 1110100. a_i in turn can stand for the discretized mask pattern, assigning a transparent element to $a_i = 1$ and an opaque one to $a_i = 0$. The cyclic autocorrelation c_l of a_i is (Baumert 1971):

$$c_l = \sum_{i=0}^{n-1} a_i a_{\bmod (i+l,n)} = \begin{cases} k & \text{if } \bmod(l,n) = 0 \\ z = \frac{k(k-1)}{n-1} & \text{if } \bmod(l,n) \neq 0 \end{cases} \qquad (3.1)$$

i.e. a single peak on a flat background. A mask pattern based on a_i consequently satisfies condition 1. a_i has the characteristic that every difference $i - j$ between a pair of $a_i, a_j = 1$ is equally sampled and therefore these arrays are also called Uniformly Redundant Arrays (URA, Fenimore & Cannon 1978).

From the autocorrelation it can be anticipated that it is advantageous with respect to condition 2 to have a difference between k and z that is as large as possible, for k determines the signal and z the background level (and its noise)[1]. The maximum difference is reached if $n = 4t - 1$, $k = 2t - 1$ and $z = t - 1$ if t is integer. These cyclic difference sets are called Hadamard difference sets (Hall 1967 and Baumert 1971) and can be classified in at least three types, according to the value of n:
  1) Quadratic residue sets: n is prime (the members of this set are given by the squares, modulo n, of the first $(n + 1)/2$ integers);
  2) Twin prime sets: $n = p(p + 2)$ for integer p, p and $p + 2$ being prime;
  3) Pseudo-noise sets: $n = 2^m - 1$ ($m > 1$ is integer).
Some Hadamard difference sets may belong to more than one class, the existence of a set with a value for n given by a class is guaranteed. The above example is a quadratic residue set as well as a pseudo-noise set. Characteristic for Hadamard sets is that $k = (n - 1)/2$, i.e. for large n the mask pattern is about half open. The cyclic autocorrelation then is:

$$c_l = \begin{cases} \frac{n-1}{2} & \text{if } \bmod(l,n) = 0 \\ \frac{n-3}{4} & \text{if } \bmod(l,n) \neq 0 \end{cases}$$

Another collection of cyclic difference sets are the so-called Singer sets, that are characterized by $n = (t^{m+1} - 1)/(t - 1)$, $k = (t^m - 1)/(t - 1)$ and $z = (t^{m-1} - 1)/(t - 1)$, where t is a prime power. The equivalent mask pattern will have smaller open fractions than those based on Hadamard sets; for $t \gg 1$ the open fraction approximates $1/t$.

A way to construct a pseudo-noise Hadamard set is the following (Peterson 1961): if $p(0), ..., p(m-1)$ are the factors of an irreducible polynomial of order m ($p(i)$ is 0 or 1) then a_i is defined by a shift register algorithm:

$$a_{i+m} = \sum_{j=0}^{m-1} p(j) a_{i+j} \qquad (i = 0, ..., 2^m - 2) \qquad (\bmod 2) \qquad (3.2)$$

The first m values of this recursive relation, $a_0, ..., a_{m-1}$, can be chosen arbitrarily: a different choice merely results in a cyclic shift of a_i.

If n can be factorized in a product of two integers ($n = p \times q$), it is possible to construct a two-dimensional array $a_{i,j}$ $(i = 0, ..., p - 1; j = 0, ..., q - 1)$ from the URA a_i $(i = 0, ...n - 1)$. The mask pattern thus arranged is called the 'basic pattern'. The ordering of a_i in two dimensions should be such, that the autocorrelation characteristic (Eq. 3.1) is preserved. This means that in a suitable extension of the basic $p \times q$ pattern, any $p \times q$ section should be orthogonal to any other $p \times q$ section. A characteristic of a URA a_i is that any array a_i^s, formed from a_i by applying a cyclic shift to its elements ($a_i^s = a_{\bmod (i+s,n)}$), is again a URA which is orthogonal to a_i. Therefore, the

---

[1]The argument followed here to meet condition 2 is simplified. In fact, the optimum open fraction of the mask pattern is also dependent on specific conditions concerning the observed sky. See e.g. Skinner (1984).
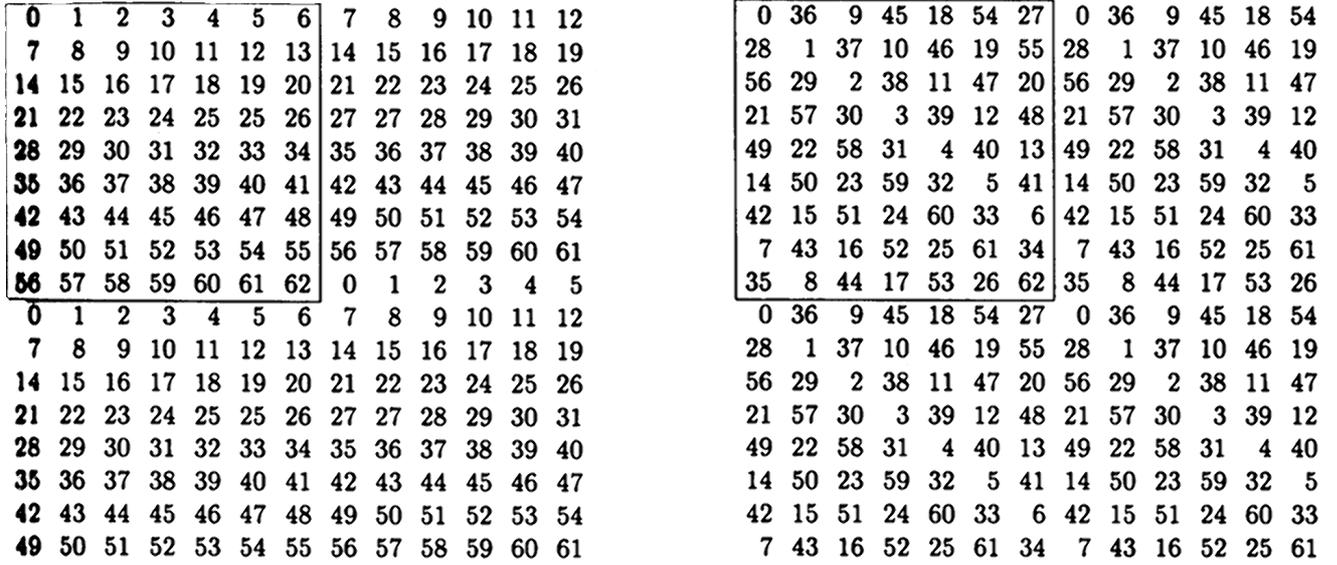
```
 0  1  2  3  4  5  6 | 7  8  9 10 11 12        0 36  9 45 18 54 27 | 0 36  9 45 18 54
 7  8  9 10 11 12 13 |14 15 16 17 18 19       28  1 37 10 46 19 55 |28  1 37 10 46 19
14 15 16 17 18 19 20 |21 22 23 24 25 26       56 29  2 38 11 47 20 |56 29  2 38 11 47
21 22 23 24 25 25 26 |27 27 28 29 30 31       21 57 30  3 39 12 48 |21 57 30  3 39 12
28 29 30 31 32 33 34 |35 36 37 38 39 40       49 22 58 31  4 40 13 |49 22 58 31  4 40
35 36 37 38 39 40 41 |42 43 44 45 46 47       14 50 23 59 32  5 41 |14 50 23 59 32  5
42 43 44 45 46 47 48 |49 50 51 52 53 54       42 15 51 24 60 33  6 |42 15 51 24 60 33
49 50 51 52 53 54 55 |56 57 58 59 60 61        7 43 16 52 25 61 34 | 7 43 16 52 25 61
56 57 58 59 60 61 62 | 0  1  2  3  4  5       35  8 44 17 53 26 62 |35  8 44 17 53 26
 0  1  2  3  4  5  6  7  8  9 10 11 12         0 36  9 45 18 54 27  0 36  9 45 18 54
 7  8  9 10 11 12 13 14 15 16 17 18 19        28  1 37 10 46 19 55 28  1 37 10 46 19
14 15 16 17 18 19 20 21 22 23 24 25 26        56 29  2 38 11 47 20 56 29  2 38 11 47
21 22 23 24 25 25 26 27 27 28 29 30 31        21 57 30  3 39 12 48 21 57 30  3 39 12
28 29 30 31 32 33 34 35 36 37 38 39 40        49 22 58 31  4 40 13 49 22 58 31  4 40
35 36 37 38 39 40 41 42 43 44 45 46 47        14 50 23 59 32  5 41 14 50 23 59 32  5
42 43 44 45 46 47 48 49 50 51 52 53 54        42 15 51 24 60 33  6 42 15 51 24 60 33
49 50 51 52 53 54 55 56 57 58 59 60 61         7 43 16 52 25 61 34  7 43 16 52 25 61
```

Figure 3.2: Schematic diagram, showing two methods of constructing a two-dimensional array from a one-dimensional URA, without loosing the autocorrelation property (Eq. 3.1): ordering by rows (left) and ordering along diagonals (right). The numbers indicate the element index of the one-dimensional array. The squares indicate the basic pattern (containing the array once). In these two examples $p = 7$, $q = 9$ and $n = 63$. The elements of the expansion to a 2×2 mosaic of the basic pattern are ordered in the same manner as the basic pattern. The last row and column of the expanded array are omitted, to avoid the autocorrelation to have more than one peak

autocorrelation characteristic of the expanded $a_{i,j}$ is fulfilled if every $p \times q$ section is a cyclic shift of the basic pattern. Two examples of valid ordering methods are shown in Fig. 3.2: ordering by rows (Miyamoto 1977) and ordering along extended diagonals (Proctor *et al.* 1979). In the latter case p and q should not have a common divisor (they should be mutually prime), otherwise one is not able to fill the basic pattern completely. Other valid orderings are possible.

The pseudo-noise arrays have the convenient property that they can easily be wrapped in almost a square of $n \gg 1$: if m is even, n can be written as $n = 2^m - 1 = (2^{\frac{m}{2}} - 1)(2^{\frac{m}{2}} + 1)$, so that p and q only differ by 2.

A problem that is encountered in the manufacturing of a two-dimensional mask plate for X-ray energies involves an opaque mask element that is completely surrounded by transparent elements. In the X-ray regime it is necessary to keep transparent elements completely open, because the use of any support material at open mask elements soon results in too much absorption of photons. Thus, an isolated opaque mask element will not have any support. Two methods may be applied to solve this problem:

1) Choose a mask pattern where no isolated opaque elements occur. Such patterns are called 'self-supporting'.
2) Include a support grid in the mask plate.

Generally the second option is chosen, because every opaque element is then supported completely along its sides while in the first option opaque elements might still be only weakly supported at some of its corners. This does not affect the ideal autocorrelation characteristic, because the pattern is not altered and remains two-valued. However, the open area will be decreased somewhat, resulting in less sensitive area.

The autocorrelation characteristic remains valid only if the coding is performed by the use of a complete cycle of a basic pattern. As soon as the coding is partial, noise will emerge in the side-lobes of the autocorrelation function. This noise can be interpreted as false peaks and thus deteriorates the imaging quality. In order to be able to record for every position in the observed
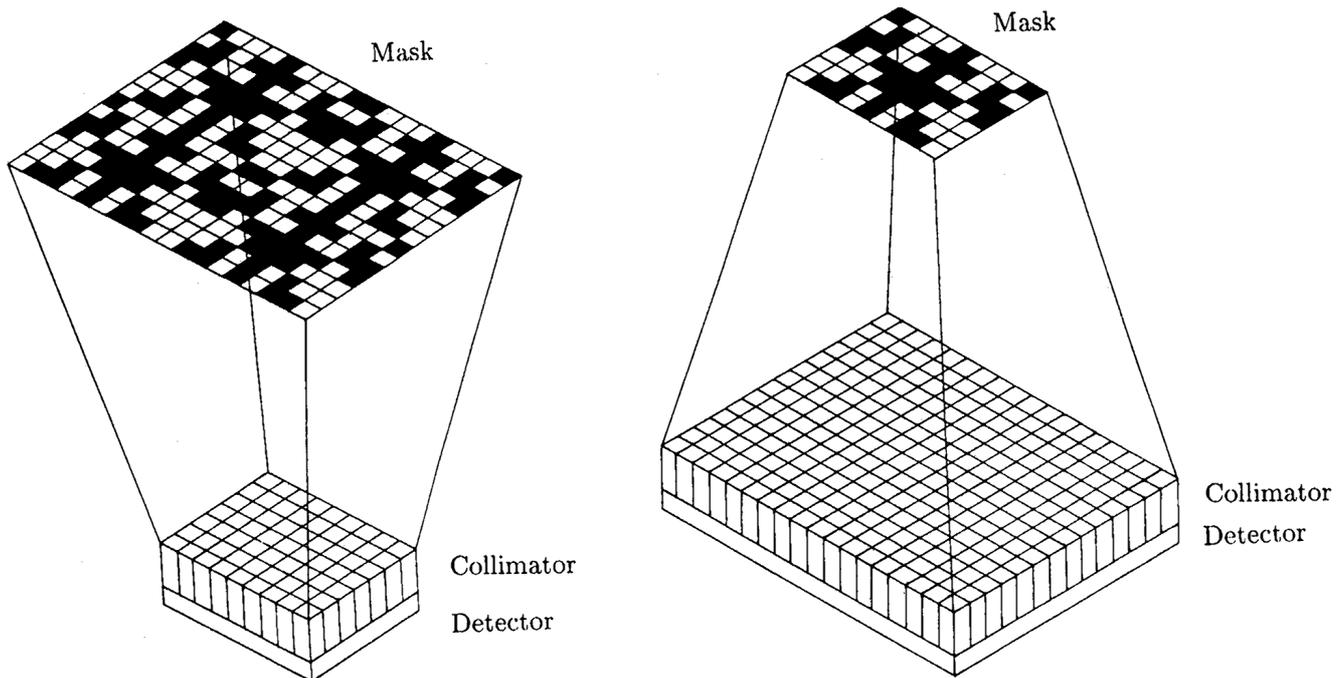
Figure 3.3: Schematic drawings of the two types of 'optimum' configurations discussed in the text. The left configuration is called 'cyclic'. Note the collimator, placed on top of the detector, necessary to confine the FOV to that part of the sky in which every position will be coded by one full basic pattern. From Hammersley (1986)

sky a full basic pattern, one needs a special optical configuration of mask and detector (see next section). Sometimes also a mask is needed that consists of more than 1 basic pattern. How such a mosaic mask is constructed has been discussed above (see Fig. 3.2).

3.4   Optical design

The optical design of a coded-mask camera is defined by the sizes of the mask, the mask elements and the detector, the number of basic patterns used in the mask, the distance between mask and detector and the size and place of an optional collimator. Apart from the imaging quality, the design determines the angular resolution and the FOV (the latter is usually expressed in the full-width at half maximum, FWHM, of the collecting area across the observed sky).

3.4.1   Optimum and simple configurations

As concluded in 3.3, for ideal imaging properties it is necessary to record for every position in the observed sky a complete cycle of the basic pattern. This can be accomplished by configuring the mask and detector in one of the following two ways[2] :

1) The mask consists of one $p \times q$ basic pattern, while the detector has a size of $(2p - 1) \times (2q - 1)$ mask elements (Fig. 3.3, right). By the implementation of a collimator in front of the detector, the observed sky is restricted to those positions in the sky from where the mask is completely projected on the detector.

2) The mask consists of a mosaic of almost 2×2 cycles of the basic pattern ($(2p - 1) \times (2q - 1)$ mask elements), while the detector is as large as one basic pattern (Fig. 3.3, left). A collimator is implemented, to restrict the observed sky, as seen from any position on the detector, to that

---

[2]Other configurations can be thought of (Proctor *et al.* 1979) that are extensions of the two mentioned here.
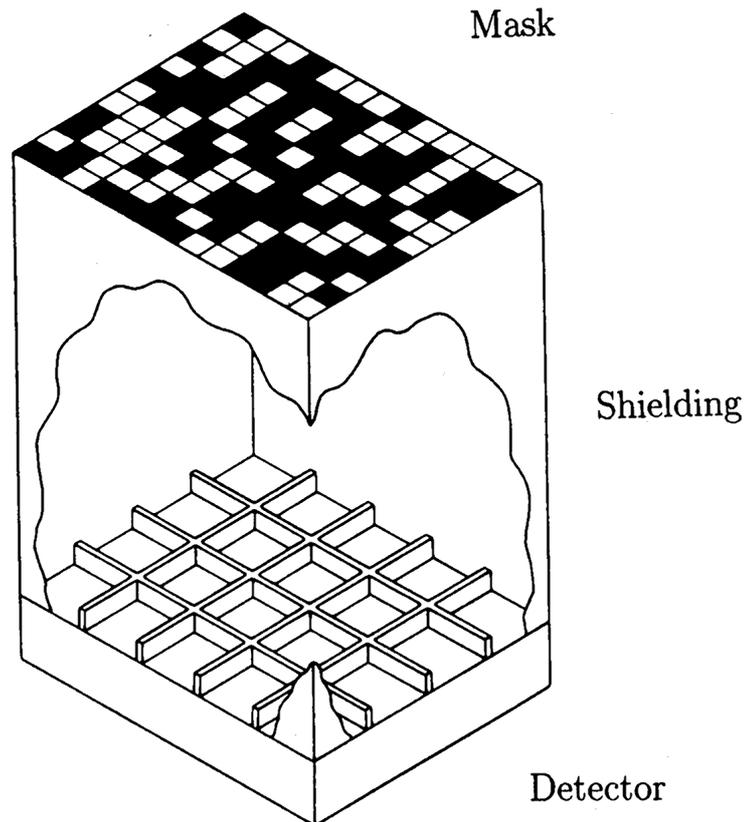
Figure 3.4: Schematic drawing of the 'simple' configuration. The sizes of the mask and detector are equal. Note that instead of a collimator, as in the optimum configurations, a shielding is used. The shielding prevents photons not modulated by the mask pattern to reach the detector. From Hammersley *et al.* (1992)

part of the sky seen through one complete cycle of the basic pattern. This type of configuration often is called 'cyclic' because of the nature of the mask.

In both types the collimator gives a pyramidical-to-zero response function to the collecting detector area over the observed sky and its use may be coupled to the need for a support structure for the entrance window of the detector (Gunson & Polychronopulos 1976). In practice the choice between both types may depend on which of the components is restricted most in size by exterior conditions: the mask or the detector. However, in astronomical applications, the argument of preservation of the collecting area prevails and the choice is usually for the cyclic type.

The above types of mask/detector configurations are called 'optimum systems' (Proctor *et al.* 1979) in the sense that the imaging property is optimum. An alternative configuration is the 'simple system'[3]. In this system the need for full coding is relaxed. The detector has the same size as the mask, which consists of one basic pattern (see Fig. 3.4). No collimator is then needed on the detector; instead a shielding is used to prevent photons that do not pass the mask from entering the detector. In a simple system only the on-axis position is coded with the full basic pattern, the remainder of the FOV is partially coded. Obviously, the off-axis sources will cause false peaks in the reconstruction. However, as will be discussed later on, this coding noise can be eliminated to a large extent in the data-processing, provided not too many sources are contained in the observed part of the sky.

If one assumes for the moment that coding noise is not relevant, the question arises how the simple system compares to the cyclic system. In order to do this comparison, it seems fair to impose on both systems the same FOV and sensitivity. This means that both have a detector of equal

---

[3]Recently, also the designation 'box system' has become popular in the literature on this subject.
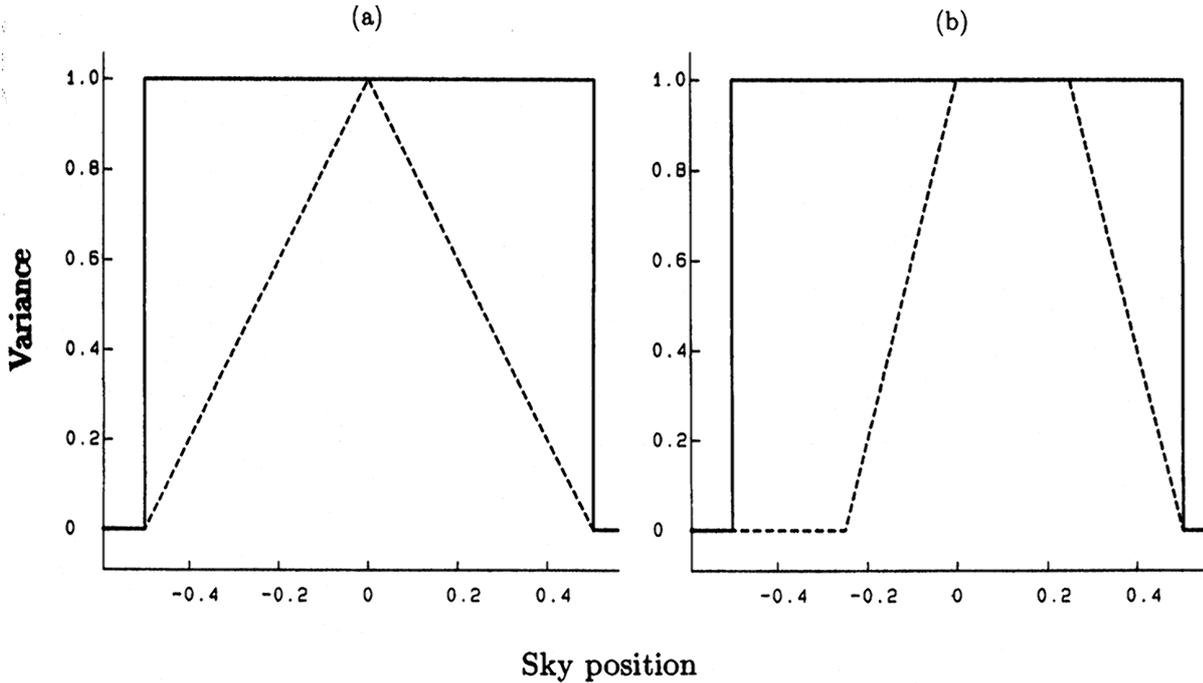
Figure 3.5: Schematic graphs for the comparison between the cyclic and the simple system, as described in the text. Plotted are the variances across the reconstructed sky, due to (**a**) the background and (**b**) an off-axis point source. Drawn curves refer to the cyclic system and dashed curves to the simple system. Sky positions and variances are given in arbitrary units. Some comments on both figures: **a.** Since both systems have the same sensitivity and FOV, the illumination by the sky background per detector element is the same. For an off-axis position, the reconstruction in the cyclic system involves all background photons, while that in the simple system only involves the photons not obscured by the shielding from that position. The variance due to the Poisson noise of background photons is therefore less in the simple system (except for the on-axis position). **b.** In a simple system an off-axis source only illuminates part of the detector, while in an cyclic system the total detector is illuminated. In both cases, the total number of detected photons from this source is the same. Reconstructing for another off-axis position in the simple system, only part (potentially even none) of the source photons give rise to Poisson noise. In the cyclic system ALL source photons give rise to Poisson noise

size, but in the cyclic system the 2×2 mosaic mask is two times closer to the detector than in the simple system, with an appropriate adjustment of the collimator's dimensions. Therefore, the angular resolution in the cyclic system is two times worse in each dimension than in case of the simple system. Most important in the comparison is the following difference between the cyclic and the simple system, concerning the reconstruction of the flux from an arbitrary direction within the observed sky: in the cyclic system all detected photons on the complete detector may potentially come from that direction, while in the simple system only photons from the section of the detector not obscured by the shielding are relevant. Therefore, Poisson noise will affect the reconstruction in the cyclic system stronger than in the simple system. This is specified graphically in Fig. 3.5. Thus, regarding the Poisson noise, the simple system is superior in sensitivity to the cyclic system (except for the on-axis position where both systems have equal properties). This conclusion is in agreement with the findings of Sims *et al.* (1980), who have studied the performance of both systems via computer simulations.

3.4.2 Angular resolution

The angular resolution is given by the angle subtended by a mask element as seen from the detector. If the mask elements are square shaped, with a size of $s_m \times s_m$ mm^2, and the distance between mask and detector is F mm, the angular resolution ϕ (FWHM) along each axis at an off-axis angle θ in the observed sky is equal to:

$$\phi_{x,y} \;=\; \arctan\left(\frac{s_m \cos^2(\theta_{x,y})}{F}\right) \text{ rad} \tag{3.3}$$

The $\cos^2$-factor is due to projection effects.

3.4.3 Field of view

The size of the FOV is of the order of the angle that the mask subtends as seen from the detector along each axis. Its precise value depends on the characteristics of an optional collimator. If the mask and detector are square and r is the ratio of the one-dimensional detector size to the mask-detector separation, the FOV for a simple system is given by:

$$\Omega_{tot} \;=\; 2\pi - 8\arcsin\left(\frac{1}{\sqrt{2(1+r^2)}}\right) \qquad \text{sr} \tag{3.4}$$

(Sims 1981). The same equation also applies to an optimum system, provided r is interpreted as the ratio of the horizontal collimator grid cell size to the cell height.

3.5 Detector requirements

The detector should make a proper recording of the projected mask pattern. Therefore, it should meet a number of requirements with respect to its spatial response.

3.5.1 Spatial resolution

Inherent to any detector system is a limited spatial resolution: the position of a detected photon is influenced by noise, emerging from various physical and electronic processes in the detector system. In general the spatial noise may be modeled by a two-dimensional Gaussian distribution function $P(x,y)$, describing the probability per unit area that the position of a count is measured within $(x - ...x + \mathrm{d}x, y - ...y + \mathrm{d}y)$ from the true position:

$$P(x,y)\mathrm{d}x\,\mathrm{d}y \;\sim\; \mathrm{e}^{-\frac{x^2}{2\sigma_x^2}}\,\mathrm{e}^{-\frac{y^2}{2\sigma_y^2}}\mathrm{d}x\,\mathrm{d}y \tag{3.5}$$

with σ_x and σ_y the standard deviations along x and y.

The projection of a mask hole is a square block function with a base size of $s_m \times s_m$. The convolution (or 'smearing') of this function with the Gaussian spatial detector resolution causes the sharp edges of the block function to be smoothed and, if the smearing dominates, the mask-hole projection becomes substantially larger than the mask hole. Fig. 3.6.a presents the FWHM of the convolution in one dimension, as a function of the FWHM of the Gaussian smearing. If the smearing is comparatively small, the extent of the mask-hole projection is not affected. Only if the FWHM of the spatial resolution is larger than about half the size of a mask hole, the projection will become seriously degraded.

Several parameters will be affected by the finite detector resolution. The angular resolution is one; it is defined by the ratio of FWHM of the mask-hole projection and the mask-detector distance F. Once the FWHM is degraded by the detector resolution, the angular resolution will also be degraded. As seen above, this will not happen as long as the detector resolution (FWHM) is limited to half the size of a mask hole.
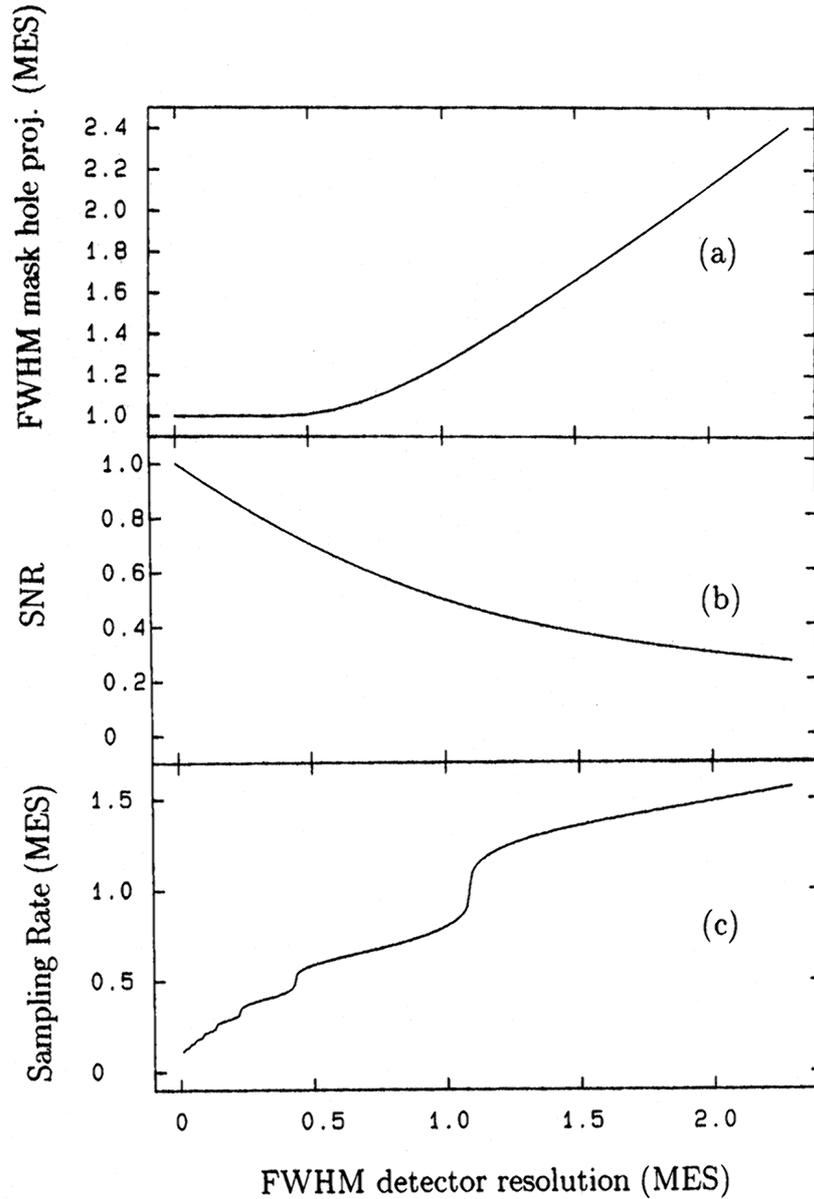
Figure 3.6: Results on three parameters of modeling a non-ideal spatial detector resolution by a Gauss function, as a function of the FWHM of the Gauss function in units of one mask-element size (MES): **a.** the FWHM of the detected mask-hole projection; **b.** the signal-to-noise ratio, SNR, of the measured intensity; **c.** the required sampling rate prescribed by the sampling theorem. The instability in the latter curve is due to the fact that the Fourier transform of the mask-hole projection is a sinc-function

In how far the position of the edge of a mask-hole projection can be derived, determines the source location accuracy (SLA) of the imaging system. The limited spatial detector resolution will smooth this edge and limit the SLA according to the proportionality:

$$\mathrm{SLA}_{x,y} \quad \sim \quad \frac{\sigma_{x,y}}{F\,\mathrm{SNR}} \qquad \mathrm{rad} \tag{3.6}$$

with SNR the ratio of the signal (the number of photons from the source through the open mask hole) to the noise (as is present in signal and background). For a justification of the dependence of SLA on SNR the reader is referred to section 5.7.

Finally, the finite detector resolution limits the sensitivity of the imaging system. Because of the broadening of the mask-hole response, generally speaking, the flux extends over a larger portion of the detector and therefore meets a larger background. The associated SNR deterioration is indicated in Fig. 3.6.b. Deterioration of the sensitivity by the limited spatial resolution of the detector depends furthermore on the specific characteristics of the detector. For instance, in a proportional counter not only fluctuations along the x, y-plane exist, but also along the optical axis due to optical depth effects. This introduces an exponential smearing function on top of the lateral Gaussian spread. This effect will be described in section 6.5.2.

3.5.2 Sampling rate

The detector data will usually be discretized by digital encoding, introducing a pseudo sampling of the continuous data. The discretization interval should be chosen such that no information is lost. This can be illustrated as follows: imagine the detector resolution is infinite. If the detector data were to be sampled at intervals equal to the size of a mask element, the projection of that element may be spread in up to four detector bins. This would potentially degrade the SNR by a factor two.

The appropriate sampling rate may be inferred from the sampling theorem (see e.g. Bracewell 1986, chapter 10), which states that a function whose Fourier transform is zero for frequencies $\nu > \nu_c$ is fully specified by values spaced at equal intervals not exceeding $\frac{1}{2}\nu_c^{-1}$. If the finite detector resolution is included, the Fourier transform of the function under consideration (one-dimensional) is given by a sinc-function multiplied by a Gaussian. This transform never remains zero beyond a certain frequency. However, a convenient cut-off frequency ν_c may be defined by requiring that P % of all the power is taken into account. Fig. 3.6.c shows the values of the sampling rate for $P = 99\%$ as a function of the detector resolution (FWHM) and provides a tool for inferring the necessary sampling rate.

3.5.3 Flat-field response of the detector

A deviation from ideal flatness of the spatial response of the detector results in a reduction of the imaging quality of the camera as a whole. Several types of deviations are probable. Some of them are sketched in Fig. 3.7 for the one-dimensional case, including linear as well as non-linear deviations. The main impact of these deviations is, that they broaden the point spread function (PSF) in the reconstruction process: for one part of the detector the mask pattern will match the recorded detector at a different shift than for another part of the detector; combining all matches results in a broadened PSF. Fig. 3.7.b shows such PSF's for the types of deviations shown in Fig. 3.7.a. This broadening of the PSF degrades the sensitivity of the camera. In a simple-type camera, the PSF not only broadens, but may also become asymmetrical since often only part of the detector is used in the reconstruction of a particular source. Therefore, only part of the deviation plays a role in the reconstructed image. This is illustrated in Fig. 3.7.b.

The degradation in sensitivity may be kept within reasonable limits, if the absolute differences between recorded and true position do not exceed typically half the size of a mask element in the respective directions (this criterium is argued in 3.5.1).

3.5.4 Tolerance on relative positioning and alignment of the detector body and mask

The tolerance for the parallelism between mask plane and detector plane can be very liberal: the scale of the projection is not affected by more than 1% as long as both planes are parallel within 8°.

Of more importance is a possible misalignment angle between mask and detector about the optical axis. If the projected mask pattern is rotated with respect to the detector x, y-plane, sensitive area may be lost because parts of the projection fall outside the detector area (see Fig. 3.8). In case
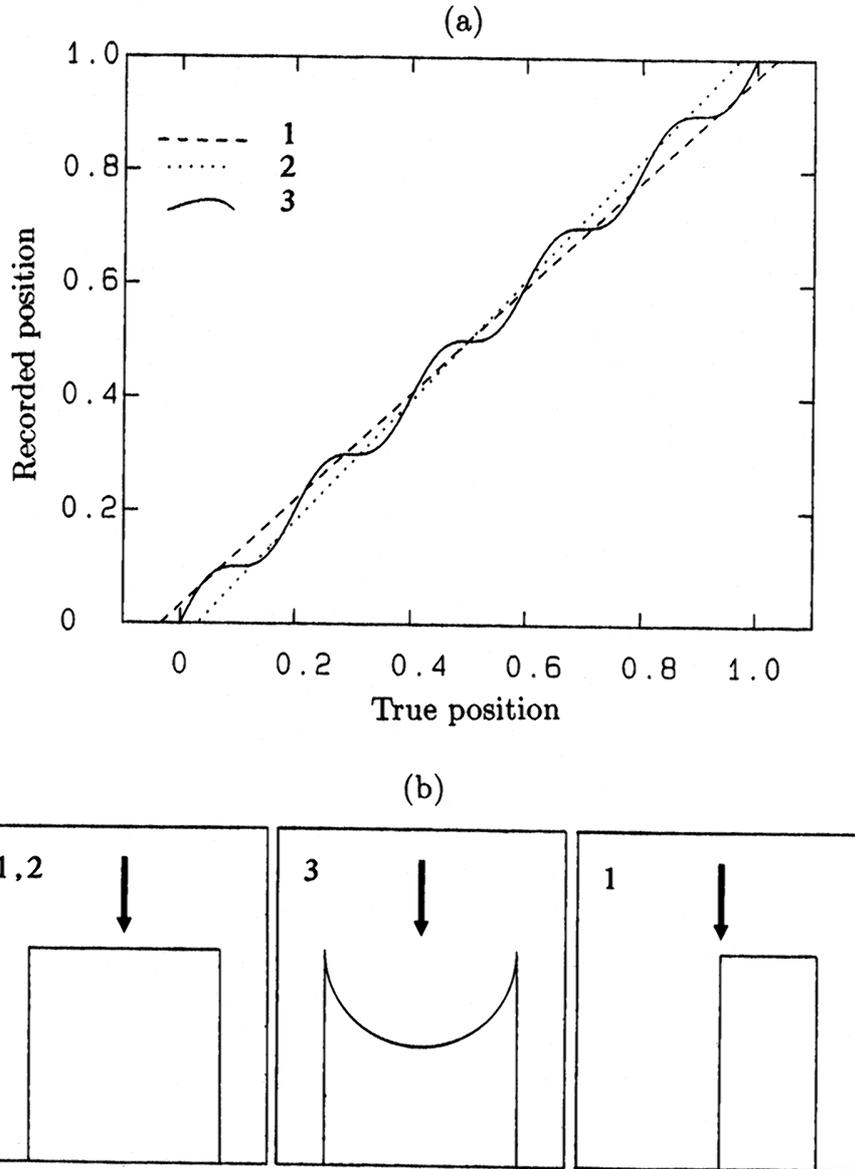
Figure 3.7: **a.** Three one-dimensional examples of a non-ideal spatial response of the detector. Plotted is the recorded position of any photon against its true position, both expressed in fractions of the detector size. An ideal detector would have a 1:1 response. **b.** Schematically, the resulting broadening of the PSF in the reconstructed image. The arrows indicate the center positions of the PSF for an ideal detector (not shown). Numbers in b correspond to the spatial responses indicated in a. The third plot in b shows for the first response the PSF if only half of the detector is used in the reconstruction. The sinusoidal response (3) results in a PSF with the form of the derivative of arcsin

of a square shaped detector and mask, the fraction of lost sensitive area amounts to

$$\frac{1}{2}\left(1 + \frac{\cos\alpha - 1}{\sin\alpha}\right)^2 \tan\alpha \qquad (0° < \alpha < 90°) \tag{3.7}$$

with α the misalignment angle. This loss can be overcome if the sensitive detector area is slightly larger than the area of the mask.

The imaging process is very sensitive to a non-zero misalignment angle (see e.g. Charalambous
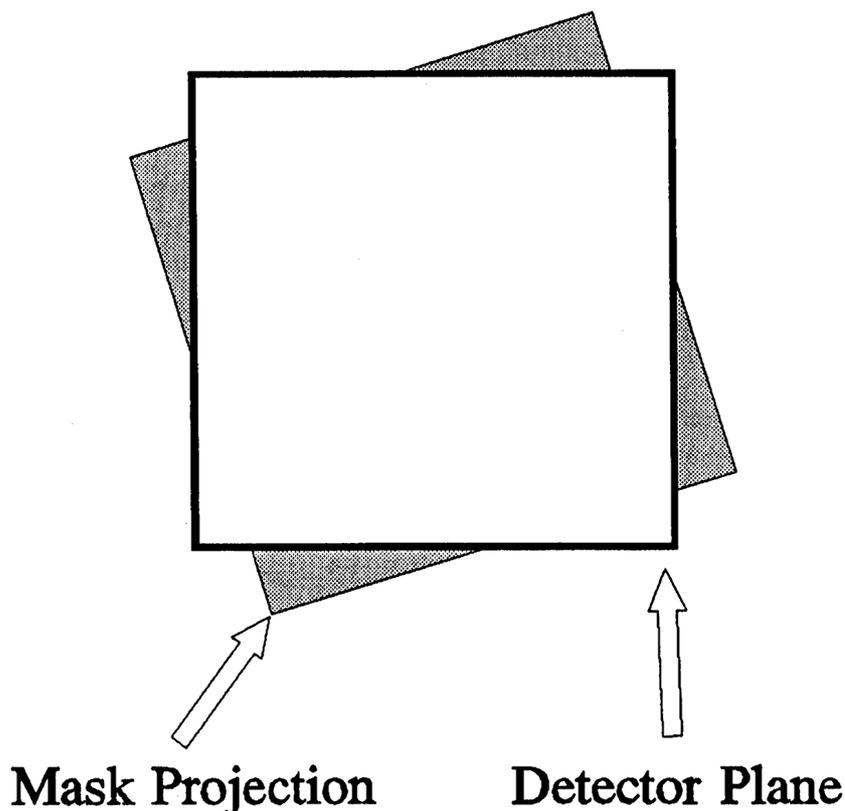
Figure 3.8: If the mask is rotated with respect to the detector about the optical axis, parts of the mask-pattern projection are lost (the grey areas). This problem can be overcome if the usable sensitive area of the detector is larger than the mask projection

et al. 1984). The point spread function (PSF) in the reconstructed sky will be considerably broadened if α exceeds roughly $\arctan(0.5 \ s_m/d_l)$, with d_l the length of the detector. A post-observation correction may largely resolve this problem, provided α is known: the detector image may be rotated over $-\alpha$, back to the reference of the mask pattern. However, a slight PSF broadening, inherent to this procedure, will be introduced (see 5.5). α can be easily calibrated by optimizing the PSF as a function of the rotation angle $-\alpha$ applied to the data. The value for α thus found, will generally apply to all data during the instrument's life time, provided the tolerance on the instrument stiffness is strict.

3.6 Reconstruction methods

Coded-mask imaging is basically a two-step procedure. After the accumulation of spatially coded detector data, the second step involves the decoding of this data, in other words the reconstruction of the observed part of the sky[4]. Since a powerful computer is needed for the reconstruction process, this is usually done off-line (particularly if the number of mask elements is large). Several reconstruction algorithms are in use. The choice for a certain algorithm depends on the specific aim (e.g. search for detections of unexpected events or timing analysis of a restricted part of the sky), the available computer memory and the type of instrument configuration. Several types of algorithms may in fact be subsequently used on the same set of detector data. This section gives a short resume of various algorithms. For clearness the discussion is illustrated with one-dimensional examples and space is discretized in steps of a size equal to that of a mask element; the conclusions

---

[4]In literature, a number of verbs are used for the same action: decode, reconstruct and deconvolve.

$$
\begin{pmatrix} d_1 \\ d_2 \\ d_3 \\ d_4 \end{pmatrix} = \begin{pmatrix} c_1 & c_2 & c_3 & c_4 \\ c_2 & c_3 & c_4 & c_1 \\ c_3 & c_4 & c_1 & c_2 \\ c_4 & c_1 & c_2 & c_3 \end{pmatrix} \begin{pmatrix} s_1 \\ s_2 \\ s_3 \\ s_4 \end{pmatrix} + \begin{pmatrix} b_1 \\ b_2 \\ b_3 \\ b_4 \end{pmatrix}
$$

$$
\begin{pmatrix} d_1 \\ d_2 \\ d_3 \\ d_4 \end{pmatrix} = \begin{pmatrix} 0 & 0 & 0 & c_1 & c_2 & c_3 & c_4 \\ 0 & 0 & c_1 & c_2 & c_3 & c_4 & 0 \\ 0 & c_1 & c_2 & c_3 & c_4 & 0 & 0 \\ c_1 & c_2 & c_3 & c_4 & 0 & 0 & 0 \end{pmatrix} \begin{pmatrix} s_1 \\ s_2 \\ s_3 \\ s_4 \\ s_5 \\ s_6 \\ s_7 \end{pmatrix} + \begin{pmatrix} b_1 \\ b_2 \\ b_3 \\ b_4 \end{pmatrix}
$$

(a)   (b)
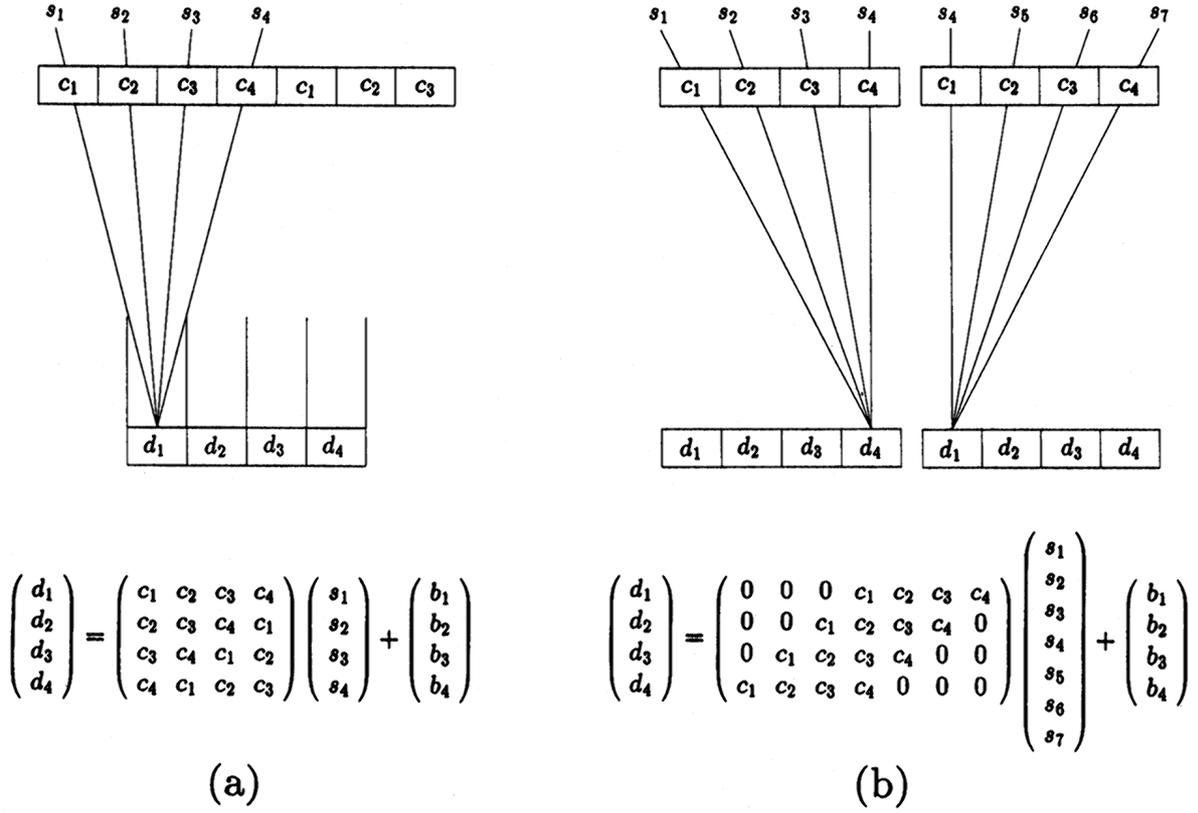
Figure 3.9: Schematic sketch of the formalism used in the text for the detection process in **a.** an optimum configuration and **b.** a simple configuration. The basic mask pattern here consists of 4 elements

do not basically differ for two dimensions and smaller steps.

The basic problem to be solved concerns the following. Let the one-dimensional vector $\vec{d}$ describe the detector (in units of counts per detector-element area), $\vec{s}$ the sky (in counts per mask element area) and $\vec{b}$ the detector background (this includes all flux which is not modulated by the mask pattern, in counts per detector element area). Suppose the detector elements are as large as a mask element. The detection process can then be described by:

$$
\vec{d} = \mathbf{C}\vec{s} + \vec{b}
\tag{3.8}
$$

where $\mathbf{C}$ is a matrix whose rows contain cyclic shifts of the basic mask pattern (see Fig. 3.9). An element of $\mathbf{C}$ is 1 if it corresponds to an open mask element and 0 otherwise. In the case of an optimum system with a basic mask pattern of n elements, $\vec{d}$, $\vec{s}$ and $\vec{b}$ contain n elements and $\mathbf{C}$ $n \times n$ elements. In the case of a simple system with a mask of n elements, $\vec{d}$ and $\vec{b}$ contain n elements, the sky vector $\vec{s}$ contains $2n - 1$ elements and the matrix $\mathbf{C}$ contains $(2n - 1) \times n$ elements (see Fig. 3.9). The problem to be solved is to reconstruct $\vec{s}$ out of this set of linear equations. Although $\vec{b}$ is unknown also, one is in principle not interested in it. An approximation for $\vec{b}$ is: $\vec{b}$ is homogeneous over the detector plane, i.e.

$$
\vec{b} = b \, \vec{i}
\tag{3.9}
$$

where $\vec{i}$ is the unity vector (consisting of only ones), b is now a single unknown scalar.

3.6.1   Linear methods

<u>Inversion.</u> This is a straightforward method to find $\vec{s}$ from Eq. 3.8: multiply $\vec{d}$ with the inverse of

$\mathbf{C}$, $\mathbf{C}^{-1}$, yielding:

$$\mathbf{C}^{-1}\vec{d} \;=\; \vec{s} + b\mathbf{C}^{-1}\vec{i} \tag{3.10}$$

Obviously $\mathbf{C}$ should be non-singular. This is not the case for a simple system, since $\mathbf{C}$ is not square. However, even if $\mathbf{C}$ is non-singular, the possibility exists that entries of $\mathbf{C}^{-1}$ are so large that the term $b\mathbf{C}^{-1}\vec{i}$ dominates the reconstruction. This will happen if rows of $\mathbf{C}$ are almost dependent on other rows, meaning that change of a few elements in a row might make it linearly dependent on other rows. $\mathbf{C}$ is then said to be 'ill-conditioned'. Fenimore and Cannon (1978) have shown that this is quite a common feature, especially for random mask patterns. This makes inversion an unfavorable reconstruction method.

<u>Cross correlation.</u> This is another obvious method for the reconstruction, cross correlating the detector image $\vec{d}$ with the mask pattern via a multiplication with a matrix. The mask pattern may be given by $\mathbf{C}$, but in practice a modified matrix is used: the so-called reconstruction matrix $\mathbf{M}$. $\mathbf{M}$ is constructed in such a way, that $\mathbf{M}\vec{d}$ evaluates directly $\vec{s}$ and cancels contributions from $\vec{b}$. Fenimore and Cannon (1978) introduced this method and called it 'balanced cross correlation'. Specifically, $\mathbf{M}$ is defined as[5]:

$$\mathbf{M} \;=\; (1+\Psi)\mathbf{C}^T - \Psi\mathbf{U} \tag{3.11}$$

where $\mathbf{C}^T$ is the transposed[6] of $\mathbf{C}$ and $\mathbf{U}$ is the unity matrix (consisting of only 1's and having the same dimensions as $\mathbf{C}^T$). Ψ is a constant and is determined from an analysis of the predicted cross correlation value: a prediction of the reconstruction can be easily evaluated if one assumes that the mask pattern is based on a cyclic difference set and the camera configuration is optimum. The expected value of the cross correlation is then (using the autocorrelation value, Eq. 3.1, for cyclic difference sets):

$$
\begin{aligned}
\mathbf{M}\vec{d} \;&=\; \mathbf{M}(\mathbf{C}\vec{s} + b\vec{i}) \\
&=\; (1+\Psi)(k-z)\vec{s} + \left[\{(1+\Psi)z - \Psi k\} \sum_i s_i + \{(1+\Psi)k - \Psi n\} b \right]\vec{i}
\end{aligned}
\tag{3.12}
$$

Apart from a scaled value of $\vec{s}$, which is the desired answer, the result also includes a bias term (the $\vec{i}$-term). It is not possible to eliminate this bias by a single value of Ψ. Rather, the $\sum_i s_i$ factor or the b factor can be canceled separately. Canceling the $\sum_i s_i$ factor involves a value Ψ of

$$
\begin{aligned}
\Psi_1 \;&=\; \frac{z}{k-z} \\
&=\; \frac{k-1}{n-k} \;,
\end{aligned}
\tag{3.13}
$$

canceling the b-factor involves Ψ to be[7]

$$\Psi_2 \;=\; \frac{k}{n-k} \tag{3.14}$$

Since k/n is the open fraction, t, of the mask pattern, Ψ_2 can be written as:

$$\Psi_2 \;=\; \frac{t}{1-t} \tag{3.15}$$

Ψ_1 approximates Ψ_2 if $k \gg 1$. The reconstruction value then reduces to:

$$\mathbf{M}\vec{d} \;=\; k\vec{s} \tag{3.16}$$

---

[5]An alternative description of $\mathbf{M}$ is: $M_{ij} = 1$ if $C_{ji} = 1$ and $M_{ij} = -\Psi$ if $C_{ji} = 0$.

[6]$\mathbf{C}^T$ instead of $\mathbf{C}$ is used to make this formulation applicable to the simple system; for the optimum system $\mathbf{C}^T = \mathbf{C}$.

[7]An interesting characteristic of the reconstructed sky is the sum of the reconstructed values. In case $\Psi = \Psi_1$ this is $\sum \mathbf{M}\vec{d} = k\sum_i s_i + nb$, i.e. the sum of all detected counts. If $\Psi = \Psi_2$ this sum is equal to 0.

Normalizing $\mathbf{M}$ results in:

$$\mathbf{M}/k \quad = \quad \frac{n/k}{n-k}\left(\mathbf{C}^T - \frac{k}{n}\mathbf{U}\right) \tag{3.17}$$

In the case of a simple system, Eq. 3.12 would also apply if the 'hard' zeros in $\mathbf{C}$ (i.e. zeros that do not arise from zero a_i-values, see Fig. 3.9) were replaced by cyclically shifted a_i's. The result of Eq. 3.16 would then imply: $(\mathbf{M}\vec{d})_i = (\mathbf{M}\vec{d})_{\text{mod }(i+n,2n-1)}$; this is a consequence of the fact that $2n-1$ unknowns are to be determined from a set of only n linear equations, which is under-determined in general. In this formulation a source at position i causes a false peak of the same strength at position $\text{mod}(i+n,2n-1)$. If the 'hard' zeros in $\mathbf{C}$ are not replaced, this does not apply directly, but an interdependence in the solution for the reconstruction remains. This interdependence is not so strong: one real peak will cause many small ghost peaks rather than a single false peak which is just as strong as the real peak. It is then possible to find a unique solution for $\vec{s}$ as long as it does not have more non-zero values than n. This search is accomplished by testing reconstructed peaks on their authenticity, the reconstruction process is then necessarily iterative. A detailed discussion of the cross correlation for a simple system is given in chapter 5.

Photon tagging (or URA-tagging). This reconstruction method is very similar to cross correlation and has been introduced by Fenimore (1987). It involves back-projecting every detected photon through the mask, towards a particular (possibly all) position in the sky field from which it could originate. If a closed mask element is 'encountered' in the back-projection, the photon is accumulated in the background contribution. If it 'encounters' an open mask element, it is accumulated in the source contribution for that position in the sky. Once all photons have been processed, the subtraction of the background from the source contributions (after proper normalization) completes the reconstruction. It is clear that this method is advantageous, in terms of computation time relative to a cross correlation, if the number of detected photons is very small with respect to the number of mask elements. The advantage may also hold if only a restricted part of the observed sky needs to be reconstructed. This latter situation may be applicable if all point sources in the sky have already been found in an analysis of the same data (e.g. by a total cross correlation) and one intends to analyze each point source in more detail, i.e. extract spectra and/or lightcurves. Skinner & Nottingham (1992) improved the method by extending it, taking into account imperfections of the detector (limited spatial resolution, 'dead spots' etc.), the support grid of the mask plate and a telescope motion.

Wiener filtering. Sims *et al.* (1980), Sims (1981) and Willingale *et al.* (1984) introduced Wiener filtering for use as a reconstruction method of coded-mask-system images. This filtering can be regarded as a weighted cross correlation (Sims 1981), weighing the Fourier transform components of the detector image with the inverse power density of the mask pattern. Thus, fluctuations in the modulation transfer function[8] of the mask pattern are smoothed. If $\frac{S}{N}(\omega)$ is the ratio of the signal power density (due to spatial fluctuations by sky sources) to the noise power density at spatial frequency ω, $C(\omega)$ the Fourier transform of the mask pattern, the Wiener filter $W(\omega)$ is defined as:

$$W(\omega) \quad = \quad \frac{\overline{C(\omega)}}{|C(\omega)|^2 + \frac{S}{N}(\omega)^{-1}} \tag{3.18}$$

Because $\frac{S}{N}$ is not known before the reconstruction is completed, a frequency-independent expression is used for it.

It is clear that Wiener filtering is especially helpful if the mask pattern is not ideal, which is the case for random and Fresnel zone patterns. However, ideal patterns such as those based on cyclic difference sets are characterized by flat modulation transfer functions (all spatial frequencies are equally present for URA-patterns, which is apparent from the definition of URAs, see 3.3). Sims

---

[8]The modulation transfer function is defined as the square root of the Fourier power spectrum.

et al. (1980) confirmed this via computer simulations and found this also to be the case if an ideal pattern is used in partial coding, such as in a simple system.

3.6.2 Iterative methods, Maximum Entropy Method

A separate class of reconstruction methods are formed by the iterative methods. These try to solve the sky vector $\vec{s}$ from Eq. 3.8 by an iterative search for the solution that is most consistent with the detector data. Three of such methods have been investigated for use in coded-mask imaging. One of these is the MAXIMUM ENTROPY METHOD (MEM) and was introduced in this field of work by Willingale (1979). Despite the good results that can be obtained with this method, a major drawback is the large amount of computer effort required, as compared to linear methods such as cross correlation. Another method, ITERATIVE REMOVAL OF SOURCES (IROS), does not have this disadvantage. IROS is in fact an extension of the cross correlation method and was introduced by Hammersley (1986) as a procedure to eliminate problems due to incomplete coding (also called 'missing data') in simple systems.

In this section MEM will shortly be addressed. IROS will be detailed in chapter 5.

MEM has gained widespread favor in different areas as a tool to restore degraded data. Introductions to the theory behind MEM as applied to image restoration can be found in Frieden (1972) and Daniell (1984), while a review is given by Narayan & Nityananda (1986). Examples of applications of MEM are given by Gull and Daniell (1978), Bryan and Skilling (1980) and Willingale (1981), while the application specifically to images from coded-mask systems are described by Sims *et al.* (1980) and Willingale *et al.* (1984). Here, a summary of the principles of MEM is presented.

MEM involves finding the one solution with the least amount of information from the set prescribed by:

$$F(\vec{s}) \equiv \chi^2 - \chi^2_{\text{expected}} = 0 \tag{3.19}$$

with

$$\chi^2 = \sum_{i=1}^{N_d} \frac{(d_i - \widehat{d_i}(\vec{s}))^2}{\sigma_i^2} \tag{3.20}$$

where $\widehat{d_i}(\vec{s})$ is a prediction of the data in the detector domain, N_d the number of detector elements, σ_i^2 the variance in the measured value of d_i and χ^2_{expected} is usually equal to N_d. The amount of information is measured through the entropy S. The minimum amount of information is equivalent to the maximum entropy. Regarding a 'correct' measure for the entropy, there is some confusion in the literature (Willingale *et al.* 1984). Ponman (1984) argues that a single correct expression for S does not exist. In view of the current basic discussion of MEM, assume S is straightforwardly given by:

$$S = -\sum_{i=1}^{N_s} p_i \log(p_i) \tag{3.21}$$

with

$$p_i = \frac{s_i}{\sum_{l=1}^{N_s} s_l}$$

where N_s is the number of sky elements in $\vec{s}$. p_i represents the probability that a given photon has arrived from sky element i rather than another. Finding the maximum of S within the set of solutions defined by Eq. 3.19 involves the solution of the Lagrange multiplier λ from:

$$\frac{\partial S}{\partial s_k} = \lambda \frac{\partial F(\vec{s})}{\partial s_k} \tag{3.22}$$

or, using Eq. 3.8:

$$
s_k = \mathrm{e}^{\left(\frac{\sum_{i=1}^{N_s} s_i \log s_i}{\sum_{i=1}^{N_s} s_i} - 2\lambda \sum_{i=1}^{N_s} s_i \sum_{i=1}^{N_d} \frac{(\widehat{d_i}(\vec{s}) - d_i)c_{ik}}{\sigma_i^2} \right)} \tag{3.23}
$$

under Eq. 3.19. Unfortunately Eq. 3.23 is transcendental in $\vec{s}$ and can only be solved using an iterative search algorithm.

Bryan and Skilling (1980) have shown that care should be taken in using Eq. 3.19 as a definition for allowable solutions. They showed that the use of Eq. 3.19, to fit the variance of the residuals $\widehat{d_i} - d_i$ to the expected value, may actually resolve a MEM solution whose residuals do not follow a Gaussian distribution. This may manifest itself as fluxes of confined sky sources that are not fully recovered and a biased background level. They proposed the use of another statistical definition of allowable solutions. Recent discussion of MEM, as applied on data of the Hubble Space Telescope (see e.g. Weir 1991) indicates that this problem is non-trivial and generally not yet fully solved. These discussions also make clear that no straightforward recipe exists yet to extract estimates for the flux accuracy from MEM solutions. However, MEM solutions do seem to provide a powerful tool to recognize extended structures.

Regarding the computational effort involved in solving Eq. 3.23 in relation to the cross correlation discussed in section 3.6.2: for every iteration two convolutions need to be calculated. The first convolution is necessary to evaluate $\widehat{d_i}$ for a given sky $\vec{s}$ (via Eq. 3.8). The second one needs to be done to convolve the difference between predicted detector and measured detector $\widehat{d_i} - d_i$ with the instrument response $\mathbf{C}$. Therefore, every iteration will roughly take two times as much computing as a cross correlation. Sims *et al.* (1980) reports a total disadvantage in computational effort of MEM relative to cross correlation of about a factor 20. It should be noted that Sims *et al.* used MEM in simulations that did not take into account the response of a window support structure on the detector (see chapters 4 and 5). Although MEM was not actually employed by the author, it is suspected that, due to this complication, the quoted factor of 20 becomes considerably higher.

References

Ables, J.G.: 1968, *Proc. Astron. Soc. Australia* **1**, 172

Aschenbach, B: 1985, *Rep. Prog. Phys.* **48**, 579

Baumert, L.D.: 1971, ”*Lecture Notes in Mathematics No. 182: Cyclic Difference Sets*” (Berlin: Springer)

Bracewell, R.N.: 1986, ”*The Fourier Transform and its Applications*” (New York: McGraw-Hill), 2nd ed.

Brandt, S., Lund, N., Rao, R.: 1990, *Adv. Sp. Res.* **10**, (2)239

Bryan, R.K., Skilling, J.: 1980, *Mon. Not. R. Astron. Soc.* **191**, 69

Caroli, E., Stephen, J.B., Di Cocco, G., Natalucci, L., Spizzichino, A.: 1987, *Sp. Sc. Rev.* **45**, 349

Charalambous, P.M., Dean, A.J., Stephen, J.B., Young, N.G.S.: 1984, *Appl. Opt.* **23**, 4118

Daniell, G.J.: 1984, *Nuc. Instr. Meth. Phys. Res.* **221**, 67

Dicke, R.H.: 1968, *Astrophys. J. Lett.* **153**, L101

Fenimore, E.E., Cannon, T.M.: 1978, *Appl. Opt.* **17**, 337

Fenimore, E.E.: 1987, *Appl. Opt.* **26**, 2760

Frieden, B.R.: 1972, *J. Opt. Soc. America* **62**, 511

Gull, S.F., Daniell, G.J.: 1978, *Nature* **272**, 686

Gunson, J., Polychronopulos, B.: 1976, *Mon. Not. R. Astron. Soc.* **177**, 485

Hall, M.: 1967, ”*Combinational Theory*” (Waltham: Blaisdell)

Hammersley, A.P.: 1986, ”*The Reconstruction of Coded-mask Data under Conditions Realistic to X-Ray Astronomy Observations*”, Ph.D. Thesis, University of Birmingham

Hammersley, A., Ponman, T., Skinner, G.K.: 1992, *Nuc. Instr. Meth. Phys. Res.* **A311**, 585

Kondo, I, Inoue, H., Koyama, K. *et al.*: 1981, *Space Sci. Instrum.* **5**, 211

Lund, N.: 1985, in "*SPIE Proc. on X-Ray Instrumentation in Astronomy*", ed. J.L. Culhane, *SPIE Proc. Ser.* **597** (Bellingham: SPIE Optical Engineering Press), 95

Makino, F., *Astro-C* team: 1987, Institute of Space and Astronautical Science, Tokyo, Research Note No. 326

Makishima, K., Miyamoto, S., Murakami, T., Nishimura, J., Oda, M., Ogawara, Y., Tawara, Y.: 1978, in "*New Instrumentation for Space Astronomy*", eds. K.A. van der Hucht and G. Vaiana (New York: Pergamon), 277

Mayer, W.: 1972, in "*X-Ray Astronomy in the Near Future*" (Neuily-sur-Seine: ESRO SP-87), 31

Mertz, L., Young, N.O.: 1961, in "*Proc. Int. Conf. on Opt. Instrum. Techniques*", ed. K.J. Habell (London: Chapman and Hall), 305

Mertz, L.: 1968, in "*Proc. Symp. on Modern Optics*", ed. J. Fox (Brooklyn: Polytechnic Press), 787

Miyamoto, S.: 1977, *Space Sci. Instrum.* **3**, 473

Narayan, R., Nityananda, R.: 1986, *Ann. Rev. Astron. Astrophys.* **24**, 127

Skinner, G.K., Nottingham, M.R.: 1992, *Nuc. Instr. Meth. Phys. Res.*, submitted

Palmer, D., Prince, T.A.: 1987, *IEEE Trans. Nucl. Sci.* **NS-34**, 71

Peterson, W.W.: 1961, "*Error Correcting Codes*" (Massachusetts: MIT Press)

Ponman, T.J.: 1984, *Nuc. Instr. Meth. Phys. Res.* **221**, 72

Proctor, R.J., Skinner, G.K., Willmore, A.P.: 1979, *Mon. Not. R. Astron. Soc.* **187**, 633

Sanford, P.: 1975, in "*X-Ray Astronomy and Related Topics*", ed. R.D. Andresen (Neuily-sur-Seine: ESRO SP-110), 25

Schnopper, H.W., Thompson, R.I., Watt, S.: 1968, *Sp. Sc. Rev.* **8**, 534

Sims, M.R., Turner, M.J.L., Willingale, R.: 1980, *Space Sci. Instrum.* **5**, 109

Sims, M.R.: 1981, "*A Wide-field Camera for X-Ray Astronomy*", Ph.D. Thesis, University of Leicester

Skinner, G.K.: 1984, *Nuc. Instr. Meth. Phys. Res.* **221**, 33

Theinhardt, J., Burk, R., Kendziorra, E., Staubert, R.: 1984, *Nuc. Instr. Meth. Phys. Res.* **221**, 288

Turner, M.J.L., Thomas, H.D., Patchett, B.E. *et al.*: 1989, *Pub. Astron. Soc. Japan* **41**, 345

Van Speybroeck, L.P.: 1987, *Astroph. Lett. Communications* **26**, 127

Weir, N.: 1991, *ST-ECF Newsletter*, No. 16, 8

Willingale, R.: 1979, Ph.D. Thesis, University of Leicester

Willingale, R.: 1981, *Mon. Not. R. Astron. Soc.* **194**, 359

Willingale, R., Sims, M.R., Turner, M.J.L.: 1984, *Nuc. Instr. Meth. Phys. Res.* **221**, 60

Chapter 4

COMIS design aspects and hardware

COMIS design aspects and hardware

Abstract – The design aspects and hardware of *COMIS* which are of prime importance to the scientific capabilities of the instrument are discussed. The description given in this chapter is used in the discussions in chapters 5 and 6.

4.1   Introduction

In this chapter, design aspects and hardware of *COMIS* are discussed which have a main impact on the scientific capabilities of the instrument. It forms an introduction to the investigations described in chapters 5 and 6. The author has emphasized the discussion to that of the internal detector configuration and the timing characteristics of the processing electronics, since these items play an important role in the in-flight calibration of the instrument performed by the author and discussed in chapter 6.

4.2   Optical design

The optical design of *COMIS* was governed by the requirement to optimize the instrument with respect to the angular resolution, given a proposed useful detector area of 30×30 cm^2. Optimization of the angular resolution involved minimizing the ratio of mask element size to mask-detector separation. The minimum mask element size was restricted by the etching technique for the mask plate to 1 mm in each dimension. The resolution of the position readout of the detector should of course match this resolution. To achieve a mask-detector separation as large as possible within the *Kvant* module, the instrument could best be placed tangent to the inner cylindrical wall of the module (see Fig. 4.1) with the pointing direction perpendicular to the symmetry axis of the module. In this way, an instrument slightly longer than 2 m could be accommodated.

A trade-off between an optimum and a simple configuration for the mask/detector combination favored the choice for a simple system. An optimum system, with a mask 4 times as large as the detector, would only fit in the module at great expense of the angular resolution, due to the substantially decreased mask-detector separation. Furthermore, it would be technically difficult to construct a collimator grid for an optimum system with a grid cell size as small as 1×1 mm^2. Since the imaging quality of simple systems is not inferior to that of optimum systems (except perhaps for the imaging of extended sources, see 5.2.4), arguments for improved resolution and sensitivity prevailed.

The geometrical characteristics of *COMIS* are given in Table 4.1. Fig. 4.2 gives a configuration sketch of *COMIS*, indicating the main parts of the instrument that will be described in some detail in the remainder of this chapter.

The telescope body, serving as a collimator shield against X-rays that do not pass through the mask plate, is made up of three 44 cm diameter tubular sections which are connected by special
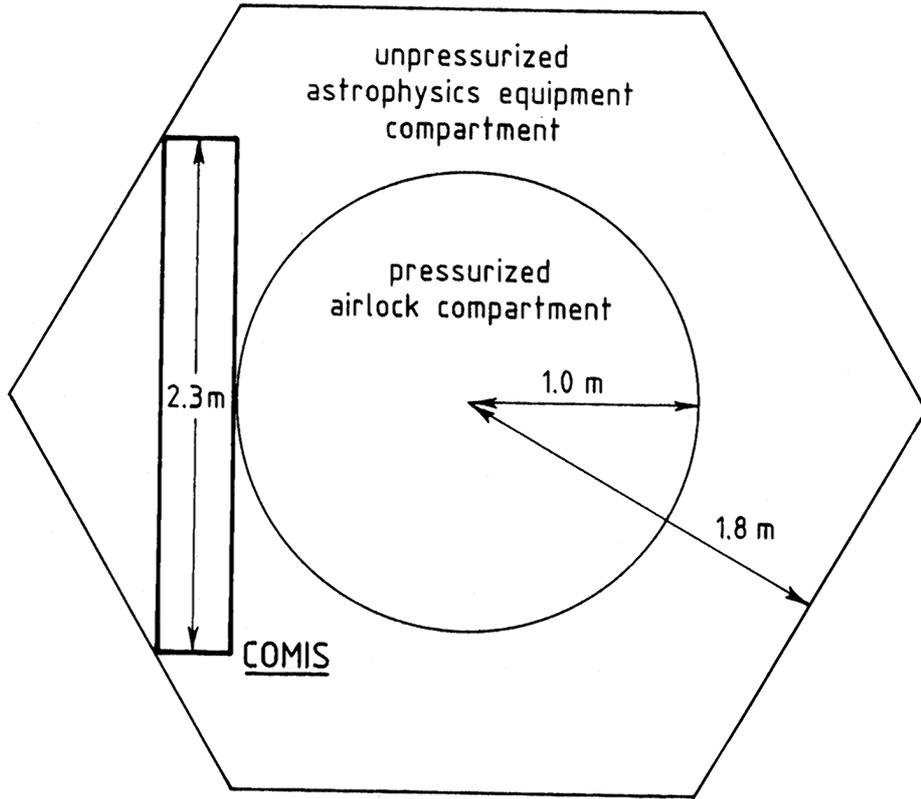
Figure 4.1: Cross section of the scientific *Kvant* module, perpendicular to the module axis, showing the optimum positioning of *COMIS* to obtain the highest angular resolution (given external conditions)

clamping rings and O-ring seals to form a rigid, air-tight tube 1.8 m long. The same clamps and rings are used to attach the detector (with its electronics) and the Command and Data Managing System (CDMS) electronics box at one end and the mask assembly and the star sensor (SS) TV camera at the other end of the body. Three kinematic mounts on the body act as a mechanical interface between the body and the module. A foil, made of 6 μm thick Kapton with an Aluminum coating, is placed in front of the mask for environmental protection and thermal stabilization. The detector with its electronics was constructed at the SRON-Laboratory for Space Research Utrecht (Netherlands) and all other components at the School of Physics and Space Research of the University of Birmingham (UK).

Table 4.1: Geometric Characteristics of *COMIS*

Mask Area	255×257 mm^2
Detector Area	256×256 mm^2
Distance Mask-Detector	1846 mm
Number of Mask Elements	255×257 (1×1 mm^2 in size)
Field of View (FWZR)	15.8×15.8 square degrees
Angular Resolution On-Axis	1.86 arcminutes
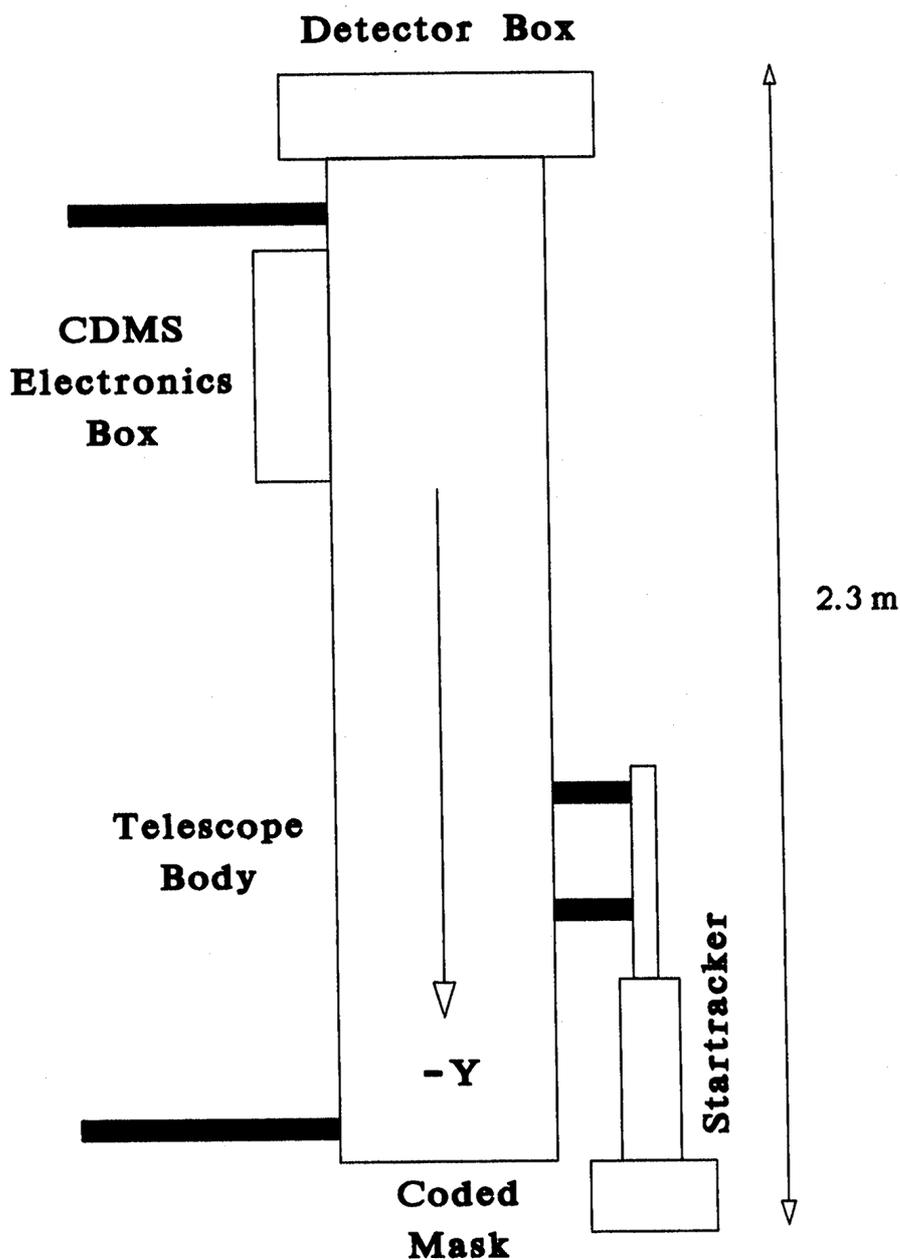
Figure 4.2: Configuration sketch, indicating the placements of the main parts of *COMIS* components (not on scale). The viewing direction of the telescope is towards the -Y instrumental coordinate direction

4.3 Mask

The mask pattern is based on a single pseudo-noise array, which was constructed using the irreducible primitive polynomial (see section 3.3)

$$X^{16} + X^5 + X^3 + X^2 + 1 \tag{4.1}$$

The $2^{16} - 1$ elements of this array are wrapped on a 255×257 matrix, ordered along extended diagonals (see section 3.3). This pattern has 32,768 open against 32,767 closed elements and is shown in Fig. 4.3. Some interesting features of the mask pattern are worth mentioning:

1. It is symmetrical with respect to the 129th row;
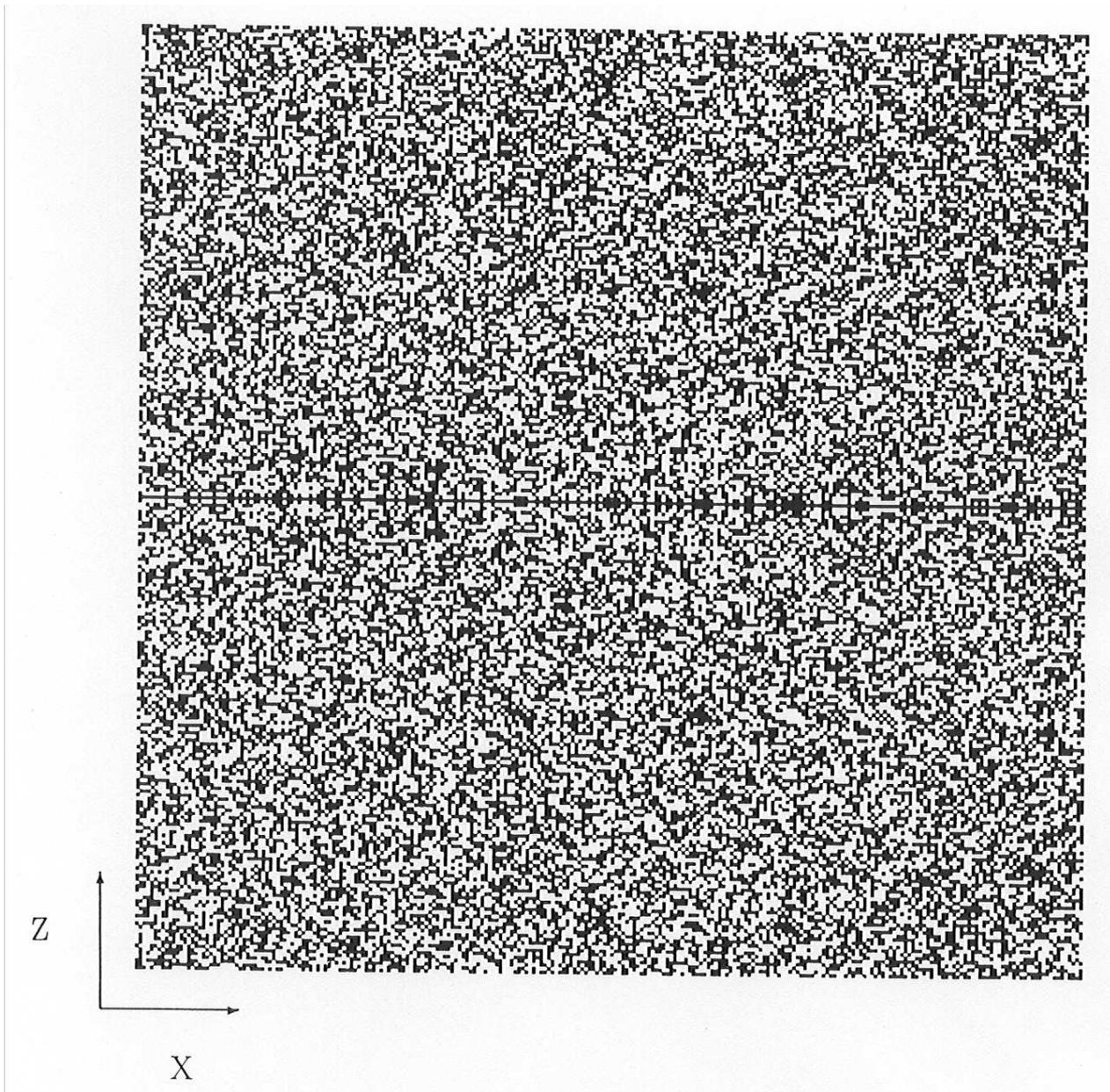
Figure 4.3: The mask pattern used in *COMIS*, in instrumental coordinates. Note the symmetry with respect to the 129th row

2. The 129th row is completely filled with opaque mask elements;
3. Every row, except the 129th, is in itself a pseudo noise array of order 8 with 128 transparent and 127 opaque elements.

The mask elements were given a size of 1×1 mm^2, thus creating a coded area of 255×257 mm^2.

The mask plate is physically manufactured from 0.1 mm stainless steel, plated on both sides with 5 μm Gold. The mask pattern, as well as a mask pattern support grid, was etched in this plate. The support grid is defined by bars 0.1 mm wide, regularly spaced at intervals of 1 mm along both dimensions. The open fraction of the mask plate is 41% (measured pre-flight).

The transparency of the closed mask area is less than 1% for photons of 18 keV or less and gradually increases via 12% at 24 keV to 30% at 30 keV. The impact of this on the coding efficiency as a function of photon energy is specified in Fig. 4.4.
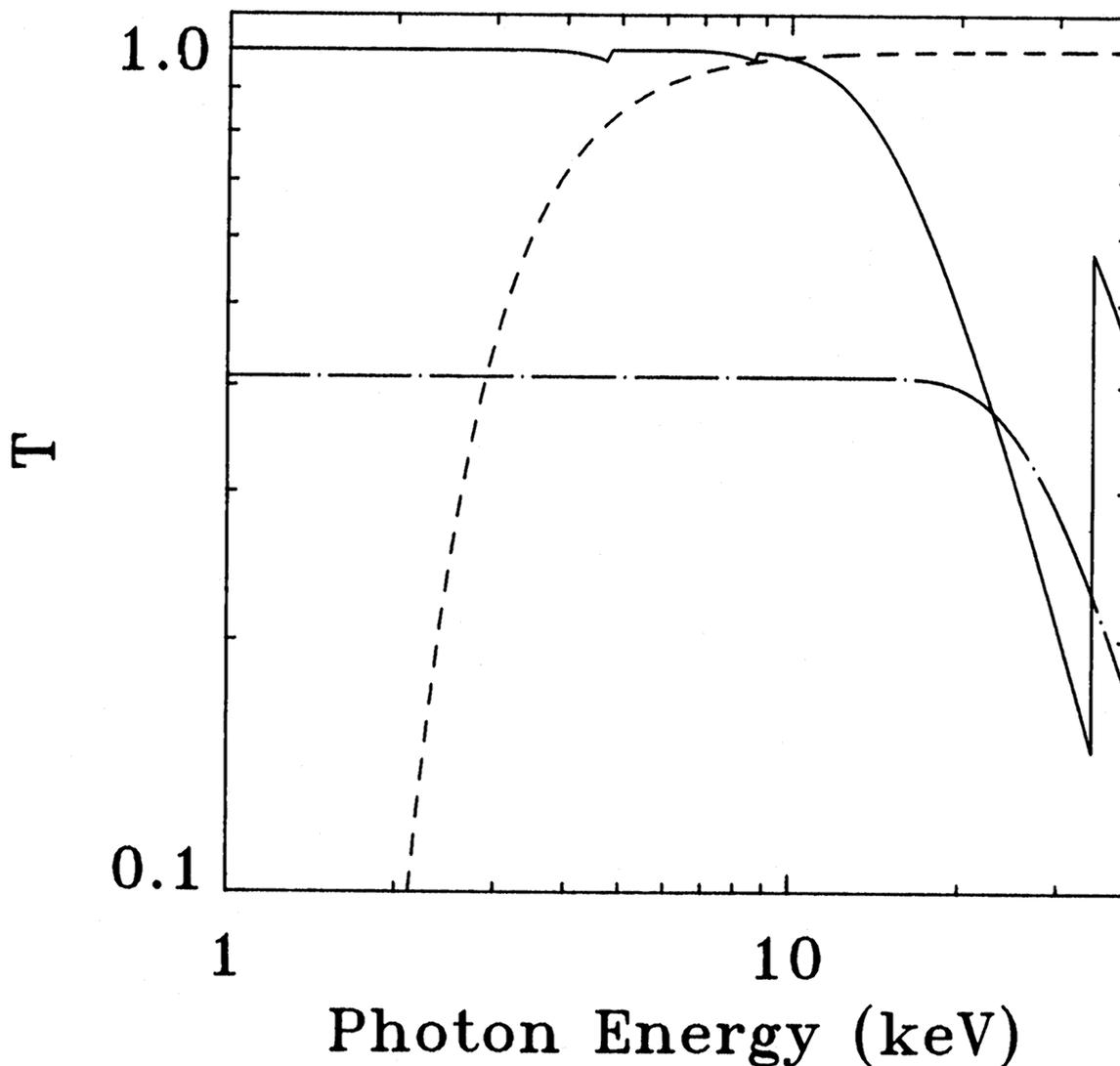
Figure 4.4: Throughput of the coding by the mask plate (dash-dotted curve) and the Beryllium entrance window (dashed) of the *COMIS* detector versus photon energy. The solid curve represents the total absorption efficiency in the Xenon gas layers of both detector halves. The energy range is plotted larger than the energy readout range of the detector (2-30 keV), since the limited spectral resolution will cause photons outside the 2-30 keV range to be detected within this range. Several edges may be noticed in the absorption curve of the gas layers: the L (at $\sim$ 5 keV) and K (34.6 keV) absorption edges of Xenon and the inclusion of the deepest detector half beyond $\sim$ 8.6 keV (due to a software AC criterium, see section 4.4.2).

The throughput of the entrance window limits the sensitivity at the low end of the energy band, while the absorption efficiency falls off at high energies. These two characteristics are most important to the total sensitivity of the detector and provide an optimum in the sensitivity between about 5 and 10 keV. The throughput of the mask is determined by its open fraction (41%) and the emerging transparency of the mask plate material beyond roughly 20 keV. Shown is the effect on the coding, as it is observed on the detector. Although more photons can pass through the mask plate beyond 20 keV, these will not contribute to a stronger coding. In fact they will degrade the coding, because they decrease the contrast between projected open and closed mask elements. On top of that, the Poisson noise of the extra photons will result in a supplemental degradation of the sensitivity of the instrument

4.4 Detector

The design of the detector, a multi-wire (position-sensitive) proportional counter, was based on the following requirement specification:

1. sensitive area $\sim$ 500 cm^2;
2. effective energy band 2-30 keV;
3. spatial resolution in both directions $\leq$0.5 mm for 2-10 keV;
4. spectral resolution 18% at 6 keV and better than 20% at 22 keV;
5. no performance degradation for count rates up to 1000 c/s;
6. optimum background rejection.

Comprehensive descriptions of the detector and its electronics may be found in Van Beek *et al.* (1984) and Mels *et al.* (1988). In this section a description is given, which focuses primarily on aspects related to the analysis of the scientific data.

The counter body, made of stainless steel, has a cylindrical shape of 498mm diameter and 92mm height. At the front, a square (256×256 mm^2 in size[1] and 200 μm thick) Beryllium entrance window is glued to the bottom of a stainless steel support structure. The throughput of this window is given in Fig. 4.4. The structure supports the window against the gas pressure in the counter. It consists of 16×16 square holes of 14.5×14.5 mm^2 surrounded by walls 1.6 mm thick and 21.8 mm high. At the back of the counter body the detector-electronics box is attached. The complete detector weighs about 120 kg.

4.4.1 Internal counter configuration

Fig. 4.5 shows a schematic drawing of the counter interior. The counter is filled with a mixture of Xe (95% weight) and CO_2 (5%) at a pressure of 1.12 bar at 20°C. Five wire grids are placed in the counter, all 288×288 mm^2 in size. One of them (K1) divides the counter in the actual photon counter (50 mm deep) and the anti-coincidence (AC) counter used for background rejection (20 mm deep). The photon counter itself is also divided into two equal volumes by the anode grid A1. Each volume consists of a 'drift' and an 'active' region, both regions being separated by the sense grids S1 and S2. The detector operates at a gas gain of 1.5×10^4, which is the optimal value for obtaining the specified position resolution. Field correction plates keep the electrical field homogeneous; slight inhomogeneities at the edge of the wire grids are kept outside the sensitive area (this area is confined to within the edges of the entrance window). For in-flight calibration purposes, the window support structure contains five Fe^{55}/6 keV radioactive sources at different positions (total countrate 7.74 c/s on March 31st 1988) and one Cd^{109}/22 keV source (0.28 c/s).

All wires are oriented along the X-axis of the detector coordinate system, except for the wires in the top sense grid S1 that are oriented along the Z-axis. Both sense grids consist of 480 wires and are used for the determination of the positions of detected photons. The diameter of these wires was made as large as possible (within the mechanical tolerances for the stress on them and the wire frame) to minimize the electrical field near the wires in order to avoid secondary pulses caused by the acceleration of positive ions. The trade-off value was 50 μm. The pitch was chosen to be 0.6 mm, similar in magnitude to the size of the electron clouds, so that binning effects in the position readout would be kept to a minimum. The interconnection scheme of the sense grid wires is given in Fig. 4.6. Each sense grid is divided into 12 'coarse sections' of 24 mm width. The signals of these coarse sections indicate the rough position of the photon absorption. Every coarse section is subsequently divided into four 'fine sections'. The equivalent fine sections of all coarse sections are interconnected. The signals of these fine sections will complete the information that is necessary to determine the position of the photon absorption at the required resolution. The principles of the position-determination algorithm may be found in Van Beek *et al.* (1984).

The anode grid A1 consists of 96 wires. The diameter and pitch of the wires as well as the high

---

[1]For symmetry reasons of the detector design, its size was not exactly matched to that of the mask pattern. This small mismatch has negligible consequences as regards to the coding noise (see section 3.6.1)
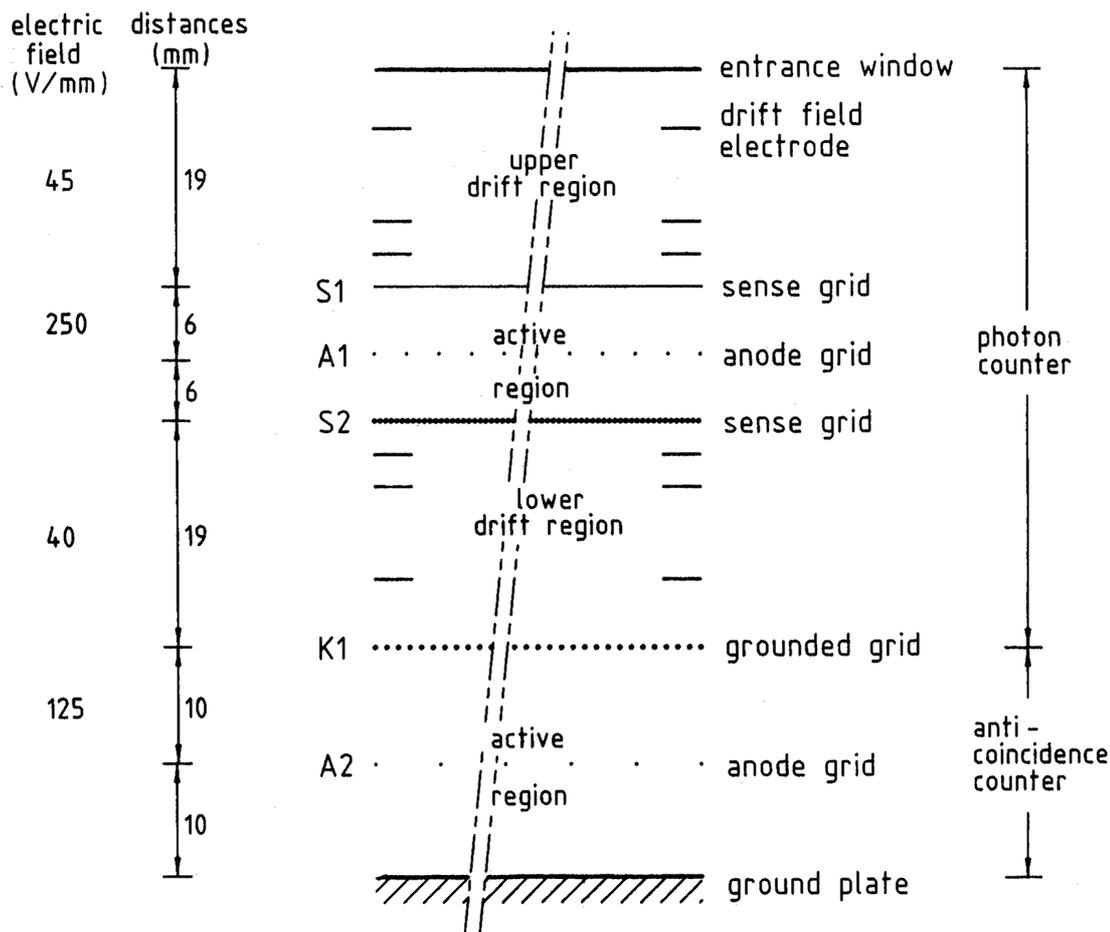
Figure 4.5: Schematic diagram of the internal structure of the detector. Note that all grid wires are oriented along the same direction, except for those in the upper sense grid S1. From: Mels *et al.* 1988

voltage were balanced to obtain simultaneously the desired gas gain, a homogeneous electrical field near the wires, an optimum detector performance and the required live time of the detector. To obtain the required gas gain (see above), the electrical field near the anode wires must reach a certain value. This may be achieved either by adjusting the high voltage applied to the wires or adjusting their diameter. The high voltage value was limited to below about 4000 V to avoid damage to the electrical circuitry and the diameter of the wires was restricted to a lower limit in order to guarantee enough life time over the damaging influence of high energy particles. The trade-off value is 20 μm. The pitch of the anode wires determines the electrical field in the active region. If it increases, the electrical field decreases. This will limit the production of unwanted UV photons. However, with an increasing pitch, the electrical field becomes less homogeneous. This is undesirable, because it results in a inhomogeneous detector response. Too large a pitch value also results in a degraded detector performance at high counting rates. Hence, the actual choice of the pitch value is a trade-off: 3 mm. All the anode wires are interconnected except for six, i.e. three at each edge of the grid, which are separately interconnected. These latter six wires define the 'edge anode' and are used for background rejection; they are located outside the sensitive area of the detector. The anode signal is used for the determination of the photon energy.

The detector geometry introduces some obstacles for the photons to be absorbed in the detector gas. First of course there is the window support structure. For normal incidence photons, the structure will block 18% of all photons before they can enter the detector. For photons that are incident at a non-zero off-axis angle this blocking will be more because of the shadowing by the
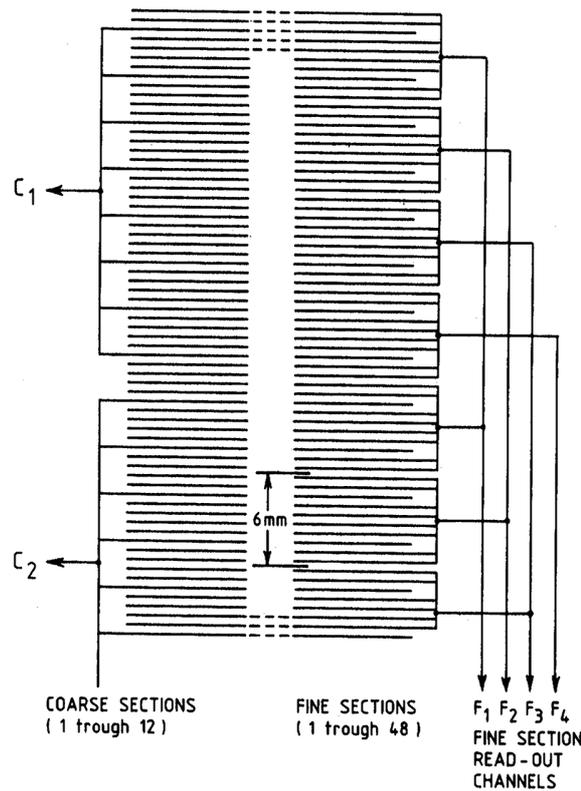
Figure 4.6: Interconnection diagram of the sense grid wires. From: Mels *et al.* 1988

support bars.

Furthermore, the wires in all grids will obstruct a certain percentage of all photons from 'travelling' any deeper in the detector. Both sense grids S1 and S2 block 8.3% of the photons, while the anode frame A1 only blocks 0.6%. Fig. 4.4 presents the total Xe absorption efficiency for photons that have entered the detector, taking also into account the blocking by the wire grids. It is noted that the blocking is of no influence on low energy photons, since only a negligible fraction of these photons can penetrate as deep as the first grid.

4.4.2   Processing electronics

The output of the detector, fed to the detector electronics, consists of 35 signals: 24 from the coarse sections, 8 from the fine sections and 1 from the anode, the edge anode and the AC counter anode A2 respectively. It is convenient to make a distinction between two parts of the electronics: the 'front-end electronics', which incorporate single-signal-processing (e.g. pre- and shaping amplifiers, linear gate stretchers and analogue-to-digital converters), and 'processing electronics', which entail the processing of combined signals. It is beyond the scope of the current description to give full details of the electronics. Only aspects related to the response and dead times are highlighted in view of their impact on the data analysis. This means that emphasis is given here to the description of the processing electronics. The processing electronics can be operated in two modes: the 'normal' and the 'backup' mode. The backup mode is intended for checkout purposes; in this mode the detector signals are directly routed to the telemetry, discarding all on-board processing. The backup mode has only been used a few times in flight and will not be addressed here anymore.

Event processing. If, due to a detector event, the anode signal exceeds a certain threshold, defined by a low level discriminator (LLD), the event is processed by the electronics. The processing of events is controlled by logic and a microprocessor (the latter is redundant). A flow diagram is given in Fig. 4.7, while some characteristic times are given in Table 4.2. Provided the busy flip-flop (which is part of the logic) is reset, the event is accepted for further processing. It is checked whether within a certain time interval the LLD of the edge anode signal or of the A2 signal, or the high level discriminator (HLD) of the anode signal were also triggered. If so, the event is rejected and the busy flip-flop and front-end electronics are reset, ready to process the next event (this is called hardware AC, since the processor was not involved; all possible subsequent AC situations are checked by the processor). If there is no hardware AC situation the processor is interrupted to perform an INPUT ROUTINE, which involves reading all signals. This includes commanding an analogue-to-digital converter (ADC) to convert the signals from the fine sections of the sense grids and the anode; all signals from the coarse sections involve single bit LLD-settings. Apart from reading, the input routine also checks the presence of invalid coarse section combinations. Invalid conditions include:

1. two coarse sections are set that are not adjacent;
2. more than two coarse sections are set;
3. only one coarse section is set at the edge of the S1 frame (note that no hardware AC occurs in the X direction).

If an event is found to be invalid in the input routine, the front-end electronics and busy flip-flop are reset and the input routine returns the processor to its original task. If the event was valid, all readings are put in a buffer, which can store up to three events, and subsequently a reset is applied. However, if the buffer becomes full with this event, no reset will take place. It is then left to the event-processing routine (see below) to reset, after it has read an event from the full buffer.

If the processor is not busy with the input routine, it is continuously sampling the buffer for data input. If present, the EVENT-PROCESSING ROUTINE is started. This routine reads the data from the buffer and starts to analyze it, i.e. calculate the X- and Z-position of the event in units of 0.375 mm, calculate in what detector plane (above or below the anode frame A1) the event is detected, rebin the ADC-readout of the anode signal from 1024 to 32 channels (see Table 6.1) and format the output that is offered to the CDMS electronics. The event-processing routine also performs a final check on the validity of the event, i.e. if an event is found to be absorbed in the lower detector plane, while its anode signal is lower than rebinned ADC channel 19 (equivalent to 8.6 keV), it is labeled invalid. This AC will introduce minor losses of valid events (up to 1-2% of all absorbed photons), in particular at photon energies of about 4.8 keV (just below the L absorption edge of Xenon) and between 7 keV and 8.6 keV. However, this check did improve the AC efficiency so dramatically, that it compensates for the losses. Finally, every 8 s the event-processing routine reads and resets five hardware rate meters (RM, also referred to as 'scalers'), that are placed at various stages in the data handling (see Fig. 4.7):

RM1: monitors the number of events that set the LLD of the anode signal;
RM2: monitors the number of events that set the LLD of the AC counter, the edge anode and/or the HLD of the anode signal. This counter therefore provides a measure of the environmental background;
RM3: monitors the number of events that are accepted for processing by the processing electronics (i.e. when the busy flip-flop is not set);
RM4: monitors the number of events that are offered to the microprocessor, i.e. have no hardware AC;
RM5: monitors the number of events that are offered to the CDMS. These are all processed valid events.

It takes the electronics 1790 μs to fully process a valid event. Thus, the maximum valid event rate that can be handled by the processor, in case there are no invalid events, is 560 events/s. The input buffer for three events ensures that the processing rate responds better to Poissonian event-rate fluctuations at mean rates below 1500 events/s (see Fig. 4.8).
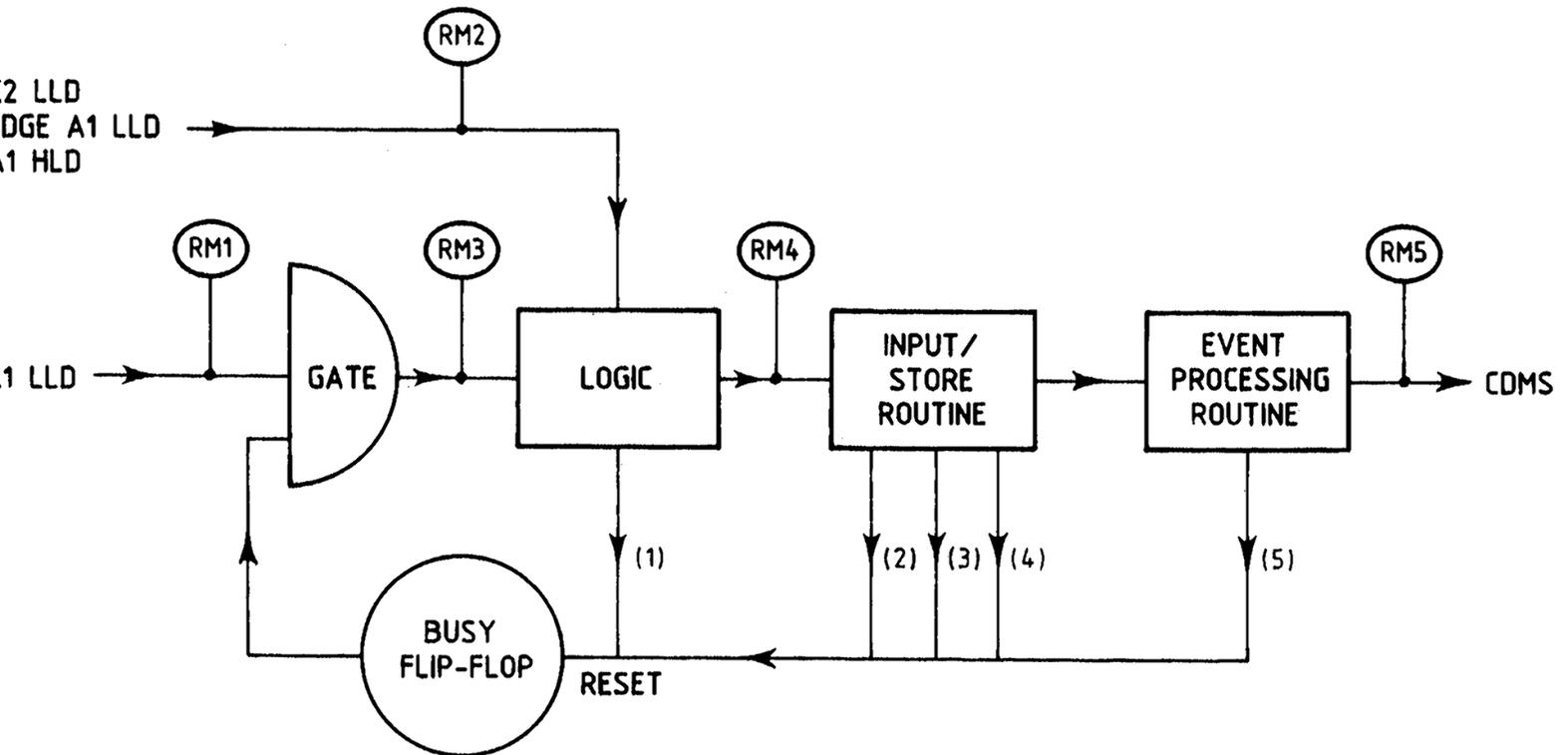
Figure 4.7: Schematic diagram of the triggering sequence of the detector electronics by an event. If the A1 LLD is set, it triggers the logic, provided the gate is open. The triggered logic will close the gate via a busy flip-flop. Furthermore, the logic checks whether the A2 LLD, edge A1 LLD or A1 HLD are set. If so, the event is discarded and the logic will reset the busy flip-flop (via (1)).

The event-processing routine runs independent of the other components shown, but can be interrupted to let the microprocessor run the input/store routine. For further details of the event handling, see text.

All numbers between parentheses indicate incidents in the event handling that reset the busy flip-flop, so that the gate is opened and the front-end electronics (not shown in this diagram) reset. The times of these incidents are specified in Table 4.2.

Finally, the positions of all rate meters (RM) are shown
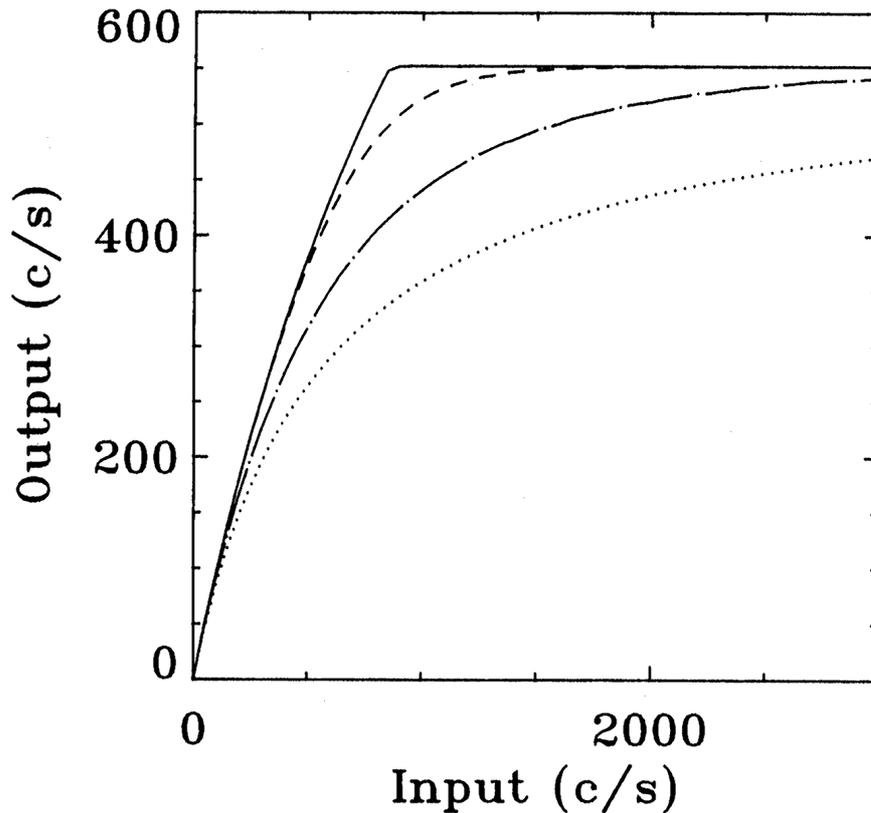
Figure 4.8: Rate response of detector electronics to valid events, in case no buffer is present (dotted curve), in case a buffer is present for 1 event (dotted-dashed), for 3 events (dashed) or for 100 events (solid). The model used to simulate responses is based on the time characteristics indicated in Table 4.2 (without the occurrence of invalid events) and includes Poisson noise on the incoming rate. Note the minor difference of the 3-event-buffer as compared to the 100-event-buffer, proving that the 3-event-buffer is large enough to compensate for most of the Poisson fluctuations

<u>Electronic efficiency losses.</u> Several effects in the front-end and processing electronics cause efficiency losses:

1. Live time of the electronics. During a fraction of the time, the electronics will be busy with the reading and processing of events. At these times the busy flip-flop is set and no additional events, valid or invalid, can be dealt with. The live time fraction can be read on an 8 s basis by the ratio of the contents of RM3 to RM1. It will be stronger proportional to the valid event rate than to the invalid event rate, because the reading and processing of valid events takes more time than that of invalid events.

2. Pile-up effects. Generally speaking, pile-up occurs if the signals of two events are too closely spaced in time, i.e. if a photon or particle hits the detector when the detector and its front-end electronics have not yet recovered from a previous hit by either a photon or particle. Recovery times are longer for particle hits than for photon hits. In chapter 6 in-flight measurements of these recovery times are assessed. The electronics dead time is not long enough to avoid this situation. In most cases the result will be an AC situation, since the 'merged' events usually violate one of the AC criteria. Therefore, a very limited number of merged events will be accepted. Moreover these events will mostly be labeled with the wrong position and energy information (this can be thought of as electronic scattering of events). See further in chapter 6.

4.5   Star sensor

The star sensor (SS) system consists of a TV camera mounted on the telescope body and electronics that is situated in the CDMS electronics box. The TV camera has a FOV of 3.9×4.2 square degrees and is sensitive to stars down to about 9th magnitude (depending on the spectral type of the star). At preset intervals (about 2 minutes) the camera is switched to a calibration mode to enable corrections on distortions of the scale of the image. In the normal operation of the SS the positions of six stars will be included in each telemetry frame. With these positions it is possible to deduce the direction of the SS axis with an accuracy better than $1'$. Due to the rigidity of the attachment of the SS, it is necessary to check the alignment between the X-ray telescope and the SS axis only once, by observing X-ray sources with accurately known positions.

To avoid damage to the TV camera by bright objects like the sun, the moon and the earth, a bright-object-sensor is placed on the mask assembly to monitor the intensity of the sky and alarm the electronics of the SS to close the shutter if the intensity becomes to high. Bright objects must be kept more than $40°$ from the SS axis. Apart from this measure, the TV camera is also equipped with a baffle.

The information of the SS is important for the analysis of the X-ray telescope since it provides the means to correct photon positions for attitude drifts of the space station. Of course the SS also provides the pointing direction of the *Kvant* module, the latter information is however less important for *COMIS*, owing to its imaging capability. It is possible to determine the pointing direction from the X-ray data alone if more than two X-ray sources with known positions are detected in the FOV. This condition is practically always satisfied when observing the galactic plane, because of the large FOV of *COMIS*.

4.6   CDMS and telemetry

The Command and Data Managing System acts as an interface between the various *COMIS* components and the module. It controls the SS operations, monitors the state of the detector, supplies voltages to various detector components from the electrical source of the space station, combines/reformats housekeeping data, SS data and X-ray data and feeds it to the telemetry system. Furthermore, the CDMS contains 1 Mbyte of read/write bulk memory to store any X-ray data (up to 293,552 events) that can not be handled by the rate of the real-time telemetry. This data may be down-loaded when the detector is not operating. A full description of the CDMS may be found in Al-Emam (1987).

The CDMS software reformats all data every second into minor frames (MIFs) of 400 bytes, of which 364 bytes are reserved for X-ray data. Each X-ray event is labeled with 10 bits X-position, 10 bits Z-position, 5 bits energy and 1 bit detector-plane identification. Thus a MIF can contain up to 112 events. Time information is added by the CDMS at the start, the center and the end of a MIF with an accuracy of 0.1 s. Eight telemetry channels of 3200 bps are open for all experiments of the *Kvant* module. The *COMIS* experiment is allowed to use up to three of these channels. In practice only one or two are used, thus enabling a direct telemetry coverage of 112 or 224 events s^{-1}. Additional coverage may be obtained if the contents of the bulk memory are down-loaded.

References

Al-Emam, O.: 1987, Ph.D. Thesis, University of Birmingham.
Mels, W.A., Lowes, P., Buurmans, H.B., Brinkman, A.C., Naber, A.P., Rook, A., Zandee, W.: 1988, *Nuc. Instr. Meth. Phys. Res.* **A273**, 689
Van Beek, H.F., Mels, W.A., Brinkman, A.C.: 1984, *IEEE Trans. Nucl. Sc.* **NS-31**, 45

Table 4.2: A summary of the most characteristic times in the processing flow[a]

Incident[b]	Condition	Reset?	Elapsed Time[c] (μs)
1	Hardware AC	y	TL + 10
2	Invalid X coarse section combination	y	TL + 136
3	Invalid Z coarse section combination	y	TL + 202
4	Event stored in buffer	if buffer is not full	TL + 570
5	Event read from buffer	if buffer was full	TP + 400
6	Invalid combination of det.plane/anode signal	n	TP + 800
7	Event accepted and offered to CDMS	n	TP + 1220

[a] Most of these incidents trigger a reset, except for the last two.

[b] The incident numbers which give rise to a reset (all except the last two) are indicated in Fig. 4.7.

[c] TL is time when logic is triggered by an event; TP is time when microprocessor starts processing an event by reading it from the buffer.

Chapter 5

Formalism and implementation of reconstruction technique

Abstract – The formalism and implementation of the reconstruction technique, as applied to data from *COMIS*, is discussed. The basis of the reconstruction technique, the cross correlation, is described, employing a by the author developed mathematical formulation which is particularly suitable to simple-configuration coded-mask cameras. New techniques are introduced to suppress Poisson noise in such a camera (potentially by up to a factor of about 2) and to deal with complications arising from the non-ideal character of the detector.

5.1   Introduction; choice of reconstruction method

An essential part of a coded-mask camera system entails the computer hardware and software for the reconstruction of the observed parts of the sky from the coded detector data. As mentioned in chapter 3, this is usually done off-line, some time after the actual observation. *COMIS* is no exception to this rule. This chapter deals with the details of the reconstruction process for *COMIS*, i.e. some specifications of the hardware and the actual algorithm implemented in the software.

In section 3.6 a number of reconstruction algorithms were reviewed that are commonly used. As was mentioned there, the choice for a particular algorithm depends on the aim of the reconstruction and the available computing power. Regarding the latter, particular care must be taken not to let the standard reconstruction take more time than the typical duration of an observation, since otherwise the handling of the incoming data stream becomes too cumbersome. In view of the available computing power for *COMIS*, it was decided to use the cross correlation as the reconstruction method, aided by several optimizing procedures. Although MEM may give better results for extended sources, it was discarded on the basis of excessive processing time.

In section 3.6.1 the cross-correlation technique was discussed in a general context. Here the cross-correlation technique is detailed for the case that the optical design is of the 'simple' type (see 3.4). In order to explain the formalism of the reconstruction problem, a discrete version of the mathematical description is chosen. This means that the distributions representing the detector and sky data are binned in arrays. The basic approach for implementation of the cross-correlation technique, specifically in the case of a simple-type coded-mask camera, has been elaborated by Hammersley (1986). This approach is reviewed in section 5.2, employing a new mathematical formulation which is particularly useful for simple-configuration coded-mask systems. Subsequently, two sections deal with two additional techniques to optimize the statistical quality of the reconstructed image. This includes a new technique to suppress Poisson noise, introduced in section 5.4. Section 5.5 describes procedures to combine observations with different pointing directions and/or orientations. Here, a new algorithm is introduced to combine flux variances in such a way that account is taken of the redistribution action necessary in combining two images. Assessment of the complications arising from the non-ideal character of the imaging concept is started in section 5.6 with a discussion of the
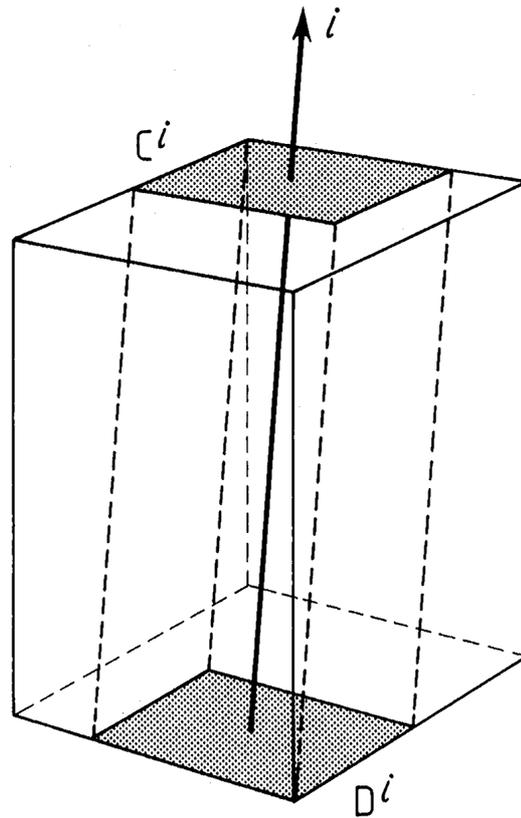
Figure 5.1: Visualization of notation, used in description of cross-correlation technique. A source is located in sky element i with a flux of s_i cts/me, projecting part of the physical mask (with elements in $\mathbf{C}^i$) on part of the detector plane (with elements of $\mathbf{D}^i$)

detector binning and its influence on the imaging of a point source. In section 5.7 the complications of non-ideal photon-detectors are considered and new techniques are introduced to deal with these. Finally, section 5.8 summarizes the actual hardware and software implementation for the data-analysis of the *COMIS* instrument, which was partly carried out by the author.

Various stages in the reconstruction are illustrated with the aid of a simulated observation; these illustrations are contained in an appendix to this chapter.

5.2   Cross-correlation technique for an 'ideal' detector in a simple system

The 'ideal' detector is defined as a detector with unlimited spatial resolution, 100% quantum efficiency and free of any obscuring elements. It is assumed that the detector is read out in elements equal in size to the mask elements and with the same total area (i.e. the simple system). Using this detector, the basic concepts of the cross-correlation technique, as employed for *COMIS*, are described. The arguments followed herein are based on the expected form of the sky, as explained in 5.2.2. To avoid at this stage complications due to maskholes being projected on more than one detector element, all sky point sources are assumed to be located in the center of a sky element.

5.2.1 Notation

Two-dimensional arrays are specified by bold capitals[1]. An element of such an array will be specified by a small letter with a single subscript. Several array names are used throughout this chapter. They are defined as follows:

D: Represents the detector, i.e. d_i is the number of counts per detector element (abbreviated as cts/de) in the ith element of the detector.

C: Represents the aperture function of the physical mask (ignoring the mask support grid). It is a two-valued array: $c_i = 1$ if the ith element of the mask is transparent and $c_i = 0$ if it is opaque.

S: Represents the part of the sky to which the detector is exposed. s_i is the flux from the sky in the ith element, in units of counts per mask element (abbreviated as cts/me).

M: Represents the array used for cross correlation with the detector (see 5.2.3). It is called the 'reconstruction array'.

R: Represents the reconstructed part of the sky, for units see **S**.

A superscript indicates a section of an array associated with a point source located in that sky element; for instance, a point source in sky element i projects a section of the mask represented by $\mathbf{C}^i$, onto a section of the detector represented by $\mathbf{D}^i$ (see Fig. 5.1). The sections $\mathbf{C}^i$ and $\mathbf{D}^i$ uniquely correspond to i.

In the forthcoming discussion the cross-correlation operation between two arrays is often used. Expressing this operation in a mathematically exact way would involve a complex expression for particularly the index range. Since the exact ranges are not crucial in the current context, this complexity is avoided by employing a symbolic notation: the cross correlation between e.g. **D** and **M** is denoted by the summation $\sum_j d_j^k m_j^k$. The indices of d and m have no literal meaning here, but it is indicated by the superscript k that both are uniquely related for the current point of the cross correlation. For illustration purposes, we give the exact expression for the cross correlation, in the one-dimensional case:

$$\sum_j d_j^k m_j^k \equiv \sum_{j=\text{maximum of } 1 \text{ and } N_d-k+1}^{\text{minimum of } N_d \text{ and } N_d+N_m-k} d_j m_{j+k-N_d}$$

where N_d and N_m are the total number of elements in **D** and **M** respectively and indices are counted from 1 onward.

5.2.2 Exposure of the detector

The sky portion to which the detector is exposed, is modeled by N point sources in sky elements $p(1)...p(N)$ and with intensities $s_{p(1)}...s_{p(N)}$ cts/me. **S** is assumed to be zero in all other elements. The ith point source projects a section $\mathbf{C}^{p(i)}$ of the mask on a section $\mathbf{D}^{p(i)}$ of the detector. All elements $d_j^{p(i)}$ of this projection paired with a transparent mask element in $\mathbf{C}^{p(i)}$ then accumulate $s_{p(i)}$ counts from this source. Detector elements paired with an opaque mask element and detector elements which are not a member of $\mathbf{D}^{p(i)}$ will not 'see' this source.

The point sources are superimposed on an isotropic (diffuse) sky background of β cts/sr/de (this sky-component is explicitly left out of **S**; although the sky background is strictly speaking part of the sky, the imaging of it is not of primary interest here). The number of sky-background counts received by each detector element depends on the solid angle of the sky viewed from this element and the open fraction t of the mask plate. Since the whole mask is visible from any detector position, the open fraction t to the sky is constant across the detector. If FOV_j is the field of view (in sr) seen from detector element j, this element will thus on average receive $FOV_j t \beta$ cts/de from the sky background.

Apart from sky radiation modulated by the mask, the detector is also exposed to a homogeneous internal 'detector background' (a background induced by e.g. cosmic rays) of b cts/de.

---

[1]The notation used in this chapter is slightly different from the one employed in chapter 3.

In conclusion, the exposed detector is described by:

$$d_j = b + FOV_j t\beta + \sum_{i=1}^{N} c_j^{p(i)} s_{p(i)} \qquad \text{cts/de} \tag{5.1}$$

The solid angle FOV_j viewed by each detector element through the whole mask decreases from the center towards the edge of the detector due to projection effects. In this ideal case, however, it is assumed that the sky background $FOV_j t\beta$ remains constant across the whole detector (true within 1% for total field of views up to $10° \times 10°$). Consequently, the sky-background term can be included in b (Eq. 5.1).

5.2.3 Cross correlation

The purpose of the cross correlation (symbol $\otimes$) between the detector array $\mathbf{D}$ and the reconstruction array $\mathbf{M}$ is to obtain a reconstructed sky that is equal to the real sky with respect to point sources, i.e. $\mathbf{R} \equiv \mathbf{D} \otimes \mathbf{M} = \mathbf{S}$. This condition prescribes the value of $\mathbf{M}$. The following discussion concerns a derivation of this value, proceeding from the expected detector illumination (Eq. 5.1). This will now be done in more detail than in section 3.6.1 and specifically for a simple type system. The description also indicates how the cross-correlation algorithm is implemented in the *COMIS* software.

Using the exposure of the detector (Eq. 5.1), application of the cross-correlation for sky element k

$$r_k = \sum_{j \in \mathbf{D}^k} d_j^k m_j^k \tag{5.2}$$

yields

$$\begin{aligned} r_k &= \sum_{j \in \mathbf{D}^k} \left(b + \sum_i c_j^{p(i)} s_{p(i)} \right) m_j^k \\ &= b \sum_{j \in \mathbf{D}^k} m_j^k + \sum_i s_{p(i)} \sum_{j \in \mathbf{D}^k} c_j^{p(i)} m_j^k \qquad \text{cts} \end{aligned} \tag{5.3}$$

The index k may address any element in $\mathbf{R}$. $c_j^{p(i)}$ is a mask element mapped by point source i onto a detector element d_j. For $k \neq p(i)$, the elements m_j^k and $c_j^{p(i)}$ have only in common that both are mapped onto the same detector element d_j^k, i.e. for that position of the sky there is 'no correlation' between the measured detector array and the mask pattern. Depending on the sky coordinates k and $p(i)$, some or even all values of $j \in \mathbf{D}^k$ may address a non-existing element $c_j^{p(i)}$, since the projections of the mask from sky coordinates k and $p(i)$ on the detector, $\mathbf{D}^k$ and $\mathbf{D}^{p(i)}$, overlap only partially or even not at all. For those detector elements outside $\mathbf{D}^{p(i)}$ but inside $\mathbf{D}^k$, $c_j^{p(i)}$ is defined to be 0.

The cross correlation is now split in an 'open' and 'closed' component, $\mathbf{R}[\mathbf{o}]$ and $\mathbf{R}[\mathbf{c}]$ respectively[2], and define the following arrays: $\mathbf{M}[\mathbf{o}]$, with opaque elements assigned a value 0 and transparent elements a value 1 and the 'reversed' version $\mathbf{M}[\mathbf{c}]$: 0 for transparent elements and 1 for opaque elements. The two components of the cross correlations then are:

$$\mathbf{R}[\mathbf{o}] = \mathbf{D} \otimes \mathbf{M}[\mathbf{o}], \tag{5.4}$$

yielding

$$r_k[\mathbf{o}] = b \sum_{j \in \mathbf{D}^k} m_j^k[\mathbf{o}] + \sum_i s_{p(i)} \sum_{j \in \mathbf{D}^k} c_j^{p(i)} m_j^k[\mathbf{o}] \qquad \text{cts,} \tag{5.5}$$

---

[2]In literature these are sometimes referred to as 'source' and 'background' component respectively.

and

$$\mathbf{R}[c] = \mathbf{D} \otimes \mathbf{M}[c] , \tag{5.6}$$

yielding

$$r_k[c] = b \sum_{j \in \mathbf{D}^k} m_j^k[c] + \sum_i s_{p(i)} \sum_{j \in \mathbf{D}^k} c_j^{p(i)} m_j^k[c] \qquad \text{cts.} \tag{5.7}$$

If there is a point source in sky element k ($p(i) = k$ for a certain i), Eq. 5.5 contains a term $s_k \sum_j c_j^k m_j^k[o]$ in which both c_j^k and $m_j^k[o]$ are either 1 for a transparent or 0 for an opaque mask element in the associated section of the mask. This implies that $\sum_j c_j^k m_j^k[o]$ is equal to $n^k[o]$, the number of transparent mask elements in the section of the mask defined by k. This term is 0 in Eq. 5.7, since the 0's and 1's are reversed in $m_j^k[c]$. Eqs. 5.5 and 5.7 then yield:

$$r_k[o] = bn^k[o] + s_k n^k[o] + \sum_{i,p(i) \neq k} s_{p(i)} \sum_{j \in \mathbf{D}^k} c_j^{p(i)} m_j^k[o] \qquad \text{cts} \tag{5.8}$$

and (if $n^k[c]$ is the number of opaque mask elements in the mask section defined by k)

$$r_k[c] = bn^k[c] + \sum_{i,p(i) \neq k} s_{p(i)} \sum_{j \in \mathbf{D}^k} c_j^{p(i)} m_j^k[c] \qquad \text{cts} \tag{5.9}$$

To eliminate the background terms and change to cts/me as unit, both components of the cross correlation are first normalized, through division by the number of mask elements associated with each of them, and subsequently the normalized 'closed' component is subtracted from the normalized 'open' component. The value for the cross correlation thus becomes:

$$r_k = \frac{r_k[o]}{n^k[o]} - \frac{r_k[c]}{n^k[c]} \qquad \text{cts/me} \tag{5.10}$$

yielding (by substitution of Eqs. 5.8 and 5.9)

$$r_k = s_k + \sum_{i,p(i) \neq k} s_{p(i)} \sum_{j \in \mathbf{D}^k} c_j^{p(i)} \left(\frac{m_j^k[o]}{n^k[o]} - \frac{m_j^k[c]}{n^k[c]} \right) \qquad \text{cts/me} \tag{5.11}$$

At the same time the variance in the count statistics (Poissonian) of r_k, $V_p[r_k]$, can be derived from $r_k[o]$ and $r_k[c]$, which are expressed in counts:

$$V_{\mathrm{p}}[r_k] = \frac{r_k[o]}{(n^k[o])^2} + \frac{r_k[c]}{(n^k[c])^2} \qquad (\text{cts/me})^2 \tag{5.12}$$

The value of this variance is further discussed in 5.2.4.

From Eqs. 5.4, 5.6 and 5.10 a direct definition of the reconstruction array $\mathbf{M}$ may be inferred:

$$m_j^k = \frac{m_j^k[o]}{n^k[o]} - \frac{m_j^k[c]}{n^k[c]} \tag{5.13}$$

or

$$m_j^k = \frac{c_j^k - t^k}{t^k (1 - t^k) n^k} \tag{5.14}$$

with $n^k = n^k[\text{o}] + n^k[\text{c}]$ and $t^k = n^k[\text{o}]/n^k$ (the open fraction of the mask pattern)[3]. The reconstruction is then given by Eq. 5.2 and the variance by

$$V_{\text{p}}[r_k] \;\; = \;\; \sum_j d_j^k \left(m_j^k \right)^2 \tag{5.15}$$

Although Eqs. 5.2 and 5.15 are more direct expressions for the cross correlation value and its variance, in the remaining discussion Eqs. 5.10 and 5.12 will be used instead, because they give more insight and in fact represent the structure of the cross-correlation algorithm implemented in the *COMIS*-software (see section 5.8).

In Eq. 5.11 it is shown that a definition for **M** is obtained which satisfies $r_k = s_k$, apart from a residual term. On average this residual term is 0 since

$$\sum_{j \in \mathbf{D}^k} \left(\frac{m_j^k[\text{o}]}{n^k[\text{o}]} - \frac{m_j^k[\text{c}]}{n^k[\text{c}]} \right) \;\; = \;\; 0 \tag{5.16}$$

and $c_j^{p(i)}$ is not correlated with the terms of this sum. The value of the residual term is dependent on point sources at positions different from sky element k which nevertheless illuminate a certain subsection of $\mathbf{D}^k$. This cross-talk introduces so-called 'coding noise' in r_k. Coding noise is not stochastic but deterministic in nature: if the source configuration within the observed sky is known, the value of the residual term can be determined for every k. In practice, the source configuration is not known before a reconstruction is actually carried out. One therefore faces the noise-like behavior of the residual term during the initial phase of the reconstruction procedure. A method to suppress this coding noise is outlined in section 5.3.

Coding noise is inevitable in the case of incomplete coding which is an inherent property of the simple-type coded-mask camera (see section 3.4).

5.2.4 Error in the reconstructed sky

Ponman and Hammersley (see Hammersley 1986) have derived an expression for the variance at each position in the reconstructed sky for a simple-type coded-mask camera. This expression includes Poisson noise due to counts modulated by the mask and due to detector-background counts. Furthermore, it includes coding noise. The expression is quite complex: it consists of 15 terms. In order to get some insight into the essence of this expression it is useful to consider a simplified version, by applying the following constraints:

1.) There is only one source with an intensity of s cts/me, at the center of the observed sky (say in sky element p).
2.) There is a homogeneous background of b cts/de.
3.) The open fraction of the mask is assumed to be independent of the section of the mask considered: $t^k = \frac{n^k[\text{o}]}{n^k} = t$ with $n^k = n^k[\text{o}] + n^k[\text{c}]$.
4.) The total number of mask elements, n, as well as nt, is $\gg 1$.
5.) The holes in the mask are randomly distributed, NOT in a PSEUDO-random manner such as for URA mask patterns (see chapter 3).

The variance in r_k (flux in cts/me) is then given by:

$$V[r_k] \;\; = \;\; \overbrace{\frac{s^2}{n^k}}^{i} + \overbrace{\frac{s}{(1-t)n^k}}^{ii} + \overbrace{\frac{b}{t(1-t)n^k}}^{iii} \tag{5.17}$$

---

[3]If t^k is assumed to be independent of k (say equal to t), Eq. 5.14 may be rewritten as:

$$\mathbf{M} \;\; = \;\; \frac{1}{t\,(1-t)\,n}\{\mathbf{C} - t\,\mathbf{U}\}$$

which is equivalent to Eq. 3.17 for an optimum system.

The origin of these three terms can be evaluated in a straightforward way:

(i) This is the variance of the residual term in Eq. 5.11 (coding noise):

$$s \sum_{j \in \mathbf{D}^k} c_j^p \left(\frac{m_j^k[\mathrm{o}]}{n^k[\mathrm{o}]} - \frac{m_j^k[\mathrm{c}]}{n^k[\mathrm{c}]} \right) \tag{5.18}$$

When reconstructing sky element k, it is unknown what the source configuration in the sky is. Therefore, the factor c_j^p in the residual term of r_k is unknown. However, it is known that this factor is either 0 or 1, with a probability of $1-t$ and t respectively. Its mean value therefore is t with a variance of $t(1-t)$. The variance $V_\mathrm{m}[r_k]$ in the residual term becomes:

$$
\begin{aligned}
V_\mathrm{m}[r_k] &= s^2 t(1-t) \sum_{j \in \mathbf{D}^k} \left(\frac{m_j^k[\mathrm{o}]}{n^k[\mathrm{o}]} - \frac{m_j^k[\mathrm{c}]}{n^k[\mathrm{c}]} \right)^2 \\
&= s^2 t(1-t) \sum_{j \in \mathbf{D}^k} \left(\left(\frac{m_j^k[\mathrm{o}]}{n^k[\mathrm{o}]} \right)^2 + \left(\frac{m_j^k[\mathrm{c}]}{n^k[\mathrm{c}]} \right)^2 \right) \\
&= s^2 t(1-t) \left(\frac{1}{n^k[\mathrm{o}]} + \frac{1}{n^k[\mathrm{c}]} \right) \\
&= \frac{s^2}{n^k}
\end{aligned}
\tag{5.19}
$$

Note that this variance is independent of the open fraction t.

(ii) and (iii) These are the variances due to the Poisson noise from the source s and the background b respectively. They can be derived from Eqs. 5.8, 5.9 and 5.12:

$$
\begin{aligned}
V_\mathrm{p}[r_k] &= b \left(\frac{n^k[\mathrm{o}]}{(n^k[\mathrm{o}])^2} + \frac{n^k[\mathrm{c}]}{(n^k[\mathrm{c}])^2} \right) + s \sum_{j \in \mathbf{D}^k} c_j^p \left(\frac{m_j^k[\mathrm{o}]}{(n^k[\mathrm{o}])^2} + \frac{m_j^k[\mathrm{c}]}{(n^k[\mathrm{c}])^2} \right) \\
&= b \left(\frac{1}{n^k[\mathrm{o}]} + \frac{1}{n^k[\mathrm{c}]} \right) + s \left(\frac{n^k t t}{(n^k[\mathrm{o}])^2} + \frac{n^k t(1-t)}{(n^k[\mathrm{c}])^2} \right) \\
&= \frac{b}{n^k t(1-t)} + \frac{s}{n^k(1-t)}
\end{aligned}
\tag{5.20}
$$

The ratio in variance due to coding noise and Poisson noise, assuming $b = 0$, equals $\frac{V_\mathrm{m}[r_k]}{V_\mathrm{p}[r_k]} = s(1-t)$. This shows that coding noise dominates Poisson noise if $s > \frac{1}{1-t}$ cts/me.

The first and last constraint imposed above, whose non-validity in practice influence the variance most importantly, are relaxed in what follows:

General source configuration. Consider first the case of a source that is off-axis instead of on-axis. In the summations contained in the derivations of Eqs. 5.19 and 5.20, only terms belonging to both $\mathbf{D}^k$ and $\mathbf{D}^p$ will contribute non-zero values. The number of these terms is the number of mask elements $n^{k,p}$ contained in this cross section. Eq. 5.17 now becomes:

$$V[r_k] = \left(\frac{s^2}{n^k} + \frac{s}{(1-t)n^k} \right) \frac{n^{k,p}}{n^k} + \frac{b}{t(1-t)n^k} \tag{5.21}$$

Consider now the case with more than one source in the observed sky. The value of the reconstruction is linearly dependent on the incident flux s of any source. The reconstruction of two skies is therefore the superposition of their individual reconstructions. The variance does not follow this superposition principle since the coding-noise variance, $V_\mathrm{m}[r_k]$, is not linear in s. However, it has been shown that the superposition may be applied when the number of sources is much smaller than n (Hammersley 1986). We can therefore expand $V[r_k]$ to:

$$V[r_k] = \sum_{i,p(i) \neq k} \left\{ \left(\frac{s_{p(i)}^2}{n^k} + \frac{s_{p(i)}}{(1-t)n^k} \right) \frac{n^{p(i),k}}{n^k} \right\} + \frac{b}{t(1-t)n^k} \tag{5.22}$$

(no source is assumed to be situated in sky element k).

If the number of sources approaches n, their imaging will be seriously degraded. This is obvious from a mathematical point of view: to extract more parameters than there are numbers in the detector data is an under-determined problem. This implicates for example that the imaging of an extended source with a simple-configuration coded-mask camera might be troublesome if its size is more than a quarter of the FOV.

The size of an extended source, which can be imaged with a simple-configuration coded-mask camera, may further be limited in special circumstances: for instance, the pattern used for *COMIS* prohibits the imaging of sources that fill homogeneously a row in the observed sky. This results from the third characteristic mentioned in section 4.3, that each row of the mask pattern has the same number of transparent and opaque elements. This illustrates that, for exceptional cases, the imaging of sources as small as just $\frac{1}{256}$th of the FOV may break down.

<u>Error for a URA mask pattern.</u> Eq. 5.19 is valid for a mask where the holes are distributed at random. As mentioned in chapter 3, the basic characteristic of URA mask patterns is that the cyclic cross correlation has a single peak with flat sidelobes. The reconstruction via cross correlation of an observed part of the sky, for which every sky position is coded by the full mask pattern, is therefore not disturbed by mask noise. This is for example the case for ANY position in the fully coded observed sky of an optimum-type coded-mask camera. In a simple-type coded-mask camera only the on-axis sky position is fully coded, so the coding-noise variance on-axis due to a point source on-axis is zero instead of $\frac{s^2}{n}$ (n total number of mask elements) for a random mask pattern. In fact, the coding-noise variance for a URA pattern scales with the fraction of the full pattern which is not covered in the cross correlation of sky element k. This fraction represents missing code. Eq. 5.19 becomes:

$$V_{\mathrm{m}}[r_k] \quad = \quad \left(1 - \frac{n^k}{n}\right)\frac{s^2}{n^k} \tag{5.23}$$

Eq. 5.23 demonstrates the improvement in the coding-noise variance in case of a URA pattern, as compared to a random pattern.

5.3 Suppression of coding noise: Iterative Removal Of Sources (IROS)

The residual term in Eq. 5.11 gave rise to coding noise (whose variance is described by Eq. 5.19 or 5.23), since it is not a priori known whether point sources at positions other than that of the reconstruction element k illuminate the detector, i.e. the factor $s_{p(i)}c_j^{p(i)}$ ($j \in \mathbf{D}^k$) is unknown. However, after an initial cross correlation a fair amount of information is available with respect to the stronger sources, which influence the residual the most. Now, a procedure is considered to suppress the coding noise after such an initial cross correlation.

The principle of the procedure is as follows: first, from the initial cross correlation a number, say N, of strong point sources well above the coding-noise level is determined at sky elements $p(1), ..., p(N)$ with estimated intensities of $s_{p(1)}[e], ..., s_{p(N)}[e]$. Next, the detector exposure to these point sources is simulated:

$$d_j[\text{simulated}] \quad = \quad \sum_{i=1}^{N} c_j^{p(i)} s_{p(i)}[e] \tag{5.24}$$

Then, this simulated detector array is subtracted from the observed detector array, described by Eq. 5.1:

$$d_j[\text{subtracted}] \quad = \quad d_j[\text{observed}] - d_j[\text{simulated}]$$

$$= b + \sum_{i=1}^{N} c_j^{p(i)} \left(s_{p(i)} - s_{p(i)}[\mathrm{e}] \right) \tag{5.25}$$

Subsequently, $d_j[\text{subtracted}]$ is cross correlated with $\mathbf{M}$. The residual term in the resulting cross-correlation value (Eq. 5.11) has become smaller, provided the estimates $s_{p(i)}[\mathrm{e}]$ were good.

The accuracy of the estimates may be improved by repeating the same procedure. It is then necessary to also include the subtraction of sources with negative fluxes in case $s_{p(i)}[\mathrm{e}]$ was overestimated ($> s_{p(i)}$), which results in a negative source intensity in the cross correlation of the 'subtracted detector'. The procedure is repeated until no (positive nor negative) significant excess with respect to the expected Poisson noise is left at the source locations. Furthermore, one has to take account of the possibility that after one iteration of this procedure, other (weaker) sources, besides those already found, may appear at a significant level. These have to be taken into consideration, so as to optimize the coding-noise suppression. This iterative procedure was developed by Hammersley (1986) and Hammersley *et al.* (1992) and is called 'iterative removal of sources' (IROS).

IROS is very efficient in suppressing the coding noise to an acceptable level; few iterations are necessary to accomplish this. In order to demonstrate this, it is illustrative to consider the errors that are left over after a single iteration. For this, Eq. 5.22 is used for the noise variance. Consider one source, say no. c: if $\Delta^c = s_{p(c)} - s_{p(c)}[\mathrm{e}]$, the contribution from this residue to the cross correlation of the subtracted detector is:

$$\Delta^c \sum_{j \in \mathbf{D}^k} c_j^{p(c)} \left(\frac{m_j^k[\mathrm{o}]}{n^k[\mathrm{o}]} - \frac{m_j^k[\mathrm{c}]}{n^k[\mathrm{c}]} \right) \tag{5.26}$$

Δ^c is not 0, since the estimate $s_{p(c)}[\mathrm{e}]$ was influenced by the coding and Poisson noise of the other $N-1$ sources and the Poisson noise of the background. The expected variance in Δ^c is given by:

$$V[\Delta^c] = \sum_{i \neq c} \left(\frac{s_{p(i)}^2}{n^{p(c)}} + \frac{s_{p(i)}}{(1-t)n^{p(c)}} \right) \frac{n^{p(i),p(c)}}{n^{p(c)}} + \frac{b}{t(1-t)n^{p(c)}} \tag{5.27}$$

with $n^{p(i),p(c)}$ the number of mask elements projected in the common part of the detector (illuminated by source i as well as source c). The variance in the new residual term due to source no. c at sky element k is ($< \Delta_c^2 >= V[\Delta_c]$):

$$\frac{V[\Delta^c]}{n^k} \frac{n^{k,p(c)}}{n^k} \tag{5.28}$$

In fact, the variance at k is due not only to source c, but to ALL N sources, so that it is described by:

$$\sum_{c=1}^{N} \frac{n^{k,p(c)}}{n^k} \left\{ \sum_{i \neq c} \left(\frac{s_{p(i)}^2}{n^{p(c)}} + \frac{s_{p(i)}}{(1-t)n^{p(c)}} \right) \frac{n^{p(i),p(c)}}{n^{p(c)}} + \frac{b}{t(1-t)n^{p(c)}} \right\} / n^k \tag{5.29}$$

This expression describes the coding-noise variance at k in the reconstruction of the subtracted detector array, due to the residues $s_{p(i)} - s_{p(i)}[\mathrm{e}]$ of all N subtracted sources. To complete the variance expression at k, the Poisson noise had to be added, which is given by:

$$\sum_{c=1}^{N} \left(\frac{s_{p(c)}}{n^k(1-t)} \frac{n^{k,p(c)}}{n^k} \right) + \frac{b}{n^k t(1-t)} \tag{5.30}$$

It is instructive to consider the upper limit of the variance derived in this way. This limit may be determined by placing all N sources at the center of the observed sky. The complete variance expression then reduces to:

$$V[r_k[\text{subtracted}]] < \left(\frac{N-1}{n} \right) \frac{\sum_{i=1}^{N} s_{p(i)}^2}{n^k} + \left(1 + \frac{N-1}{n} \right) \frac{\sum_{i=1}^{N} s_{p(i)}}{n^k(1-t)} +$$
$$+ \left(1 + \frac{N}{n} \right) \frac{b}{n^k t(1-t)} \tag{5.31}$$

The fact that the actual coding-noise variance will be smaller for a URA pattern does not interfere with the upper-limit estimate in Eq. 5.31.

Analysis of Eq. 5.31 shows that the total coding-noise variance is reduced to at most $(N-1)/n$ times its original value, the point-source-induced Poisson-noise variance is increased to at most $1 + (N-1)/n$ times its original value and the background Poisson-noise variance is increased to at most $1 + N/n$ times its original value. In conclusion, if the number of sources N is small with respect to the number of mask elements n, the coding-noise variance is practically eliminated and the Poisson-noise variance remains constant. The efficiency of IROS is large, no more than one or occasionally two iterations (in case extra point sources are found after the first iteration) are needed for an adequate suppression of the coding noise.

5.4 Suppression of Poisson noise: weighing detector subsections

In wide-field-imaging applications, the simple-type coded-mask camera presents a major advantage with respect to the optimum-coded camera. As was shown in section 3.4.1, Poisson-noise levels are smaller in the former type of camera because only a section of the complete detector is used for the coding of every sky position. Thus, fewer background counts influence the noise level in the reconstruction. In fact, this characteristic of the simple-type camera may be used to suppress the level of Poisson noise even further, thus utilizing the simple-type characteristic to the most. It involves the weighing of detector sections during the reconstruction. For the *COMIS* instrument this procedure may in some cases result in a suppression of Poisson noise by a factor of 2 in standard deviation. In the following, we introduce this procedure for a simplified case.

Consider an observed sky with one off-axis point source with intensity s cts/me in sky element i, which projects n^i mask elements onto the detector. Besides the source counts, the detector also detects a background of b cts/de. Suppose it is required to reconstruct a sky position k, not coincident with the point source ($k \neq i$); the relevant section of the detector consists of n^k elements. Assume that part of the projection of the mask by the point source is contained in the detector section relevant for the reconstruction of sky position k, with $n^{k,i}$ elements overlapping. The detector section used in the reconstruction of k may be thought of as two parts: that part, which is not illuminated by s ($n^k - n^{k,i}$ elements) and the remainder ($n^{k,i}$ elements), see Fig. 5.2. The expected contributions from these parts to the Poisson variance of the reconstruction are (again assuming $t^k = t$ to be constant):

$$V_{k,1} \;=\; \frac{b}{n^k t(1-t)} \frac{n^k - n^{k,i}}{n^k} \tag{5.32}$$

and

$$V_{k,2} \;=\; \frac{s + b/t}{n^k(1-t)} \frac{n^{k,i}}{n^k} \tag{5.33}$$

respectively. These combine to:

$$V_{\mathrm{n}} \;=\; \frac{b}{n^k t(1-t)} + \frac{s}{n^k(1-t)} \frac{n^{k,i}}{n^k} \tag{5.34}$$

(see also Eq. 5.22). However, one may also proceed differently by cross correlating on the two parts separately, yielding $r_{k,1}$ (from the detector part with $n^k - n^{k,i}$ elements):

$$r_{k,1} \;=\; \frac{r_{k,1}[\mathrm{o}]}{n^k[\mathrm{o}] - n^{k,i}[\mathrm{o}]} - \frac{r_{k,1}[\mathrm{c}]}{n^k[\mathrm{c}] - n^{k,i}[\mathrm{c}]} \tag{5.35}$$

and $r_{k,2}$ (from the part with $n^{k,i}$ elements):

$$r_{k,2} \;=\; \frac{r_{k,2}[\mathrm{o}]}{n^{k,i}[\mathrm{o}]} - \frac{r_{k,2}[\mathrm{c}]}{n^{k,i}[\mathrm{c}]} \tag{5.36}$$
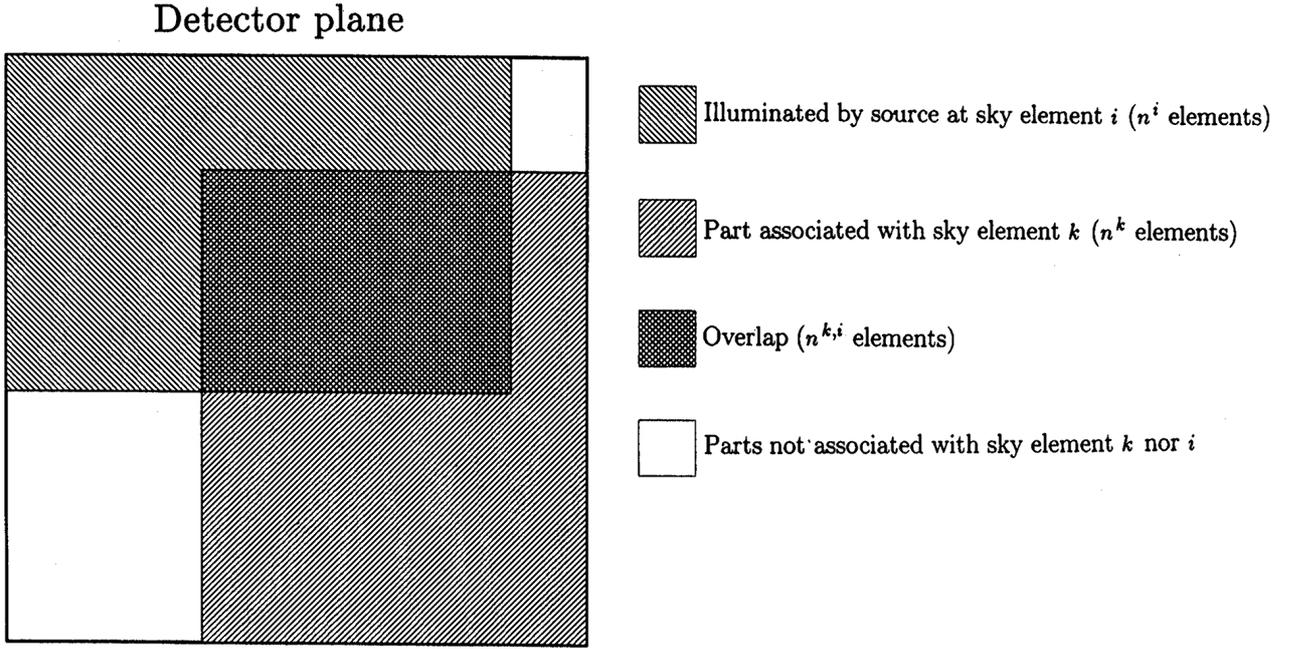
Detector plane

Figure 5.2: A source at sky element i illuminates n^i detector elements. Assume that another sky element k needs to be reconstructed. The associated detector can be thought to consist of two sections: a section that coincides with the illumination by the source (with $n^{k,i}$ detector elements overlapping) and the remainder ($n^k - n^{k,i}$ elements)

The variances of the two parts become:

$$V_{k,1} \quad = \quad \frac{b}{(n^k - n^{k,i})t(1-t)} \tag{5.37}$$

and

$$V_{k,2} \quad = \quad \frac{s + b/t}{n^{k,i}(1-t)} \tag{5.38}$$

The two estimates of the reconstructed sky, $r_{k,1}$ and $r_{k,2}$, can then be combined by calculating their weighted mean as follows:

$$r_k \quad = \quad \frac{\frac{r_{k,1}}{V_{k,1}} + \frac{r_{k,2}}{V_{k,2}}}{\frac{1}{V_{k,1}} + \frac{1}{V_{k,2}}} \tag{5.39}$$

with a variance

$$V_{\mathrm{w}} \quad = \quad \frac{1}{\frac{1}{V_{k,1}} + \frac{1}{V_{k,2}}} \tag{5.40}$$

Substitution of (5.37) and (5.38) yields:

$$V_{\mathrm{w}} \quad = \quad \frac{b}{n^k t(1-t)} \left(1 - \frac{n^{k,i}/n^k}{1 + b/ts} \right)^{-1} \tag{5.41}$$

The ratio of V_{n} to V_{w} can be expressed as:

$$\frac{V_{\mathrm{n}}}{V_{\mathrm{w}}} \quad = \quad 1 + K_1(1 - K_1)\frac{K_2^2}{1 + K_2} \tag{5.42}$$

with $K_1 = \frac{n^{k,i}}{n^k}$ and $K_2 = \frac{s}{b/t}$. It is clear that always $V_{\mathrm{w}} < V_{\mathrm{n}}$.

This illustration shows that it is worthwhile in the reconstruction of any position to consider dividing the detector plane in several sections in which the count density is constant, cross correlating every detector section separately and weight averaging the results with the inverse Poisson-noise variance. Here, this procedure is referred to as WA. In case there is more than one point source in the observed sky, the value for the combined Poisson variance also leads to the same result of effectively suppressing the Poisson noise. The amount of noise suppression is dependent on the dynamic range of the count densities of the detector sections selected in the procedure, which is given by K_2 in the above example. In the case of *COMIS* the maximum value of K_2 (defined by the countrate of the strongest point sources and that of the background) is about 10. For a particular value of K_2, the maximum suppression is obtained for a sky position where $K_1 = \frac{1}{2}$. This leads to a maximum suppression factor for the Poisson-noise standard deviation of about 2 for *COMIS*.

Like in IROS, one needs to know the source locations in the observed sky, before a WA procedure can be carried out[4]. Again, the positions of the strongest sources in the observed sky are already obvious from an initial cross correlation. Since they contribute most strongly to the Poisson noise, together with the contributions of the sky and detector background, they largely determine the most effective subdivision of the detector plane.

5.5 Combining reconstructed sky images of different observations

To improve the sensitivity for a particular part of the sky, it is often required to combine observations with different pointing directions and/or orientations that have overlapping sky coverage. Combination of observations is also required if an observation comprises a stack of short exposures with slightly different pointing directions and/or orientations. The latter condition is typical for *COMIS*, where a one-day observation on a single target is subdivided by eclipses and transitions through the South Atlantic Anomaly (see chapter 2). During these interruptions the attitude of the *Mir* station shifts significantly with respect to the angular resolution.

The combination of different observations may be done in the detector plane as long as the effective area for each position in the observed sky is not substantially affected. Also, there should not be any change in the roll angle about the optical axis, since this requires rotation of photon positions in the detector plane about a center that is dependent on the direction of the photon which is not known.

When a combination is not possible in the detector plane, it should be done in the sky plane. For this, one selects one of the images as a base frame. The coordinates of all elements in the subsidiary image have to be transformed to this base frame. Such a transformation is in principle three-dimensional, since an image represents a projection of part of the celestial sphere on the plane, tangent to the sphere and perpendicular to the optical axis. Skinner *et al.* (1987) have described this transformation. For small FOVs this transformation can be reduced to simple plane geometry, which involves a rotation succeeded by a translation:

$$\vec{p} = (R)\vec{p'} + \vec{t} \tag{5.43}$$

with

$$(R) = \begin{pmatrix} \cos\phi & -\sin\phi \\ \sin\phi & \cos\phi \end{pmatrix} \tag{5.44}$$

where $\vec{p}$ is the two-dimensional position of the center of a bin from the subsidiary frame in the base frame, $\vec{p'}$ its position in the subsidiary frame, $\vec{t}$ a translation vector and ϕ the rotation angle from the base frame to the subsidiary frame.

<u>Redistribution.</u> The coordinate transformation indicates where each subsidiary bin $r_k[\mathrm{s}]$ is situated with respect to the base grid. The next task is to redistribute each subsidiary bin on the base

---

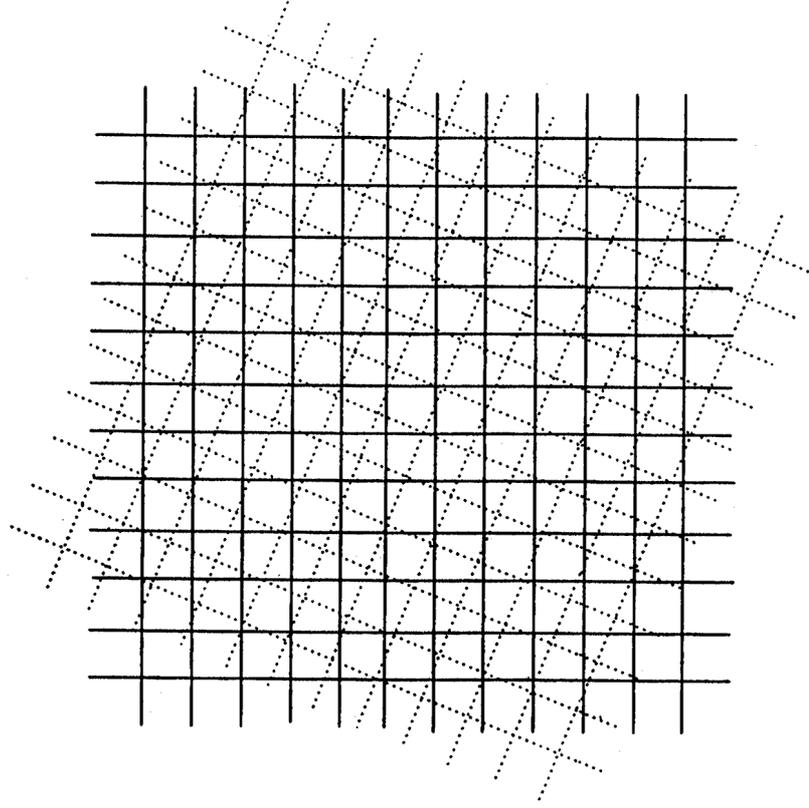[4]Unlike in IROS, estimates of the source intensities are not needed in WA.

Figure 5.3: An example of a subsidiary grid (dashed lines) projected on the base grid, at an angle unequal to a multiple of 90°. Each subsidiary bin has a different redistribution on the reference grid. This redistribution can be quite complex, i.e. involving long calculations

grid. One does not know from where within the subsidiary bin the flux $r_k[\mathrm{s}]$ originated. The redistribution therefore needs to be done proportional to the fraction of the subsidiary bin covered by the appropriate base bins. It is assumed here that all base and subsidiary bins are square and equal in size (see Fig. 5.3). Thus, a possible change of the angular size of sky bins across the observed sky is neglected (see section 3.4.2).

The calculation of the redistribution fractions becomes rather complex and CPU-time-consuming if the angle between both grids differs from a multiple of $\pi/2$. Two methods have therefore been proposed to speed up the redistribution calculation at the expense of some accuracy:

1. Over-sampling of subsidiary bins (Hammersley 1986). Each subsidiary bin is divided in n equally sized sub-bins. The position of the center of each sub-bin with respect to the base grid is calculated and the $\frac{1}{n}$th part of the bin value is assigned to the appropriate base bin. The number of calculations is proportional to n and the accuracy of this redistribution is of the order of $1/n$.

2. Disregard of the orientation of the subsidiary-bin edges with respect to the base grid (Patterson 1990). The edges of the subsidiary bin are assumed to be parallel to the base grid. The calculation of the redistribution fractions is then done through a calculation of the rectangular areas of the subsidiary bin covered by the four possible base bins. The accuracy of this redistribution is of the order of

$$\frac{1}{2}\left(1 + \frac{\cos\phi - 1}{\sin\phi}\right)^2 \tan\phi \qquad (5.45)$$

(see section 3.5.4), with ϕ the actual angle modulo $\pi/2$ between subsidiary and base grid.

The choice for one of these approximate methods or the exact method for the calculation of the redistribution is obviously a trade-off between the accuracy and the calculation time required.
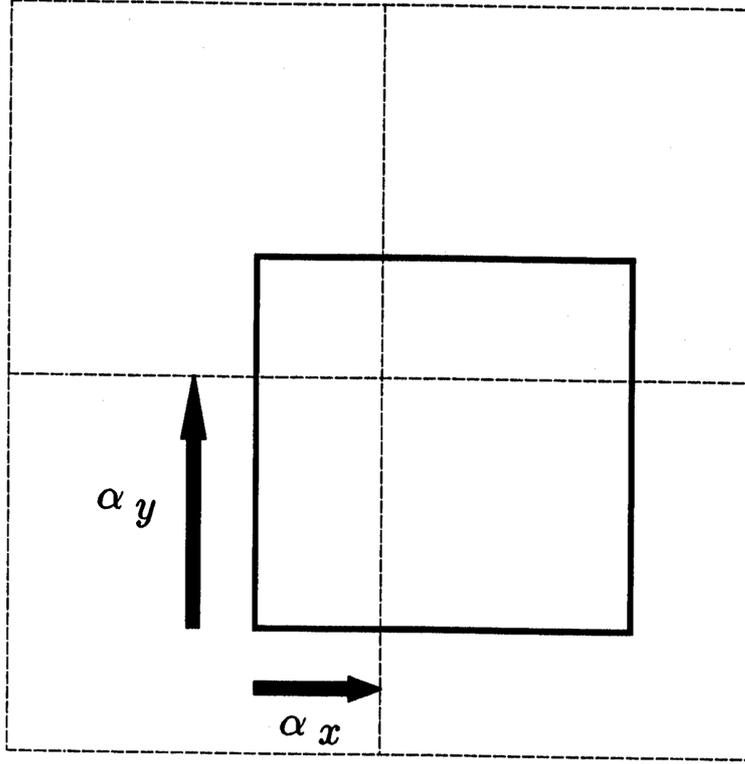
Figure 5.4: An example of a projection of an open mask element on the detector grid, if the latter has the same size as the mask elements. $\alpha_{x,y}$ define the redistribution of the mask element on the detector grid

We introduce the algorithm for the combination of the fluxes, given the redistribution fractions. Consider a base bin i, which covers fractions $\alpha_{i,k1},...,\alpha_{i,kn}$ of the subsidiary bins $k1,...,kn$, whose flux values are $r_{k1}[\text{s}],...,r_{kn}[\text{s}]$ and variances are $\sigma_{k1}^2[\text{s}],...,\sigma_{kn}^2[\text{s}]$. If $r_i[\text{b}]$ is the flux value of the base bin and $\sigma_i^2[\text{b}]$ its variance, then the fluxes of the subsidiary bins are combined with it, after weighing with the associated redistribution fraction divided by the variance, following:

$$r_i[\text{sum}] \quad = \quad \frac{r_i[\text{b}]/\sigma_i^2[\text{b}] + \alpha_{i,k1}r_{k1}[\text{s}]/\sigma_{k1}^2[\text{s}] + \alpha_{i,k2}r_{k2}[\text{s}]/\sigma_{k2}^2[\text{s}] + ...}{1/\sigma_i^2[\text{b}] + \alpha_{i,k1}/\sigma_{k1}^2[\text{s}] + \alpha_{i,k2}/\sigma_{k2}^2[\text{s}] + ...} \tag{5.46}$$

The variance in $r_i[\text{sum}]$ is:

$$\sigma_i^2[\text{sum}] \quad = \quad \frac{1/\sigma_i^2[\text{b}] + \alpha_{i,k1}^2/\sigma_{k1}^2[\text{s}] + \alpha_{i,k2}^2/\sigma_{k2}^2[\text{s}] + ...}{(1/\sigma_i^2[\text{b}] + \alpha_{i,k1}/\sigma_{k1}^2[\text{s}] + \alpha_{i,k2}/\sigma_{k2}^2[\text{s}] + ...)^2} \tag{5.47}$$

Thus the combined flux estimate is always better than each of the contributions. It is noted that in the expression for $\sigma_i^2[\text{sum}]$ account has been taken of the decrease in variance of the subsidiary image by the redistribution process.

5.6   Detector binning; finely-sampled balanced correlation

Until here, it has been assumed that each mask element is projected in exactly one detector element. In other words, each sky point source was located in the center of a sky element. In practice, this is mostly not true. A point source can be located anywhere in a sky bin or may even possess a finite extent.

If a point source is located at an arbitrary position within a sky bin, the projection of every open mask element on the grid of the detector is as depicted in Fig. 5.4. Generally, each mask hole

projection is sampled by four detector elements which cover the following fractions of a mask element: $O_1 = \alpha_x \alpha_y$, $O_2 = \alpha_x(1-\alpha_y)$, $O_3 = (1-\alpha_x)\alpha_y$ and $O_4 = (1-\alpha_x)(1-\alpha_y)$. The reconstruction of the point source will also be divided in four sky bins, each bin scaled to the fractions just mentioned, because the same splitting will occur for every projected mask hole. In the worst case the highest fractional value is only 0.25 (if $\alpha_x = \alpha_y = 0.50$). This reasoning does not apply to noise peaks in the reconstructed sky away from the source position. A different phasing of the detector binning will not alter the noise characteristics in the reconstructed sky at non-source positions.

The phasing of the detector binning may be optimized with respect to the source position, in order to accumulate most of the flux in a single bin, so that the source is 'lifted' as far as possible above the noise. Clearly, this phasing is different for each source and can be applied only if the source positions are known beforehand. During an initial reconstruction this information is not available and an optimum bin phasing is not possible: identification of the sources needs to be done first. However, one may suppress the influence of a bad bin phasing by carrying out the cross correlation with a step size smaller than the mask-element size. This was first proposed by Fenimore & Cannon (1981) and is referred to as 'finely-sampled balanced correlation'. If s is the step size, in units of a mask-element size ($s < 1$), α_x and α_y will at most be s, instead of 1, and the worst bin phasing ($\alpha_x = \alpha_y = \frac{s}{2}$) implies a fractional value for the highest source bin of $(1-\frac{s}{2})^2$ which is always better than 0.25. The lower limit for s is of course governed by the resolution of the detector position readout. For *COMIS* this lower limit is 0.375 and, when taken as the step size of the cross correlation, results in a worst case fractional value of 0.66 for the highest source bin.

Some important points should be noted:

- a substantial enlargement of the computational effort of the cross correlation is involved when the step size of the cross correlation is decreased. For instance, in the case of *COMIS* a step size of 0.375 instead of 1 mm involves a factor of ~ 7 more CPU-time and memory usage (when using fast Fourier transforms, array lengths must be equal to a power of 2; thus, the disadvantage may be even larger, see section 5.8). It may be worthwhile to consider the usage of slightly larger steps, at the expense of some sensitivity (actually a step size of 0.5 mm is used, implying a worst case point source coverage by the highest bin of 0.56 of the total point-source flux, while the increase of computational effort is 'only' a factor of 4);

- one should be aware that, when using finely-sampled balanced correlation, in a reconstructed sky the bins are no longer statistically independent; care should be taken when estimating accuracies of point-source fluxes and positions.

5.7 Complications in non-ideal situations

5.7.1 Effect of window support structure on reconstruction

As described in chapter 4, incoming photons are not only blocked by the camera shielding but also by bars of the detector entrance-window support structure. The detector elements which are under such a bar or in its shadow for a sky element k will not 'see' a potential source at k. A correct estimate of the intensity of such a potential source in the kth sky element of the reconstruction involves therefore a revision of the active area: the normalization performed in Eq. 5.9 by dividing $r_k[\text{o}]$ by $n^k[\text{o}]$ and $r_k[\text{c}]$ by $n^k[\text{c}]$ must be modified to divisions by $a^k[\text{o}]$ and $a^k[\text{c}]$ respectively, where $a^k[\text{o}]$ is the number of UNOBSCURED detector elements 'seen' from k through transparent mask elements and $a^k[\text{c}]$ the number of UNOBSCURED detector elements behind opaque mask elements.

In principle, one wants the cross correlations $r_k[\text{o}]$ and $r_k[\text{c}]$ only to be performed on the detector subsection that is not obscured by the window support structure, as seen from sky position k. The exclusion of counts in the obscured detector parts would result in a smaller Poisson-noise level. To actually do this, a different subsection would have to be used for every point in the reconstructed sky (disregarding the shadowing by the telescope shielding). However, this procedure implies a lot more computer effort, i.e. apart from detector area selection per reconstruction element, the cross correlations will also have to be calculated directly and not via the fast Fourier transform

(for details, see section 5.8). The effort would then exceed the level of acceptability for the ratio of processing time to observation time. Also, the finite detector resolution and the photon-penetration effect (see 6.5) cause photons from k to be detected in the shadows of the support bars as seen from k. Therefore, there is a certain benefit in using the complete detector plane for the reconstruction of sky element k. Detector-area selection is therefore not applied.

Two problems arise from the new normalization. The first concerns the sky background term in Eq. 5.1, which was conveniently included in the b-term. This inclusion is no longer justified, since the support structure will strongly modulate the illumination by the sky background: the field of view, as seen from each detector element (FOV_j), now strongly varies across the detector plane. Fig. 5.5 illustrates how FOV_j, as seen from three characteristic detector positions, may be restricted. The illustration shows that FOV_j ranges from 0 sr to about one quarter of the full FOV (in the 2-dimensional case). Furthermore, the number of mask elements that are projected on a detector element by the diffuse sky background no longer equals that of the total mask; the total mask can no longer be viewed from every position on the detector. Thus, the mask open fraction in the sky background term of Eq. 5.1 depends on j. t_j is defined as the open fraction of that part of the mask which can be viewed from detector position j.

The second problem is that the detector background term will give an additional non-zero term in the equation for the reconstruction, since, due to the different normalization, b is not 100% subtracted anymore (the summation over the detector background terms in Eqs. 5.8 and 5.9 still result in $bn^k[\text{o}]$ and $bn^k[\text{c}]$ because b is homogeneous over the WHOLE detector, including positions under the support structure or in its shadow).

Applying the normalization $a^k[\text{o}]$ and $a^k[\text{c}]$ to $r_k[\text{o}]$ and $r_k[\text{c}]$ respectively and applying the cross correlations to the COMPLETE detector, r_k now becomes (compare with Eq. 5.11):

$$r_k \;=\; s_k + b\left(\frac{n^k[\text{o}]}{a^k[\text{o}]} - \frac{n^k[\text{c}]}{a^k[\text{c}]}\right) + \beta \sum_{j\in\mathbf{D}^k} FOV_j t_j \left(\frac{m_j^k[\text{o}]}{a^k[\text{o}]} - \frac{m_j^k[\text{c}]}{a^k[\text{c}]}\right) +$$

$$+ \sum_{i,p(i)\neq k} s_{p(i)} \sum_j c_j^{p(i)} \left(\frac{m_j^k[\text{o}]}{a^k[\text{o}]} - \frac{m_j^k[\text{c}]}{a^k[\text{c}]}\right) \tag{5.48}$$

Note that a potential source in k is still normalized correctly (see s_k term) and that the sky background term looks very similar to the residue term for point sources (the last term of Eq. 5.48). The coding noise now comprises three terms, related to point sources, sky background and detector background.

The extra residue terms, introduced by inclusion of the support structure, can be suppressed in a manner similar to that for the point sources. In fact this is more straightforward since b and β are usually fairly well known for a particular instrument from independent in-flight calibration measurements on empty sky fields (i.e. without any compact X-ray sources in the observed sky). Furthermore, β is fairly constant, considering the predominant extra-galactic contribution, and the detector background is usually correlated in a well-known fashion with the particle background environment captured by the earth's magnetic field (see chapter 6). The suppression may be achieved by subtraction of the detector background and the support-structure-modulated sky background (see e.g. Covault *et al.* 1991); here this procedure is referred to as BASUB. The subtraction can be performed directly on the detector data before any reconstruction procedure is employed[5].

The dimensions of the window support structure for the *COMIS* detector (see 4.3) give rise to values for $a^k[o,c]$ that differ considerably from $n^k[o,c]$. The blocking by the structure amounts to 18% for an on-axis point source and increases towards the edge of the observed sky to 48% per illuminated support grid cell (the exact value depends on the precise location of the illumination with respect to the support structure). If BASUB is not applied, calculations show that the ratio R of the coding-noise variance, introduced by the background terms in Eq. 5.48, to the Poisson-noise variance induced by each of the background components is roughly given by:

$$R \;=\; 3.4 \times 10^{-6}\, B_d\, T \tag{5.49}$$

---

[5]However, the extraction of Poisson-noise variances from the original data must be accounted for.
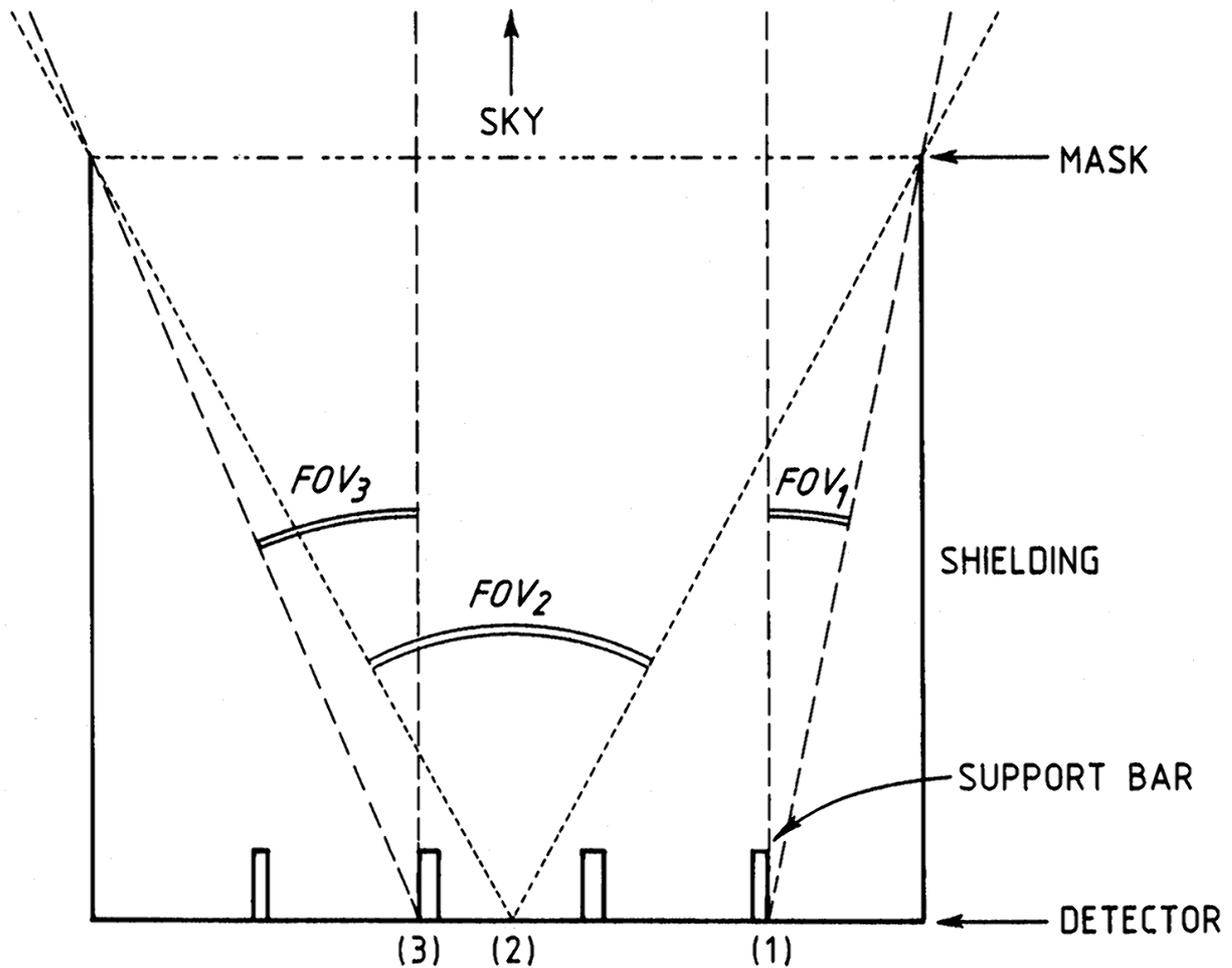
Figure 5.5: Sketch of how the FOV, as seen from three characteristic detector positions, is restricted. In the first position, right next to a detector entrance-window support structure bar, the FOV is strongly limited, on the one side by the support bar and on the other side by the nearest part of the telescope shielding. At the third position the limitation by the shielding is not so strong, since it is relatively far away. Finally, at the second position where the FOV is only limited by the shielding, the FOV is largest. Although this sketch is no truthful representation of *COMIS*, it correctly illustrates viewing conditions in this instrument

for the detector background and

$$R = 8.5 \times 10^{-7} \, B_s \, T \qquad (5.50)$$

for the sky background (B_d and B_s are the detector and sky background respectively in cts/s, normalized to the WHOLE *COMIS* DETECTOR). T is the observation time in s. In chapter 6 in-flight measurements of B_d and B_s are described. These have resulted in nominal values of 19 cts/s and 23 cts/s per whole detector respectively, for the total energy band of *COMIS*. Thus, the coding noise from the background, due to the support structure, is dominated by the detector-background contribution and becomes significant if the observation time exceeds roughly 10^4 s. As mentioned in chapter 2, typical observation times are 10^3 s. Therefore, BASUB is only worthwhile if data sets are combined (e.g. all data of one day of observations on the same target). It should be noted that in this criterium no Poisson noise due to point sources in the observed sky is considered.

In section 5.4, WA was introduced as a tool to suppress the Poisson noise. The essence of this method is to divide the detector-plane in a number of sections with constant count-density, cross-

correlate each section and averaging the results by weighing with the inverse Poisson variance. If a support structure has to be taken into account, a problem arises with respect to the number of calculations needed. In order to explain this problem it is necessary to discuss in more depth the calculation of $a^k[o]$ and $a^k[c]$. When no support structure is present, the equivalent entities $n^k[o]$ and $n^k[c]$ may be found by cross-correlating $\mathbf{M}[o]$ and $\mathbf{M}[c]$ with the unity matrix of the same dimensions (the latter representing the active detector plane). This calculation may be done relatively fast by the use of fast Fourier transforms (FFTs, see 5.8). This does not apply to the calculation of $a^k[o]$ and $a^k[c]$ since the shadowing by the support structure yields for every k another active section of the detector plane. Therefore, the values of both cannot be calculated via cross-correlations of $\mathbf{M}[o]$ and $\mathbf{M}[c]$ with a unique matrix and the use of FFTs is impossible. Instead, one is forced to compute the number of open and closed 'active' mask elements directly by calculating for every k the position on the detector of the projection of every open and closed mask element. This requires a lot more computing time (i.e. $\sim$50 hours CPU-time on the *COMIS* data-analysis system) than the calculation of $n^k[o]$ and $n^k[c]$. However, $a^k[o]$ and $a^k[c]$ only need to be calculated once and can subsequently be applied to an arbitrary observation.

In case a WA procedure is used, the latter conclusion does not apply. The 'active number' of open and closed mask elements in the cross correlation of every detector part then depends on that particular part, which is set by the point sources in the observation under consideration and is in principle different for every observation. Thus, one would have to calculate $a^k[o]$ and $a^k[c]$ again for every observation and detector part separately. If WA is used in conjunction with the reconstruction of the complete observed sky, one is confronted with a tremendous computational effort which is prohibitively large. By choosing to reconstruct only small parts of the observed sky (e.g. to reconstruct only the point sources found so far, to reach a better signal-to-noise ratio), inclusion of the WA procedure is feasible.

The problem encountered in using WA during the reconstruction of the complete observed sky can be circumvented at the expense of some active detector area: one might consider using only those parts of the detector that are exposed to the complete observed sky, in other words, those parts that will never lie in the shadow of the support structure as seen from any possible sky-position[6] (see Fig. 5.6). In that case, the calculation of $a^k[o]$ and $a^k[c]$ becomes just as straightforward as that of $n^k[o]$ and $n^k[c]$ because the active detector area is not restricted by the support structure (but will still have to be done for every different observation). In the case of *COMIS* this means that 35% of the detector area is not used. For a potential on-axis source this excludes 35% of the photons. This percentage decreases for off-axis sources and is zero for a source at the edge of the observed sky. It is a trade-off between the calculated loss of photons and the estimated amount of Poisson-noise suppression whether the application of this simplified WA (SWA) is fruitful in terms of better statistics on large parts of the observed sky as compared to discarding SWA all together.

5.7.2 Derivation of fluxes and positions of point sources in a reconstructed sky

If it were not for the finite spatial resolution of the detector, fluxes of point sources would be simply given by the value of the reconstructed sky in the pixel where the source is located. In this case, the source is always confined to one pixel (although this may involve changing the phase of the cross correlation, see section 5.6). The point-source position is then given by the center of this pixel. However, the spatial resolution usually is finite and complicates the derivation of the point-source flux and position since the source will be 'smeared' over several neighboring pixels in the reconstructed sky. This smearing is described by the point spread function (PSF). In its continuous form, the PSF is characterized by the normalized function $f(x-x_0, y-y_0)$ which specifies per unit area the fraction of the point-source flux contained in the infinitesimal area $(x-x_0...x-x_0+\mathrm{d}x, y-y_0...y-y_0+\mathrm{d}y)$, when the point source is located at position (x_0, y_0). In this continuous form the point-source image

---

[6]The two problems mentioned earlier, concerning the influence of the detector and sky background on the reconstruction when there is a support structure, do not apply anymore then; BASUB, the subtraction of the backgrounds in the detector plane, is therefore not necessary.
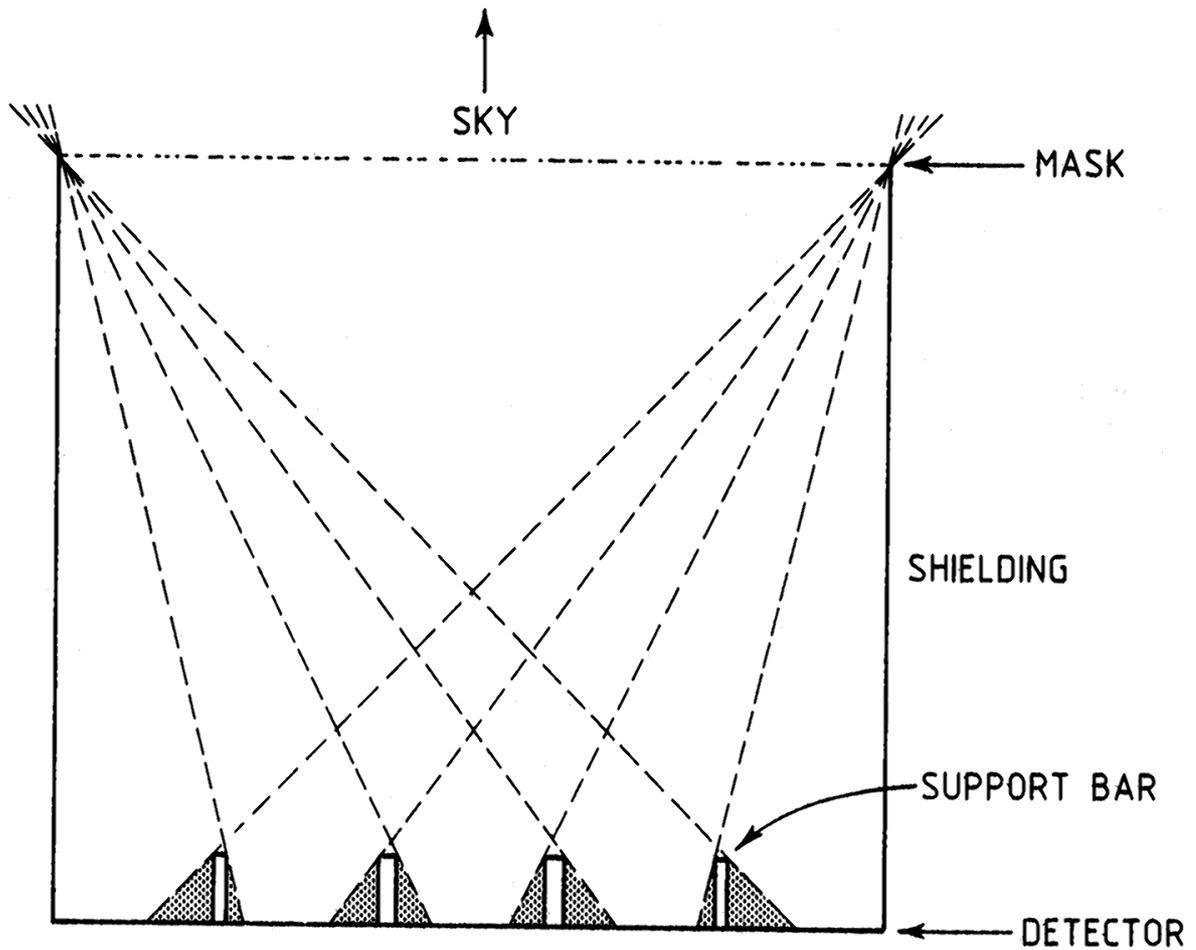
Figure 5.6: This sketch shows the longest shadows that can be thrown by different support window bars. The detector areas outside the shaded regions will never lie in the shadow of a bar for any possible sky position and may be used in a simplified weight averaging procedure (SWA)

is given by:

$$\rho(x,y) \quad = \quad s\, f(x-x_0, y-y_0) + l \qquad \text{flux/area} \tag{5.51}$$

where s is the total point-source flux and accounting for a constant background level l. Actually, the PSF will be integrated on a regular grid with bin-sizes $\Delta x \times \Delta y$ and sampled at (x_i, y_i), yielding a reconstructed sky of:

$$\rho_i \quad = \quad \rho(x_i, y_i) = s\, f^b(x_i, y_i) + L \qquad \text{flux} \tag{5.52}$$

where $L = l\, \Delta x\, \Delta y$ and

$$f^b(x_i, y_i) \quad = \quad \int_{x_i - \frac{1}{2}\Delta x}^{x_i + \frac{1}{2}\Delta x} \int_{y_i - \frac{1}{2}\Delta y}^{y_i + \frac{1}{2}\Delta y} f(x - x_0, y - y_0)\mathrm{d}x\, \mathrm{d}y \tag{5.53}$$

The extraction of the point-source flux and position, given the PSF, may be obtained by applying a maximum-likelihood method on the appropriate part of the reconstructed sky. This involves minimizing the S-statistic (Lampton *et al.* 1976)

$$S \quad = \quad \sum_{i=1}^{N} \frac{(r_i - \rho_i)^2}{\sigma_i^2}\,, \tag{5.54}$$

leaving free simultaneously s, x_0, y_0 and L (N is the number of pixels in the appropriate part of the sky, r_i the observed value of the reconstructed sky at element i and σ_i^2 its variance). If the model ρ_i is consistent with the data r_i and the deviations $\frac{r_i - \rho_i}{\sigma_i}$ are independent and approximately Gaussian distributed with a zero mean (see e.g. Bevington 1969), the minimum value $S_{\min}$ is a sample from the probability distribution of Pearson's χ^2-statistic for $N - N_p$ degrees of freedom (N_p is the number of parameters for which a solution is searched and is 4 in this case). The model is regarded to be discrepant with the data if the integrated probability

$$\alpha \equiv \int_{S_{\min}}^{\infty} f(\chi^2_{N-N_p}) \mathrm{d}\chi^2 \tag{5.55}$$

is smaller than a certain threshold value, where $f(\chi^2_{N-p})$ is the probability distribution of χ^2 for $N - N_p$ degrees of freedom. Lampton *et al.* argue that a threshold value of 10% is a reasonable compromise between security of conclusions and sensitivity toward detecting false models.

Given a correct model, errors on all parameters with a certain confidence level $P\%$ may be determined. The $P\%$ confidence-level region in parameter space is conditioned by the contour (Lampton *et al.* 1976):

$$S = S_{\min} + \chi^2_{N_p}(P) \tag{5.56}$$

with χ^2 distributed for a number of freedoms equal to the number of parameters N_p. For a simultaneous fit of all four parameters, a confidence level of 68% is equivalent with $\chi^2_4(68\%) = 4.7$. Often, so-called '1-sigma' errors are quoted, because they are easier to infer. For a parameter with a fitted value of p the 1-sigma error σ_p is defined by:

$$S(p + \sigma_p) = S(p) + 1.00 \tag{5.57}$$

For the four parameters considered here, working out Eq. 5.57 (to the second order Taylor expansion) and including Eqs. 5.52 and 5.54 results in:

$$\sigma_s^2 = \frac{1}{\sum \frac{\left(f_i^b\right)^2}{\sigma_i^2}} \tag{5.58}$$

$$\sigma_{x_0}^2 = \frac{1}{s^2 \sum \frac{\left(\frac{\partial f^b}{\partial x}\right)_i^2}{\sigma_i^2}} \tag{5.59}$$

$$\sigma_{y_0}^2 = \frac{1}{s^2 \sum \frac{\left(\frac{\partial f^b}{\partial y}\right)_i^2}{\sigma_i^2}} \tag{5.60}$$

$$\sigma_L^2 = \frac{1}{\sum \frac{1}{\sigma_i^2}} \tag{5.61}$$

These 1-sigma errors indicate the accuracy of estimating all parameters separately at a 68% confidence level, or simultaneously at a confidence level of 21%.

Typical for the PSF of *COMIS* is that it depends on photon energy, on off-axis angle and, slightly, on time. A treatment of the PSF is given in section 6.5.

5.8 Implementation of the reconstruction technique in the computer

5.8.1 Computer hardware

The computer hardware, used for the processing of the *COMIS* data, consists of the following main components:

- A *Data General MV/15000* minicomputer. This multi-user system has a nominal speed of 0.5 Mflops (million floating-point operations per second) and a memory size of 16 Mbyte, of which about 4 Mbyte is reserved for network processes and the operating system. All *COMIS* software runs on this computer.

- An *Analogic AP500* array processor, which is coupled to the *MV/15000* system. This machine has a nominal speed of 9 Mflops and a memory size of 4 Mbyte. It has an interface to the *MV/15000* system, that allows transfer rates of about 100 Kbyte/s.

- A disk with a capacity of 600 Mbyte. The average IO transfer rate between the disk and the *MV/15000* memory is about 100 Kbyte/s.

5.8.2 Standard reconstruction algorithm for the total observed sky

The raw data (before any reconstruction) consists of a detector image chosen within a particular photon-energy range and time interval (i.e. a fraction or the whole of an observation). This image has a resolution between 0.375×0.375 mm^2 (the readout resolution of the detector electronics, see chapter 4) and 1×1 mm^2 (the size of all mask elements). At first, an initial cross-correlation procedure is applied to the data. This involves three steps. The first one involves the most demanding calculation: the cross correlations according to Eqs. 5.4 and 5.6. In order to speed up these calculations, they are carried out with the aid of fast Fourier transforms (FFTs, see e.g. Bracewell 1986, chapter 18), utilizing the cross-correlation theorem:

$$\mathbf{R}[\text{o}] = \mathcal{F}^{-1} \left(\mathcal{F}(\mathbf{D}) \, \overline{\mathcal{F}(\mathbf{M}[\text{o}])} \right) \tag{5.62}$$

($\mathcal{F}$ represents the discrete Fourier transform and $\overline{value}$ the complex conjugate of *value*). Analogously the cross correlation $\mathbf{R}[\text{c}]$ is computed. The FFT-algorithm nominally performs $\frac{n}{2} \log_2 n$ multiplications (n being the total number of elements of the arrays involved) and $n \log_2 n$ additions, if n is a power of 2. The calculation described by Eq. 5.62 thus involves $n(1 + \frac{3}{2} \log_2 n)$ multiplications and $3n \log_2 n$ additions. A direct calculation of the cross correlation would require n^2 multiplications and additions. Thus, the reduction in the number of calculations is considerable: if $n = 512 \times 512$, the advantage in the number of multiplications is about a factor 10^4. Hammersley (1986) investigated several other algorithms to speed up the calculation but found that the use of FFTs provides the fastest method. Furthermore, he optimized the well-known FFT algorithm by minimizing the memory usage and restricting some of the calculations, gaining another factor of about 4 in speed (see Skinner *et al.* 1987). This routine is employed in the cross-correlation software developed for the *MV/15000* system.

The best performance is achieved if the calculation is done in the array processor (in this machine standard FFT-routines have been provided by the manufacturer). However, the speed of the total procedure is heavily constrained by the IO speed between the main system and the array processor. In addition, the memory size of the array processor is limited. In practice, this means that complete (i.e. for the whole observed sky) cross correlations are best done completely on the *MV/15000* system if a step size smaller than 1 mm is used; otherwise the use of the array processor is most efficient.

The second step in the cross-correlation procedure pertains to the division of the 'open' and 'closed' cross correlations, $r_k[\text{o}]$ and $r_k[\text{c}]$, by their respective active areas, $a^k[\text{o}]$ and $a^k[\text{c}]$. The calculation of $a^k[\text{o}]$ and $a^k[\text{c}]$ is again very demanding (≈ 50 hours CPU-time, see 5.7.1), but may conveniently be calculated prior to particular observations since they are constants (provided no SWA is done). The resulting arrays are then stored on disk and can be applied to an arbitrary observation.

The final step of the cross-correlation procedure concerns the subtraction of the 'closed' from the 'open' component, to arrive at the reconstructed sky (Eq. 5.10), and the addition of both components, to determine the variance of the Poisson noise (Eq. 5.12).

A typical single-user elapse time for a complete cross correlation with a step size of 1 mm is 3 minutes on the array processor. If a step size of 0.5 mm is utilized in the cross correlation, the procedure is done completely in the *MV/15000* system and takes about 25 minutes single-user elapse time.

The initial cross correlation is as a standard followed by an IROS procedure. IROS also incorporates BASUB, described in 5.7.1 (this cannot be done earlier, since the Poisson-noise variance array must be inferred from the original detector data in the initial cross correlation). The complete IROS procedure (see section 5.3) entails:

1. a search for strong significant point sources in the initially reconstructed sky and an estimate of positions and fluxes of these sources (via a fit with the expected PSF). The significance threshold is defined with respect to the local rms-value in the initially reconstructed sky. If no source is found, IROS is terminated;

2. a simulation of the illumination of the detector by these sources, followed by a subtraction of this simulated data from the real data. In principle, the simulated illumination of the detector would not only involve the calculation of the projected mask onto the detector (including the shadowing by the window support structure), but also convolution with the PSF contributions solely from the detector (this includes the detector spatial resolution and the photon-penetration effect, see section 6.5). This convolution would be rather time-consuming, because the PSF depends on the position of the point source in the sky. However, the procedure is simplified by assuming that each 'smeared' point source (in the reconstructed sky) consist of a number of ideal point sources. The detector illumination can then be calculated without convolutions. One should bear in mind that IROS becomes then slightly less efficient since the calculated detector image is not fully representative anymore. This is due to the fact that shadowing by the support structure is now different from a single (smeared) point source. However, this circumstance was found to be of negligible influence relative to other sources of noise.
   At this point, also BASUB (see section 5.7.1) can be carried out. The intensities of the background components are determined beforehand from an independent in-flight calibration;

3. the cross correlation of the 'subtracted detector' (omitting the calculation of the Poisson-noise variance estimate);

4. a check on residues in the newly reconstructed sky at the positions of the located sources and a search for additional sources that might introduce significant coding noise. If residues and other sources are present, a next iteration is started (turning back to the procedure in 2, but skipping subtraction of background levels);

5. a check on the spatial characteristics of the residue detector data. If IROS has been a complete success, this response should be flat and the total number of residue counts should be zero, both of course within the statistical accuracies dictated by the Poisson noise. If this is not the case, this may arise from the presence of an extended X-ray source that went unnoticed in the search for point sources, or actual background levels that deviate from the expected values. If the latter occurs, an estimate of the correction to the assumed background levels may be determined from the residue detector by extracting the strengths of the typical spatial responses of the detector to both detector background (homogeneous) and sky background (modulated by the support structure). Subsequently, these corrections can be applied to the residue detector. If an extended X-ray source gives rise to an unexpected residue detector, a separate analysis of the detector data is needed to give clues to the characteristics of this source;

6. the recovery of all the point-source flux values, that have been subtracted from the detector data, IN THE LAST RECONSTRUCTED SKY. The resulting sky array is the solution of the IROS procedure.

Usually 1 or sometimes 2 iterations are necessary to complete IROS, implying 1 or 2 more cross correlations. However, these cross correlations do not need as much calculations and IO as the initial cross correlation, because no variances need to be calculated in IROS (the original variance array remains valid).

Whether the SWA procedure (see 5.7.1) will be applied, this is decided after the initial cross correlation by estimating the gain in sensitivity that this procedure may potentially result in for the

current observation. If this gain turns out to be worthwhile, all cross correlations are substituted by the SWA procedure and BASUB is discarded.

5.8.3 Reconstruction for selected parts of the observed sky

Once a reconstruction and analysis of the whole observed sky in a conveniently wide energy band and time interval has been performed, one is in principle familiar with all significant point sources in that observed sky. A logical next step is a more detailed investigation of these sources, i.e. a temporal and spectral study. In order to do so, the data is divided in separate time and energy bins and reconstructions are performed on each of them. The difference with the procedure discussed in the previous section is that only small parts of the observed sky need to be reconstructed, i.e. those parts in the immediate neighborhood of the point sources[7]. This difference is important since it implies another cross-correlation algorithm. The use of FFTs is no longer crucial (in terms of computer run times) and relevant (the use of FFTs automatically involves a reconstruction of the total observed sky); direct correlation has now become appropriate.

IROS may remain mandatory in this case because the fluxes of all sources will change relatively, depending on their individual spectra and timing behavior. Thus, it also remains necessary to reconstruct EVERY point source, although one might only be interested in one of them. However, owing to the smaller amount of counts involved in selecting part of the data of an observation, the ratio of the coding-noise variance to the Poisson-noise variance will be substantially less than that for the whole observation and may become negligible. In this case one might consider omitting IROS.

In conclusion, the algorithm that is used in the reconstruction of selected parts of the observed sky if the point source distribution is known, basically looks like the procedure for the total observed sky outlined in the previous section, except for the following items:

- the cross correlation is performed directly on small parts of the observed sky and may include a WA procedure (depending on the estimated gain in signal-to-noise ratio) to be applied on detector subsections that are defined by the source distribution found from the previous reconstruction of the total observed sky.

- in case the data is split in energy bands, the background spectra should be taken into account in their subtraction from the detector data;

- no search for point sources is necessary.

References

Bracewell, R.N.: 1986, "*The Fourier Transform and its Applications*" (New York: McGraw-Hill), 2nd ed.

Bevington, P.R.: 1969, "*Data Reduction and Error Analysis for the Physical Sciences*" (New York: McGraw-Hill)

Covault, C.E., Grindlay, J.E., Manandhar, R.P., Braga, J.: 1991, *IEEE Trans. Nucl. Sc.* **NS-38**, 591

Fenimore, E.E., Cannon, T.M.: 1981, *Appl. Opt.* **20**, 1858

Hammersley, A.P.: 1986, "*The Reconstruction of Coded-mask Data under Conditions Realistic to X-Ray Astronomy Observations*", Ph.D. Thesis, University of Birmingham

Hammersley, A., Ponman, T., Skinner, G.: 1992, *Nuc. Instr. Meth. Phys. Res.* **A311**, 585

Lampton, M., Margon, B., Bowyer, S.: 1976, *Astrophys. J.* **208**, 177

Patterson, T.G.: 1990, "*A Study of the Galactic Bulge, Large Magellanic Cloud and Cygnus Region with a Simple Configuration Coded-mask X-Ray Telescope*", Ph.D. Thesis, University of Birmingham

---

[7]The reconstruction cannot be restricted only to the exact positions of the point sources, since the full PSF has to be recovered.

Skinner, G.K, Ponman, T.J., Hammersley, A.P., Eyles, C.J.: 1987, *Astrophys. Sp. Sc.* **136**, 337

Appendix 5.A. Illustration of the reconstruction algorithm with a simulated observation

In this Appendix, the various aspects of the reconstruction algorithm, as discussed in chapter 5, are illustrated with the aid of a simulated observation. The results are displayed in Figs. 5.A.a through 5.A.k.

The basis of the simulated observation is:

- the *COMIS* instrument (see chapter 4), which consists of a 256×256 mm^2 detector and a 255×257 mm^2 mask plate with mask elements 1×1 mm^2 in size. The detector bins are equal in size to the mask elements; thus, the reconstructed sky consists of 510×512 elements;

- a simulated observation of 1000 s on a part of the sky which contains 2 point sources with intensities $s_1 = 2.0 \times 10^{-2}$ cts/s/me and $s_2 = 1.2 \times 10^{-4}$ cts/s/me and located at the centers of sky elements $(x, y) = (127, 257)$ and $(191, 257)$ respectively (x- and $y-$coordinates are counted from 1 onward). Accounting for the effective area of *COMIS* (see chapter 6), these intensities correspond to 1 Crab and 6 mCrab respectively over the total energy passband of *COMIS* (2-30 keV).

  Apart from point sources, a sky background of 23 cts/s and a detector background of 19 cts/s per whole detector is assumed. These are the nominal values for *COMIS* (see chapter 6).

The results will now be discussed and visualized by Figs. 5.A.a–k. Figures 5.A.a through 5.A.e refer to an ideal detector (i.e. without an entrance-window support structure and any smearing effects).

a. This plot shows the illuminated detector, averaged over all columns (both sources illuminate the detector in the range $y = 1 - 255$). Clearly distinguishable are two regions: one is illuminated only by background (0.63 cts/de on average), the other is also illuminated by source 1 as well as source 2 (10.69 cts/de on average). The region which is only subject to flux from source 2 and background is not identifiable. The noise in this plot is due to the coding by the mask pattern and the Poisson noise.

b. This plot shows the 257th row of the initial cross correlation (this row contains both point sources), according to Eq. 5.10. Source 1 ($x=127$) is very significant, but source 2 ($x = 191$) is drowned in the noise. Immediately apparent is also the reduction in noise above $x = 383$. In this region, only that part of the detector plane is used in the cross correlation which is not illuminated by source 1 ($n^{k,p} = 0$ in Eq. 5.21 if $p = 127$). This again clearly shows the advantage of the simple system against the optimum system (see section 3.4).

  The strong noise is dominated by coding noise induced by source 1. This can be checked for the position of source 2, using a combination of Eqs. 5.21 and 5.23. The coding-noise variance at $x = 191$ due to source 1 is (only using the x-indices in the notation):

$$\left(1 - \frac{n^{191}}{n}\right) \frac{s_1^2}{n^{191}} \frac{n^{191,127}}{n^{191}} \tag{5.63}$$

Substituting the values of s_1, n^{191} (191×255) and $n^{191,127}$ (127×255) yields for the standard deviation: 3.8×10^{-2} cts/me. The Poisson-noise variance at $x = 191$ is given by:

$$\frac{s_1}{(1-t)n^{191}} \frac{n^{191,127}}{n^{191}} + \frac{b}{t(1-t)n^{191}} \tag{5.64}$$

corresponding to a standard deviation of 2.4×10^{-2} cts/me. The combined standard deviation is 4.5×10^{-2} cts/me.

The coding noise is present in a wide range of spatial frequencies. The plot clearly shows fluctuations on small scales as well as on large scales (see e.g. the positive bias in the center region of the image and the negative bias at the left side and compare this plot with Fig. 5.A.c where coding noise is eliminated; Fig. 5.A.g shows the large scale fluctuations more prominently). Furthermore, it increases towards the left edge. This increase can be derived from Eq. 5.63: if, instead of 191, $x < 127$ is chosen, the first and second factor increase (the last factor then is 1). An increase also applies to the Poisson noise given by Eq. 5.64.

c. This plot shows the reconstruction at $y = 257$ after application of IROS (see section 5.3) with respect to source 1. In relation to Fig. 5.A.b, the coding noise is eliminated, leaving only Poisson noise. Source 1 has been recovered in the reconstructed sky (see item 6 in section 5.8.2).

d. Finally, the WA procedure, as a tool to suppress Poisson noise (see section 5.4), is applied. In this case, the detector was divided in two parts: the part which was and the part which was NOT illuminated by source 1. The Poisson noise is then suppressed in that part of the reconstructed sky where only part of the counts from source 1 contribute to the Poisson noise, i.e. between $x = 127$ and $x = 383$. This is most clear in Fig. 5.A.e. The reduction in Poisson-noise standard deviation in this illustration is maximum at $x = 255$ (about a factor 2).

e. This plot shows for every x-position at $y = 257$ the root-mean-square (rms) value about the local average in a 7×7 bins surrounding area for three cases: in the initial cross correlation (1), the IROS result (2) and the IROS/SWA result (3). Apparent is the improvement in the suppression of the noise at the various stages in the reconstruction process.

Figures 5.A.f through k also refer to the *COMIS* instrument but now the entrance-window support structure is included in the simulation (see section 5.7.1).

f. This is a plot of the detector image, showing the average values over all columns (equivalent of Fig. 5.A.a). Note the modulation by the support structure, clearly visible for the part of the detector illuminated by source 1, but also slightly visible in the part only illuminated by the background (the sky background is modulated by the support structure). The average pixel values are less than in Fig. 5.A.a, due to the blocking by the structure.

g. This is the equivalent of Fig. 5.A.b but now the average over all columns of the initial cross-correlation result is shown to highlight the modulation by the support structure (this modulation has a periodicity of about 16 pixels). This modulation is not eliminated by applying only IROS; additional subtraction of background (BASUB) or application of SWA is necessary (see Fig. 5.A.i and j). Note the high bias values at the center of the image due to the coding noise introduced by source 1.

h. This figure shows the result of the complete reconstruction, averaged over the columns, after application of IROS and SWA. No BASUB is applied (the modulation by the support structure of the sky background is implicitly made obsolete through the selection of detector-parts in SWA, see section 5.7.1 and Fig. 5.6). Note the disappearance of the modulation in this reconstruction.

i. This figure refers to the same reconstruction as in Fig. 5.A.h but here the result is shown at $y = 257$. This figure should be compared with the next one.

j. This plot is the result of the reconstruction using BASUB instead of SWA. Here the support structure modulation has also disappeared. However, the noise is stronger here than in Fig. 5.A.i (see also next figure) and provides a strong case for SWA for this particular source configuration. In short, one can say that the gain in sensitivity due to the application of SWA outweighs the loss of source counts due to the selection of detector parts implicit to SWA (the reasoning behind this selection is discussed in section 5.7.1).

k. This is the equivalent of Fig. 5.A.e, but now for the initial cross correlation presented in Fig. 5.A.g (1), the IROS/SWA reconstruction result presented in Figs. 5.A.h and i (2) and the IROS/BASUB reconstruction result presented in Fig. 5.A.j (3). Again, like in Fig. 5.A.e, the IROS/SWA reconstruction is superior in the region between $x = 127$ and 383.
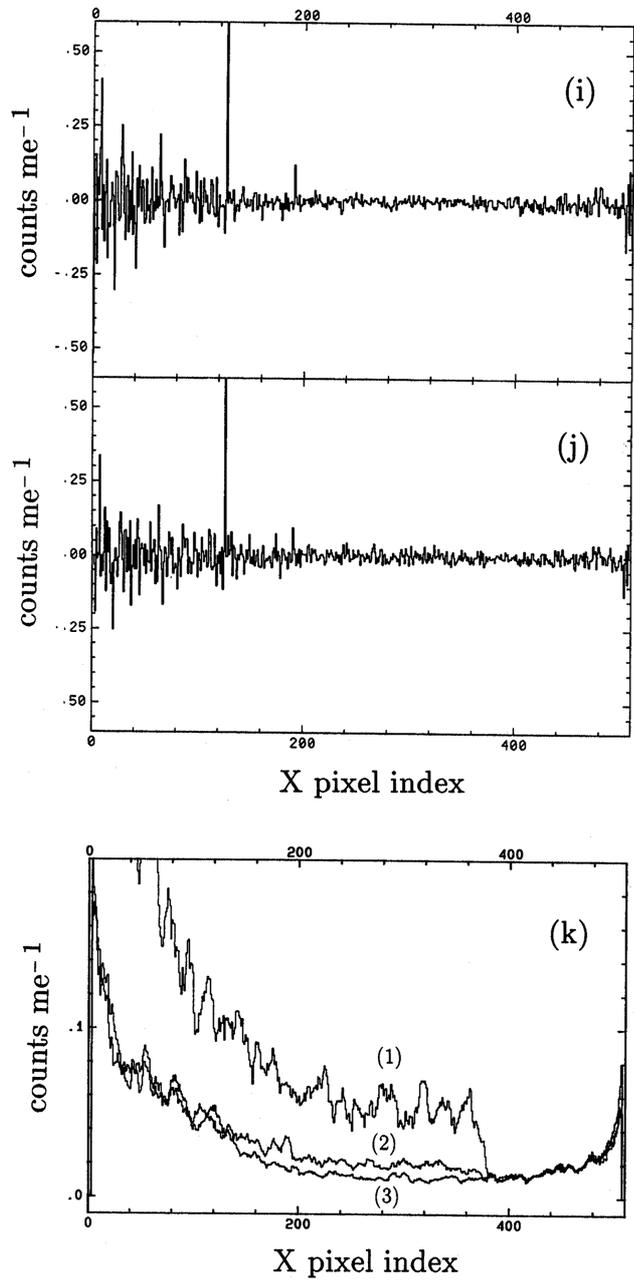
(a)

counts

X pixel index

(b)

counts me^{-1}

(c)

counts me^{-1}

X pixel index
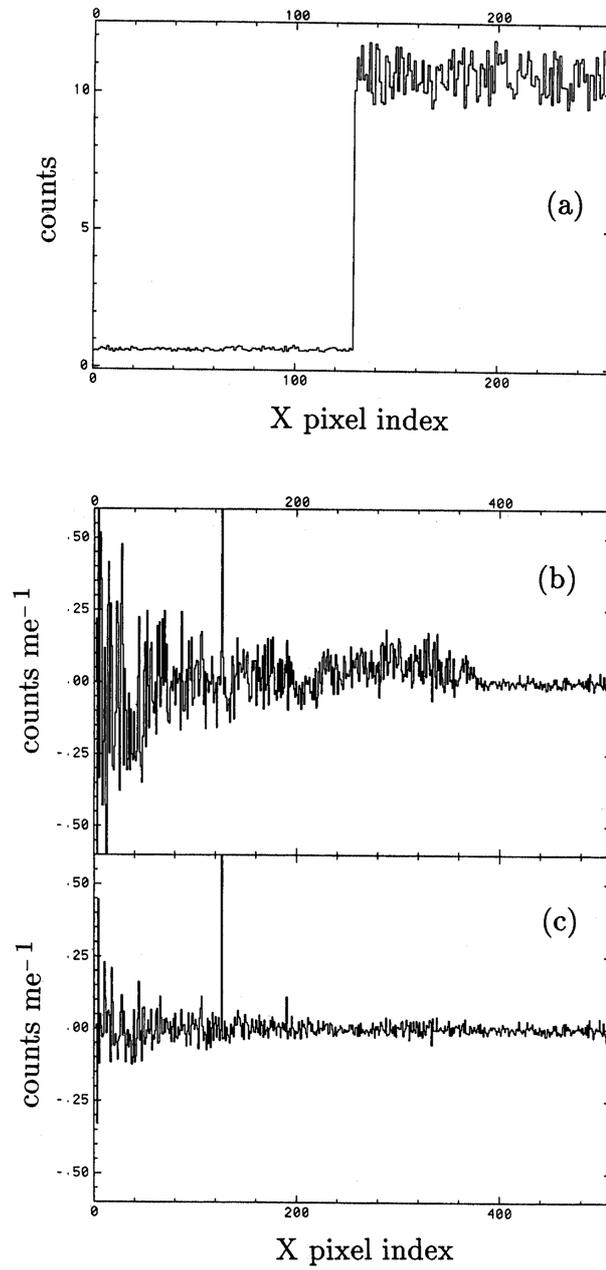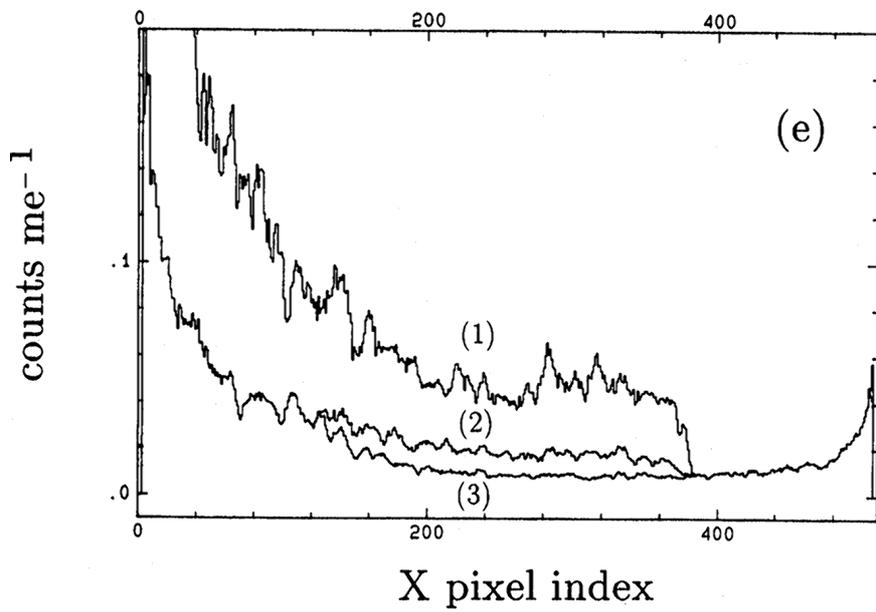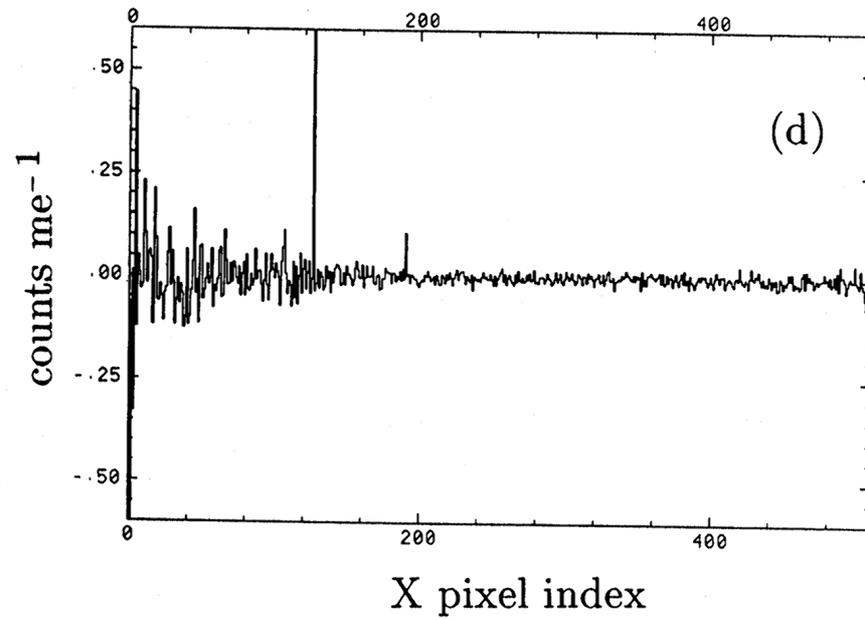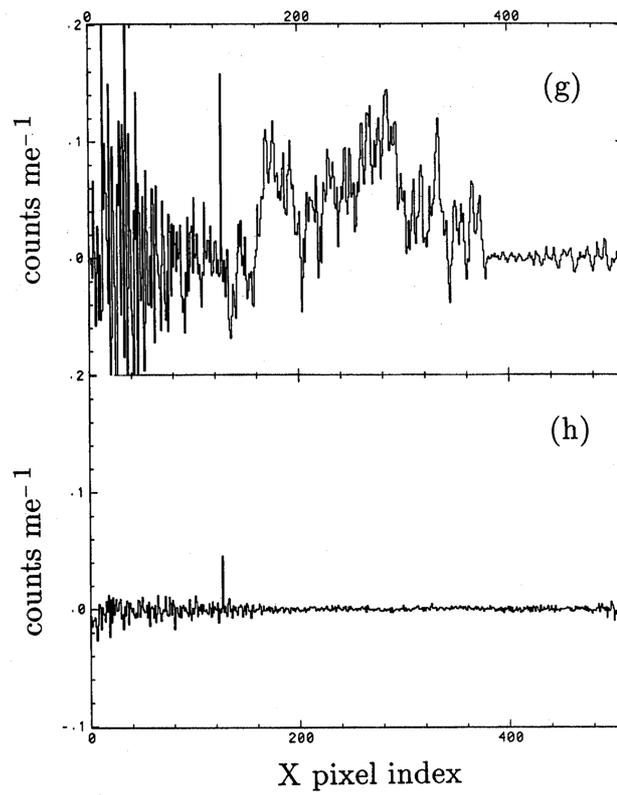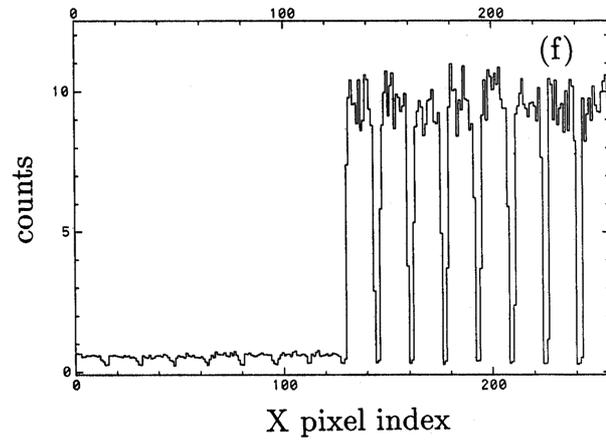
Figs. 5.A.a-c

Figs. 5.A.d-e

Figs. 5.A.f-h

Figs. 5.A.i-k

Chapter 6

COMIS calibration and performance

COMIS calibration and performance

    Abstract – The in-flight calibration and the performance verification of the *COMIS* instrument, as performed by the author, are discussed. This includes the spectral response of the detector, detector dead time effects, the point-spread function, the levels of sky and detector background and the anti-coincidence efficiency of the detector.

6.1 Introduction

In this chapter pre- and in-flight calibration items, carried out by the author, are assessed that are relevant to the analysis of scientific data, e.g. the spectral response of the detector, dead times in the detector, the point-spread function and the levels of the detector and sky background. The last two items are of particular importance to the proper reconstruction of point source fluxes, as discussed in chapter 5. Subject of the assessment is the status of *COMIS* as it was from October 20th 1988 onwards, after the exchange of the original flight detector with the spare detector during an extra vehicular activity of Soviet cosmonauts. The original flight detector was used for observations between June and September 1987. Aspects of the in-flight calibration of this detector can be found in Patterson (1990). Since October 1988, two other conditions for the operations have become important. Firstly, the bulk memory in the CDMS electronics box (see chapter 4) experienced malfunctions. Data retrieval was therefore limited to real-time telemetry. Secondly, the star sensor malfunctioned in May 1988; unfortunately, a repair attempt in October 1988 failed. Therefore, no star-sensor data was available afterwards. This is of particular importance to the point spread function and consequently to the sensitivity.

6.2 Spectral response

6.2.1 Photon energy - ADC channel relation

The relation between X-ray energy and anode pulse height, as sampled by the analog-to-digital converter (ADC), is slightly non-linear. The pulse height shows some saturation at high levels, due to the space-charge effect near the anode wires: the large space charge of the electron clouds, due to the absorption of high energy photons, causes a distortion of the electric field near the wires; thus, the proportionality between energy and number of avalanche electrons is reduced[1]. This non-linearity can be well approximated by:

$$E \;=\; A + Bp + Cp^2 \tag{6.1}$$

where E is the photon energy, p the measured pulse height (expressed in continuous ADC channels) and A, B and C constants.

---

[1]The space-charge effect takes also place at high counting rates. It will then affect the overall ADC-energy relation.

Relation 6.1 was calibrated pre-flight by measuring the response of the detector to integral illuminations by strong Fe^{55} and Cd^{109} radioactive sources and to a slit illumination by a Cu target. The radioactive sources emit X-ray lines at the K-complex with mean energies of 5.96 and 22.62 keV respectively, while the Cu target emits X-ray lines with a mean energy of 8.14 keV. These measurements were performed at several settings of the high voltage, in order to have calibration points for relation 6.1 when the gas gain changes in flight between -50% and $+50\%$ from its nominal value. Thus, representative values for A, B and C were found. At nominal gas gain, the quadratic term contributes from less than 1% at 2 keV to about 10% at 22 keV to the observed energy.

6.2.2   Resolution

The spectral resolution R of the detector is defined as the ratio of the photon energy to the full width at half maximum (FWHM) of the line spread function. In a proportional counter R is in principle determined by the statistical spread in the number of primary and avalanche electrons. The resulting energy dependency of R typically obeys a one-over-square-root law. However, in a MULTI-WIRE proportional counter, variations in the gas gain across the detector plane usually occur, resulting in modulations of the number of avalanche electrons and thus of the recorded photon energy. The gas gain variations are caused by:

1. deviations in the ideal positioning of the wire grids. Deviations from parallelism between grid-planes and between anode wires, as well as non-uniformities in the anode wire thicknesses, cause inhomogeneities in the electric field, resulting in a position-dependent gas gain. The effect may be considered stable and energy-independent. Positioning tolerances were defined such, that gain variations would be limited to at most 5%. The most prominent gain variation resulting from slight misalignment has a large spatial scale relative to the pitch of the anode wires;

2. space-charge effect. As indicated in 6.2.1, the space-charge effect causes a saturation of the relation between photon energy and ADC channel towards high energies. In fact, this does not only depend on photon energy and counting rate but also on the location of the photon absorption in the detector, i.e. whether this happened in the drift or active region and at what position with respect to the location of the anode wires.

   If the photon is absorbed in the drift region, the electron cloud will be compressed when passing a sense grid. This compression does not happen when the photon is absorbed in the active region. The space-charge effect (which increases with higher electron densities in the charged cloud) is consequently more serious for absorption in the drift region, resulting in a lesser gain. This means that the $E(p)$ relation for photons absorbed in the active region actually differs from the relation for those absorbed in the drift region. Photons in the low-energy part of the passband will, because of their relatively small mean free path, mostly be absorbed in the upper drift region and thus follow only the corresponding $E(p)$ relation. However, high-energy photons have also a large probability of being absorbed in the active region (e.g. 35% of all absorbed photons at 25 keV). Accordingly, the pulse height distribution will be broadened towards higher energies, thus worsening the spectral resolution.

   Consider two extreme locations of the photon absorption with respect to the anode wires: right on top of a wire (p1) or precisely in between two wires (p2). The space-charge effect will be less for p2 than for p1, because in the former case the electron cloud will be divided over two anode wires[2]. This results in a periodicity of the gain which equals the anode wire pitch with maxima at photon positions in the middle between two anode wires and most pronounced for high-energy photons ($\pm 2\%$ at 23 keV).

An X-ray point source in the FOV of *COMIS* will generally illuminate a part of the detector plane which has dimensions larger than 3 mm along both axes. Gain variations with a small scale relative to this illumination, as well as those depending on the depth of the photon-absorption, are accounted for by including them as a contribution to the spectral resolution. Large scale effects (item 1 above) are also implemented as a contribution to the spectral resolution, but this contribution is calculated

---

[2]Actually, the gain may be influenced by other effects too, but those are relatively unimportant for the current electrical detector configuration.

	1	2	3	4	5	6	7	8	9	10	11	12	13	14	15	16
16	-7.3	-6.2	-4.8	-3.3	-0.9	-0.6	-1.1	-0.5	0.4	0.4	1.6	1.3	1.7	2.1	2.4	1.6
15	-7.7	-6.4	-5.4	-3.6	-2.8	-1.6	-0.8	-0.2	0.5	1.6	3.1	3.1	2.9	2.3	1.9	1.9
14	-7.9	-6.2	-4.9	-4.0	-2.5	-1.3	-1.3	-0.7	0.6	1.6	1.1	1.2	1.7	1.8	1.2	2.1
13	-6.4	-5.5	-3.9	-3.0	-2.2	-0.6	-0.6	0.3	1.0	1.4	1.7	2.2	2.0	1.7	1.2	0.8
12	-4.9	-4.2	-2.7	-2.1	-0.4	0.3	0.8	1.5	1.6	1.9	1.8	1.6	1.5	1.9	1.2	1.6
11	-4.5	-2.7	-2.0	-1.0	-0.1	1.2	1.2	1.6	2.3	2.5	2.5	2.9	2.8	2.5	1.8	1.4
10	-3.1	-2.0	-1.2	-0.7	0.4	1.1	1.6	2.1	2.2	3.3	3.5	3.3	2.9	2.5	2.3	1.5
9	-2.6	-0.9	-0.3	0.2	0.9	1.7	2.4	2.5	2.9	3.1	3.5	3.4	2.8	2.6	1.6	1.7
8	-1.8	-0.9	0.0	0.8	1.4	1.9	1.9	2.4	2.2	3.5	3.3	3.0	3.3	3.0	1.8	1.6
7	-2.9	-1.6	-1.0	-0.2	0.4	1.3	1.5	1.9	2.0	2.8	2.1	2.4	1.5	1.2	0.5	0.2
6	-1.5	-0.5	0.8	1.3	1.4	2.3	3.0	3.4	2.9	3.4	2.8	2.1	1.7	1.8	0.9	0.8
5	-1.3	-0.4	0.2	0.9	1.1	2.2	2.6	2.8	2.9	3.3	3.0	2.1	2.2	1.5	0.6	0.3
4	-1.6	-0.8	0.0	0.2	1.0	1.7	1.9	1.6	2.0	2.4	1.5	1.3	0.9	0.3	-0.6	-1.7
3	-2.3	-1.6	-0.8	-0.3	0.4	1.6	1.1	1.3	1.0	1.1	0.3	-0.2	-0.6	-0.4	-1.6	-2.3
2	-2.5	-1.6	-1.2	-1.2	-1.0	-0.2	-0.4	0.1	-0.5	-0.6	-1.0	-1.4	-1.8	-2.8	-3.4	-4.1
1	-1.9	-1.2	-0.7	-0.2	-0.1	1.1	1.0	1.3	1.1	0.5	0.3	0.2	0.0	-0.4	-1.9	-2.5

Figure 6.1: Percentage deviation in gain for 16×16 cm^2 detector bins, with respect to the weighted average over total detector plane

for each sky position separately (from every different sky position, a different part of the detector is illuminated).

The pre-flight calibration of the $R(E)$ relation was done on spatially resolved detector data, i.e. in detector cells of size 16×16 mm^2. The resolution per cell was determined at X-ray energies (2.01, 5.96, 8.14 and 22.62 keV) and resulted in measured resolutions of 30% at 2 keV, 17.7% at 6 keV and 18% at 22 keV. Thus, the $R(E)$ relation is quite flat except for the low end of the energy scale. This flatness is mainly due to the space-charge effect mentioned above. The spectral resolution is modeled by:

$$\frac{1}{R} = KE^{\frac{1}{2}} + LE + ME^{\frac{3}{2}} \tag{6.2}$$

with constant K, L and M. Fig. 6.1 presents for each 16×16 cm^2 cell the percentage deviation in gain from the detector average. This table, as well as Eq. 6.2, are needed for an appropriate spectral analysis of detected X-ray sources.

6.2.3 Efficiency as a function of energy

Apart from potentially being blocked (by the telescope shielding, the entrance-window support structure or the wire grids), incoming photons traverse a stack of materials that have energy-dependent transparencies before they reach the detector gas. In the gas, the photons also have an energy-dependent absorption probability. Materials and gas were chosen such as to optimize the sensitivity of the instrument to photons with X-ray energies between about 2 and 25 keV, with a maximum in the 5 to 10 keV range. The materials used are mentioned in chapter 4 and include: a thermal foil made of kapton with an aluminum coating, a mask plate made of stainless steel with a gold plating and an entrance window made of beryllium with an epoxy coating. It has been made certain that the entrance window has an area homogeneity of better than 2% in thickness.

Several other processes influence the efficiency to a second-order degree. One relates to the escape of fluorescence photons from xenon. If such an escape occurs, the detector will not register all energy from the incident photon but only an energy which differs with an amount equal to the energy of the escaped photon. The probability of such an escape depends on the mean free path of
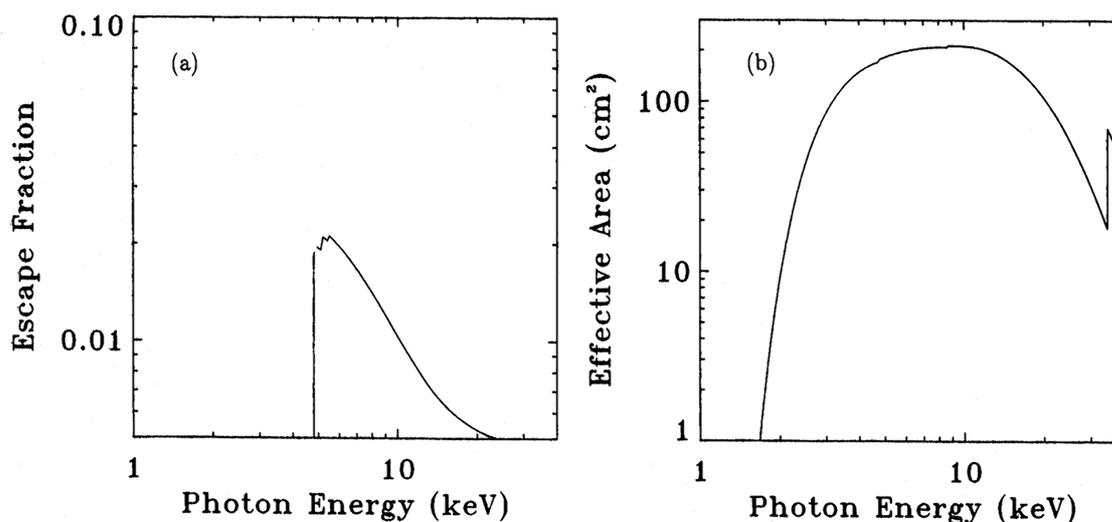
Figure 6.2: **a.** Fraction of incident photons giving rise to L-escape photons, as a function of the energy of the incident photons. **b.** Effective area of *COMIS* as a function of photon energy, excluding the presence of escape spectra. Note that the passband is limited in practice to 1.7-30.2 keV

the fluorescence photon and on the detector geometry. If the fluorescence photon does not escape from the detector but is re-absorbed, two situations can occur, depending on the distance in the detector plane between the position of the re-absorption and the position of the absorption of the incident photon. If this distance is too large ($>$ 24 mm), the combination of the photo-electron and the absorbed fluorescence photon will give rise to an anti-coincidence situation (see chapter 4) and the event is rejected; if the distance is small, the combined events will be accepted as a single event with irrelevant position information since the detector measures the average position of both charge clouds. In the passband of *COMIS*, escape effects arise due to ionization of the Xenon K-shell for photon energies larger than 34.58 keV and due to ionization of the three Xe L-shells that have a mean ionization energy of 5.0 keV. Escape effects from both the K-shell and the L-shell complex are not severe: on the one hand is the fluorescent yield[3] of the L-shell relatively small (i.e. 0.11, from Bertin 1975), on the other hand does the incident spectrum normally contain relatively few photons in excess of the K-shell energy. In Fig. 6.2.a, the fraction of the incident photons that will produce an L-escape photon is plotted as a function of energy. This fraction is maximally 0.02. The average energy taken away by the escape photon (averaged over all possible L shells) is 4.35 keV. 60% of all photons with an energy higher than 34.58 keV will result in K-escape photons. Normally, incoming photons of such a high energy are rejected by the HLD. However, due to the escape effect, the registered energy will be 30.36 keV less (on average) and such photons will be qualified. For a Crab-like spectrum this means that 60% of the flux at 40 keV will contribute less than 1% to the incident flux at 10 keV (this value follows mainly from the ratio of the incident flux at 40 keV to that at 10 keV and the ratio of the instrument efficiency at both energies).

Another item with a second order influence on the efficiency is the non-zero transparency of closed mask elements to photons with X-ray energies higher than about 18 keV (the transparency is then higher than 0.01, see 4.3). This will result in a SMALLER sensitive area: since the reconstruction process (see chapter 5) necessitates a maximum contrast between transparent and opaque mask elements, a non-zero transparency of the 'opaque' elements results in a smaller 'efficiency' of the reconstruction process. In other words, with opaque mask elements becoming transparent it becomes more difficult to recognize the mask pattern.

The combination of the transparencies of all materials and the gas, combined with the detector

---

[3]The fluorescent yield is defined as the ratio of all emitted fluorescence photons per unit time and the total number of shell vacancies formed during the same time (Bertin 1978).
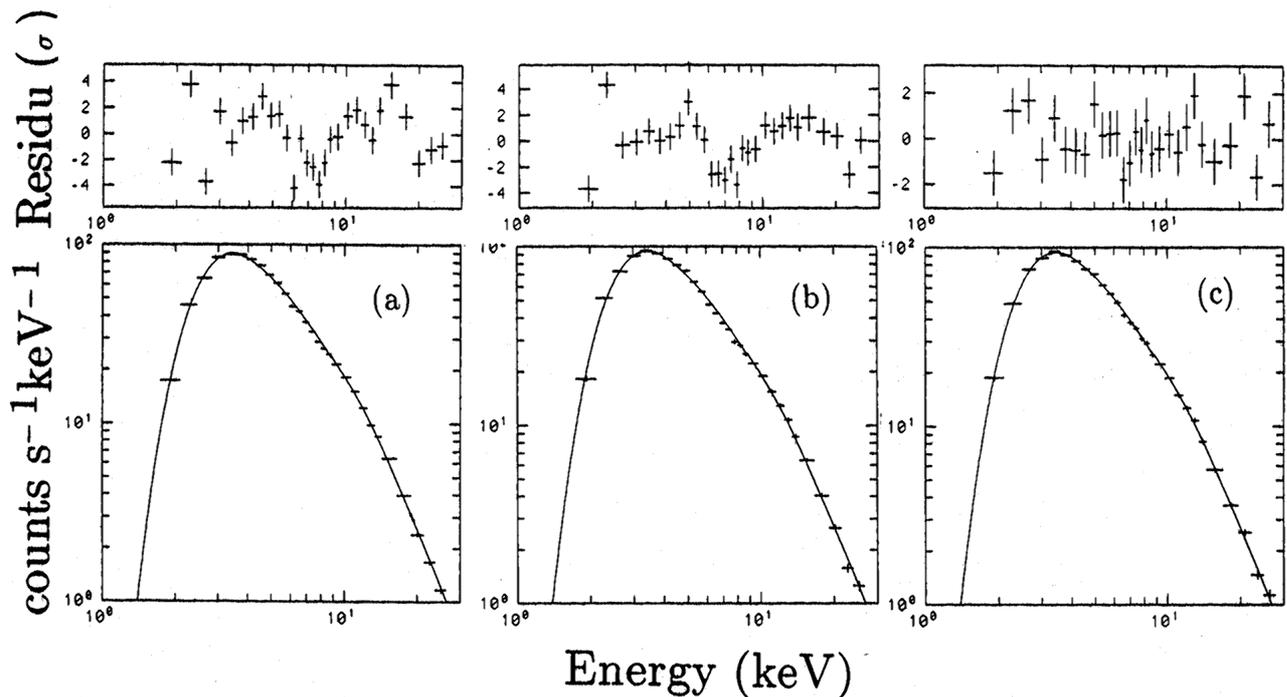
Figure 6.3: **a.** Observed spectrum of the total Crab source, obtained in Oct. 1988, with nominally defined energy channels (from Eq. 6.1). Note the wave-like residual with respect to the best-fit power-law model spectrum (see text), this was attributed to a differential non-linearity in the boundaries of the ADC-channels. **b.** Same as a, but for spectrum obtained in Feb. 1989. **c.** Feb. 1989 Crab spectrum, but now using the $E(p)$ relation, corrected for the presumed ADC non-linearity. Note the improvement in residuals

geometric area, obscuration factors and the loss through AC and escape of fluorescence photons, defines the sensitive area as a function of X-ray energy. Fig. 6.2.b shows the sensitive area as a function of X-ray energy (escape effects are not included here, since their magnitude depends on the incident spectrum). The most important sensitivity reduction at low energies arises from absorption by the entrance window; at high energies the transparency of the detector gas prevails. Especially noteworthy are the L-edge absorption feature of Xenon at 5 keV and the 8.6 keV edge arising from the AC of low energy photons that are absorbed below the anode grid.

6.2.4 In-flight calibration with Crab

Because the spectrum of the Crab X-ray source is easily detectable, well defined and presumed to be stable, observations of this X-ray source provide one of the best means to calibrate the spectral response of any X-ray instrument in flight (Toor & Seward 1974). During the first year of its operations *COMIS* performed two sets of Crab source observations, the first in October 1988 and the second in February 1989. These observations include off- and on-axis positions for the source. Since no other X-ray sources were detected in the same FOV, the intensity of the Crab in each energy channel could be determined directly from the detector by extracting all events from the part of the detector plane which was illuminated by the Crab nebula and correcting the event rate for the background as it is determined from the remainder of the detector plane. The resulting spectrum of the Crab nebula was subsequently tested with a set of power-law spectra convolved with the expected spectral response of *COMIS*. If the expected response is correct, the best-fit model spectrum should be consistent with previous measurements.

The procedure described above was applied to the October 1988 observations (see

Fig. 6.3.a). The first and last energy channel were excluded from this analysis, because their lower and upper boundary respectively are not accurately known (they are determined by the value of the LLD- and HLD-settings respectively). The best-fit power-law model spectrum[4] has a photon index $\Gamma = 2.10$ and a hydrogen column density of $N_H = 3.7 \times 10^{21}$ H-atoms cm^{-2}, this spectral form is consistent with previous reports (Toor & Seward 1974, Charles *et al.* 1979, Schattenburg & Canizares 1986). Although the overall form of the observed spectrum is satisfactory and confirms the expected spectral response of the instrument, the deviations between observed and expected spectrum are statistically significant since the χ_r^2 value of the fit amounts to 6.1. Apparently, a 'ripple' in the spectral response is present. This 'ripple' was attributed to a differential non-linearity in the widths of the ADC-channels. Since pre-flight measurements of this non-linearity are not available, the October 1988 Crab data were used to calibrate this effect. The widths of the energy-channels were corrected by an iterative process to arrive at an acceptable χ_r^2, thereby using the position of the 5.96 keV line of the Fe^{55} in-flight calibration (IFC) sources as a reference point. The result of this procedure was then verified with the second set of Crab data with a satisfactory result (χ_r^2 reduced from 3.8 to 1.3, see Figs. 6.3.b and c). Regular checks on the revised $E(p)$ relation confirmed this result. Table 6.1 presents the relation between energy normal mode channels (see 4.4.2), ADC-channels and the corresponding channel boundaries in keV. The errors in the channel widths are also given, which derive from the count statistics of the first set of Crab data. For most observations, this accuracy exceeds that of the counting statistics and does not severely degrade the performance of a spectral analysis. In any arbitrary observation this error is always added quadratic to the statistical error. The third-order correction term now applied to the $E(p)$ relation (on top of the quadratic relation given in Eq. 6.1) amounts up to 5% per normal mode energy channel.

Given the corrected $E(p)$ relation and the acceptable value for χ_r^2, the following 68% confidence-level intervals for the parameters of the fitted power-law model spectrum apply: $\Gamma = 2.10^{+0.02}_{-0.01}$, $N_H = (3.7^{+1.5}_{-1.0}) \times 10^{21}$ H-atoms cm^{-2} and $C = 9.2 \pm 0.4$ phot s^{-1}cm^{-2}keV^{-1}. These values agree with the previous reports mentioned above.

6.3   Dead times as determined from rate meters

As mentioned in 4.4.2, the detector electronics can not always cope with incoming photons or particles without interference from a previous detection. A distinction was made between two effects that cause interference: either the detector electronics is still busy processing a previous event, or pile-up occurs with a previous event. These two effects result in a dead time of the detector.

Another loss of effective integration time is due to the coverage by the telemetry. The telemetry is fed with data on a 1 sec basis (in MIFs, see 4.6). If a MIF is full within less than a second (depending on the number of telemetry channels available, this is after 112 or 224 events), the data accumulated in the remainder of that second is lost.

The above three processes reduce the live-time fraction of the instrument. This can be summarized by:

$$LTF \quad = \quad LTF_{\text{ep}}\ LTF_{\text{pu}}\ LTF_{\text{tel}} \tag{6.3}$$

with LTF the total live-time fraction and LTF_{ep}, LTF_{pu} and LTF_{tel} the live-time fractions of the event-processing electronics, the pile-up effect and the telemetry respectively.

A straightforward method to determine the effective integration time is to count the number of photons registered from the IFC sources. The strength of the combined Fe^{55} IFC sources is high enough to permit a measurement of the integration time with an accuracy of order 1% for a typical observation of 1000 s. However, if one chooses to use smaller time bins, this accuracy deteriorates

---

[4]The power-law spectrum is defined as $F = C\ e^{-\sigma(E)}\ E^{-\Gamma}$, with F the flux in phot s^{-1}cm^{-2}keV^{-1}, E the photon energy in keV, $\sigma(E)$ the cross section of the interstellar matter in cm^2 per H atom, Γ the power-law photon index and C a normalization constant.

Table 6.1: *COMIS* energy channels[a]

N.M.	ADC	Width	Energy(KeV)	error (%)
1	0 - 9	10	1.700 - 1.788	—
2	10 - 11	2	1.788 - 2.150	2.1
3	12 - 13	2	2.150 - 2.546	1.3
4	14 - 15	2	2.546 - 2.910	1.1
5	16 - 17	2	2.910 - 3.301	0.9
6	18 - 19	2	3.301 - 3.683	0.9
7	20 - 21	2	3.683 - 4.080	0.9
8	22 - 23	2	4.080 - 4.483	1.0
9	24 - 25	2	4.483 - 4.898	1.0
10	26 - 27	2	4.898 - 5.316	1.0
11	28 - 29	2	5.316 - 5.735	1.1
12	30 - 31	2	5.735 - 6.152	1.2
13	32 - 33	2	6.152 - 6.548	1.3
14	34 - 35	2	6.548 - 6.968	1.3
15	36 - 37	2	6.968 - 7.378	1.4
16	38 - 39	2	7.378 - 7.789	1.5
17	40 - 41	2	7.789 - 8.195	1.6
18	42 - 43	2	8.195 - 8.616	1.6
19	44 - 45	2	8.616 - 9.048	1.7
20	46 - 49	4	9.048 - 9.936	1.3
21	50 - 53	4	9.936 - 10.853	1.4
22	54 - 57	4	10.853 - 11.793	1.5
23	58 - 61	4	11.793 - 12.733	1.7
24	62 - 65	4	12.733 - 13.677	1.9
25	66 - 69	4	13.677 - 14.693	2.0
26	70 - 78	9	14.693 - 17.146	1.6
27	79 - 87	9	17.146 - 19.658	2.0
28	88 - 96	9	19.658 - 22.072	2.7
29	97 -105	9	22.072 - 24.554	3.3
30	106 -114	9	24.554 - 27.209	4.2
31	115 -125	10	27.209 - 30.200	—

[a] 126 ADC-channels are binned in so-called normal mode (N.M.) channels by the on-board microprocessor. This table gives their relationship. The energy boundaries were determined from the nominal relation (defined by Eq. 6.1), optimizing the fit of the model spectrum to the Crab spectrum (Fig. 6.3), by adjusting the energy widths of the N.M. channels. The measured position of the 5.96 keV line of the Fe^{55} IFC sources served as a reference point to this procedure. The lower and upper boundary of the total energy range are set by the LLD and HLD respectively. The last column indicates the errors in the energy widths of the channels, resulting from the statistical accuracy of the Crab spectrum.

to an unacceptable level and it becomes necessary to make use of an alternative method which is based on the readings of the rate meters (see section 4.4.2). These meters can provide information in time intervals of 8 sec (i.e. the readout frequency of the rate meters) to determine LTF_{ep}, LTF_{pu} and LTF_{tel} separately. This is described in the following subsections.

6.3.1   Live-time fraction of event input and processing

The dead time associated with the occupation of the detector electronics with the input and processing of an event can have different values (see Table 4.2). The value depends on the type of event, i.e. valid or invalid, and on the cause of a possible rejection. The time scales range from 10 μs (rejection because of a hardware AC situation) to 570 μs (when the event has passed through the input routine). If the event buffer is full the time scale may extend to as much as 1790 μs.

The live-time fraction of the event processing, LTF_{ep}, can be determined straightforwardly by

$$LTF_{\text{ep}} \quad = \quad \frac{N3}{N1} \tag{6.4}$$

where $N1$ and $N3$ represent the measured values of rate meters 1 and 3. Since the processing time of valid events is much larger than that of invalid events, LTF_{ep} will in general be most sensitive to the valid event rate.

6.3.2   Live-time fraction due to pile-up effect

The pile-up effect occurs if a photon or particle hits the detector while the detector is not fully recovered from a hit by a previous photon or particle. In general, the detector is fully recovered when no LLDs are set anymore. The LLDs monitor the output signal from the shaping amplifiers which in turn integrate and differentiate the output signal from the pre-amplifiers (see Brinkman *et al.* 1985). Several situations may occur in the amplifier chain:

1. The energy release in the detector by a photon or particle is so high that the pre-amplifier saturates. A subsequent hit by a particle or photon will then remain 'unnoticed' by the shaping amplifier;
2. The combination of the secondary pulse of a previous event, due to the residual acceleration of gas ions near the sense grids, and the primary pulse of the new event will cause an AC situation; the new event is rejected;
3. During the shaping time the detector is again hit and the shaping amplifier responds to the superposition of both signals. The probability for this effect is small compared to the two previous effects, since the shaping time (about 10 μs) is in general much smaller than the mean time interval between hits (of order 100 μs).

The result of pile-up is that a valid event will remain unnoticed, be rejected or be tagged with erroneous position/energy. The latter result can be thought of as electronic scattering in the spatial and energy domain. To which degree the integration time is affected depends on the exact nature of the background environment and on the spectrum of the X-ray sky that is observed. For details on this subject the reader is referred to Mason (1981). The pile-up effect in-flight was modeled by considering two components, i.e. valid and invalid events, each assigned with typical dead times. The choice for this two-component model is of course inherent to the available in-flight information. The energy spectrum of both components was assumed to be constant. If the valid and invalid event rate, incident on the photon counter, are given by N_v and N_i (c/s) respectively and the dead times by τ_v and τ_i (s), the associated live-time fraction, LTF_{pu}, is given by:

$$LTF_{\text{pu}} \quad = \quad \text{e}^{-N_v \tau_v}\, \text{e}^{-N_i \tau_i} \tag{6.5}$$

The rate meters do not provide a direct measurement of N_v and N_i. However, it turned out to be easy to find a measure for N_i: investigating observations for which it could be anticipated that the rate of incident valid events was reasonably constant, but with background-event rates (indicated by RM2 which counts events in the guard and edge counter) within a representative wide range, it
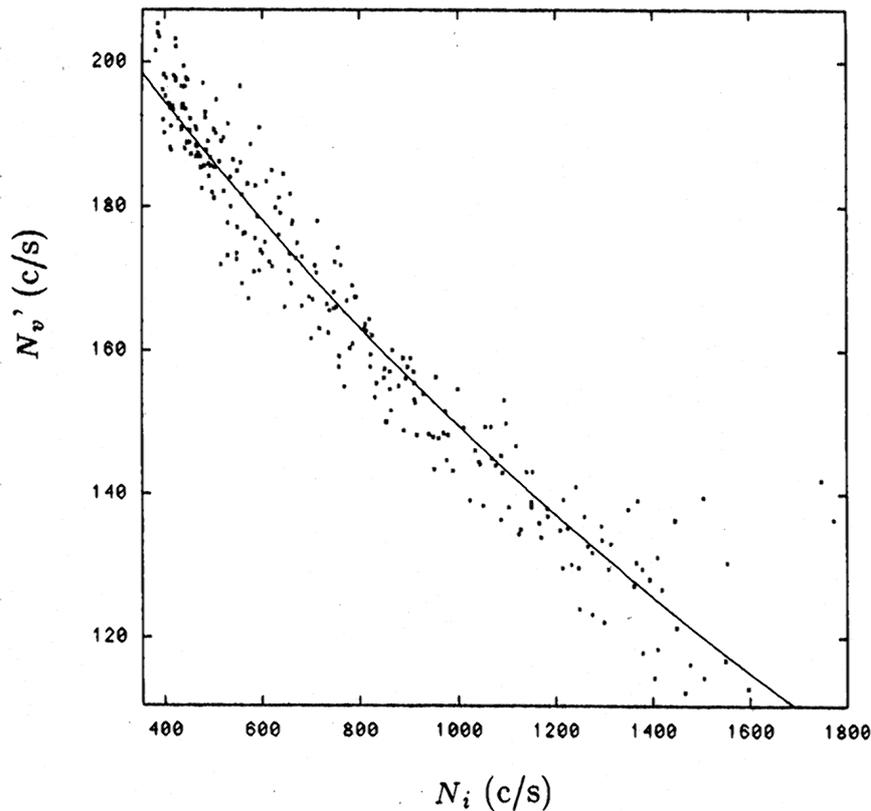
Figure 6.4: Valid event rate N'_v (this is equal to N_v, except for a reduction by the pile-up effect) against the rate of invalid events N_i for three sets of observations with approximately equal and constant N_v. The solid curve is the exponential function $N_v \, \mathrm{e}^{-N_i \tau_i}$ with a fitted value for τ_i of 44×10^{-5} s. Analysis of a more complete set of data revealed τ_i to be $(40 \pm 2) \times 10^{-5}$ s

was found that 82±1% of the RM2 counts give rise to AC situations occurring in the photon counter (as measured through $N5 - N3$, corrected for the event-processing live-time). Therefore:

$$N_i \;\; = \;\; 0.82 \, N2 \tag{6.6}$$

Using the same set of data, the dead time τ_i could be determined by investigating the relationship between the counted valid event rate (as measured by RM5, corrected for the event-processing live-time) and N_i (see Fig. 6.4). This procedure was repeated for a number of observations, with different but constant incident valid-event rates, resulting in $\tau_i = (40 \pm 2) \times 10^{-5}$ s. The background event rate in-flight ($N2$) is usually 250 c/s or more, the equivalent live-time fraction is 92% or less.

As a next step the dead time τ_v was determined. This involved a procedure analogous to that for τ_i, only switching the conditions for the incident valid- and invalid-event rates (i.e. using a subset of all data with a reasonably constant background rate level but a representative range in valid-event rates). Since τ_v is expected to be much lower than τ_i, a substantially larger range in valid-event rates is needed to measure this effect. Mostly, valid-event rates do not exceed a few hundred c/s; therefore, Sco X-1 observations were used to enlarge the range to a few thousand c/s. The result is: $\tau_v \approx 30\mu s$. This is very close to the shaping time and it may be assumed that this dead time is almost entirely due to the third pile-up effect mentioned above. In most situations (valid event rate equivalent to 3 Crab or less) the live-time fraction due to this dead time is more than 97%. The minor effect of this dead time compared to the dead time introduced by the invalid events results in a live-time fraction due to pile-up which can be determined in good approximation from ($N2$ in
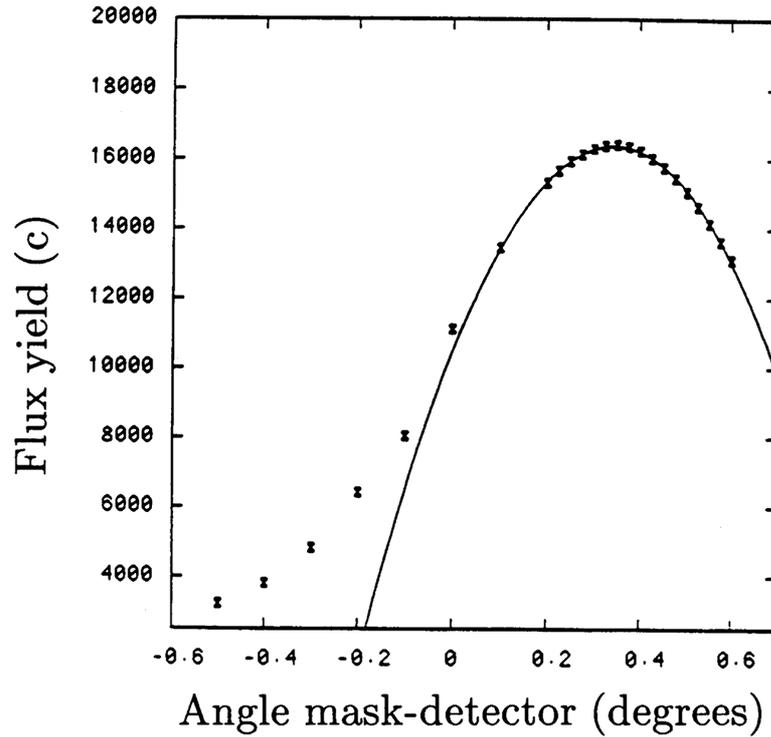
Figure 6.5: Optimization of the yield of reconstructed flux, as a function of the angle over which all detected photons are rotated in the detector plane with respect to the mask coordinate frame. The yield is maximum at an angle of $0°34$

c/s):

$$LTF_{\mathrm{pu}} \quad = \quad \mathrm{e}^{-3.3\times 10^{-4}N2} \tag{6.7}$$

6.3.3   Telemetry coverage

RM5 indicates how many valid events are processed and offered to the telemetry. From the number of telemetry channels it is known how many events are down-loaded. The telemetry coverage can therefore be determined from the ratio:

$$LTF_{\mathrm{tel}} \quad = \quad \frac{112 \;\; \mathrm{or} \;\; 224}{N5} \tag{6.8}$$

if $N5$ is more than 112 and 224 c/s respectively. If $N5$ is less, all events are down-loaded and the coverage is 100%.

6.4   In-flight calibration of the mask-detector misalignment angle

To determine the misalignment angle between mask and detector around the telescope axis (see 3.5.4), the yield of the reconstructed flux was optimized as a function of the angle $-\alpha$ over which events are rotated in the detector plane before reconstruction. As a measure of the yield, the value of the highest pixel within the point spread function was chosen. This procedure was applied to an observation of the Crab nebula. The result is given in Fig. 6.5, the rotation angle $-\alpha$ was determined to be 0.34 degrees from the +X axis to the +Z axis.
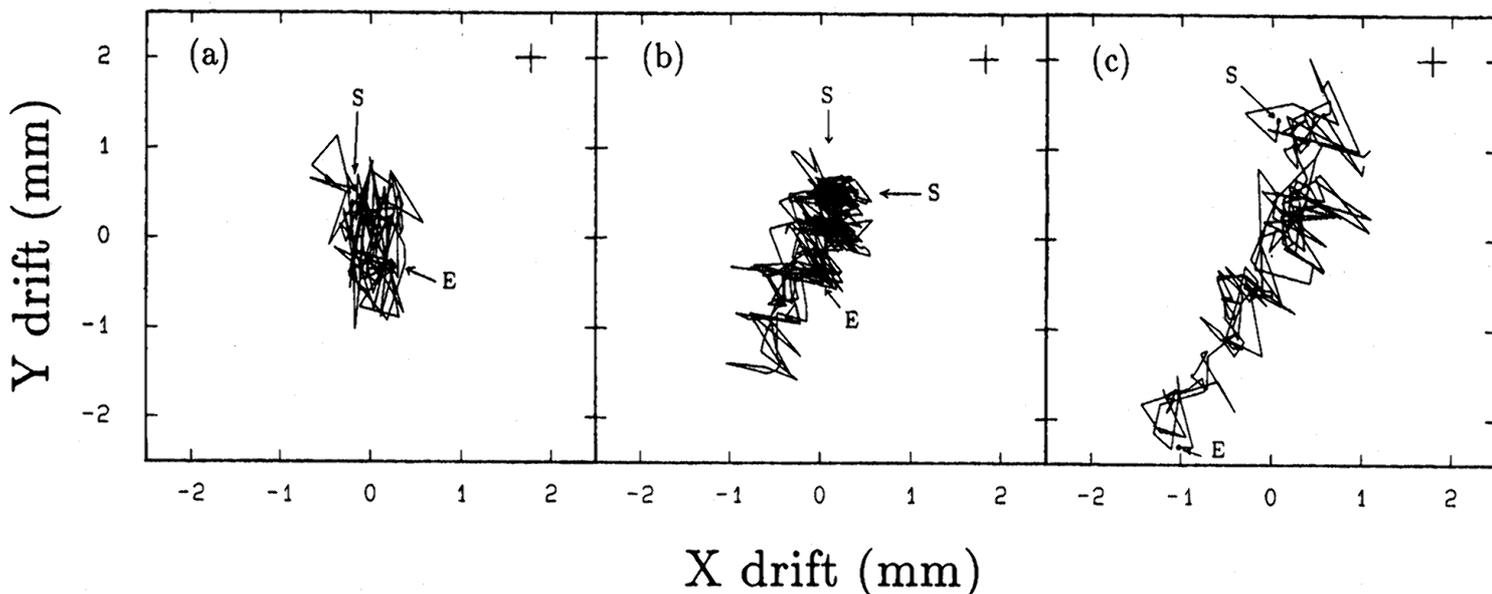
Figure 6.6: Three examples of drifts, as they are observed in the detector plane. The 'S' and 'E' points indicate the start and end of the observation respectively

6.5 Point Spread Function (PSF)

The PSF (see 5.7.2) $f(x - x_0, y - y_0)$ is defined as the normalized function that describes the spatial response of the imaging system to a point source at the observed sky at position (x_0, y_0), i.e. $f(x - x_0, y - y_0)$ is the fraction of the total flux per unit area of a point source per unit area at position (x_0, y_0) found in the interval $(x - x_0 .. x - x_0 + \mathrm{d}x, y - y_0 .. y - y_0 + \mathrm{d}y)$. Detailed knowledge of the PSF is essential for the assessment of fluxes and positions of detected point sources with maximum accuracy, or for the determination of upper limits of the flux in the case of non-detections of candidate sources.

The shape of the PSF is prescribed by mainly four items. These items introduce dependencies on a number of parameters, such as the photon energy E, the location (x, y) and time of observation. In the following subsections these four items will be discussed. We conclude in subsection 6.5.5 by evaluating the effect of the PSF on the sensitivity.

6.5.1 Pointing stability

Once the observatory has slewed onto the target position, the stability of the pointing is maintained through the inertia of the 55 ton *Mir* space station and several ancillary systems. The remaining instabilities are typically $2'$ in magnitude (Sunyaev *et al.* 1988). To study the characteristics of this instability, data obtained with the SS during the first year of *Kvant*-operations was investigated. Since it is to be expected that the nature of the instabilities is strongly coupled to the mass configuration of the space station and because this configuration did not change during the bulk of the *Kvant*-observations[5] (when the SS data was no longer available), features in the SS data are expected to be representative of the characteristics of the pointing instability during these observations.

Fig. 6.6 illustrates the time dependence of the pointing instability, expressed in mm's on the detector plane with respect to the average pointing, for three observations. These examples show that the instability may be considered as consisting of two components: the drift, or systematic

---

[5]apart from an occasionally docked *Progress* space freighter. The *Mir* space station configuration was expanded on December 6th 1989 with the *Kvant*-2 and on June 10th 1990 with the *Kristall* module, to reach a total mass of about 90 tons.
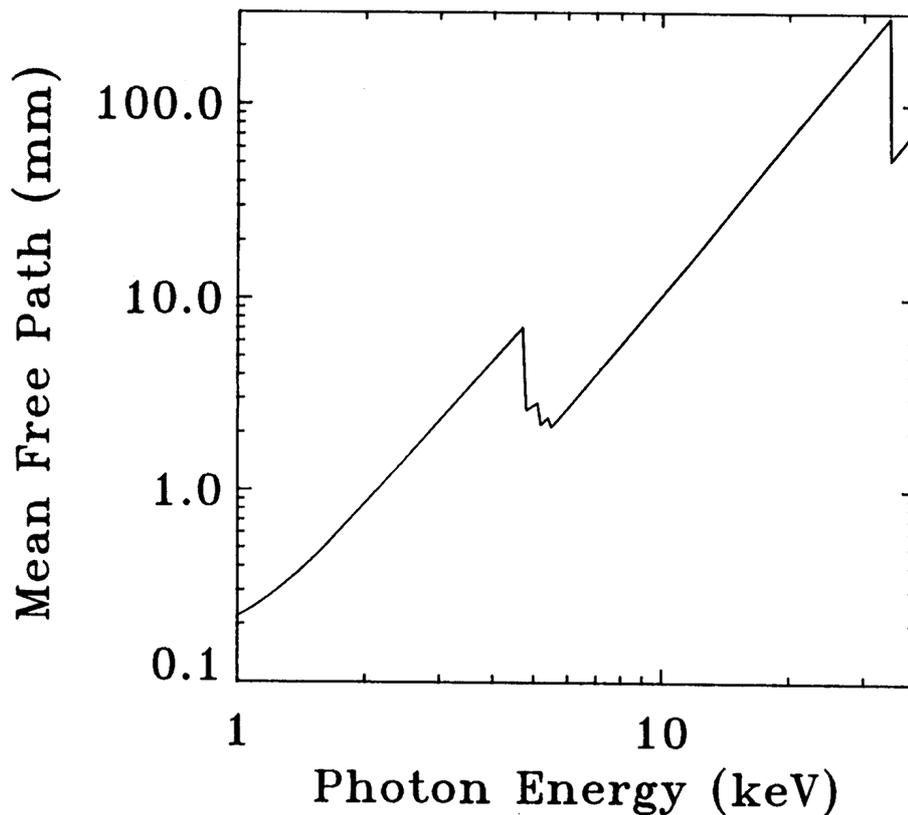
Figure 6.7: Mean free path of photons in the Xenon gas of the detector as a function of photon energy (note that the depth of the *COMIS* photon counter is 50 mm). Around 5 keV the L-edges of Xenon influence the mean free path considerably

movement of the pointing during an observation, and the jitter, or short time scale fluctuations around the drift component. A study of 247 observations with the SS has shown that:

1. there is no preference for one drift speed. It may be as small as 0.002 and as large as 0.010 $'$/s. Also, the speed may change during an observation within these limits;

2. there is a slight preference in the drift direction: 50% of all determined drift directions favor the angle range 0-50°, measured from the +Z to +X axis or -Z to -X axis;

3. in 85% of all cases the jitter along each axis has a value between 0.15$'$ and 0.48$'$ rms on a time scale of several tenths of seconds. Sunyaev et al. (1988) have found that the jitter shows oscillations with a period of 60-100s;

4. no significant rotation component occurs during one observation.

Given the rather erratic nature of these results, it is hard to model the influence of the pointing stability on the PSF if no SS data are available. Particularly the uncertainty in the drift speed poses a problem: in a typical observation of 1000 s the drift can amount to 6$'$, thereby dominating the PSF. This uncertainty can be decreased to a fraction of the angular resolution (1.86$'$) by either reconstruction of the observed sky with a time resolution of typically 100 s or by taking, in the fitting of the model to the observed PSF, the drift as a free parameter. In practice the latter option is chosen because it requires an acceptable computing effort, contrary to the former option.

6.5.2   Photon penetration

This effect also has a large influence on the shape of the PSF. Photons may be absorbed at any depth d within the detector (however, note some restrictions discussed in 4.4.2). The probability
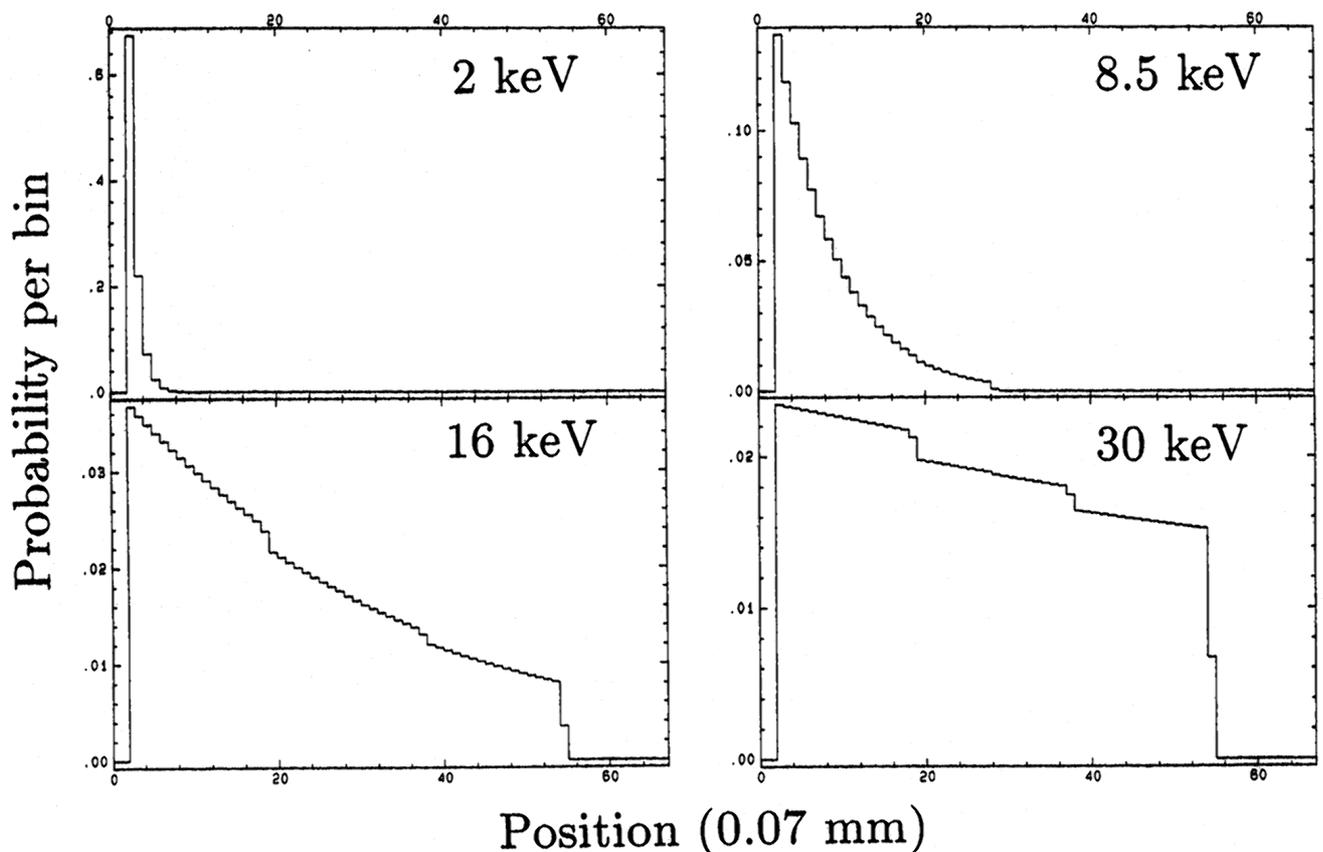
Figure 6.8: The probability distribution due to photon penetration, projected on the detector plane. The X-ray point source has an off-axis angle of 4°. The four figures refer to increasing photon energies. At low energies, photon penetration hardly plays a role; at higher energies, an asymmetrical tail develops which cuts off at positions corresponding to that of the grid planes and to the bottom of the detector

$P(d)$ of photon absorption in a layer Δd at a depth d is proportional to:

$$P(d) \quad \sim \quad e^{-d/l(E)}T(d)\Delta d \tag{6.9}$$

with $l(E)$ the mean free path of a photon with energy E (see Fig. 6.7) and $T(d)$ a function representing the blocking by the three detector wire grids and the cut-off by the bottom of the detector. The projection of $P(d)$ onto the sky plane influences the PSF. This extends to $D(E)\tan\alpha$, where $D(E)$ is the maximum depth for photons of energy E (the energy-dependence results from hardware rejection, see 4.4.2) and α the off-axis angle of the incident photons. In the case of *COMIS* the extent may amount to 9.8 mm in the detector plane (equivalent to 18.3′ in the sky plane) for photons coming from a corner of the FOV. Fig. 6.8 illustrates the projected distribution at 4 energies for a point source at an off-axis angle of 4°. The distribution is exponential in shape with 4 cuts (from 3 wire grids and the bottom of the detector), depends on photon energy and on the location of the point source with respect to the center of the FOV.

6.5.3 Noise in the position-readout system of the detector

As described in chapter 4, the position of the photon absorption is derived from the center of gravity Z of the charge distributions, induced by the avalanche on both sense grids S1 and S2 (see Fig. 4.5). This center is derived via the position-determination algorithm in the on-board microprocessor that uses the fine and coarse section signals as input. The noise in the measured position is mainly
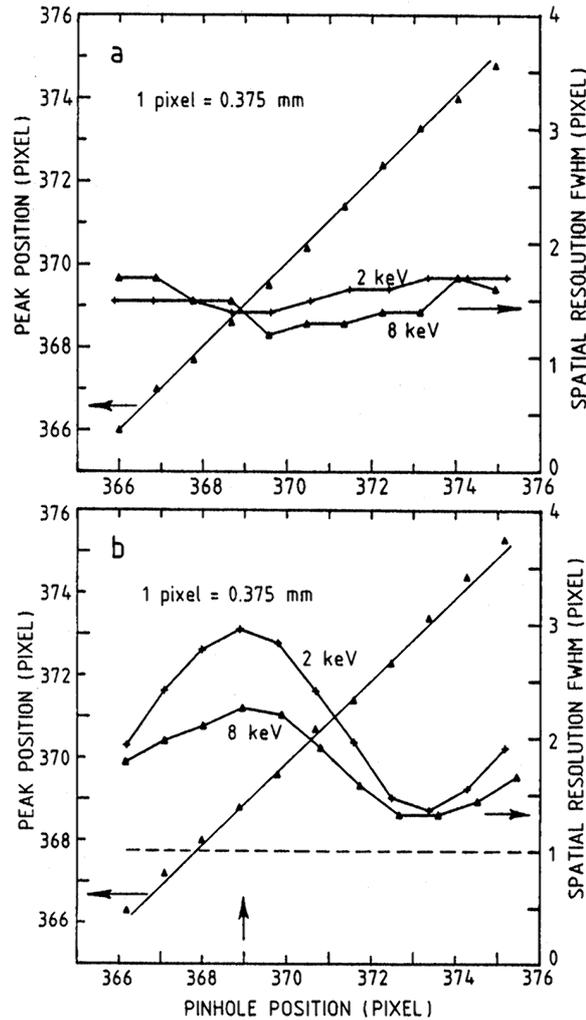
Figure 6.9: Pre-flight measurements of the position resolution and linearity in the detector plane along the direction parallel to the anode wires (**a.**) and for the other direction (**b.**). The vertical arrow indicates the position of an anode wire. These results were obtained by measuring the spatial response to X-ray illumination through 0.1 mm pinholes at photon energies of 2 and 8 keV

determined by two items: the spread in Z and the resolution of the readout.

The spread in Z is caused by the non-zero range of the photo-electron and Xe fluorescence photons, by electron diffusion and by UV photon emission near the anode wires. These effects, except electron diffusion, dominate the position resolution at high photon energies.

The resolution of the readout scheme, in the direction perpendicular to that of the anode wires, is mainly determined by the combination of thermal noise in the readout electronics and non-linearity in the relation between true photon-absorption position and Z. The non-linearity is corrected for in the readout scheme but its influence remains on the position resolution. This effect is particularly strong at low photon energies. For a more detailed discussion of the position resolution the reader is referred to Mels *et al.* (1988). The noise distribution can satisfactory be modeled by a 2-dimensional Gaussian with different standard deviations along the X- and Z-direction. Note that the position readout is discretized in bins of 0.375×0.375 mm^2.

Fig. 6.9 shows pre-flight measurements of the spatial response of the detector at several photon energies. These measurements were conducted by illuminating the detector through 0.1 mm diameter pinholes. Clearly visible is the deterioration of the resolution towards lower energies in the Z-

direction. Also indicated in Fig. 6.9 is the linearity of the readout system. The non-linearity is limited to 0.08 mm maximum in both directions, the non-linearity over the whole detector is less than 0.15 mm.

Another in-flight check was done on the spatial response of the detector at high background rates. For this purpose, the spatial response to the Fe^{55} IFC sources was analyzed. It was confirmed that there is no degradation in the spatial response for background rates up to 1000 c/s (as measured by RM2).

6.5.4   Spatial response to reconstruction algorithm

During the reconstruction process, via cross-correlation of the mask pattern with the detector image (see chapter 5), another 'smearing' of the PSF is introduced. This can best be understood by considering a single mask hole. The detector image consists of the projection of one mask hole. During the reconstruction process an imaginary mask hole is slid over the projected mask hole and the amount of flux in the cross section is evaluated. Moving the imaginary mask hole across the projected mask hole (as is done in the cross-correlation in discrete steps), one gets a pyramid-shaped spatial response with a FWHM along each dimension equal to the size of the mask hole in that dimension. This contribution to the PSF is constant.

6.5.5   Point source location accuracy (SLA) and sensitivity

The PSF, as governed by the above four items, has a significant influence on the accuracy at which point sources can be located and on the accuracy of the flux determination. With an increasing size of the PSF, the source flux will be distributed over more pixels; since the Poisson noise per pixel remains essentially constant (this is typical for a coded-mask imaging system), the sensitivity for flux and position determination degrades.

   In Fig. 6.10 the predicted 1σ errors (see Eqs.5.56-59)[6] in the 2-30 keV band for a source with a Crab-like spectrum as a function of off-axis angle are presented, thus indicating the effect of photon penetration on the sensitivities. The errors are given relative to the error for an ideal PSF (i.e. a mask-element sized block function). All instrument parameters have been fixed at their nominal values in this illustration; the jitter has been assumed to be negligible here. The best performance is obtained at the center of the observed sky. The accuracies deteriorate towards larger off-axis angles, up to 20% for flux and 60% for location measurements. If a jitter of $1.9'$ is assumed, these accuracies degrade at the center of the observed sky with 30% and 60% respectively. In practice, the strongest sources within one *COMIS* observation of typically 1000 s will have a significance of ~ 100. This corresponds to a typical flux error of 1% and a location error of $10''$. Therefore, Fig. 6.10 indicates that the best flux accuracy (when no drift or jitter is present) is $\sim 2\%$ and the best SLA $\sim 16''$ for *COMIS*.

6.6   Detector and sky background

As outlined in 5.7.1, the quality of a reconstruction may be improved by subtracting from the detector data an estimate of the spatial response to the detector and sky background.

6.6.1   Sources of backgrounds

The sky background considered here relates to the isotropic extra-galactic X-ray emission. Marshall *et al.* (1980) found that this emission could, between photon energies 3 and 50 keV, best be described by free-free emission from an optically thin plasma of $kT = 40 \pm 5$ keV, with a flux of 3.2 keV keV^{-1} cm^{-2} sr^{-1} s^{-1} at 10 keV. Due to the isotropic nature and the independence of time, the detector

---

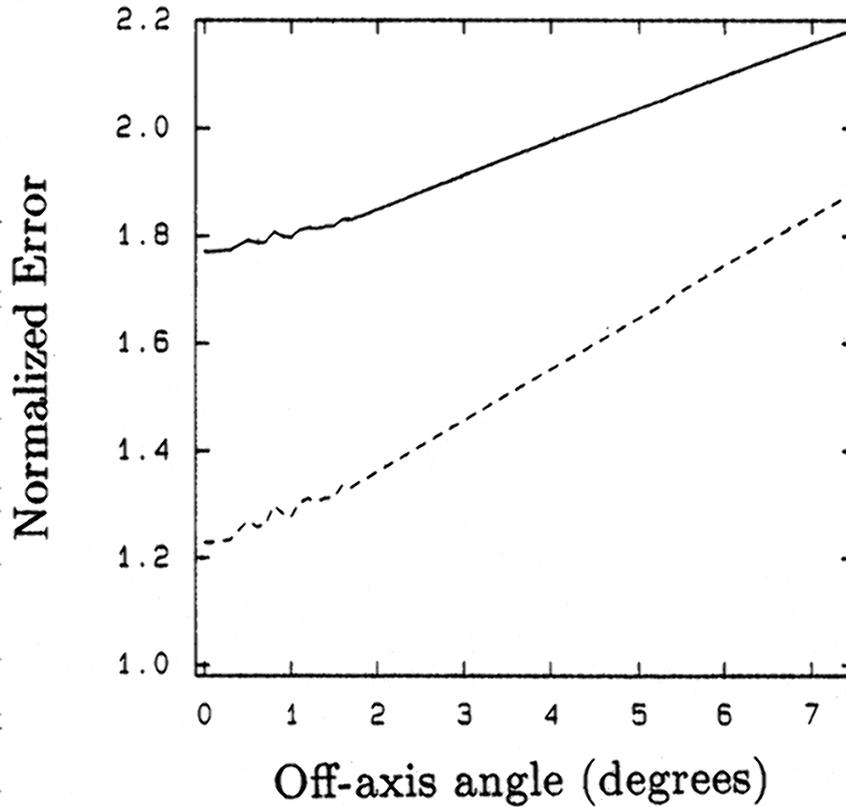[6]These errors are, for 4 parameters, equivalent to a confidence level of 21%.

Figure 6.10: 1σ errors for flux (solid curve) and location (dashed curve) in the 2-30 keV band for a source with a Crab-like spectrum, normalized to the situation when the PSF is a mask-element sized block function. The noise at small angles is numerical

response to this sky background is independent of the pointing direction and thus the same for any observation.

The above-mentioned spectral model was convolved with the spectral response of *COMIS* and multiplied with the FOV-response factor (FOV_j, see 5.7.1) and the effective area. This results in an expected countrate of 23 ± 2 c/s.

The detector background is caused by interactions of high-energy photons (outside the energy passband of the instrument) and particles with the detector material. The interaction with the solid detector-components may give rise to secondary X-ray emission through Compton scattering, nuclear interactions, fluorescence and the creation of radioactive isotopes. Moreover, ionization loss due to Compton electrons and other particles may also contribute to the detector background. The role of each of these effects in the *COMIS* detector has not been evaluated separately. The analysis of the detector background involved only an in-flight check on its overall spectrum and spatial distribution, and on the efficiency of the AC. The detector background is of course particularly dependent on the position of the instrument with respect to the South Atlantic Anomaly (SAA) and on the solar activity.

6.6.2   Background measurements

Spectral measurements of the sky and detector backgrounds were done with the aid of 8 observations pointed at the X-ray source H2251-035. These observations were chosen since no point sources were detected within the observed sky and the galactic latitude ($b^{\mathrm{II}} = -53°5$) was sufficiently high to ensure that on top of detector background only the extra-galactic diffuse X-ray background was present. Also, it was made sure that the detector background, as indicated by the readout of RM2
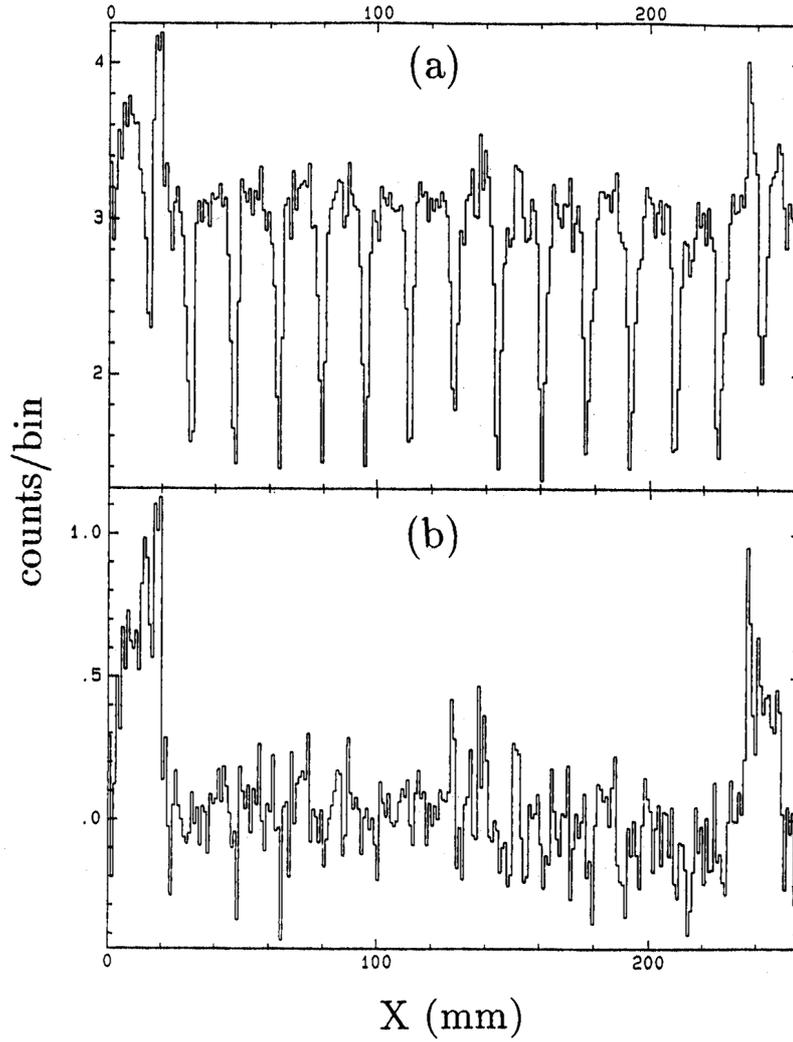
Figure 6.11: Histogram of detector, summed over all Z-coordinates, **a.** before subtraction of sky and (homogeneous) detector backgrounds and **b.** after subtraction. Note the residues at the edges, due to a lesser AC efficiency. The typical error is 0.1 c/bin

(given by $N2$), was constant during the observations, to allow for an absolute calibration point in the relation between the background countrate and $N2$. $N2$ was on average 562 c/s in this set of data. To disentangle the detector background from the sky background, use was made of the fact that the sky background is strongly modulated by the entrance-window support structure, in contrast to the detector background. Therefore, a model was made for the spatial response of the detector to the sky background in each energy channel. Apart from the support structure modulation, the model takes into account photon penetration and the spatial resolution of the detector. The model can be expressed as:

$$d_i = b + A_i(E)\beta \qquad (6.10)$$

with i the index of the detector bin, d_i its countrate in c/s/cm^2, b the countrate due to the detector background (assuming a flat spatial response), β the countrate in c/s/cm^2/sr due to the sky background and $A_i(E)$ the solid angle to which detector bin i is exposed (convolved with the photon-penetration function and the detector spatial resolution at photon energy E). This model was fitted for each energy channel to the detector data (except for 20 mm wide edges, to avoid edge effects), integrated over all 8 observations. Fig. 6.11 shows histograms across the detector, summed
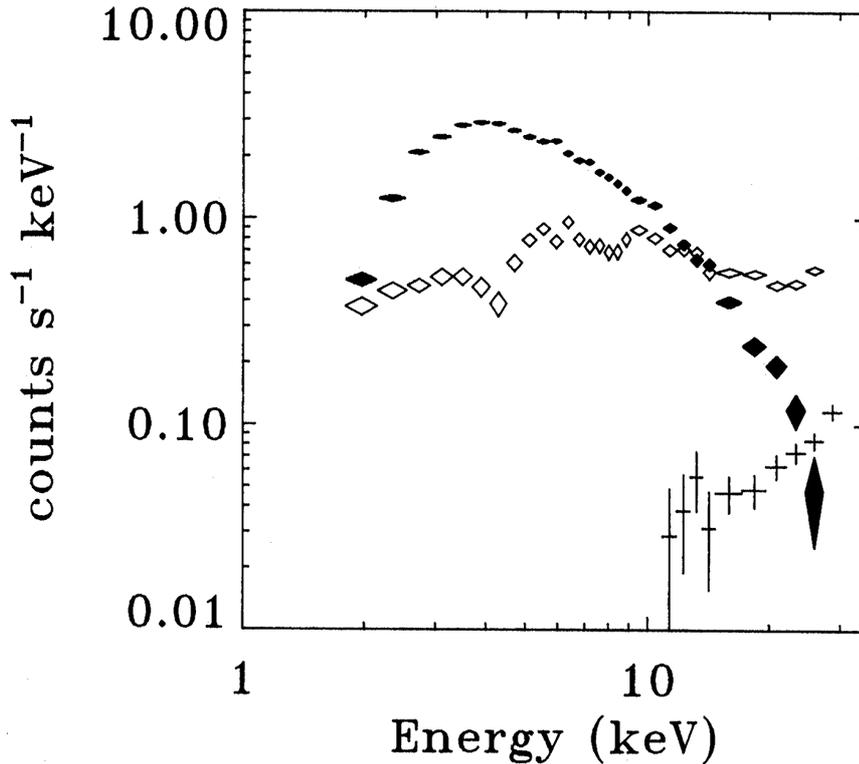
Figure 6.12: Countrate spectra of three background contributions: the sky background (filled diamonds), the detector background (open diamonds) and the edge detector background (crosses)

over all energy channels, before and after the fit results to sky and detector background were subtracted from the COMPLETE detector (including the edges not used in the fit). It is clear that the modulation of the support structure is satisfactorily cancelled out, but a residue remains along two edges (parallel to the Z-axis). This is due to the fact that along these edges only software AC is applied, whereas along the other two edges only hardware AC is incorporated (see 4.4). Apparently, the software AC is less effective than the hardware AC.

Fig. 6.12 shows the spectra obtained for the sky background, the homogeneous detector background and the edge background just described. Fitting the sky background spectrum to bremsstrahlung model spectra yielded a satisfactory best-fit ($\chi_r^2 = 0.96$) of $kT = 43 \pm 5$ keV with a total countrate of 22.8 ± 0.2 c/s on the whole detector, this result is in agreement with that obtained by Marshall *et al.* The homogeneous detector background spectrum can best be modeled with a flat c/s/keV spectrum with a total countrate of 18.0 ± 0.2 c/s, while the edge detector background only shows up at the high-energy end of the spectrum with a typical countrate of 1.3 ± 0.2 c/s.

To determine the AC efficiency in-flight a set of 17 observations was chosen, pointed at SN1987a. This set was useful, because the countrate due to compact X-ray sources (mainly LMC X-1, X-2, X-3 and X-4) was low compared to the background rates and reasonably constant in time. Furthermore, the data covered a large range of values for $N2$, indicating a large range in environmental background rates. Care was taken to avoid inclusion of high background rates due to solar activity (this type of background is characterized by large flares in $N2$). All data were binned in $N2$-intervals of 125 c/s, and it was evaluated how fast the rate of valid events increased with $N2$. The result is given in Fig. 6.13, showing a clear correlation due to a limited AC efficiency. The efficiency derived from these data is $98.1 \pm 0.1\%$ with respect to $N2$. Together with the absolute calibration point mentioned above, the $N2$-dependence of B_d (detector background countrate on the whole detector) in the total energy passband is given by:

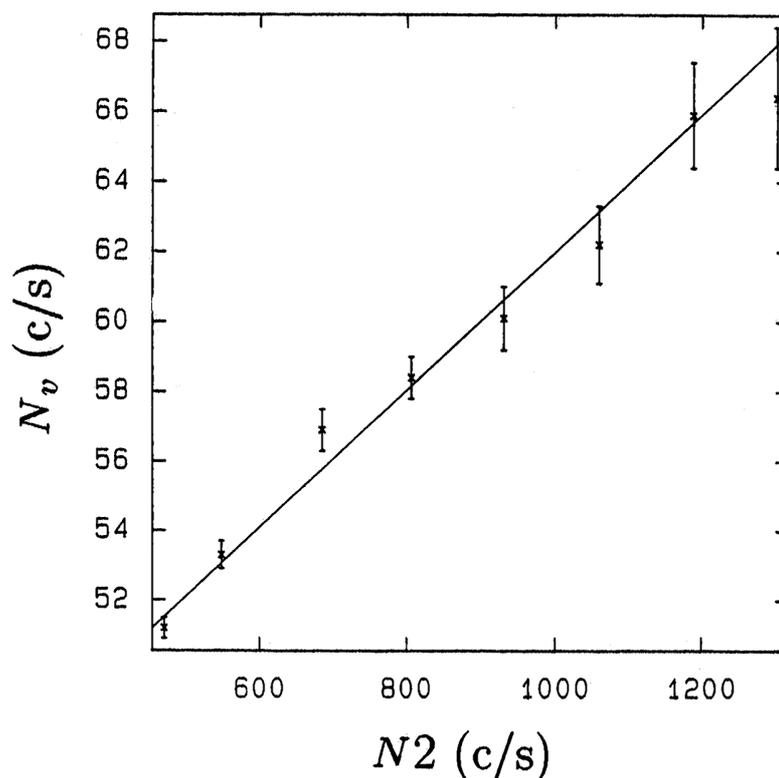$$B_d = 7.3 + 0.019\,N2 \qquad \text{c/s} \tag{6.11}$$

Figure 6.13: Measurements on the AC efficiency, using 17 observations of the SN1987a-field. N_v is the valid event rate on the total detector in the total energy passband and $N2$ the event rate detected by RM2 (counting the events on the edge anode, in the AC detector and those setting the HLD)

References

Bertin, E.P.: 1975, *"Principles and Practice of X-Ray Spectrometric Analysis"* (New York: Plenum Press), 2nd ed.

Bertin, E.P.: 1978, *"Introduction to X-Ray Spectrometric Analysis"* (New York: Plenum Press)

Brinkman, A.C., Dam, J., Mels, W.A., Skinner, G.K., Willmore A.P.: 1985, in *"Proc. Non Thermal and Very High Temperature Phenomena in X-Ray Astronomy"*, eds. G.C. Perola and M. Salvati (Roma: Università "La Sapienza"), 263

Charles, P.A., Kahn, S.M., Bowyer, S., Blissett, R.J., Culhane, J.L., Cruise, A.M., Garmire, G.: 1979, *Astrophys. J. Lett.* **230**, L83

Marshall, F.E., Boldt, E.A., Holt S.S. *et al.*: 1980, *Astrophys. J.* **235**, 4

Mason, I.M.: 1981, *"The Environmental Background in Detectors for X-Ray Astronomy"*, Ph.D. Thesis, University of London

Mels, W.A., Lowes, P., Buurmans, H.B., Brinkman, A.C., Naber, A.P., Rook, A., Zandee, W.: 1988, *Nuc. Instr. Meth. Phys. Res.* **A273**, 689

Patterson, T.G.: 1990, *"A Survey of the Galactic Bulge, Large Magellanic Cloud and Cygnus Region with a Simple Configuration Coded-Mask X-Ray Telescope"*, Ph.D. Thesis, University of Birmingham

Schattenburg, M.L., Canizares, C.R.: 1986, *Astrophys. J.* **301**, 759

Sunyaev, R.A., Gilfanov, M.R., Churazov E.M. *et al.*: 1988, *Sov. Astron. Lett.* **14**, 296

Toor, A., Seward, F.D.: 1974, *Astron. J.* **79**, 995

Part II

COMIS/TTM
Data Overview
&
Analysis/Interpretation of
Selected Objects
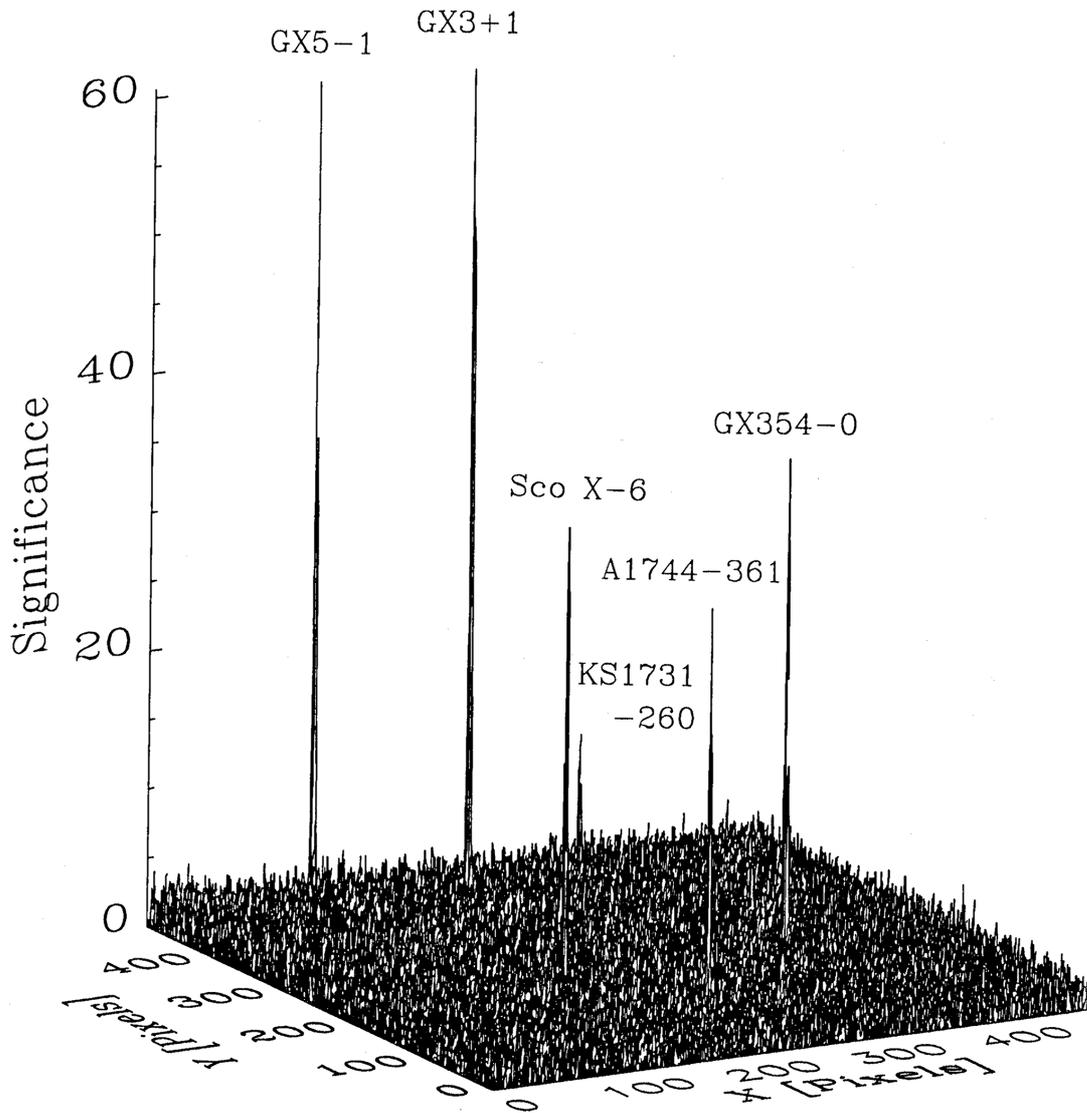
A 3-D image representation of a combination of COMIS/TTM observations aimed at the galactic center. The image shown measures 15×15 square degrees and the observations were carried out on August 22nd and 23rd, 1989, with a total exposure time of 3.8 h. The intensities are expressed in significance with respect to the Poisson standard deviation, within the full photon energy passband of COMIS/TTM.

The observed part of the sky contains 12 significantly detected sources, of which the 6 most significant ones are visible in this illustration. In Chapter 7 all sources are discussed.

Chapter 7

Monitor-results of TTM during Oct. 1988 − Feb. 1992

Monitor-results of the coded-mask imager **TTM** during the period October 1988 − February 1992

Abstract – An overview is given of the monitor results of TTM during October 1988 to February 1992, obtained by the author. These results have been extracted from an archive which the author constructed from the data, employing a $1\frac{1}{2}$ h time resolution and resolving the spectral data in four separate bands. For 60 sources, of the 65 detected in total, an indication is given on the observed X-ray variability and spectral properties. A few sources are discussed in slightly more detail: A1118–616, Cen X–3, A1744–361 and GX5–1.

7.1   Introduction

The prime objective of the coded-mask camera TTM is to MONITOR the X-ray sky. In particular, its capability pertains to a quick localization of burst and (weak) transient events in the galactic-bulge region of the sky where the crowding of X-ray point sources has hampered other X-ray monitors (i.e. simple collimating instruments). TTM's relatively large field of view provides a considerable a priori probability of detecting such events.

Although TTM was already launched in April 1987, as part of the *Röntgen* observatory aboard the scientific *Kvant* module of the space station *Mir* (Sunyaev *et al.* 1987), operations started at a regular rate from October 1988 onwards[1]. After $3\frac{1}{2}$ years of operation, during which TTM has covered 12% of the sky, it seems appropriate to evaluate the results of its monitoring capability.

An archive has been established of all X-ray sources detected with TTM[2]. The contents of this archive will be discussed here. This entails a summary of the typical behavior of most of the detected sources. In addition, a few selected sources are considered in slightly more detail.

7.2   Characteristics of the observing program

During the period October 1988 till February 1992, TTM observed the X-ray sky during 591 *Mir* orbits. Of these observations, 20% were performed in the rocking mode (see chapter 2). In Fig. 7.1 a contour map is shown of the sky coverage by TTM. Fourteen separate sky fields can be distinguished in this map. These fields have been given a label which refers to the object of main interest in the field. Table 7.1 lists for each field the exposure time and Fig. 7.2 shows the observation times for each field in a time table.

The time table shows that most of the observations (i.e. 78% of the total exposure time) were carried out during the first year of operation, 1989. Afterwards, the priority of *Mir* operations was

---

[1]For a description of *Röntgen* operations, the reader is referred to chapter 2.

[2]and also of known sources not detected, but those are not considered here.
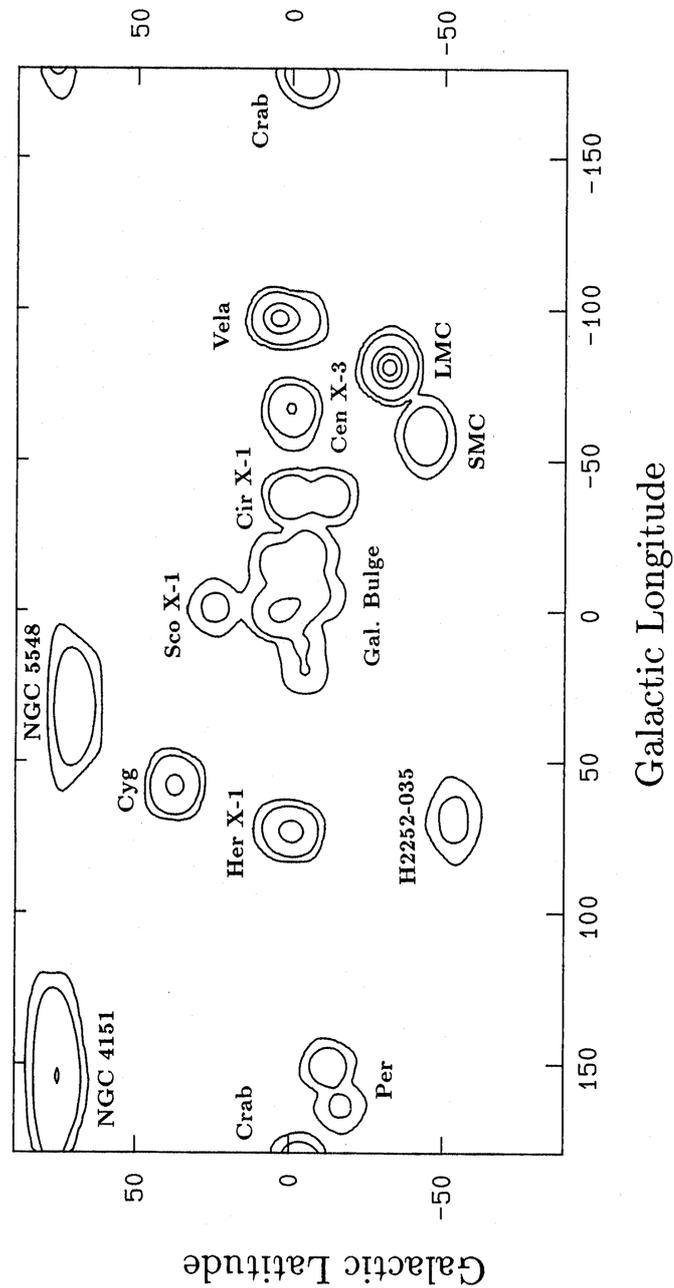
Figure 7.1: Contour map of coverage of *TTM* within the whole sky. ontours are given for 4×10^4, 4×10^5, 4×10^6, 8×10^6 and 12×10^6 cm^{2}s

Table 7.1: Targets observed with *TTM* (see also Fig. 7.1)

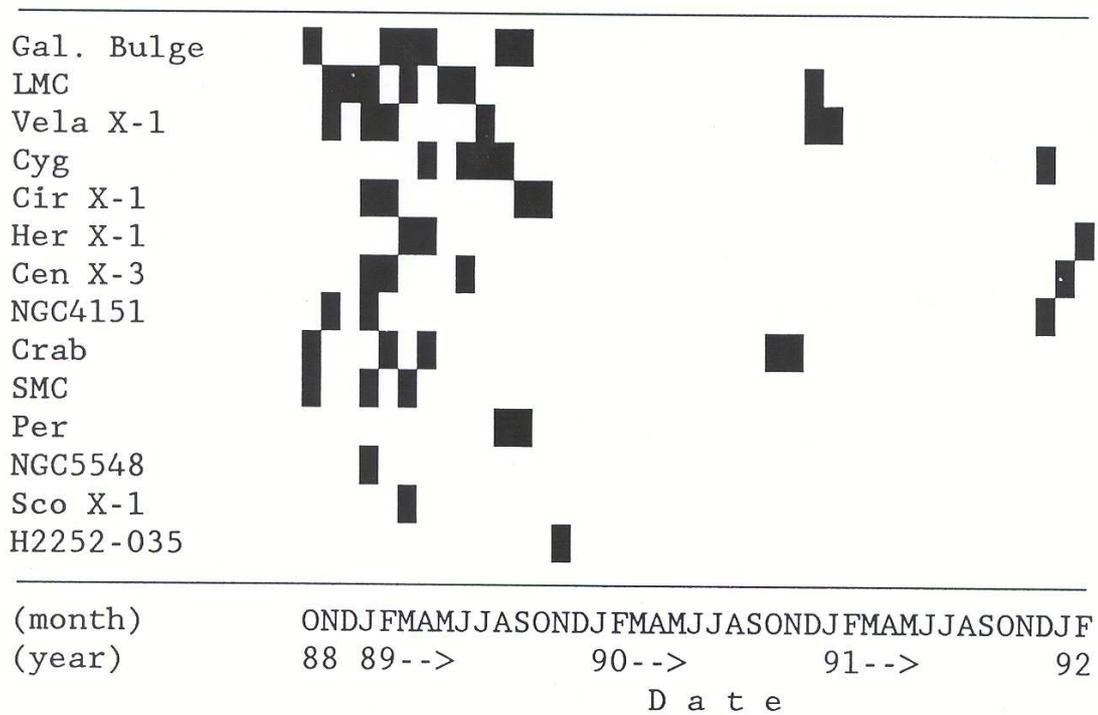| Target	Obs.	Exposure	% Exp.
		s	
Galactic Bulge	126	92187	17.0
LMC	108	97189	18.0
Vela X-1	66	79308	14.7
Cyg	61	65248	12.1
Cir X-1	35	36035	6.7
Her X-1	34	34113	6.3
Cen X-3	31	29856	5.5
NGC4151	28	22316	4.1
Crab	28	21021	3.9
SMC	23	15737	2.9
Per	20	14501	2.7
NGC5548	9	14187	2.6
Sco X-1	14	13525	2.5
H2252-035	8	5641	1.0
Total	591	540864	

Figure 7.2: Time table of observation times for the 14 targets defined in Fig. 7.1 with a resolution of one calendar month.

shifted to other subjects and operations with the *Röntgen* observatory were carried out irregularly, with long intermissions.

During the period considered, the observing program of *Röntgen* was flexible: much attention was given to 'targets of opportunity', i.e. X-ray sources which require almost instantaneous observation because of their erratic behavior. One such source is located in the Large Magellanic Cloud (LMC), which for this reason is in the top of the observing program (Table 7.1). This source is supernova 1987a which exploded a few months prior to the launch of the *Röntgen* observatory. Several *Röntgen* instruments detected SN1987a while *TTM* data provided a history of upper limits (Sunyaev *et al.* 1987, 1990a). As a bonus, the high priority of the LMC field resulted in a large archive on LMC X-1, X-2, X-3 and X-4.

Of prime interest to *TTM* is the galactic bulge which is the best observed field. Within the field the region around the galactic center was best covered (see Fig. 7.1).

The fourth field of interest was the Cygnus field. This field received extra attention after the X-ray outburst of V404 Cyg (=GS2023+338) in May 1989. Furthermore, *TTM* discovered another X-ray transient in this field (KS1947+300) and obtained large databases on Cyg X-1 and X-3.

Other fields mainly relate to observations of particular X-ray sources, e.g. the Crab nebula (used as an in-flight calibration source, see chapter 6), Her X-1, X Per, Cen X-3 and Vela X-1.

7.3   An archive of *TTM* observations

An archive of **TTM** observations

With *TTM*, a total of 65 X-ray sources was detected. 60 of these were significant in single observations while the remaining five (PSR0540-693, KS1732-273, 1E1740.7-2942, KS1741-293 and 1E1743.1-2843) were detected after combining observations. An archive was set up which contains the fluxes of the former 60 sources as measured on a *Mir* orbit by orbit basis within 4 separate spectral bands.

7.3.1   Construction of the archive

Not all observations are suitable for a full analysis in the sense that well-calibrated fluxes of all detected point sources in the observed sky can be extracted. In particular the observations performed in rocking mode pose a problem. Since no star sensor data are available, the time-dependence of the countrate of the total detector is used to determine the times when the observatory is slewed from the on- to an off-source pointing and vice versa. This is only possible when a celestial X-ray source significantly contributes to the total countrate of the detector. The change in total countrate then yields the rocking times, provided the intrinsic variability of the X-ray source is not of a disturbing influence. 64 out of 114 rocking mode observations lack the presence of a suitable X-ray source in the observed part of the sky and are excluded from the analysis.

From the remaining 50 rocking mode observations another 36 are excluded because it is impossible to determine the drift of the observatory (see 6.5.1) with sufficient accuracy.

Several non-rocking mode observations are excluded too, for a variety of reasons: too many telemetry errors, obscuration of part of the observed sky by the earth and excessive environmental background levels. In total 481 observations are acceptable for a full analysis. This includes all but one observation pointed at the galactic-bulge field.

For the construction of the archive, a choice has to be made for the timing and spectral resolution to be employed. These choices are mainly prescribed by the available computing power. Most of the computing time is spend on decoding the sky from detector data and modeling the drift component of the point spread function (see 6.5.1). The best compromise between timing and spectral resolution was found to be given by a time-bin length of 1 *Mir* orbit and four spectral bands within the total passband: 1.8–4.5 (B1), 4.5–7.4 (B2), 7.4–9.9 (B3) and 9.9–28 keV (B4). The definition of the spectral bands is based on an investigation of the best combination of signal-to-noise ratios in all 4 bands for a variety of bright X-ray sources.

7.3.2 General characteristics of archive

The archive contains 2052 observations on 60 sources; 1371 of these provide upper limits. Tables 7.3.2.a-c show a summary of the archive, specified per source. The table is split into three parts for three observing periods separately, in order to give a rough indication of the temporal behavior of some sources. The three periods were defined after consideration of the time table (Fig. 7.2). Tables 7.3.2.a-c have the following entries:

Column 1: Source designation.

Column 2: The most common name given to the X-ray source (NO reference is given here to counterparts at other wavelengths).

Column 3: Type of variability known for the source: A=Atoll-type variability, B=bursts, E=total eclipses in a binary, EP=partial eclipses, F=rapid variability, FQ=fast quasi-periodic oscillations (frequency > 1 Hz), M=orbital modulation (i.e. dips or eclipse of part of an accretion disk corona), P=pulsations, RT=recurrent transient behavior, SQ=slow quasi-periodic oscillations (frequency < 1 Hz), T=transient behavior, Z=Z-type variability. Information was taken from Bradt & McClintock (1983), Damen (1990), Ebisawa *et al.* (1989), Hasinger & Van der Klis (1989), Makino *et al.* (1992), Parmar & White (1988), Shibazaki (1989), Skinner *et al.* (1987), Skinner *et al.* (1990), Tanaka (1989) and Van der Klis (1989).

Column 4: Source type: L=low-mass X-ray binary, H=high-mass X-ray binary, G=in globular cluster, S=supernova remnant, B=black hole candidate. From Bradt & McClintock (1983), Goranskii *et al.* (1991), Tanaka (1989), Van der Klis (1989) and Van Paradijs (1991). An asterisk indicates that the source type has been inferred from the X-ray characteristics of the source, not via identification with an optical counterpart. If both an asterisk and a question mark are given the source type has been inferred by the author from the X-ray characteristics.

Column 5: The number of observations of the source.

Columns 6–7: The minimum intensity and error measured with *TTM*, in c s^{-1}cm^{-2} (2–28 keV). If the minimum refers to an upper limit ('<'), a 3σ value is given. The reader may convert the intensity to Crab units (2–28 keV) through division by 1.75.

Columns 8–9: The maximum intensity and error measured with *TTM*, in c s^{-1}cm^{-2} (2–28 keV).

The next four entries indicate roughly the spectrum of each source. An average 4-band spectrum was constructed out of all detections, which was fitted with a power-law and a thermal bremsstrahlung model spectrum, in both allowing for low-energy absorption due to circumstellar/interstellar gas of cosmic abundances, using the cross-section values provided by Morrison & McCammon (1983). The table entries refer to the best fit.

Column 10: Type of the best-fit model spectrum, Type=1 for a power-law spectrum and Type=2 for a thermal bremsstrahlung spectrum. If the value is marked with an asterisk the best fit formally does not sufficiently describe the observed spectrum, in the sense that the Pearson's chi-square test predicts only a 1% or less probability that the observed chi-square value results from a statistical fluctuation. In this case no errors are provided in the next two columns.

Column 11: Value of the best-fit power-law photon index[3] (if Type=1) or the best-fit kT in keV (if Type=2) and the 68% confidence-level interval for this value.

Column 12: The logarithm of the best-fit value for N_{H}, the hydrogen column density in H cm^{-2} of the absorbing gas, and the 68% confidence-level interval for this value.

Column 13: The flux (erg s^{-1}cm^{-2} in 2–28 keV) evaluated from the best spectral fit.

---

[3]i.e. if the flux (in phot s^{-1}cm^{-2}keV^{-1}) of the power-law spectrum is proportional to $E^{-\Gamma}$ with E the photon energy, Γ is defined as the photon index

Table 7.2: Statistics of detected sources; a. Oct.88–Nov.89

Source	Common Name	Type Var.	Src. Type	# Obs.	Intensity (min err)	Minimum	Maximum	Intensity (max err)	Type	Index	log(N_H)	Flux	Ref.
X0115−737	SMC X-1	E,P	H	19		<.012	.070	.005	1	$1.7^{+0.1}_{-0.1}$	$22.7^{+0.1}_{-0.1}$	1.2×10^{-9}	(2)
X0352+309	X Per	P	H	4		.011	.021	.002	1	$2.2^{+0.4}_{-0.4}$	<22.4	3.5×10^{-10}	
X0521−720	LMC X-2		L	117		.014	.054	.005	2	$5.8^{+0.3}_{-0.3}$	$22.1^{+0.2}_{-0.2}$	4.9×10^{-10}	(6)
X0531+219	Crab	P	S	10		1.687	1.790	.058	1	$2.1^{+0.1}_{-0.1}$	$21.8^{+0.1}_{-0.3}$	3.0×10^{-8}	
X0532−664	LMC X-4	E,P	H	117		.007	.054	.009	1	$1.0^{+0.1}_{-0.1}$	$22.4^{+0.1}_{-0.2}$	7.3×10^{-10}	(6)
X0535+262	A0535+26	RT,P	H	10		1.736	2.654	.112	1*	1.3	22.6	4.1×10^{-8}	(2)
X0538−641	LMC X-3		H,B	117		.005	.070	.011	1*	3.0	<21.7	3.7×10^{-10}	(6)
X0540−697	LMC X-1	SQ	H,B	117		.013	.041	.007	1*	4.3	22.6	4.5×10^{-10}	(6)
X0834−430	GRS0834-430	T,P	H*?	29		<.013							
X0836−429	MX0836-42	T,B	L*?	29		<.012							
X0900−403	Vela X-1	E,P	H	29		<.010	.300	.008	1*	1.4	22.9	3.3×10^{-9}	(2)
X1118−616	A1118-61	T,P	H*?	14		<.008			1*				
X1119−603	Cen X-3	E,SQ	H	14		<.010	.307	.005	1	1.8	22.9	4.9×10^{-9}	(2)
X1145−619	4U1145-61	T,P	H	14		<.011	.056	.006	1	$2.4^{+0.2}_{-0.2}$	$23.0^{+0.1}_{-0.1}$	7.1×10^{-10}	
X1145−616	1E1145.1-6141	T,P	H	14		<.010							
X1516−569	Cir X-1	T,B,FQ,F	H?	15	.006	.247	.432	.010	1*	1.7	22.9	6.4×10^{-9}	
X1538−522	Nor X-2	E,P	H	15		<.021	.070	.013	1	$1.5^{+0.9}_{-0.7}$	<23.0	1.2×10^{-9}	
X1543−624	4U1543-62		L	29		<.012	.079	.015	1	$2.7^{+0.6}_{-0.5}$	$22.5^{+0.3}_{-1.2}$	1.2×10^{-9}	
X1608−522	GX331-1	A,T,B	L	5	.032	.157	.296	.030	2	$4.4^{+3.0}_{-1.7}$	<22.5	2.9×10^{-9}	
X1617−155	Sco X-1	Z,FQ	L	14	5.064	23.090	34.652	9.242	2*	5.6	22.5	3.6×10^{-7}	
X1624−490	4U1624-49	M	L	5	.015	.042	.108	.015	2	$4.0^{+0.7}_{-1.0}$	$23.1^{+0.2}_{-0.3}$	1.3×10^{-9}	
X1627−673	4U1626-67	P,SQ	L	29		<.020	.069	.006	1*	1.3	<21.3	7.2×10^{-10}	(9)
X1630−472	Nor X-1	RT,M	L*	10	.024	.340	.427	.033	2	$2.4^{+0.2}_{-0.2}$	$23.0^{+0.1}_{-0.1}$	5.2×10^{-9}	
X1636−536	4U1636-53	A,B	L	7		<.045	.183	.011	2	$4.8^{+0.8}_{-0.7}$	$22.2^{+0.3}_{-1.1}$	2.3×10^{-9}	
X1642−455	GX340+0	Z,FQ	L*	14	.016	.591	.990	.042	2	$6.0^{+0.2}_{-0.2}$	$22.9^{+0.1}_{-0.2}$	1.1×10^{-8}	
X1656+354	Her X-1	E,M,P	L	17		<.008	.027	.003	1	$1.5^{+0.4}_{-0.4}$	$23.2^{+0.3}_{-0.3}$	6.4×10^{-10}	
X1659−487	GX339-4	F,FQ	L,B	14		<.024	.469	.048	2	$1.0^{+0.1}_{-0.1}$	$22.6^{+0.1}_{-0.1}$	7.1×10^{-9}	
X1700−377	4U1700-37	E	H	12	.028	.030	.338	.036	1	$1.4^{+0.3}_{-0.3}$	<22.7	4.2×10^{-9}	
X1702−429	GX-14.1	B	L*	22	.017	.036	.178	.023	1	$2.2^{+0.2}_{-0.2}$	$22.4^{+0.3}_{-0.5}$	1.6×10^{-9}	(5)
X1702−363	GX349+2	Z,FQ	L	12	.046	1.005	2.147	.052	2*	6.2	22.7	2.5×10^{-8}	
X1705−440	4U1705-44	A,B	L*	21	.053	.212	.639	.019	2	$5.4^{+0.2}_{-0.2}$	$22.6^{+0.1}_{-0.1}$	7.7×10^{-9}	
X1708−407	4U1708-40		L*	23	.024	.050	.203	.045	2	$7.2^{+3.0}_{-2.0}$	$22.5^{+0.3}_{-0.7}$	1.2×10^{-9}	(3)

Table 7.2.a—Continued

Source	Common Name	Type Var.	Src. Type	# Obs.	Intensity			Type	Spectral Characteristics			Ref.
					Minimum	Maximum			Index	log(N_H)	Flux	
X1724—307	1E1724-307	B	G	65	.014	.077	.012	1	$2.1^{+0.2}_{-0.1}$	$22.6^{+0.1}_{-0.3}$	7.9×10^{-10}	
X1728—337	GX354-0	A,B	L*	50	.077	.310	.031	2	$9.2^{+0.5}_{-0.6}$	$22.5^{+0.1}_{-0.1}$	2.8×10^{-9}	(5)
X1728—247	GX1+4	P	L	51	.009	.072	.009	1	$1.8^{+0.6}_{-0.2}$	$23.0^{+0.1}_{-0.2}$	8.4×10^{-10}	
X1728—169	GX9+9	A,M	L	10	<.107	.663	.072	2	$7.2^{+2.6}_{-1.7}$	<22.5	8.1×10^{-9}	
X1731—260	KS1731-260	T,B	L*	62	<.030	.235	.035	2	$5.6^{+0.2}_{-0.5}$	$22.3^{+0.1}_{-0.2}$	2.5×10^{-9}	(7)
X1732—304	SLX1732-304	B,FQ	G	62	.020	.037	.010	1	$2.0^{+0.6}_{-0.7}$	$22.6^{+0.7}_{-1.0}$	4.4×10^{-9}	
X1735—444	GX347-7	A,B	L	19	.130	.393	.013	2*	8.2	22.1		
X1735—269	SLX1735-269			62	.014	.043	.008	2	$11.0^{+7.6}_{-3.0}$	<22.5	5.5×10^{-10}	
X1742—294	A1742-294	B	L*	62	<.021	.088	.025	2	$8.0^{+1.8}_{-1.3}$	$22.8^{+0.1}_{-0.1}$	8.6×10^{-10}	
X1744—361	A1744-36	T		34	<.013	.137	.008	2	$6.2^{+0.6}_{-0.5}$	$21.9^{+0.2}_{-0.8}$	1.6×10^{-9}	
X1744—300	SLX1744-300	B	L*	62	.019	.040	.007	1	$2.0^{+0.3}_{-0.3}$	$22.6^{+0.3}_{-0.6}$	6.4×10^{-10}	(5)
X1744—299	SLX1744-299			62	.008	.046	.007	1	$2.6^{+0.4}_{-0.4}$	$23.0^{+0.2}_{-0.2}$	7.2×10^{-10}	(5)
X1744—265	GX3+1	A,B,FQ	L*	62	.547	.837	.017	2*	4.8	22.7	9.9×10^{-9}	
X1746—370	4U1746-37	B	G	34	.014	.063	.010	2*	8.6	<22.1	5.1×10^{-10}	
X1755—338	Sco X-6	M	L	43	.028	.323	.061	1	$4.1^{+0.1}_{-0.1}$	$22.8^{+0.1}_{-0.1}$	1.6×10^{-9}	
X1758—250	GX5-1	Z,FQ	L*	62	1.283	2.522	.051	2*	4.6	22.7	2.5×10^{-8}	
X1758—205	GX9+1	A	L*	25	.627	1.407	.094	2*	5.6	22.7	1.7×10^{-8}	
X1811—171	GX13+1	A	L*	9	.416	.581	.020	2	$2.8^{+0.2}_{-0.2}$	$22.8^{+0.1}_{-0.1}$	6.6×10^{-9}	
X1813—140	GX17+2	M,Z,B,FQ	L	9	.897	1.230	.032	2	$5.2^{+0.2}_{-0.2}$	$22.6^{+0.1}_{-0.1}$	1.5×10^{-8}	
X1820—303	4U1820-30	M,A,B,FQ	G	5	.775	.798	.024	2	$7.4^{+0.8}_{-0.6}$	$22.3^{+0.1}_{-0.2}$	1.2×10^{-8}	
X1822—371	Sgr X-1	PE	L	17	.042	.094	.018	1	$1.5^{+0.1}_{-0.1}$	$22.7^{+0.1}_{-0.2}$	1.5×10^{-9}	
X1826—235	GS1826-24	T	B	5	<.030	.062	.011	1	$1.0^{+0.6}_{-0.9}$	<23.4	1.1×10^{-9}	(3)
X1850—087	4U1850-08	B	G	4	.014	.032	.007	1	$2.1^{+1.0}_{-0.7}$	<22.8	3.8×10^{-10}	
X1947+300	KS1947+300	T	H	22	<.037	.198	.038	1	$1.1^{+0.2}_{-0.3}$	<22.4	4.0×10^{-9}	(1)
X1956+350	Cyg X-1	F	H,B	32	.476	1.046	.020	1*	1.7	21.9	1.4×10^{-8}	(4,8)
X2023+338	GS2023+338	T,F	L,B	32	.066	.537	.010	1	$1.6^{+0.1}_{-0.1}$	$22.7^{+0.1}_{-0.1}$	4.7×10^{-9}	(4,8)
X2030+407	Cyg X-3	PE	L	19	.213	.758	.016	2*	2.8	23.1	5.9×10^{-9}	

Table 7.2: Statistics of detected sources; a. Oct.88-Nov.89

| Source	Common Name	Type Var.	Src. Type	# Obs.	Minimum	Maximum	Type	Index	log(N_H)	Flux	Ref.
X0115−737	SMC X-1	E,P	H	19	$<.012$	$.070 \pm .005$	1	$1.7^{+0.1}_{-0.1}$	$22.7^{+0.1}_{-0.1}$	1.2×10^{-9}	(2)
X0352+309	X Per	P	H	4	$.011$	$.021 \pm .002$	1	$2.2^{+0.4}_{-0.4}$	<22.4	3.5×10^{-10}	
X0521−720	LMC X-2		L	117	$.014$	$.054 \pm .005$	2	$5.8^{+0.3}_{-0.3}$	$22.1^{+0.2}_{-0.2}$	4.9×10^{-10}	(6)
X0531+219	Crab	P	S	10	$1.687 \pm .081$	$1.790 \pm .058$	1	$2.1^{+0.1}_{-0.1}$	$21.8^{+0.1}_{-0.2}$	3.0×10^{-8}	
X0532−664	LMC X-4	E,P	H	117	$.007$	$.054 \pm .009$	1	$1.0^{+0.1}_{-0.1}$	$22.4^{+0.1}_{-0.2}$	7.3×10^{-10}	(6)
X0535+262	A0535+26	RT,P	H	10	$1.736 \pm .049$	$2.654 \pm .112$	1*	1.3	22.6	4.1×10^{-8}	(2)
X0538−641	LMC X-3		H,B	117	$.005$	$.070 \pm .011$	1*	3.0	<21.7	3.7×10^{-10}	(6)
X0540−697	LMC X-1	SQ	H,B	117	$.013$	$.041 \pm .007$	1*	4.3	22.6	4.5×10^{-10}	(6)
X0834−430	GRS0834-430	T,P	H*?	29	$<.013$						
X0836−429	MX0836-429	T,B	L*?	29	$<.012$						
X0900−403	Vela X-1	E,P	H	29	$<.010$	$.300 \pm .008$	1*	1.4	22.9	3.3×10^{-9}	(2)
X1118−616	A1118-61	T,P	H*?	14	$<.008$						
X1119−603	Cen X-3	E,SQ	H	14	$<.010$	$.307 \pm .005$	1	1.8	22.9	4.9×10^{-9}	(2)
X1145−619	4U1145-61	T,P	H	14	$<.011$	$.056 \pm .006$	1	$2.4^{+0.2}_{-0.2}$	$23.0^{+0.1}_{-0.1}$	7.1×10^{-10}	
X1145−616	1E1145.1-6141	T,P	H	14	$<.010$						
X1516−569	Cir X-1	T,B,FQ,F	H?	15	$.247 \pm .006$	$.432 \pm .010$	1*	1.7	22.9	6.4×10^{-9}	
X1538−522	Nor X-2	E,P	H	15	$<.021$	$.070 \pm .013$	1	$1.5^{+0.9}_{-0.7}$	<23.0	1.2×10^{-9}	
X1543−624	4U1543-62		L	29	$<.012$	$.079 \pm .015$	1	$2.7^{+0.6}_{-0.5}$	$22.5^{+0.3}_{-1.2}$	1.2×10^{-9}	
X1608−522	GX331-1	A,T,B	L	5	$.157 \pm .032$	$.296 \pm .030$	2	$4.4^{+3.0}_{-1.7}$	<22.5	2.9×10^{-9}	
X1617−155	Sco X-1	Z,FQ	L	14	23.090 ± 5.064	34.652 ± 9.242	2*	5.6	22.5	3.6×10^{-7}	
X1624−490	4U1624-49	M	L	5	$.042 \pm .015$	$.108 \pm .015$	2	$4.0^{+0.7}_{-1.0}$	$23.1^{+0.2}_{-0.3}$	1.3×10^{-9}	
X1627−673	4U1626-67	P,SQ	L*	14	$<.020$	$.069 \pm .006$	1*	1.3	<21.3	7.2×10^{-10}	(9)
X1630−472	Nor X-1	RT,M	L*	10	$.340 \pm .024$	$.427 \pm .033$	2	$2.4^{+0.2}_{-0.2}$	$23.0^{+0.1}_{-0.1}$	5.2×10^{-9}	
X1636−536	4U1636-53	A,B	L	7	$<.045$	$.183 \pm .011$	2	$4.8^{+0.8}_{-0.7}$	$22.2^{+0.3}_{-0.1}$	2.3×10^{-9}	
X1642−455	GX340+0	Z,FQ	L*	14	$.591 \pm .016$	$.990 \pm .042$	2	$6.0^{+0.2}_{-1.1}$	$22.9^{+0.1}_{-0.1}$	1.1×10^{-8}	
X1656+354	Her X-1	E,M,P	L	17	$<.008$	$.027 \pm .003$	1	$1.5^{+0.4}_{-0.4}$	$23.2^{+0.3}_{-0.3}$	6.4×10^{-10}	
X1659−487	GX339-4	F,FQ	L,B	14	$<.024$	$.469 \pm .048$	2	$1.0^{+0.1}_{-0.1}$	$22.6^{+0.1}_{-0.1}$	7.1×10^{-9}	
X1700−377	4U1700-37	E	H	12	$.030 \pm .028$	$.338 \pm .036$	1	$1.4^{+0.2}_{-0.3}$	<22.7	4.2×10^{-9}	
X1702−429	GX-14.1	B	L*	22	$.036 \pm .017$	$.178 \pm .023$	1	$2.2^{+0.3}_{-0.2}$	$22.4^{+0.3}_{-0.5}$	1.6×10^{-9}	(5)
X1702−363	GX349+2	Z,FQ	L	12	$1.005 \pm .046$	$2.147 \pm .052$	2*	6.2	22.7	2.5×10^{-8}	
X1705−440	4U1705-44	A,B	L*	21	$.212 \pm .053$	$.639 \pm .019$	2	$5.4^{+0.2}_{-0.2}$	$22.6^{+0.1}_{-0.1}$	7.7×10^{-9}	
X1708−407	4U1708-40			23	$.050 \pm .024$	$.203 \pm .045$	2	$7.2^{+3.0}_{-2.0}$	$22.5^{+0.3}_{-0.7}$	1.2×10^{-9}	(3)
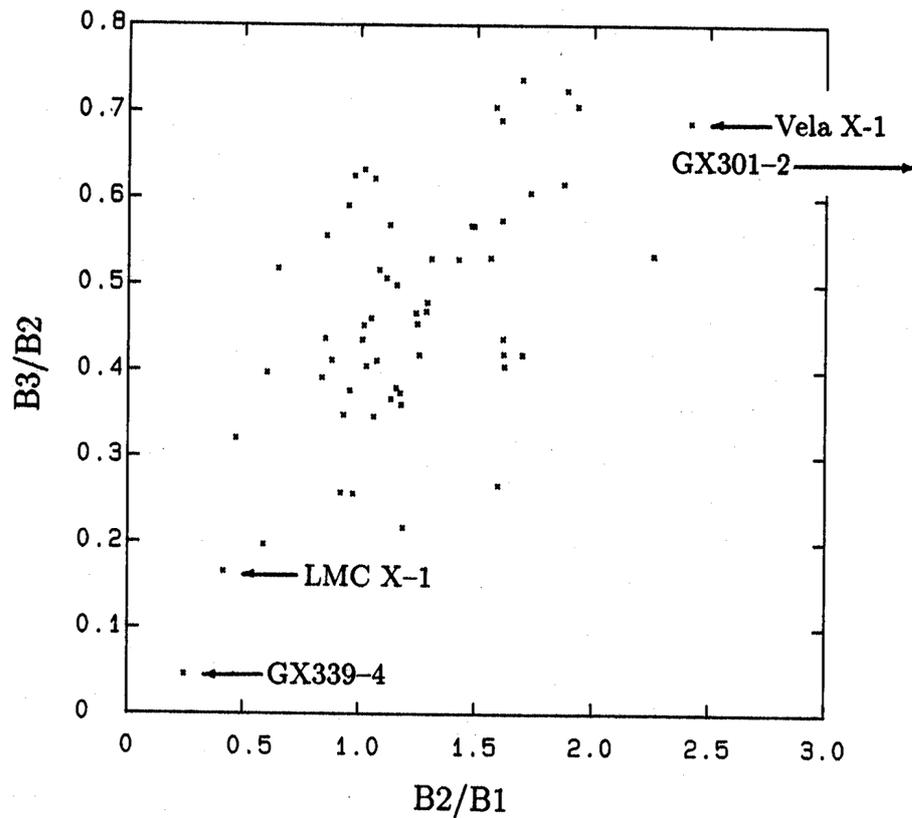
Figure 7.3: A diagram of the average hardness ratios of all sources listed in Table 7.3.2. A few exceptional sources have been indicated. GX301–2 falls outside the diagram boundaries: for this source B2/B1=5.6

The last column lists references to papers concerning analysis of *TTM* data of the appropriate source and observation period: (1) Borozdin *et al.* 1990, (2) Gilfanov *et al.* 1989, (3) In 't Zand *et al.* 1989, (4) In 't Zand *et al.* 1992, (5) Patterson *et al.* 1989, (6) Sunyaev *et al.* 1990a, (7) Sunyaev *et al.* 1990b, (8) Sunyaev *et al.* 1991a and (9) Sunyaev *et al.* 1991b.

The intensities quoted in columns 6–9 occasionally possess large errors. However, one should note that these values do not refer to the statistical significance of the detection, which is always larger than 3, but that the error in the intensity is increased due to the calibration inaccuracy of the PSF in particular.

A wide variety of sources has been monitored by *TTM* with fluxes between 3.5×10^{-10} (X Per) and 3.7×10^{-7} erg s^{-1}cm^{-2} (Sco X–1). In order to get an idea of the large variety of spectra that were obtained, a diagram is shown in Fig. 7.3 of B3/B2 versus B2/B1 for all sources. B3/B2 refers to the hardness of the high-energy continuum and B2/B1 to that of the low-energy continuum. The latter hardness is a good measure for the low-energy absorption. The upper region of this diagram (i.e. roughly above B3/B2∼ 0.6) contains the typical hard spectra of the high-mass X-ray binaries (among them several pulsars, e.g. Vela X-1, Cen X-3, A0535+262 and GX301-2). The lower region (i.e. below B2/B1∼ 0.3) contains sources with very soft spectra, most notably the black hole candidates GX339-4 and LMC X-1. Noteworthy is the relatively high B2/B1 value for GX301−2, which indicates the presence of exceptionally strong low-energy absorption in the spectrum of this pulsar.

Most of the sources have been detected in the galactic-bulge field. In Fig. 7.4, the sensitivity which *TTM* obtained in this field is given, together with 38 detected point sources. This includes three previously unknown sources: KS1731−260 (Sunyaev *et al.* 1990b), KS1732−273 and

Table 7.2: Bursts detected and identified with *TTM*, in chronological order

Burst No.	Date in 1989	T^a_{start}	e-Decay Time s	Hardening[b]	Peak Int. Crab	Identification	Ref.[c]
1	Mar 24	70337	7.7±1.1	0.38±0.13	1.41±0.16	X1702−429	(1)
2	Mar 25	72246	4.3±0.8	0.95±0.30	1.05±0.14	X1702−429	(1)
3	Mar 31	71779	3.6±0.4	0.77±0.22	0.99±0.10	X1728−337	(1)
4	Apr 1	68651	7.7±1.4	0.51±0.20	0.32±0.04	X1744−300	(1)
5	Apr 2	64590	6.6±0.6	0.61±0.11	1.47±0.14	X1702−429	(1)
6	Aug 16	50936	6.8±0.4	0.64±0.09	1.19±0.10	X1731−260	(2)
7	Aug 20	48709	11.7±2.3	0.27±0.11	0.45±0.07	X1741−293	(3)
8	Aug 22	13615	10.2±1.6	0.83±0.21	0.43±0.05	X1741−293	(3)
9	Aug 22	19975	7.2±2.6	0.33±0.20	0.20±0.04	X1742−294	
10	Aug 22	30665	4.5±0.3	0.71±0.09	1.64±0.14	X1728−337	
11	Aug 31	6776	6.5±1.1	1.17±0.37*	0.39±0.05	X1731−260	(2)
12	Aug 31	11527	6.7±0.8	0.32±0.07*	0.47±0.05	X1731−260	(2)
13	Sep 4	9882	6.1±0.7	0.49±0.12*	0.62±0.06	X1731−260	
14	Sep 9	27936	4.9±0.4	0.68±0.11	1.87±0.09	X1728−337	

[a] The start time of the burst is expressed in seconds after 0^h U.T. of the current date. The typical error in this value is 2 s.

[b] The hardening is defined as the ratio of the decay time in 9.9–28 keV to that in 5.7–9.9 keV; the values indicated with an asterisk are defined differently, in order to obtain better statistics: the ratio of the decay time in 5.7–9.9 to that in 1.8–5.7 keV.

[c] References: (1) Patterson *et al.* 1989, (2) Sunyaev *et al.* 1990b, (3) In 't Zand *et al.* 1991. On the remaining bursts no paper has been published yet.

KS1741−293. The latter two sources are discussed separately in chapter 8. The best sensitivity was achieved near the sources GX1+4 and KS1731−260.

7.3.3   Burst events

Burst events were detected from 6 sources. Two of these (KS1731−260 and KS1741−293) are transient sources discovered with *TTM* and thus extend the known population of bursters. Four burst sources were observed to burst more than once. A list of all 14 detected burst events is given in Table 7.2. The table excludes 3 other detected burst events which could not be attributed to a point source because they were too weak to allow for an adequate positioning. For details on burst analysis methods on *TTM* data the reader is referred to Patterson *et al.* (1989).

Ten bursts have been identified as Type I bursts, since they show significant spectral softening during decay. The other 4 bursts did not allow an assessment of their spectral evolution, due to insufficient photon statistics.

7.3.4   Remarks on individual sources

In the following, some remarks are given on each of the 60 sources listed in Table 7.3.2. These remarks are partly based on investigations of hardness-hardness diagrams (like Fig. 7.3) and hardness-intensity diagrams (like Fig. 7.7) for each source.

It is emphasized here that remarks placed on variability refer to a time resolution of 1 *Mir* orbit and that quoted intensities (in Crab units) are for the total passband (2−28 keV).

X0115–737: No significant variability could be detected during the times when SMC X-1 was out of eclipse.

X0352+309: Marginally detected during four observations on Aug 17, 1989.

LMC Sources (X0521–720, X0532–664, X0538–641 and X0540–697): The LMC field was regularly observed between November 1988 and June 1989 and on Dec 22, 1990. Most of the observations were pointed at the vicinity of X0540–697 (and the nearby sources SN1987a and PSR0540–693). Hence, the sensitivity was largest in that region. For a more detailed discussion of these observations, we refer to Sunyaev *et al.* (1990a).

X0531+219: The Crab nebula X-ray source was used as in-flight calibration source, see chapter 6.

X0535+262: The Be X–ray binary A0535+26 (orbital period 111 d), located 4°4 from the Crab nebula, was observed during its April 1989 outburst, on the 9th and 14th of that month. Motch *et al.* (1991) have defined a classification scheme for A0535+26 outbursts from earlier data. They differentiate between 'normal' and 'giant' outbursts. 'Giant' outbursts are characterized by a time of peak flux which does not coincide with periastron passage. Two such outbursts were detected in 1975 and 1980, the latter with the smallest peak flux of 1.5 Crab (1-10 keV). Nine 'normal' outburst, which do happen at periastron passage, were found to have fluxes less than 0.78 Crab. The outburst observed with *TTM* has a peak flux of 0.98 Crab. Since it happened at periastron passage it is here classified as a 'normal' outburst.

TTM observations revealed the pulsar signal and showed that the pulsar continued to spin-up (Gilfanov *et al.* 1989) since previous measurements with *Hakucho* (Nagase 1984). It remains an open question whether the neutron star is only spun-up during flaring phases.

X0834–430 and X0836–429: GRS0834–430 (=GRS0831–429) was first detected in February 1990 by instruments aboard *Granat* (Sunyaev *et al.* 1990c) and was seen to be in outburst another 4 times during the next 2 years (Sunyaev *et al.* 1992). *TTM* detected both this source and MX0836–42 in January 1991. GRS0834–430 is probably a Be X-ray binary, since it has a hard spectrum and shows pulsations (Makino *et al.* 1990 and Sunyaev *et al.* 1992). MX0836–42 is a source of burst events (Makino *et al.* 1990) and therefore probably is a low-mass X-ray binary.

X0900–403: The pulsar Vela X–1 was shown by *TTM* observations in 1989 to continue with its spin-down phase (Gilfanov *et al.* 1989). This phase started in 1979 and was last observed in 1984 with the *Tenma* satellite (Sato *et al.* 1986a). Vela X-1 was regularly below the detection limit: on Nov 24−25, 1988, Jan 23−26, 1989, Jul 3−4, 1989, Dec 28, 1990 and Jan 11−12, 1991. These times are in accordance with the ephemeris for eclipses as given by Sato *et al.*

X1118–616: First detection since 1975. See section 7.4.

X1119–603: See section 7.4.

X1145–619: This Be X-ray binary and recurrent transient was seen during Feb 4−6, 1989 at a level of 25 mCrab.

X1145–616: This Be X-ray binary and recurrent transient was seen during Jan 15, 1992 at a level of 20 mCrab.

X1223–624: GX301–2 was observed only twice, on Jan 11, 1992 when the orbital phase of this high-mass X-ray binary was 0.85–0.86 (ephemeris from Sato *et al.* 1986b). It showed the heaviest low-energy absorption of all detected sources, although it is known to exhibit low-energy absorption of about an order of magnitude in N_H higher (e.g. Haberl 1991). Due to the short observation time, the pulse period (∼700 s) could not be well constrained.

X1516–569: Cir X-1 was regularly observed from Jan 27 to Feb 2, 1989 when it was seen to vary with a factor of ∼ 2 about an average of 0.17 Crab. The hardness ratio B3/B2 was positively correlated with intensity.

X1538–522: Nor X-2 was only once just above the *TTM* detection limit: on Feb 2, 1989 at a level of 40 mCrab.

X1543–624: This source was detected three times just above the detection limit.

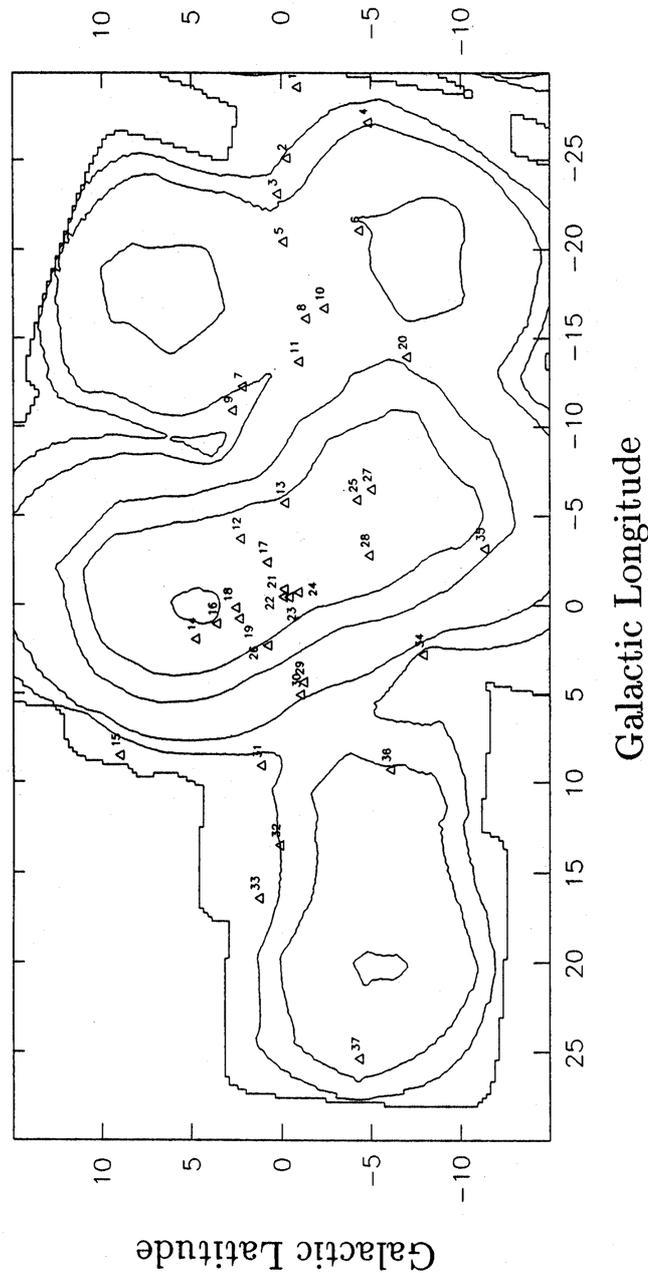*X1608–522*: Observed on Mar 24, 1989 when it was detected at a mean level of 0.12 Crab. No

Figure 7.4: Contour map of sensitivity in galactic-bulge field. Contours are 5, 7.5, 10, 20, 30 and 2000×10^{-4} c s^{-1} cm^{-2} and increase outward. Numbered points refer to the following detected X-ray sources: 1=X1608−522, 2=X1624−490, 3=X1630−472, 4=X1636−536, 5=X1642−455, 6=X1659−487, 7=X1700−377, 8=X1702−429, 9=X1702−363, 10=X1705−440, 11=X1708−407, 12=X1724−307, 13=X1728−337, 14=X1728−247, 15=X1728−169, 16=X1731−260, 17=X1732−304, 18=X1732−273 (=KS1732−273, see In 't Zand *et al.* 1991), 19=X1735−269, 20=X1735−444, 21=X1741−297 (=1E1740.7-2942, see Skinner *et al.* 1991), 22=X1741−293 (=KS1741-293, see In 't Zand *et al.* 1991), 23=X1742−294, 24=X1744−299, 25=X1744−361, 26=X1744−265, 27=X1746−370, 28=X1755−338, 29=X1758−258, 30=X1758−250, 31=X1758−205, 32=X1811−171, 33=X1813−140, 34=X1820−303, 35=X1822−371, 36=X1826−235, 37=X1850−087

spectral changes could be detected.

X1617–155: Sco X-1 was observed as part of a multi-wavelength campaign on Mar 9−13, 1989. The large errors on the minimum and maximum intensity, quoted in Table 7.3.2, arise from problems to assess the dead-time-corrected integration times for this brightest celestial X-ray source by the conventional method. During the *TTM* observations, Sco X-1 was in its flaring branch (Pan *et al.* , in preparation).

X1624–490: This source (the 'big dipper') was observed on Mar 24, 1989, exhibiting variability with a factor of 2, while remaining in the same spectral state.

X1627–673: A pulse period of 7.6610 ± 0.0002 s was measured on Sep 13, 1989 (Sunyaev *et al.* 1991b).

X1630–472: Observed on Mar 24−25, 1989 at a constant level of 0.22 Crab.

X1636–536: Observed on Mar 24 and Sep 11, 1989. On the latter day, the source was not detected and at least 2 times as weak as on the former day, when its intensity was 0.09 Crab.

X1642–455: GX340+0 was observed on Mar 24−25 and Sep 11, 1989. While exhibiting variability, its spectral state remained constant.

X1656+354: Her X-1 was detected only marginally once, on Mar 12, 1989 at a level of 15 mCrab, at phase 0.9 ± 0.1 of its 35 days cycle (ephemeris from Kahabka 1987). On three other occasions, two near phase 0.5 and one near 0, its flux remained below 9 mCrab.

X1659–487: The black hole candidate GX339–4 (see e.g. Tanaka 1989) was observed during three periods. On Mar 24, 1989, the source was in a bright/soft state at a mean intensity of 0.24 Crab. On Apr 2, 1989, the source was seen to decline by a factor of $2\frac{1}{2}$ while staying in a soft state. Four months later, on Sep 11–12, it was in an off-state with an intensity at least 20 times as low. Off-states have been observed previously for this source (e.g. Motch *et al.* 1985).

X1700–377: This source was undetectable on Mar 25, 1989, when it was in eclipse according to the ephemeris provided by Haberl *et al.* (1989).

X1702–429: While exhibiting strong variability, this source revealed no change in spectral state. Three bursts were detected from X1702–429, of which two showed significant spectral softening during decay.

X1702–363: Out of 12 observations, GX349+2 was observed to flare during 2 observations on Feb 11, 1989 with a significantly harder spectrum than during the remaining observations.

X1705–440: While showing considerable variability, the spectral state was not observed to change.

X1708–407: This source was seen slightly above the detection limit on 12 occasions. A refined position could be obtained (In 't Zand *et al.* 1989).

X1724–307: This source in Terzan 2 was always detected slightly above the detection threshold.

X1728–337: While showing considerable variability, no spectral variability could be detected. Three bursts were detected from this source.

X1728–247: GX1+4 was detected just above the detection limit during two periods: Aug 16, 1989 and Aug 31 till Sep 9, 1989. The peak intensity was 41 mCrab on Sep 3.

X1728–169: While showing no variability at first, GX9+1 was seen to decline during Sep 11, 1989 with at least a factor of 2.

X1731–260: This transient source was discovered with *TTM* and first detected on Aug 16, 1989. The peak intensity occurred on Aug 23 at a value of 0.13 Crab. Four bursts were detected from it. The source was seen to be active also in September 1990 with *ROSAT*[4] and in March 1991 with

---

[4]No paper was yet published about *ROSAT* results on KS1731−260 when this chapter was written (June 1992).

Granat/Sigma (Barret *et al.* 1992). The fact that it has been detected by these diverse instruments suggests that it was detectable over a very wide range of photon energies of ~ 0.1 to ~ 150 keV. For further details on *TTM* measurements, the reader is referred to Sunyaev *et al.* (1990b).

X1732–304: The flux of this source in Terzan 1 was seen to be approximately 3 times as high as measured in 1985 with *Spacelab-2 XRT* (Skinner *et al.* 1987).

X1735–444: While showing considerable variability, no spectral changes could be detected.

X1735–269: This source did not show any significant variability and was seen at a flux level about 2 times as high as measured in 1985 with *Spacelab-2 XRT* (Skinner *et al.* 1987).

X1742–294: No spectral variability was detected for this galactic center source. One burst was detected from it. This is the first time a burst could definitely be attributed to this source.

X1744–361: First detection since 1976. See section 7.4.

X1744–300/X1744–299: In the current analysis, no special consideration was given to the small angular distance between both these sources (2.8′, Skinner *et al.* 1990). Therefore, the tabled information is preliminary. One burst was detected from X1744–300.

X1744–265: GX3+1 shows a slight but significant positive correlation between hardness ratio and intensity.

X1746–370: This source in NGC6441 was always detected slightly above the detection threshold, at a level of ~ 15 mCrab.

X1755–338: While showing considerable variability, no change in spectral state was observed.

X1758–250: A large history of spectral states was obtained. See section 7.4.

X1758–205: Although variable with a factor of 2, the data did not reveal large spectral variability.

X1811–171: GX13+1 was observed 9 times in March 1989. It was variable with a factor of 1.5, but showed no large spectral variability.

X1813–140: For GX17+2 the same remarks apply as for X1811–171.

X1820–303: During 5 observations on Sep 9−10, 1989 this globular cluster source showed considerable spectral variability, while no significant intensity variations were detected.

X1822–371: Showed strong (factor of 3) variability, while the spectrum remained constant.

X1826–235: The transient and black hole candidate GS1826−24 (Tanaka 1989) was observed with *TTM* on Mar 19, 1989. A refined position was obtained (see In 't Zand *et al.* 1989).

X1850–087: During 4 observations on Mar 17, 1989 this globular cluster source was marginally detected at 17 mCrab.

X1947+300: This transient was discovered on Jun 8, 1989 and remained above the detection limit till Jun 15, 1989. The spectrum of KS1947+300 is quite hard, suggesting that it is a Be X-ray binary. This is supported by the nature of the alleged optical counterpart, an OB star with Hα emission (Goranskii *et al.* 1991).

X1956+350: Cyg X-1 was always observed in its high and hard state. See also chapter 9.

X2023+338: This transient was observed during the decay phase of its 1989 outburst over a total time period of 3 months. For a description of the data analysis we refer to In 't Zand *et al.* (1992, see chapter 9).

X2030+407: Cyg X-3 was seen to vary with a factor of 4, while essentially preserving a constant spectrum.

_____

The quoted information was obtained from a popular paper by A. Dyer, *Astronomy*, June 1991 issue, page 43.
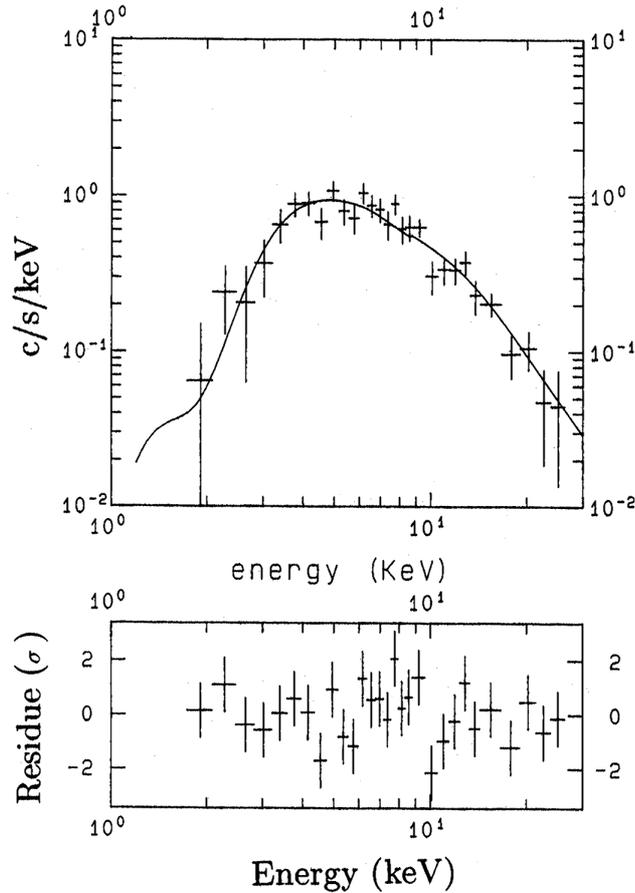
Figure 7.5: Fully resolved spectrum of A1118–616. The solid line shows the best-fit power-law model with $\Gamma = 1.8$ and $N_{\mathrm{H}} = 1.2 \times 10^{23}$ H cm^{-2}

7.4 Discussion of selected sources

Some of the detected sources show features worth discussing separately in slightly more detail.

X1118–616: A1118–616 is a transient which was seen in outburst once before. *Ariel-V* detected it for ~ 44 days from Dec 17, 1974 onwards (Eyles *et al.* 1975). The maximum occurred ~ 8 days after the first detection at a level of ~ 500 mCrab (8–20 keV). Ives *et al.* (1975) found an oscillating signal in the data, with a large modulation depth of 85% and a period of 405.3±0.6 s. This was later shown to be the first long-period X-ray pulsar (Fabian *et al.* 1975) and is situated in a Be X-ray binary.

   TTM detected A1118-616 seventeen years later, while carrying out observations on the Cen X-3 field on Jan 13−16, 1992. The source was found to have an average intensity of ~ 40 mCrab. Previous observations of this field, during Jun 4, 1989, showed the source to be at least ~ 10 times less bright. The data was checked for the presence of a pulsed signal, but this could not be found. An upper limit is placed on the modulation depth of 15% (90% confidence) for a pulsation with a period of 405–406 s. Fig. 7.5 shows the spectrum obtained on A1118–616. It can be satisfactorily described by a power-law model with a photon index of $\Gamma = 1.8 \pm 0.3$ and $N_{\mathrm{H}} = (1.2 \pm 0.5) \times 10^{23}$ H cm^{-2} ($\chi_r^2 = 1.0$). This is softer than the spectrum during peak flux in 1974, when Γ was 0.91 ± 0.05 (and $N_{\mathrm{H}} = (5.8 \pm 0.6) \times 10^{22}$ H cm^{-2}).

   Most probably, *TTM* detected the on-set of the outburst of A1118–616. *Granat* observations with the all-sky monitor *Watch*, conducted 12 days later on Jan 28−30, 1992 (Lund *et al.* 1992), revealed that the source was again at an intensity level similar to the *Ariel-V* peak intensity. Also this data contained the pulsation again, with a period consistent with that of 17 years before.
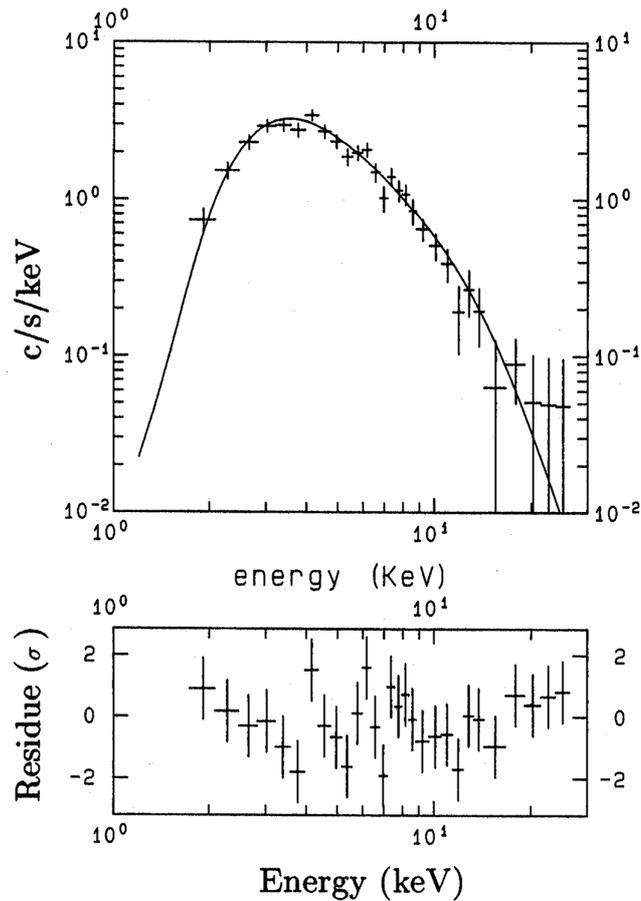
Figure 7.6: Fully resolved spectrum of A1744–361. The solid line shows the best-fit thermal bremsstrahlung model with $kT = 7.2$ keV and no absorption

X1119–603: The latest data on Cen X-3 was obtained on Jan 14-16 1992. The pulse period was measured to be $P = 4.8192 \pm 0.0005$ s (for the solar system barycenter and corrected for the orbital motion of the binary). This implies that P decreased since *TTM*'s 1989 observations (Gilfanov *et al.* 1989) at a mean rate of $\dot{P} = (-1.1 \pm 0.2) \times 10^{-3}$ s yr^{-1}. The *TTM* pulse period is reasonably consistent with the 'wavy' pulse-period history found by Tsunemi (1989) from data covering 16 years. Tsunemi modeled the pulse-period change by a linear spin-down and a secular sinusoidal disturbance with a half-amplitude of 1.3 ms. He argued periodic stellar activity (with a period of ~ 9 years) to be the most plausible explanation for the 'wavy' disturbance. The pulse-period value found with *TTM* is 0.0019 ± 0.0005 s above the value of 4.8173 ± 0.0008 s expected from the empirical formula provided by Tsunemi and therefore does not rule out his model. However, although the linear spin-down is confirmed, the statistical accuracies of both the *TTM* measurement and the empirical model do not provide a valuable calibration of the 'wavy' disturbance.

   Cen X-3 was undetectable on Feb 4, 1989 and Jan 13, 1992. These times are in compliance with the ephemeris of eclipse as given by Murakami *et al.* (1983).

X1744–361: The transient source A1744–361 has been seen once in outburst before, with *Ariel-V* during February–April 1976 (Carpenter *et al.* 1977). *TTM* measurements revealed that the source was again in an active state $13\frac{1}{2}$ years later on Aug 22–23, 1989 at a relatively constant level of ~ 60 mCrab, about 3 times less bright than in 1976. It was undetectable on Mar 20 and Sep 9, 1989, when it was at least 10 times as weak. The spectrum (see Table 7.3.2 and Fig. 7.6) is indicative for a soft transient: $kT = 7.2 \pm 1.5$ keV and $N_H < 10^{22}$ H cm^{-2} ($\chi_r^2 = 0.9$).

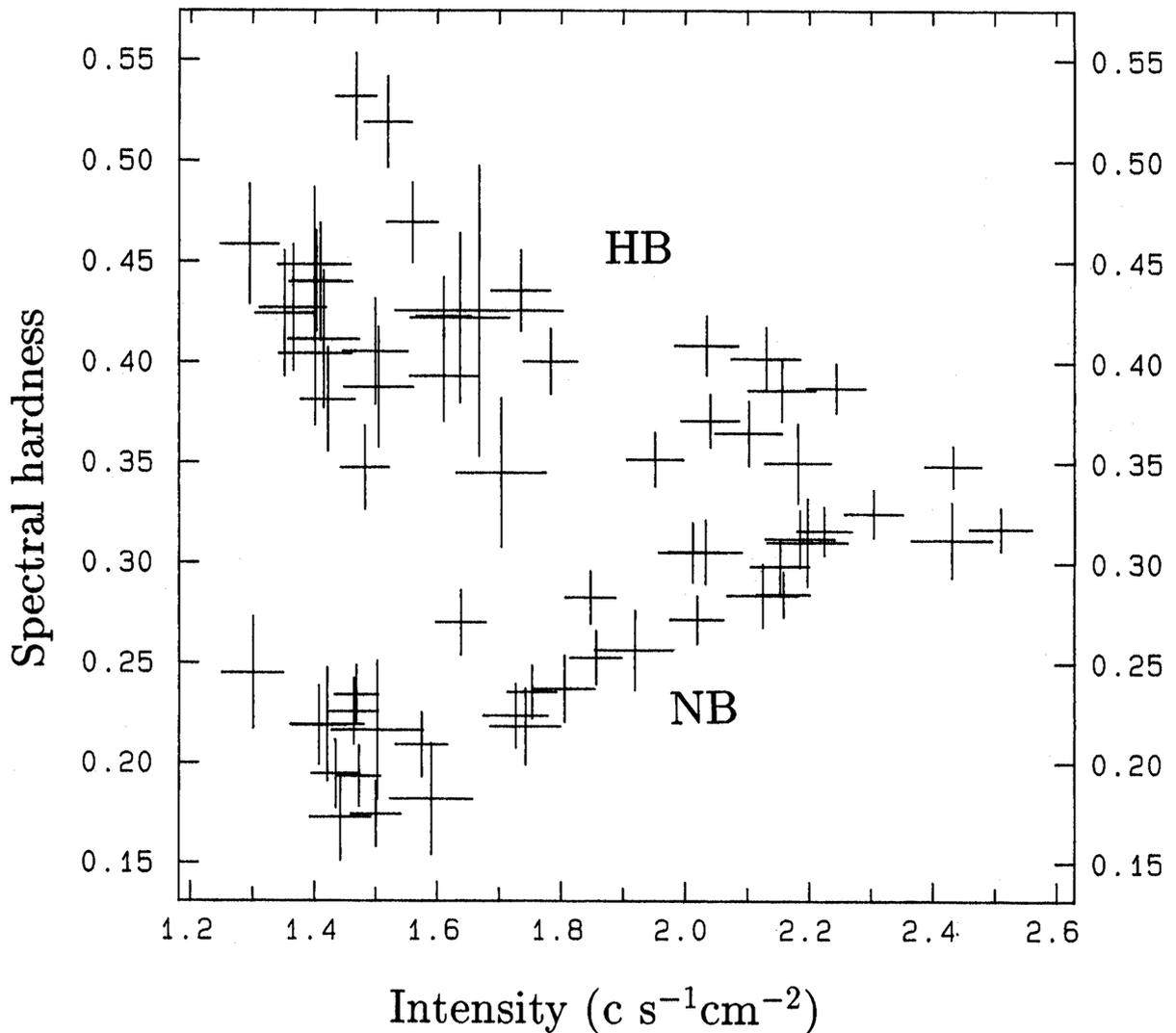*X1758–250*: The well-known 'Z-source' GX5–1 (Hasinger & Van der Klis 1989) was observed during

Figure 7.7: Spectral hardness versus intensity diagram of GX5-1. In this case the hardness is defined as the ratio of the intensity in 7.4–28 to that in 1.8–7.4 keV. The intensity is measured in the full passband. Note the jump in the transition from normal branch (NB) to horizontal branch (HB)

62 observations in 1988 and 1989, with a total exposure time of 16.2 h. The measured hardness-intensity diagram (Fig. 7.7) clearly shows the normal branch (NB) and the horizontal branch (HB). GX5–1 was found to be on the NB during 3 and on the HB during 5 separate periods (i.e. periods separated by at least 3 days).

The hardness-intensity diagram indicates that GX5–1 has, on average, preference for only part of the HB: the region of intensities near 2 c s^{-1}cm^{-2} is characterized by a low density of measurements. A one-dimensional Kolmogorov-Smirnov test (e.g. Press *et al.* 1986) applied to the distribution of the points projected on a line describing each branch ($H = 0.551 - 0.081\ I$ for the HB and $H = 0.033 + 0.121\ I$ for the NB, where H is the spectral hardness as defined in Fig. 7.7 and I the intensity in 2-28 keV) yields probabilities of 1 and 48 per cent for the HB and NB respectively that the observed distribution is randomly sampled from a uniform distribution. A confirmation of the same type of non-uniformity in the HB is provided by independent measurements: a similar feature is present in the data obtained with *Hakucho* during July-August 1980 (see Shibazaki & Mitsuda 1983).

A physical explanation for the low-density region is not readily available. Although it is not

clear from the *TTM* data whether this region is physically related to the HB-NB transition point (the 'apex'), we speculate on the possibility that it is. A rough model for the spectral behavior in another Z-source (Cyg X-2), suggested by Hasinger *et al.* (1990) after a multi-wavelength study, may provide a clue. Hasinger *et al.* suggest that the HB-to-NB transition is due to a thickening of the accretion-disk which is initiated by an increase of the mass accretion rate. At the apex the accretion disk suddenly engulfs the whole magnetosphere. The additional cool disk material in the line of sight causes the softening of the observed spectrum by Compton degradation and thus changes the hardness-intensity relation. The sudden change of accretion-disk thickness in the transition is presumed to arise from a postulated instability. The above-mentioned region in the Z pattern in GX5–1 near the apex seems to support the idea of this postulated instability: the time scale of spectral variability near the apex seems to be, on average, shorter than nominally for the NB and the HB. However, more theoretical study is needed, for instance to explain the fact that the low-density region appears at one side of the apex only and whether the relation between this region and the apex is real. The *TTM* observations on GX5–1 are further investigated (Blom 1992).

7.5   Summary and conclusion

In total, *TTM* monitored 65 point sources during the first $3\frac{1}{2}$ years of operation. Most of these sources were detected in the galactic-bulge field which *TTM* observed for $\sim 20\%$ of the time.

A variety of X-ray sources was detected, with a dynamic range of 10^3 in flux and with very soft to very hard spectra. *TTM* data provided information to extract the time variability in intensity and spectrum of these sources, on time scales from seconds (e.g. burst events, 'long' pulsations) to months (e.g. transient behavior and long-term variability).

The observations revealed the detection of 4 previously unknown transient sources (3 in the galactic-bulge field) and 14 burst events (all in galactic-bulge field). Furthermore, 2 transients, known to have erupted previously only once in 1974–1976, were detected. Bearing in mind that the available data does not really permit accurate population studies of transients, the data suggests a frequency of transients $\gtrsim 20$ mCrab in the galactic-bulge field of $\sim$1 every three days.

Moreover, valuable data on the pulse-period histories of several long-period pulsars (Cen X-3, Vela X-1, 4U1627-673, A0535+262) have also become available.

The results reported here stress the importance of monitoring the galactic-bulge region with a wide-field coded-mask camera. They show good promise for the *SAX* wide-field cameras (Jager *et al.* 1989), due for launch in 1994, which are expected to have a far better duty cycle than *TTM*.

TTM continues to conduct observations on an intermittent basis[5]. The instrument still functions nominally, almost 4 years after 'first light'.

References

Barret, D., Bouchet, L., Mandrou, P *et al.*: 1992, *Astrophys. J.* **394**, 615

Blom, J.J.: 1992, private communication

Borozdin, K., Gilfanov, M.R., Sunyaev, R.A. *et al.*: 1990, *Sov. Astron. Lett.* **16**, 345

Bradt, H.V.D., McClintock, J.E.: 1983, *Ann. Rev. Astron. Astrophys.* **21**, 13

Carpenter, G.F., Eyles, C.J., Skinner, G.K., Wilson, A.M., Willmore, A.P.: 1977, *Mon. Not. R. Astron. Soc.* **179**, 27P

Damen, E.: 1990, Ph.D. Thesis, University of Amsterdam

Ebisawa, K., Mitsuda, K., Inoue, H.: 1989, *Pub. Astron. Soc. Japan* **41**, 519

Eyles, C.J., Skinner, G.K., Willmore, A.P., Rosenberg, F.D.: 1975, *Nature* **254**, 577

Fabian, A.C., Pringle, J.E., Webbink, R.F.: 1975, *Nature* **255**, 208

Gilfanov, M.R., Sunyaev, R.A., Churazov, E.M. *et al.*: 1989, *Sov. Astron. Lett.* **15**, 291

Goranskii, V.P., Episov, V.F., Lyutyi, V.M., Shugarov, S.Yu.: 1991, *Sov. Astron. Lett.* **17**, 399

---

[5]This remark covers the situation of the instrument till June 1992.

Haberl, F., White, N.E., Kallman, T.R.: 1989, *Astrophys. J.* **343**, 409

Haberl, F.: 1991, *Astrophys. J.* **376**, 245

Hasinger, G., Van der Klis, M.: 1989, *Astron. Astrophys.* **225**, 79

Hasinger, G., Van der Klis, M., Ebisawa, K., Dotani, T., Mitsuda, K.: 1990, *Astron. Astrophys.* **235**, 131

In 't Zand, J.J.M., Patterson, T.G., Brinkman, A.C. *et al.*: 1989, in ''*Proc. 23rd ESLAB Symp. on Two Topics in X-Ray Astronomy*'', eds. J. Hunt and B. Battrick (Noordwijk: ESA SP-296), 693

In 't Zand, J.J.M., Heise, J., Brinkman, A.C. *et al.*: 1991, *Adv. Sp. Res.* **11**, (8)187 (chapter 8)

In 't Zand, J.J.M., Pan, H.-C., Bleeker, J.A.M., Skinner, G.K., Gilfanov, M.R., Sunyaev, R.A.: 1992, *Astron. Astrophys.*, in press (chapter 9)

Ives, J.C., Sanford, P.W., Bell Burnell, S.J.: 1975, *Nature* **254**, 578

Jager, R., In 't Zand, J.J.M., Schuurmans, J.J., Heise, J., Mels, W.A., Brinkman, A.C.: 1989, *SPIE Proc. Ser.* **1159**, 2

Kahabka, P.: 1987, Ph.D. Thesis, MPE, München

Lund, N., Brandt, S., Castro-Tirado, A.J.: 1992, IAU Circ. No. 5448

Makino, F., *Ginga* team: 1990, IAU Circ. No. 5139

Makino, Y., Kitamoto, S., Miyamoto, S.: 1992, in ''*Proc. Frontiers of X-Ray Astronomy*'', eds. Y. Tanaka and K. Koyama (Tokyo: Universal Academy Press), 167

Morrison, R., McCammon, D.: 1983, *Astrophys. J.* **270**, 119

Motch, C., Ilovaisky, S.A., Chevalier, C., Angebault, P.: 1985, *Sp. Sc. Rev.* **40**, 219

Motch, C., Stella, L., Janot-Pacheco, E., Mouchet, M.: 1991, *Astrophys. J.* **369**, 490

Murakami, T., Inoue, H., Kawai, K *et al.*: 1983, *Astrophys. J.* **264**, 563

Nagase, F., Hayakawa, S., Tsuneo, K. *et al.*: 1984, *Pub. Astron. Soc. Japan* **36**, 667

Patterson, T.G., Skinner, G.K., Willmore, A.P. *et al.*: 1989, in ''*Proc. 23rd ESLAB Symp. on Two Topics in X-Ray Astronomy*'', eds. J. Hunt and B. Battrick (Noordwijk: ESA SP-296), 567

Parmar, A.N., White, N.E.: 1988, *Memoria S. A. It.* **59**, 147

Press, W.H., Flannery, B.P., Teukolsky, S.A., Vetterling, W.T.: 1986, ''*Numerical Recipes*'' (Cambridge: Cambridge University Press)

Sato, N., Hayakawa, S., Nagase, F. *et al.*: 1986a, *Pub. Astron. Soc. Japan* **38**, 731

Sato, N., Nagase, F., Kawai, N., Kelley, R.L., Rappaport, S., White, N.E.: 1986b, *Astrophys. J.* **304**, 241

Shibazaki, N., Mitsuda, K.: 1983, in ''*High Energy Transients in Astrophysics*'', ed. S.E. Woosley (New York: American Institute of Physics), 63

Shibazaki, N.: 1989, in ''*Proc. 23rd ESLAB Symp. on Two Topics in X-Ray Astronomy*'', eds. J. Hunt and B. Battrick (Noordwijk: ESA SP-296), 237

Skinner, G.K., Willmore, A.P., Eyles, C.J. *et al.*: 1987, *Nature* **330**, 544

Skinner, G.K., Foster, A.J., Willmore, A.P., Eyles, C.J.: 1990, *Mon. Not. R. Astron. Soc.* **243**, 72

Skinner, G.K., Pan, H.-C., Maisack, M. *et al.*: 1991, *Astron. Astrophys.* **252**, 172

Sunyaev, R.A., Kaniovsky, A., Efremov, V. *et al.*: 1987, *Nature* **330**, 227

Sunyaev, R.A., Gilfanov, M.R., Churazov, E.M. *et al.*: 1990a, *Sov. Astron. Lett.* **16**, 55

Sunyaev, R.A., Gilfanov, M.R., Churazov, E.M. *et al.*: 1990b, *Sov. Astron. Lett.* **16**, 59

Sunyaev, R.A., *Granat* team: 1990c, IAU Circ. No. 5122

Sunyaev, R.A., Kaniovsky, A., Efremov, V. *et al.*: 1991a, *Sov. Astron. Lett.* **17**, 123

Sunyaev, R.A., Aref'ev, V., Borozdin, K. *et al.*: 1991b, *Adv. Sp. Res.* **11**, (8)5

Sunyaev, R.A., Grebenev, S., Dennis, M., Goldwurm, A., *Granat* team: 1992, IAU Circ. No. 5437

Tanaka, Y.: 1989, in ''*Proc. 23rd ESLAB Symp. on Two Topics in X-Ray Astronomy*'', eds. J. Hunt and B. Battrick (Noordwijk: ESA SP-296), 3

Tsunemi, H.: 1989, *Pub. Astron. Soc. Japan* **42**, 453

Van der Klis, M.: 1989, *Ann. Rev. Astron. Astrophys.* **27**, 517

Van Paradijs, J.: 1991, in ''*Neutron Stars: Theory and Observation*'', eds. J. Ventura and D. Pines (Dordrecht: Kluwer Academic Publishers), p. 245

Chapter 8

Two new X-ray transients near the galactic center

J.J.M. in 't Zand[*], J. Heise[*], A.C. Brinkman[*], R. Jager[*], G.K. Skinner[‡], T.G. Patterson[‡], H.-C. Pan[‡], M.R. Nottingham[‡], A.P. Willmore[‡], O. Al-Emam[‡], R.A. Sunyaev[§], E.M. Churazov[§], M.R. Gilfanov[§], N.S. Yamburenco[§]

[*] SRON-Laboratory for Space Research, Sorbonnelaan 2, 3584 CA Utrecht, The Netherlands
[‡] School of Physics and Space Research, University of Birmingham, Edgbaston, Birmingham B15 2TT, UK
[§] Space Research Institute, Profsoyuznaya 88/32, Moscow 117296, Russia

Abstract – Analysis of data obtained in 1989 with the X-ray wide-field camera *TTM* of the *Röntgen-Kvant-Mir* observatory revealed the existence of two new X-ray transients: KS1732$-$273 and KS1741$-$293, the latter of which is situated in the error boxes of MXB1742$-$29 as well as MXB1743$-$29. Significant detections of KS1741$-$293 were made on 3 consecutive days during which it exhibited 2 bursts.

8.1   Introduction

A sky field of 6×6 square degrees centered on the galactic center (GC) contains at least 17 X-ray point sources in the $3-10$ keV energy band. In Table 8.1 these sources are listed. Most of these sources are strongly variable and till now only three of them have been classified as persistent sources. Possibly the three *Einstein* sources are persistent also since they have been confirmed from *Spacelab-2 XRT* data (/8/). The same is true for SLX1744$-$299/300 and SLX1735$-$269: they have been confirmed from *TTM* data (see e.g. /13/).

Most of the remaining sources in Table 8.1 are transients and burst sources. Due to the large error boxes of the burst sources these could possibly be identified with other point sources listed in Table 8.1.

In this paper we present the discovery of two transient sources near the GC (KS1732$-$273 and KS1741$-$293) and discuss some of their characteristics.

Table 8.1: Known X-ray point sources (3-10 keV) in a 6×6 square degrees region centered on the galactic center

Source	Characteristic[a]	Ref.	Remark
4U1735-28	T (1971)	/1/	
GX3+1	P	[b]	
A1742-293	P	[b]	
A1742-289	T (1975)	/2/	
GX+0.2,-0.2	T (1976)	/2/, /3/	
GX+1.1,-1.0	T? (1976)	/3/	
MXB1742-29	B (1976)	/10/	Identification possible with A1742-294 and KS1741-293
MXB1743-29	B (1976)	/10/	Identification possible with 1E1742.5-2859 and KS1741-293
MXB1743-28	B (1976)	/10/	Identification possible with 1E1743.1-2843
H1743-32	T (1977)	/4/	
1E1740.7-2942	P?	/6/	Hardest source in region
1E1742.5-2859	P?	/7/	Coincident with Sgr A* West
1E1743.1-2843	P?	/7/	
SLX1732-304	P+B (1985)	/8/	Situated in Terzan 1
SLX1735-269	P?	/8/	
SLX1737-282	?	/8/	
SLX1744-299/300	P?+B (1985)	/9/	Double source
GS1741-282	T (1987)	/5/	
KS1732-273	T (1989)	This paper	
KS1741-293	T+B (1989)	This paper	

[a] P = Persistent source, T = Transient (between parentheses the year of detected appearance), B = burst source (between parentheses the year when the bursts were detected). If a question mark is given, the characteristic is unclear.
[b] These sources are referred to in many X-ray studies of the galactic center region, see for a list in e.g. /14/.

8.2   Observations

The observations were carried out with the X-ray wide-field camera *TTM* (/11/). This coded mask camera has a passband of $2-30$ keV and a field of view of 16×16 square degrees full-width to zero-response (FWZR) at an angular resolution of 2 arcminutes at 6 keV. The instrument is located in the *Kvant* module of the Soviet manned space station *Mir* as part of the *Röntgen* X-ray observatory. Since its turn-on in October 1988 the GC has been one of the prime targets.

The GC was observed on 12 days, most of them (9) in August-September 1989. The center of the field of view was pointed either at the GC, GX1+4 or KS1731$-$260. This basically implies 3 different sensitivities for the GC region. The observation time is typically 20 minutes per orbit. Table 8.2 lists for each day the total observation time and the time span between the start of the first and the end of the last orbit when measurements were being carried out. In total, the GC was observed for about 15 hours.

8.3   Results and discussion

The data were combined into one image per day of observation in the energy passband $3-10$ keV. Significant peaks were found in the images of 5 days at 2 positions where previously no X-ray point

Table 8.2: Some characteristics of the data on the GC and intensities for KS1732−273 and KS1741−293

Date	Exposure s	Time span[a] h	KS1732−273 (1)[b]	(2)[b]	KS1741−293 (1)[b]	(2)[b]
21-Oct-88	2520	5	<10		<20	
20-Mar-89	4300	8	22	11	< 6	
1-Apr-89	2310	2	<15		<10	
16-Aug-89	5900	$5\frac{1}{2}$	< 5		< 8	
20-Aug-89	7870	$9\frac{1}{2}$	< 5		27	12
21-Aug-89	7200	$9\frac{1}{2}$	< 5		28	10
22-Aug-89	7100	8	<10		23	15
23-Aug-89	6400	8	<10		< 5	
31-Aug-89	3670	5	< 7		<10	
3-Sep-89	1230	2	<10		<17	
4-Sep-89	3720	22	23	13	<11	
5-Sep-89	1720	5	<10		<15	

[a] Duration between start of first and end of last observation during the current data set;
[b] (1) = Intensity in mCrab (in case of no detection a 3σ upper limit is given), (2) = Significance of detection
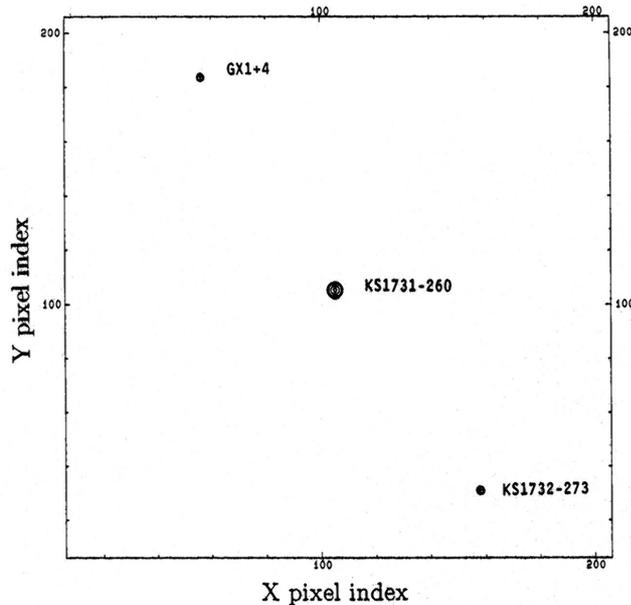
Figure 8.1: Sources observed in the immediate neighborhood of KS1732−273. Contours are given at significance levels of 5, 6, 7, 8, 10, 20, 30 σ. The sky coverage of this map is 3.1×3.1 square degrees

source was known to exist. Table 8.2 lists for each observation day the detected fluxes for these two sources, in case of no detection a 3σ upper limit is given. As can be derived from Table 8.2, the two sources vary at least with about a factor 5, given the peak flux and the lowest upper limit found.

8.3.1 KS1732−273

As Table 8.2 shows, KS1732−273 was detected on two days, March 20th and Sep 4th, 1989. The flux at both dates was comparable at 22 mCrabs (3−10 keV). A contour map of the immediate vicinity of the source is shown in Fig. 8.1. KS1732−273 is situated near GX1+4 and the X-ray transient burst
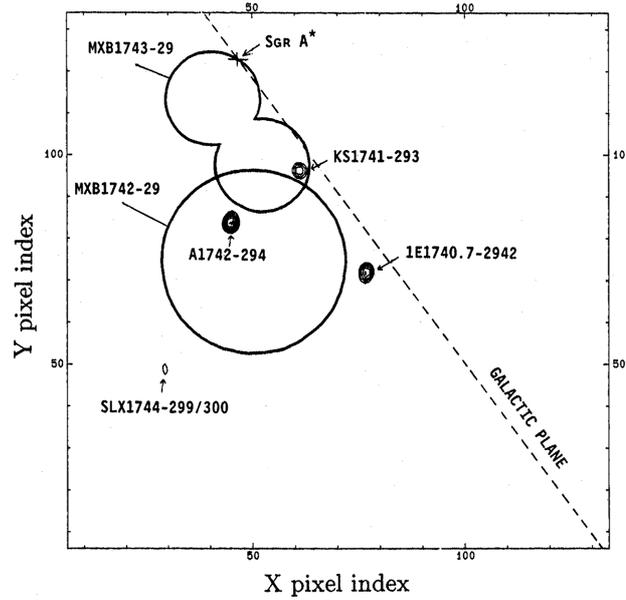
Figure 8.2: Contour map of the region observed near the GC, where Sgr A* West (not detected) is situated. Contours are given in significance steps of 0.5 in $5-8\sigma$. Furthermore, the error boxes of two *SAS-3* burst sources are given. The new transient burst source KS1741−293 is inside the error box of MXB1743−29 and just outside that of MXB1742−29. The sky coverage of this map is 2.0×2.0 square degrees

source KS1731−260, which was recently discovered by *TTM* (/12/). Using the known positions of GX354−0, GX5−1 and GX3+1, KS1732−273 was localized at:

R.A. = 17^{h} 32^{m} 54^{s}, Dec. = $-27°$ $23'$ $42''$ (1950.0 Equinox) or
$l^{\mathrm{II}} = 0°.163$, $b^{\mathrm{II}} = 2°.591$

with an error circle radius of $1'$ (90% confidence level).

Because of poor statistics it is difficult to determine the shape of the spectrum of KS1732−273 with reasonable accuracy. However, the shape is compatible with a thermal bremsstrahlung spectrum with a temperature of about $kT = 3$ keV and a hydrogen column density N_H of less than 10^{23} cm^{-2}.

The source could not be identified with any other source in any wavelength regime (SIMBAD database, Strassbourg, June 1990).

8.3.2   KS1741−293

This source was detected on 3 consecutive days (August 20−22, 1989) at a comparable flux level of about 26 mCrabs. A contour map of the observed vicinity of KS1741−293 is shown in Fig. 8.2. KS1741−293 is located less than 0.5 degree from the galactic center, at

R.A. = 17^{h} 41^{m} 38^{s}, Dec. = $-29°$ $19'$ $53''$ (1950.0 Equinox) or
$l^{\mathrm{II}} = -0°.441$, $b^{\mathrm{II}} = -0°.065$

with an error circle radius of $1'$ (90% confidence level). With *TTM*, the following sources were detected in the vicinity of the GC: A1742−294, 1E1740.7−2942, SLX1744−299/300, KS1741−293; not shown in Fig. 8.2: 1E1743.1−2843, GX3+1, Terzan 1, SLX1735−269.

Shown in Fig. 8.2 are also the error boxes of the burst sources detected in 1976 with *SAS-3* (/10/). KS1741−293 is located near the edges of both the (95% confidence level) error boxes of MXB1743−29 and MXB1742−29. KS1741−293 could therefore possibly be identified with either

Table 8.3: Parameters of 2 bursts (1 and 2) of KS1741−293

Burst No.	1	2
Start time (days since Aug 1st, 0^h UT.)	19.56378	21.15758
Duration (s)	28 +/- 4	28 +/- 4
Number of counts	300 +/- 32	900 +/- 70
Peak flux (mCrab, 2-30 keV)	425 +/- 53	302 +/- 28
Blackbody temperature (keV)	2.5 +/- 0.5	2.8 +/- 0.5
Energy in 10^{39} ergs at an assumed distance of 10 kpc	6	4

one burst source.

A thermal bremsstrahlung fit to the total spectral data of KS1741−293 yields that the hydrogen column density must be less than $N_H = 10^{23}$ cm^{-2} and the temperature more than $kT = 6$ keV.

8.3.3   Bursts from KS1741−293

Two bursts were detected from KS1741−293, on August 20th and 22nd, 1989. Characteristics of the bursts are given in Table 8.3. Fig. 8.3 displays the time profile of the second burst in three energy bands and Fig. 8.4 the blackbody spectral fit to this burst at peak intensity. Details about the extraction of burst data can be found in /12,13/.

Because KS1741−293 may be identified with either MXB1742−29 or MXB1743−29, it is interesting to compare the time profile of bursts from the latter source with that of KS1741−293. Lewin *et al.* (/10/) reported a double peaked profile structure for 7 out of 8 bursts which they could attribute to MXB1743−29, the two peaks being separated by 6 to 8 seconds (depending on the energy band considered). The two bursts reported here do not show a double peaked time profile (see Fig. 8.3). To check the significance of NOT observing the double peaked time profile, as was the case for MXB1743−29, the time profile of the burst of KS1741−293 was binned in 3 s intervals in the energy band 8−19 keV (in this energy band the double peaked nature of the bursts observed with *SAS-3* is most prominent). Taking into account the expected peak separation and checking for all possible phases of the binning, it was found that the observed intensity ratio excludes a double peak structure in the *TTM* data at a confidence level of 99.7% when compared with the minimum to maximum intensity ratio seen in the double peaked bursts reported by Lewin *et al.* (/10/).

The burst emitting area radii of the two bursts from KS1741−293 are comparable at $R = (6.0 \pm 0.5)$ x (D/10 kpc) km, where D is the distance of KS1741−293 to earth.

References

1. E. Kellogg, H. Gursky, S. Murray, H. Tananbaum, R. Giacconi: 1971, *Astrophys. J. Lett.* **169**, L99
2. C.J. Eyles, G.K. Skinner, A.P. Willmore, F.D. Rosenberg: 1975, *Nature* **257**, 291
3. R.J. Proctor, G.K. Skinner, A.P. Willmore: 1978, *Mon. Not. R. Astron. Soc.* **185**, 745
4. H. Gursky, H. Bradt, R. Doxsey *et al.*: 1978, *Astrophys. J.* **223**, 973
5. K. Mitsuda, T. Takeshima, T. Kii, N. Kawai: 1990, *Astrophys. J.* **353**, 480
6. P. Hertz, J.E. Grindlay: 1984, *Astrophys. J.* **278**, 137
7. M.G. Watson, R. Willingale, J.E. Grindlay, P. Hertz: 1981, *Astrophys. J.* **250**, 142
8. G.K. Skinner, A.P. Willmore, C.J. Eyles *et al.*: 1987, *Nature* **330**, 544
9. G.K. Skinner, A.J. Foster, A.P. Willmore, C.J. Eyles: 1990, *Mon. Not. R. Astron. Soc.* **243**, 72
10. W.H.G. Lewin, J.A. Hoffman, J. Doty *et al.*: 1976, *Mon. Not. R. Astron. Soc.* **177**, 83P
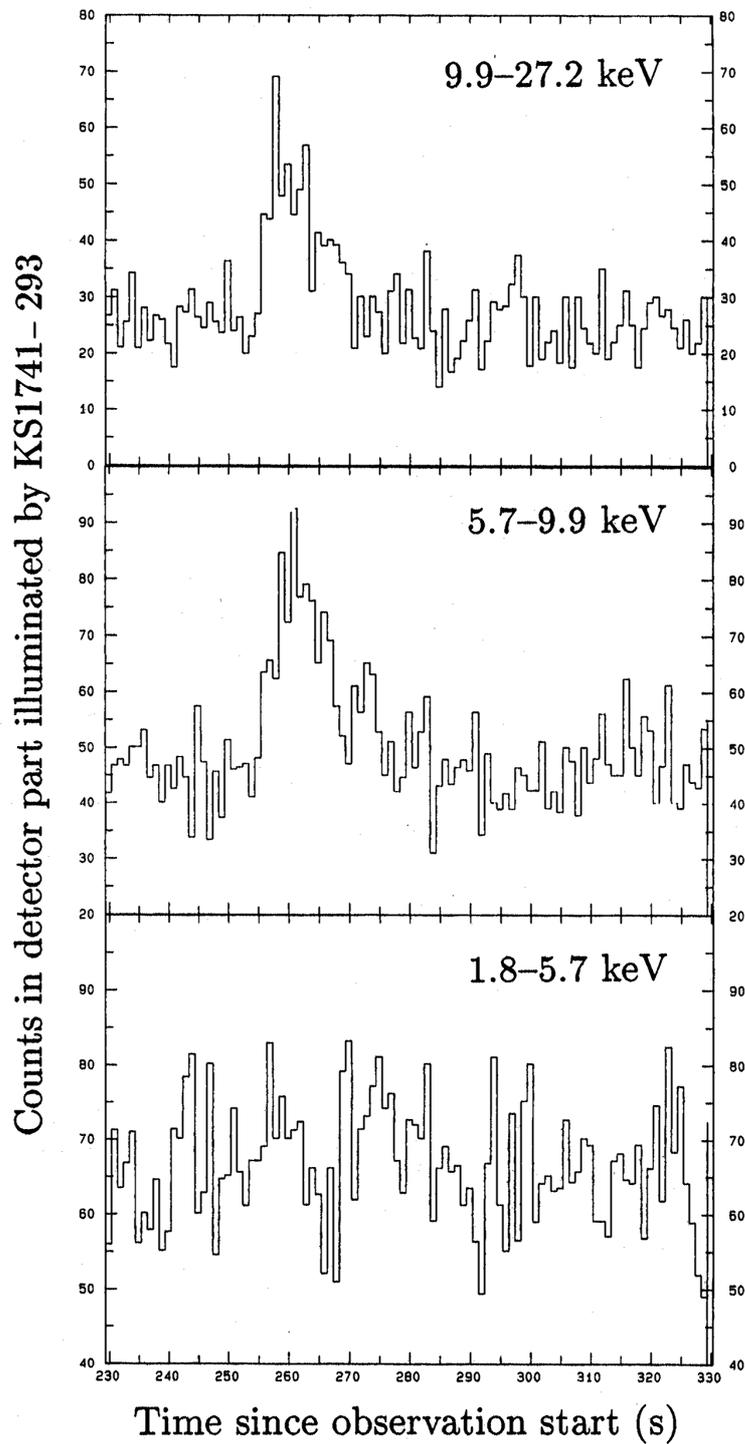11. J.J.M. in 't Zand, R. Jager, J. Heise *et al.*: 1988, in "*Proc. Workshop on Timing Neutron*

Figure 8.3: Time profile of the second and most significant burst detection, of KS1741−293 on August 22nd, 1989. The intensity is given in raw counts per second, neither corrected for background radiation nor for dead time effects. A double-peak structure, as observed by *SAS-3* for MXB1743−29, is absent at a 99.7% confidence level
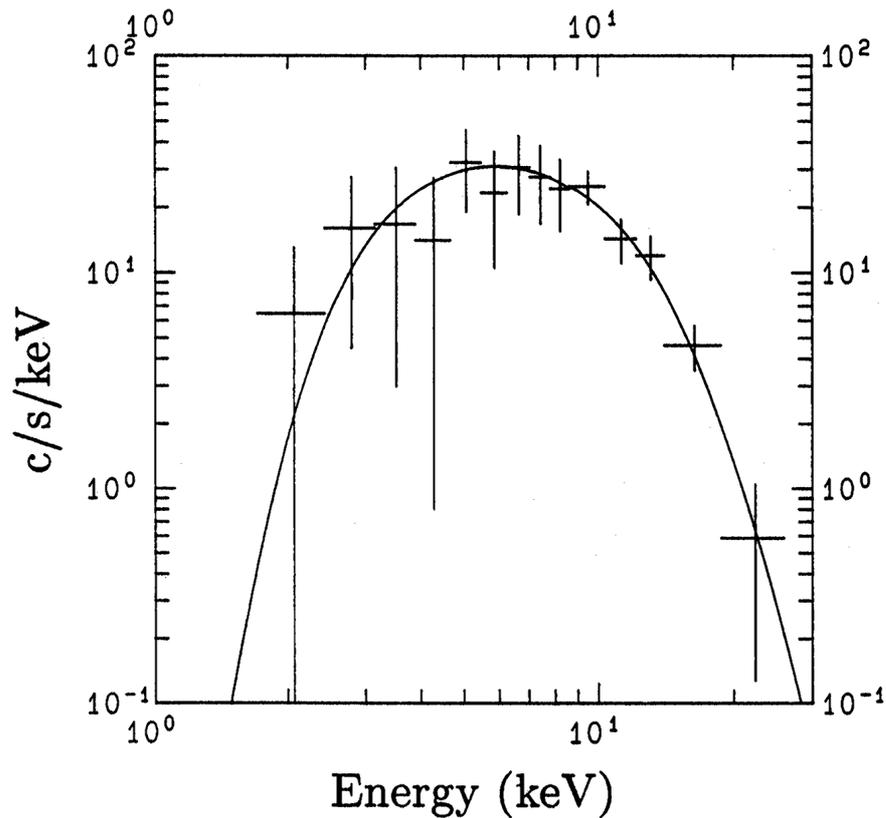
Figure 8.4: Blackbody fit (solid curve) to the spectrum of the second burst of KS1741−293 during peak intensity. The best fit temperature is $kT = 2.8 \pm 0.5$ keV

Stars", eds. H. Ögelman and E.P.J. van den Heuvel, NATO ASI Series No. C262 (Dordrecht: Kluwer Academic Publishers), 317

12. R.A. Sunyaev, E.M. Churazov, M.R. Gilfanov *et al.*: 1989, in *"Proc. 23rd ESLAB Symp. on Two Topics in X-Ray Astronomy"*, eds. J. Hunt and B. Battrick (Noordwijk: ESA SP-296), 641

13. T.G. Patterson, G.K. Skinner, A.P. Willmore *et al.*: 1989, in *"Proc. 23rd ESLAB Symp. on Two Topics in X-Ray Astronomy"*, eds. J. Hunt and B. Battrick (Noordwijk: ESA SP-296), 567

14. H.V.D. Bradt, J.E. McClintock: 1983, *Ann. Rev. Astron. Astrophys.* **21**, 13

Note added after publication

The source 1E1740.7-2942 was in October 1990 discovered to be an occasional strong emitter of γ-radiation, suggestive of 511 keV annihilation line radiation (see Bouchet *et al.* 1991, *Astrophys. J. Lett.* **383**, L45). A separate analysis of *TTM* data on this source is given by G.K. Skinner *et al.* (1990, *Astron. Astrophys.* **252**, 172).

Chapter 9

The spectral variability in 2–28 keV of GS2023+338 during its 1989 outburst

J.J.M. in 't Zand[⋆], H.C. Pan[‡], J.A.M. Bleeker[⋆], G.K. Skinner[‡], M.R. Gilfanov[§], R.A. Sunyaev[§]

[⋆] SRON - Laboratory for Space Research, Sorbonnelaan 2, 3584 CA Utrecht, the Netherlands
[‡] School of Physics and Space Research, University of Birmingham, Edgbaston,
  Birmingham B15 2TT, U.K.
[§] Space Research Institute, Profsoyuznaya 88/32, Moscow 117296, Russia

Abstract –   The X-ray transient GS2023+338 (=V404 Cyg in the optical band), a close binary containing a black hole candidate, was observed with the coded mask X-ray camera *TTM* of the *Röntgen* observatory on the *Kvant* module of *Mir* during June–August 1989, when it was in outburst. We report here the results of an analysis of these observations which mainly addresses the SPECTRAL variability of the transient on time scales between minutes and months.

The spectral signatures of this variability were found to consist of a fluctuating low-energy absorption with a time scale of $\sim 1\frac{1}{2}$ h, whose amplitude decreased on a time scale of ~ 1 month, and a slowly decreasing Compton-reflected component, on top of a power-law spectrum with essentially a constant photon index of 1.6–1.7. The fluctuating low-energy absorption could be satisfactory modeled by a varying column density of cold matter, with a dynamical range of at least a factor of ~ 40 and ranging up to $N_{\rm H} \approx 4.5 \times 10^{23}$ H cm^{-2}. This variability most probably originated in dynamical processes. Apart from spectral variability, a wavelength-independent variability is apparent, which had time scales down to at least minutes, on top of a general decay with an e-folding decay time of 32 days. The long-term trends suggest that the environment of the compact object became progressively more transparent by accretion of the circumstellar matter onto the compact object. The total mass transferred to the compact object during the complete outburst was, through equivalence with the radiated energy during the total outburst, found to be $\sim 2 \times 10^{-9}$ $(D/1 \text{ kpc})^2$ M$_\odot$. This is equivalent to an average mass transfer rate from the companion during the quiescent stage since the last outburst of the optical counterpart of $(4\text{–}12) \times 10^{15}$ $(D/1 \text{ kpc})^2$ g s^{-1}, which is similar to that observed in other transient low-mass X-ray binaries, as long as $D < 3$ kpc.

In many of its spectral aspects, GS2023+338 resembles the galactic black hole candidate Cyg X-1 in its 'hard' state.

Keywords: Accretion, accretion disks – Black holes – Novae and cataclysmic variables – V404 Cyg – X-rays: stars

9.1 Introduction

On May 21st, 1989 the X-ray transient GS2023+338 was discovered with the All-Sky Monitor (ASM) on board the *Ginga* satellite (Makino 1989). A few days later, this transient was identified with V404 Cyg (Wagner *et al.* 1989a), an optical nova known to have erupted in 1938 (Wachman 1948), 1956 and possibly 1979 (Richter 1989), indicating a recurrence time of less than about 20 years. Given a distance of >1.5 kpc (Charles *et al.* 1989) and the large X-ray brightness (up to 21 Crab units in the band 1–37 keV, Tanaka 1989) it became clear that GS2023+338 must involve a low-mass X-ray binary (LMXB), containing a compact object which is either a neutron star or a black hole, and a low-mass, possibly evolved, primary.

The X-ray behavior during the 1989 outburst, as observed with instruments on the *Ginga* satellite (Kitamoto *et al.* 1989, Tanaka 1989) and the *Röntgen* observatory onboard the manned space station *Mir* (Sunyaev *et al.* 1991), was unique for a transient source in two respects. Firstly, the intensity of the X-ray source exhibited strong variability on all measured time scales (down to 2 ms), with extreme jumps of up to a factor of 500 within one minute. Secondly, the X-ray spectrum showed large variations in shape, particularly during the first 10 days. Modelling the spectrum with a power-law, Kitamoto *et al.* (1989) found the photon-index to change from 0.00 on May 21st, via –2.5 on May 23rd to -1.4 after June 1st. Largely variable and complex absorption was seen. The trends as seen in the X-ray lightcurve (Kitamoto *et al.* 1989, Kitamoto 1990) are fairly well reproduced in the optical lightcurve, strongly suggesting that the optical light originated from reprocessing of X-rays in matter surrounding the compact object (Wagner *et al.* 1991).

Because of the resemblance between the rapid variability seen in GS2023+338 and that in the black hole candidate (BHC) Cyg X-1 (in its 'hard state'), Tanaka (1989) suggested the possibility of a new BHC in GS2023+338. This suggestion was also supported by the very hard spectrum (up to 300 keV) observed (Sunyaev *et al.* 1991). Several attempts were made by a number of authors to find (orbital) periodicities in the lightcurve (e.g. Wagner *et al.* 1991, Gotthelf *et al.* 1991, Udalski & Kaluzny 1991, Leibowitz *et al.* 1991) and the radial velocity curve (e.g. Haswell & Shafter 1990, Casares *et al.* 1991, Wagner *et al.* 1989b) to infer orbital parameters of the system, and hence to obtain a handle on the compact object's mass. Only recently Casares *et al.* (1992) have succeeded in measuring beyond any doubt the radial velocity curve of the companion star with data obtained in the summer of 1991, when the optical light was not dominated anymore by reprocessed X-rays. They found an orbital period of 6.5 days and a lower limit to the compact object's mass of 6.26 $M_\odot$, making this the best BHC yet.

The X-ray instruments of the *Röntgen*-observatory on the *Kvant* module of the manned space station *Mir*, which cover a wide photon energy range of 2 till 300 keV, have made measurements of GS2023+338 during June-August 1989. These measurements have been presented already in a paper by Sunyaev *et al.* (1991). The work reported in the present paper involves an extension to that presented by Sunyaev *et al.* , i.e. a more detailed assessment is made of the spectral variability of GS2023+338, employing data in the 2–28 keV band.

9.2 Observations

The observations discussed here were performed with *TTM*, a coded mask X-ray camera that is part of the *Röntgen* observatory onboard the *Kvant* module of the manned space station Mir. *TTM* was built jointly by the SRON-Laboratory for Space Research Utrecht and the University of Birmingham and is operated in collaboration with the Space Research Institute, Moscow. This camera images 8×8 square degrees full-width at half-maximum (FWHM) of the sky with an angular resolution of 2

Table 9.1: Log of *TTM*-observations on the GS2023+338 field

Date (1989)	Number of observations[a]	Exposure time[b]
June 8	3	3800
June 9	4	4990
June 10	7[r]	3190
June 15	3	750[c]
July 6	4	3860
July 7	4	4470
July 8	6[r]	2120
July 9	5[r]	1860
July 10	5	6170
July 11	6	7420
August 19	6	7320
Total	53	45950

[a] One orbit defines one observation. [r] = 'rocking mode' observation, which results in about half the usual exposure time on the target.
[b] Combined exposure time for each date in seconds.
[c] Due to eclipses by the Earth, the effective exposure time on the object was limited in these observations.

arcminutes FWHM. The detector is a 95% Xenon filled position-sensitive proportional counter with a geometric open area of 540 cm^2 and sensitive between 2 and 30 keV with an energy resolution of 18% FWHM at 6 keV. For a more complete description of *TTM* we refer to In 't Zand *et al.* (1988). It is important to note that the sensitivity of a coded mask camera is not only determined by the detector efficiency, but also by the configuration of celestial X-ray sources in the observed part of the sky; in short, there is cross-talk between X-ray sources. Specifically for the GS2023+338 field this means that the sensitivity is somewhat suppressed by the presence of the nearby (bright) sources Cyg X-1 and Cyg X-3.

In general, the *Röntgen* observatory (Sunyaev *et al.* 1987) can perform observations for 10 to 30 minutes during the low environmental background period of each $1\frac{1}{2}$ hour orbit. During 11 days in 1989, between June 8th and August 19th, 53 orbits were devoted to observations of GS2023+338. In total the source was observed for about 13 hours. Table 9.1 presents a log of the *TTM* observations on GS2023+338.

9.3   The data: lightcurve and spectrum

Lightcurves, as measured by *TTM* in the 2–6 and 6–28 keV bands, are shown in Fig. 9.1 with a time resolution of 1 *Mir* orbit. Several interesting phenomena may be inferred from this:

1. within a time span of slightly more than two months, the average X-ray brightness between 2 and 28 keV declined with a factor of 7, corresponding to an e-folding decay time of ∼35 days;

2. there is considerable variability from measurement to measurement, up to a factor of 2 in intensity;

3. the variability is much stronger in the low energy band than in the high energy band, particularly in June.

The latter aspect is very clear from Fig. 9.2, which shows combined spectra from 2 days of observation in June, indicating a large fluctuation in the low-energy part of the spectrum. This was already
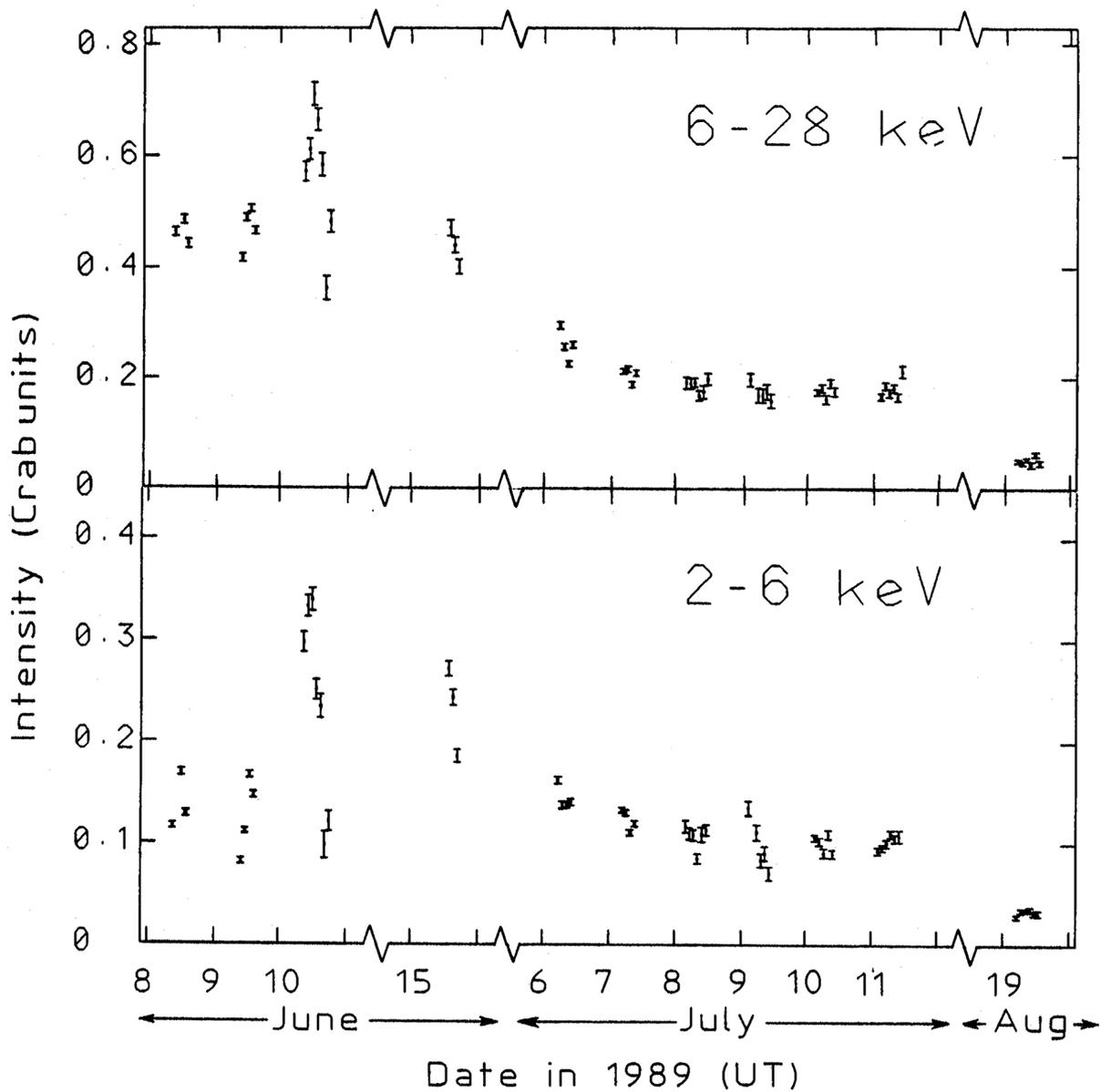
Figure 9.1: *TTM*-lightcurves of GS2023+338 in two separate passbands. Intensities are expressed in Crab units (i.e. normalized on the countrate for the Crab in the same energy interval) and the time resolution is one *Mir* orbit. Times are given in UT for the center of each orbit. Note the jumps in the time axis

noted by Tanaka (1989) and Sunyaev *et al.* (1991). It is also apparent from Fig. 9.2 that the spectra are complex. The complexity observed in these data has already been indicated by Sunyaev *et al.* (1991). They found that the June spectra contain breaks in the 2–28 keV range near 4–5 keV and 9–10 keV and suggest that these may be due to an integrated contribution of emission originating in different zones of an accretion disk with different temperatures. In this paper a model is proposed for this spectral structure. The prominent spectral structure, present in the June spectra, is less obvious at later dates.
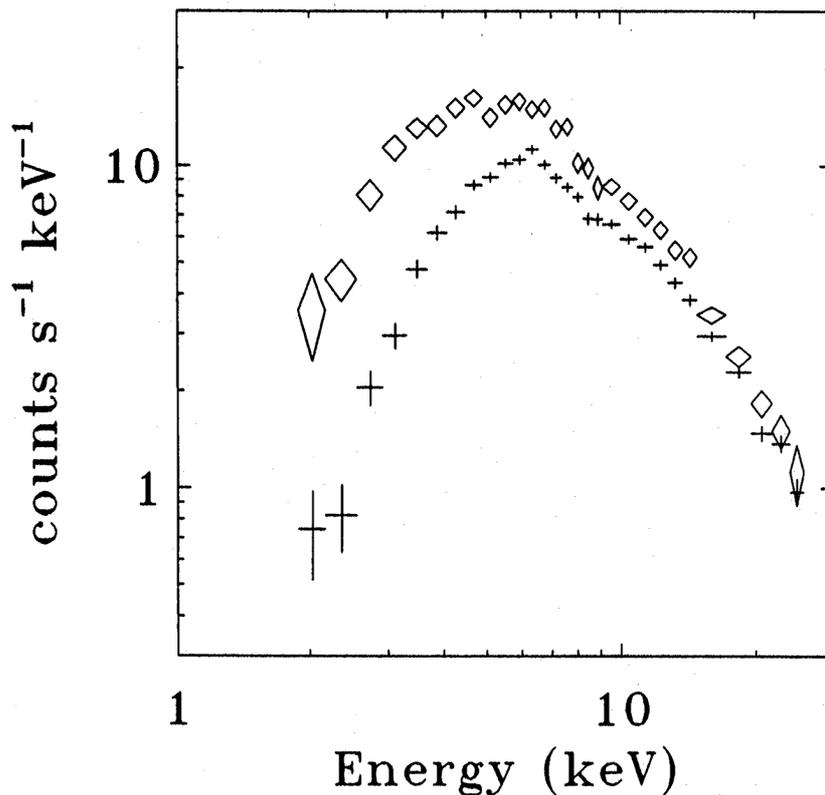
Figure 9.2: Average count-spectra of GS2023+338 for two days of observation in 1989: June 8th (crosses) and 10th (diamonds)

9.4 Spectral variability

9.4.1 Analysis method

From the rough analysis, discussed in 9.3, it is clear that the data suggest two types of spectral variability: a fast and strongly fluctuating low-energy modulation and an apparently slower change in the remaining part of the spectrum. To model the observed spectral variability, we choose to employ an empirical approach. In this approach we first try to solely fit the modulation of the low-energy component without as yet making any model assumption on the shape of the intrinsic spectrum (we define the 'intrinsic' spectrum to be the spectrum without low-energy modulation). This method, if successful, allows the study of spectral properties other than the low-energy modulation with higher statistical accuracy, through the combination of spectra that are corrected for the low-energy modulation, and may consequently be more restrictive towards a spectral model for the source.

In order to investigate the low-energy modulation independent from the intrinsic spectrum, we developed the method of differential absorption measurement. In this method, it is assumed a priori that the intrinsic spectrum remains constant over the analysis period and that the varying low-energy modulation can be solely attributed to a fluctuating low-energy absorption. The associated absorption measure is determined differentially, i.e. it is analyzed how much the spectrum is absorbed at any moment relative to when the absorption was least in the whole data set.

Hence, in this method the total spectrum incident on the detector is described by

$$F(E,t) \;=\; C(t)\,\mathrm{e}^{-\sigma(E)N_{\mathrm{H}}(t)}\,F_{\mathrm{C}}(E) \tag{9.1}$$

with $C(t)$ a time-dependent normalization factor, $\sigma(E)$ the cross section of a cold gas of cosmic abundance per H-atom (from Morrison & McCammon 1983) and $N_{\mathrm{H}}(t)$ the time-dependent term of

the total absorbing hydrogen column density, excluding a constant value for the interstellar matter. $F_C(E)$ represents the intrinsic spectrum. In the differential absorption measurement, $F_C(E)$ is cancelled out through division by a 'reference spectrum', thus acquiring ratio spectra. The choice of the reference spectrum is straightforward: the weighted average of those spectra that show the least low-energy absorption. Values for $N_H(t)$ and $C(t)$ derive from fits to the modulation $C(t) \, e^{-\sigma(E)N_{H(t)}}$, convolved with the response of the detector[1]. Results for Pearson's χ^2-test indicate whether the used model is correct, i.e. whether the chosen reference spectrum is indeed representative of the intrinsic spectrum, and provide a verification of the a priori assumption on the constancy of the shape of the intrinsic spectrum.

Since the intrinsic spectrum is slowly variable, it must be anticipated that different reference spectra need to be defined for several periods. The number of necessary different reference spectra follows from the χ^2-tests. It is noted that N_H and C values found for sets of ratio spectra with different reference spectra are in principle not directly comparable.

9.4.2   Results on GS2023+338

We applied the method of differential absorption measurement to the TTM data of GS2023+338, resolving the data in the highest possible time resolution permitted by the statistical quality of the data for this kind of analysis, i.e. 250 s. Only the data taken during June 8-10 were thus resolved because only in that period heavy low-energy absorption was observed (cf. Figs. 9.1 and 9.2). Furthermore, all data were processed with a 1 Mir-orbit time resolution ($=1\frac{1}{2}$ h). Experimenting with the method of differential absorption measurement on the data of GS2023+338 resulted in the necessity to define two different reference spectra, for the June and July-August periods separately. This indicates a typical time scale of one month in the intrinsic spectral variability.

Apart from N_H and C, we also present the results with the parameter C_E, which is defined as the factor $e^{-\sigma(E)N_H(t)}$ convolved with the instrument response and integrated over the full passband; C_E indicates the relative effect of the low-energy absorption on the total 2-28 keV intensity. The results for all three parameters, as well as for the reduced value of χ^2 for the best-fit model, are presented in Fig. 9.3 for the one-orbit ('low') time resolution and in Fig. 9.4 for the 250 s ('high') time resolution. From the reduced values of χ^2 it is clear that the model generally describes the TTM data well. We note that the use of two different reference spectra has practically no influence on the comparability of N_H and only slightly on that of C: $C=1$ is equivalent to a 2-28 keV luminosity of $1.8 \times 10^{36}(D/1 \text{ kpc})^2$ erg/s in June and $1.7 \times 10^{36}(D/1 \text{ kpc})^2$ erg/s in July-August.

It is evident from Figs. 9.3 and 9.4 that a strong fluctuation of N_H is present during the June observations. The N_H-values are well above the detection threshold of $\sim 10^{22}$ H-atoms per cm^2. The dynamic range in N_H was found to be at least a factor of $\sim$40, with a maximum N_H found in the high time resolution of $(4.5 \pm 1.0) \times 10^{23}$ H-atoms per cm^2 on June 9.42394 (UT) , corresponding to a maximum absorption of $\sim$40% in the full energy band.

Evaluating the high time resolution (Fig. 9.4), it appears that the N_H-fluctuations do not persist towards shorter time scales: within one Mir orbit there is no significant fluctuation from measurement to measurement. In order to check this quantitatively, we calculated the extra spread that is present in the data on top of the statistical spread (the spread is defined here as the root mean square of the sum of the quadratic residues with respect to the weighted mean). The resulting rms values, expressed in percentages of the weighted mean, are given in Table 9.2. The rms value for C_E does indeed show no evidence of being larger in the high than in the low time resolution. Furthermore, this value is significant only for the June data. The fluctuations in N_H degraded in July and August with at least a factor of 10, as compared to the June period.

---

[1]In fact, a rough model must be used for the intrinsic spectrum in the models for the modulation by the low-energy absorption, particularly because of escape effects in the detector (see e.g. Bertin 1975, chapter 6). A power-law spectrum, roughly describing the observed spectrum, is sufficient for this.
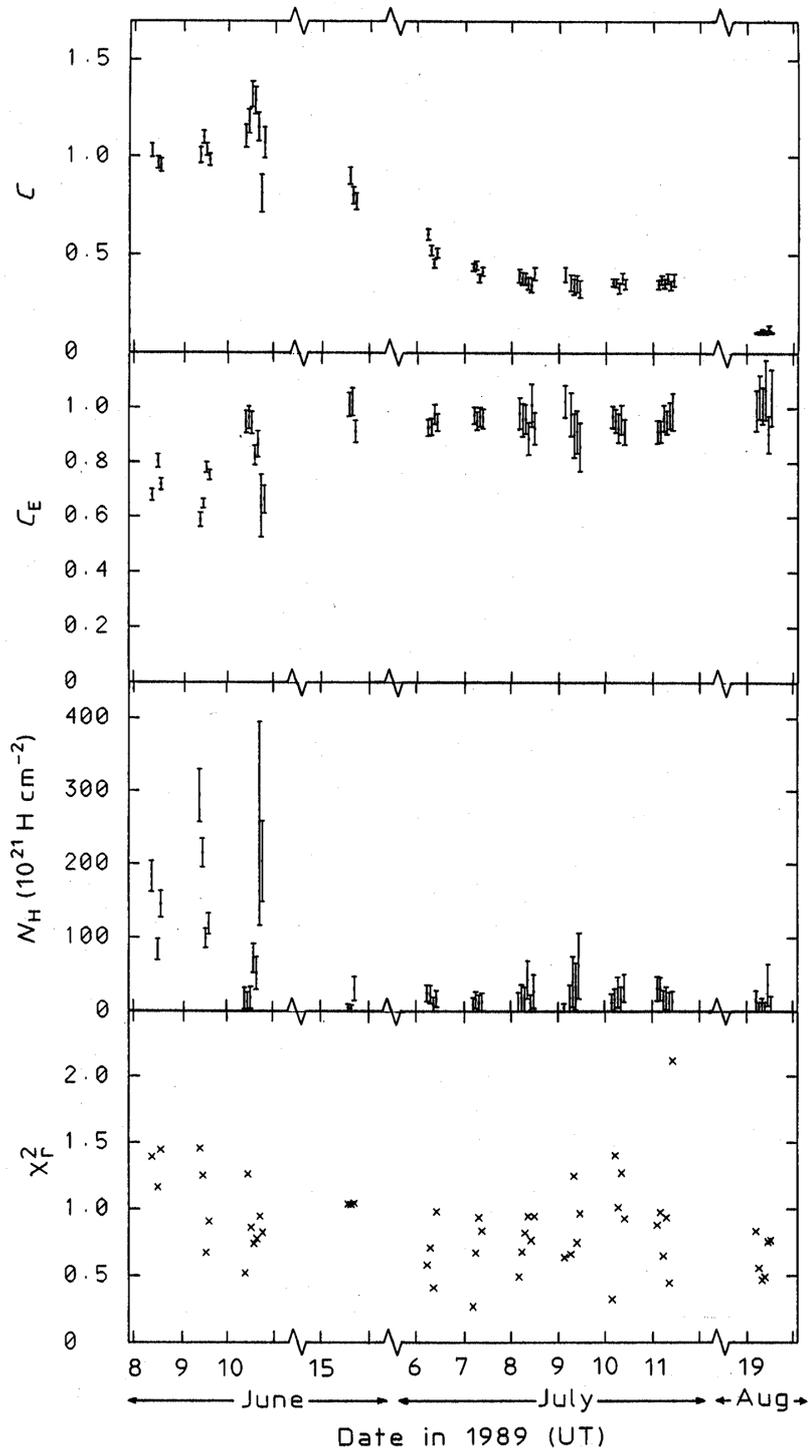
Figure 9.3: Results of modelling the spectral variability of GS2023+338 with a time resolution of one *Mir* orbit (cf. Fig. 9.1), from top to bottom: normalized energy-independent brightness (C), fractional intensity in total passband due to absorption (C_E), the variable component of the column density (N_H in H-atoms per cm^2) and χ_r^2, the result for the statistical test of the applied model
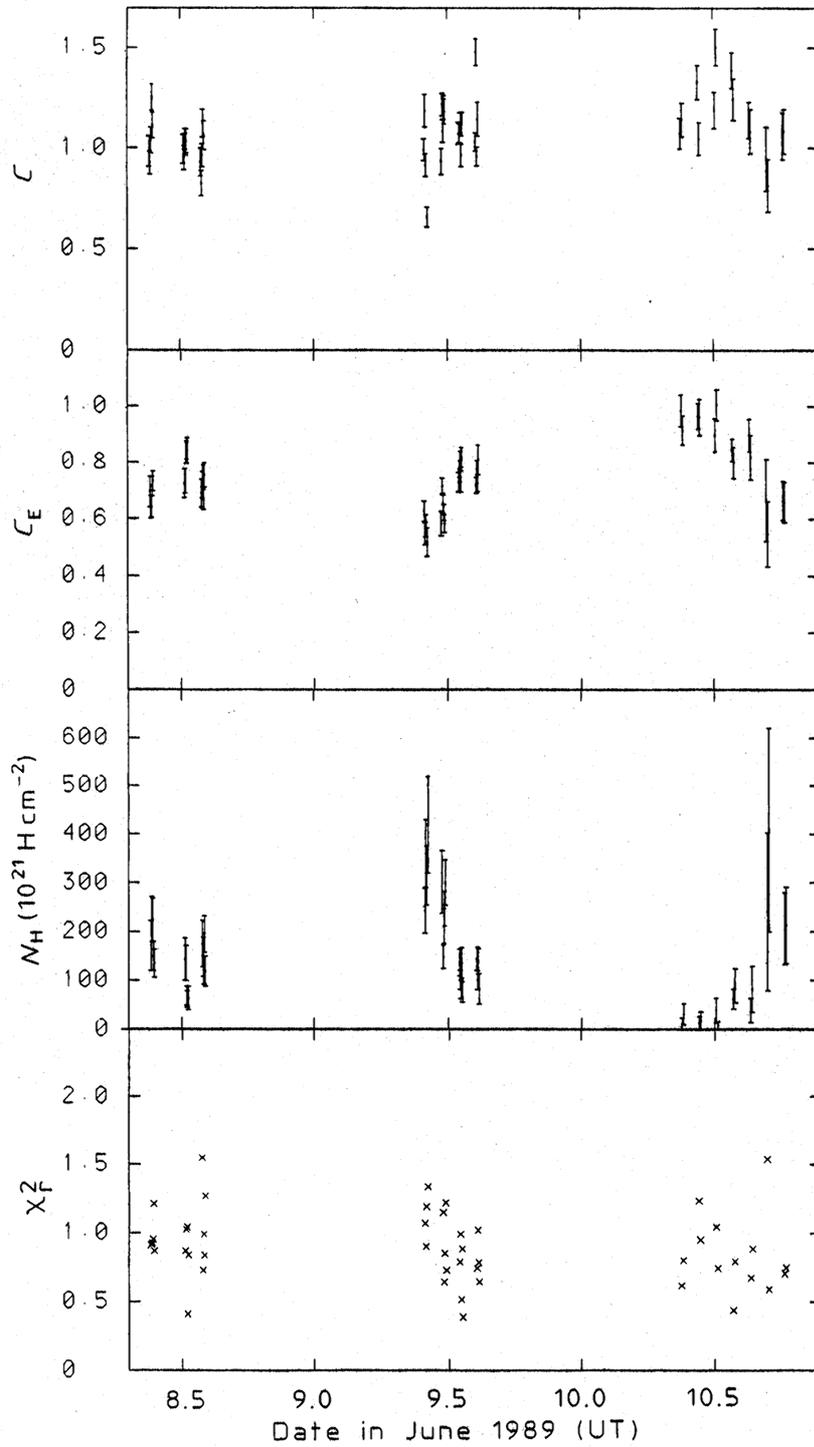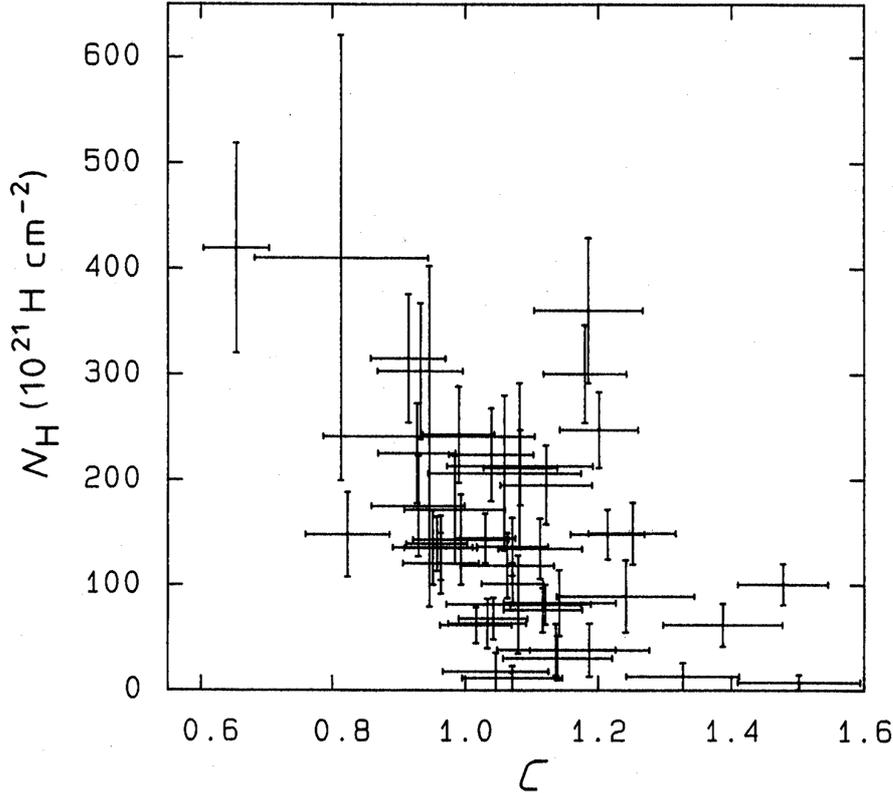
Figure 9.4: Same as Fig. 9.3, but now with a time resolution of 250 s and only for the data obtained on June 8–10

Table 9.2: Fractional *rms* values for intensities C and C_E, for all data. Upper limits are 3σ-values.

Period (1989)	Time-resolution	*rms* (%) in C	*rms* (%) in C_E
June 8–10	250 s	13.1 ± 1.4	13.1 ± 1.4
June 8–10	1 orbit	8.3 ± 1.7	12.1 ± 2.4
July 6–11	1 orbit	15.5 ± 2.1	<1.1
August 19	1 orbit	<3.5	<4.7

Figure 9.5: The relationship between N_H and C for June 8–10 in high time resolution

Regarding C, this intensity shows significant variability within the June and July data, although this variability is of a more monotonous nature in July than it is in June. Contrary to the time scale of the variability in C_E, the variability in C does show evidence for extending down to 250 s during June. Applying Pearson's χ^2 test, a $<3\%$ probability was found for the *rms* value to be the same in both time resolutions.

Figure 9.5 shows the correlation between C and N_H in the June 8–10 data. The linear correlation coefficient between these two parameters in June 8-10 is -0.32, with a probability of $<2\%$ that the observed correlation occurred by chance. However, leaving out two points with extreme C values enhances the probability to $< 15\%$, so that we conclude that the proof of correlation is only marginal.

In conclusion, the intensity variability on time scales smaller than $\sim 1\frac{1}{2}$ h can, given the quality of the data, be attributed entirely to an energy-independent variability, while on longer time scales the variability due to fluctuations in the thickness of the absorbing matter in the line of sight becomes important. Given the sampling of the data, the shape of the intrinsic spectrum does not show significant variability on time scales less than about a week.

Since we could decouple the intrinsic intensity fluctuations C from the fluctuation due to the

varying low-energy absorption (which was particularly strong in June), we could determine the e-folding decay time independent from the fluctuation in the low-energy absorption. We found it to be 31.6±0.7 days, which is slightly less than the value determined from the total brightness decay.

The long-term variability of the intrinsic spectrum is illustrated in Fig. 9.6 where we present the estimated incident photon spectra per month of observation. These spectra are normalized to the average C per period. A separate panel in Fig. 9.6 shows the intrinsic spectrum on a daily basis, to indicate the slow evolution of the intrinsic spectrum. Furthermore, the spectrum of Cyg X-1, as measured simultaneously with TTM, is shown for comparison. Figure 9.6 clearly demonstrates evolution in the form of the intrinsic spectrum. Characteristic in the June spectrum is a sag beyond 6–7 keV in an otherwise power-law like spectrum. The sag is also present in the July spectrum, but to a lesser degree. Such a sag was also noticed in *Ginga* data of GS2023+338 by Inoue (1989), who found this to be quite reminiscent of spectra of active galactic nuclei (AGN). AGN spectra can often be explained with a three-component model: a power-law spectrum, a component originating in Compton-reflection of the power-law spectrum against cold or slightly ionized matter and an Fe-K fluorescence line at 6.4 keV. This model may be described by:

$$F = \left(K\, E^{-\alpha}\, [1 + r\, R(E, \alpha)] + I_{\mathrm{Fe}} \right)\, e^{-\sigma(E) N_{\mathrm{H}}} \qquad \text{photons s}^{-1}\text{cm}^{-2}\text{keV}^{-1} \qquad (9.2)$$

with α the photon index of the power law, $R(E, \alpha)$ the magnitude of the Compton-reflected component expressed in that of cold matter with a covering factor $\Omega/4\pi = \frac{1}{2}$, r a scaling factor, and I_{Fe} the flux of the iron line. The function $R(E, \alpha)$ has been specified by Lightman & White (1988) and White *et al.* (1988); it takes into account elastic scattering up to ~ 15 keV and Compton down-scattering of hard X-rays beyond this energy.

We were able to explain the TTM intrinsic spectra satisfactorily with this model, as did Tanaka (1990) for *Ginga*-spectra taken earlier on in the outburst (in late May 1989). In order to do so, we kept the column density of the interstellar matter at a value of 6×10^{21} H-atoms cm^{-2}, consistent with the amount of reddening observed in the optical spectrum (Charles *et al.* 1989). Furthermore, we used the function $R(E, \alpha)$ applicable to slightly ionized material (i.e. $\xi_0 = 0.02$, with ξ_0 the ionization parameter as defined by Lightman & White 1988). Fits with the model to the intrinsic spectrum per month of observation revealed that the spectrum evolves to a smaller reflection component, while the power-law index remains essentially constant at a value of $\alpha = 1.6 - 1.7$ (see Fig. 9.7 for confidence regions in α/r parameter space, and Fig. 9.8 for the best fit to the intrinsic June spectrum). The fraction of the total 2-28 keV luminosity produced by the reflected component decreased from 0.19 ± 0.02 in June, via 0.11 ± 0.02 in July to an upper limit of 0.08 in August (errors are 1σ).

We also applied the above-mentioned spectral model to the Cyg X-1 spectrum shown in Fig. 9.6. The Cyg X-1 spectrum also shows a significant amount of Compton-reflection and a power-law index similar to that of GS2023+338. The best fit parameters for this spectrum are: $r = 0.4 \pm 0.1$ and $\alpha = 1.70 \pm 0.04$ (χ^2/ν=57.2/26).

9.5   Discussion

With a time resolution of 250 s, the maximum luminosity within the TTM passband was found on June 10.51113 (center of time bin in UT) at a level of 2.8×10^{36} $(D/1 \text{ kpc})^2$ erg/s (corrected for circumstellar absorption). One may extend this result to 300 keV, by using the results found with other instrument aboard *Röntgen* (Sunyaev *et al.* 1991), to $\sim 11 \times 10^{36}$ $(D/1 \text{ kpc})^2$ erg/s. This is less than the Eddington limit for a compact object mass larger than 6.26 M$_\odot$ (8×10^{38} erg/s), as long as $D \lesssim 9$ kpc. Given the distance estimate of Charles *et al.* (1989) of 1.5–3 kpc, a near-Eddington luminosity can be ruled out for this period. However, during the *Ginga* observations of late May the source was observed to be about 50 times as bright and a near-Eddington luminosity could very well have occurred (Tanaka 1989). The assumption of a near-Eddington luminosity for
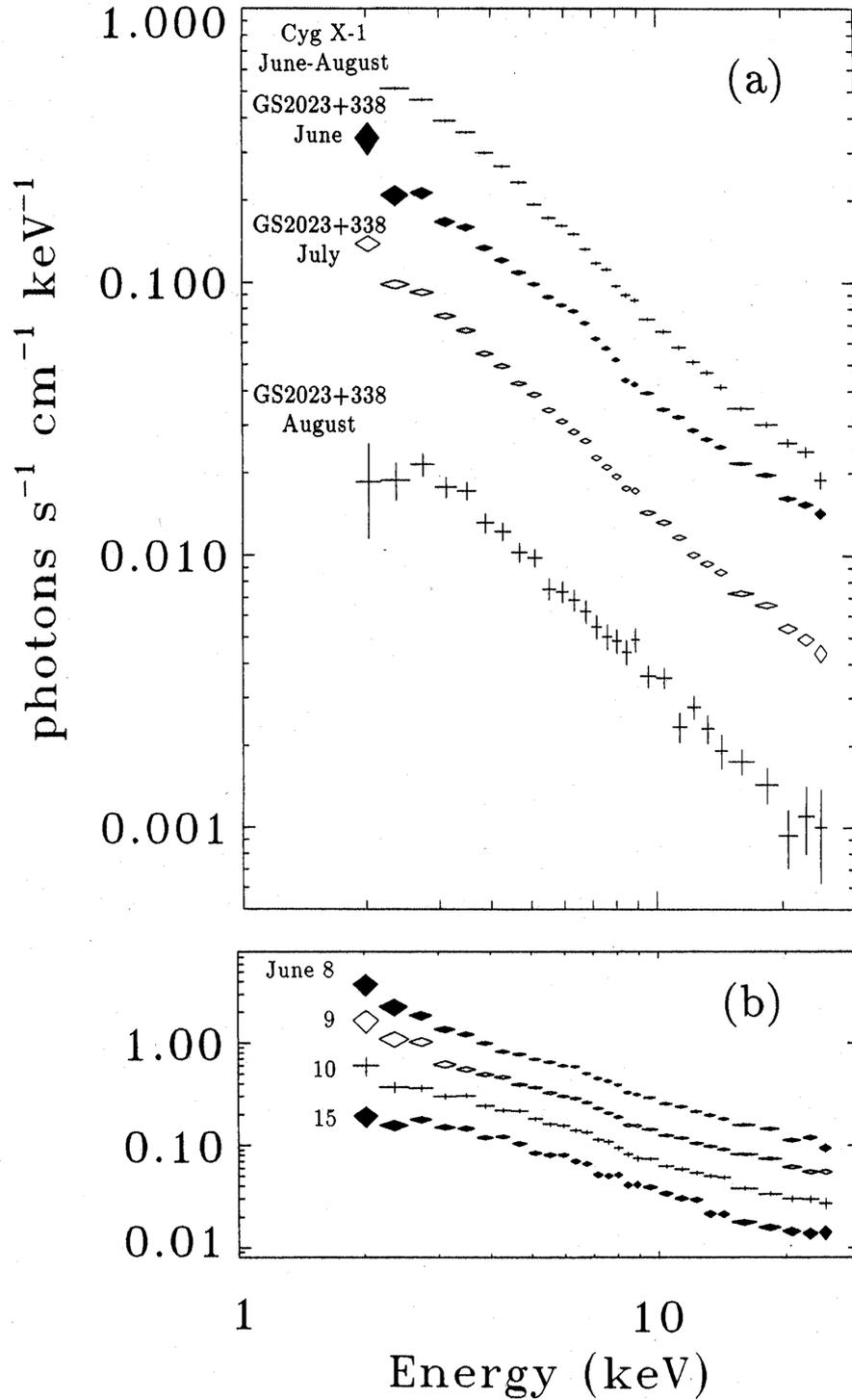
Figure 9.6: **a.** Photon spectrum of GS2023+338, corrected for absorption, separately for all observations obtained in June, July and August. For comparison we have included the spectrum of Cyg X-1, combined from 43 observations listed in Table 9.1 and offset by a factor of 2. Cyg X-1 did not show strong spectral variability during this period. **b.** The intrinsic spectrum of GS2023+338 in arbitrary flux units on a daily basis during June
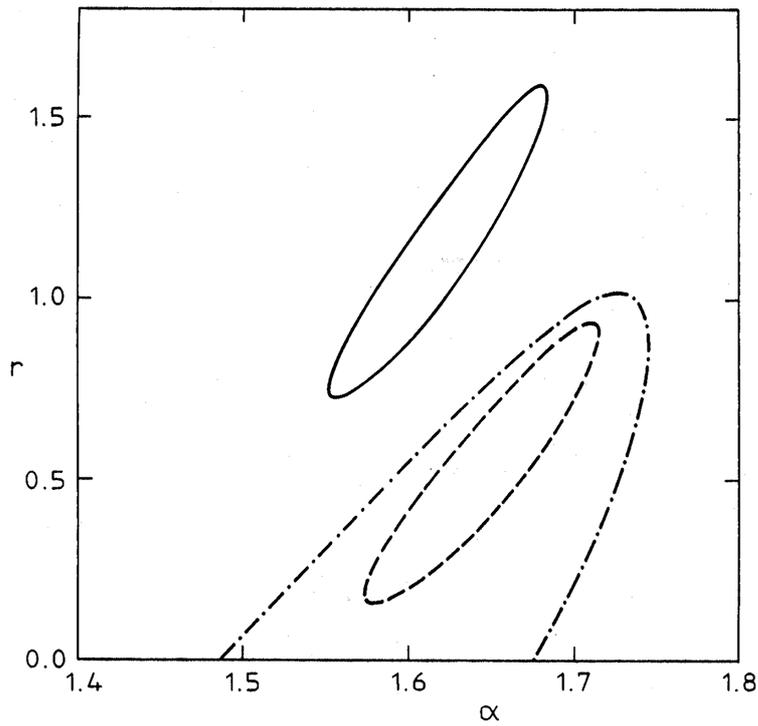
Figure 9.7: 90% confidence regions for the solution of α and r, for June (solid curve), July (dashed curve) and August (dashed-dotted curve). The accompanying minimum χ^2/ν values are: 36.9/26 (June), 25.8/21 (July), 17.42/26 (August)
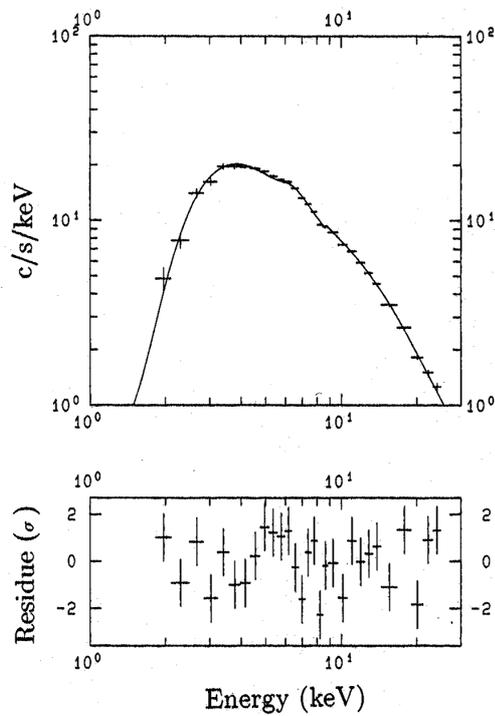
Figure 9.8: Best-fit model spectrum (according to Eq. 9.2) to the intrinsic count-spectrum of June ($\alpha = 1.60$, $r = 1.0$)

GS2023+338 is supported by evidence for a 1–37 keV flux saturation on May 30th at a level of $1.5 \times 10^{38} \, (D/1 \text{ kpc})^2$ erg/s (Tanaka 1989).

GS2023+338 is different from other X-ray transient BHCs in the sense that its spectrum never showed evidence for a black-body (BB) component, commonly seen in 2–30 keV spectra of LMXBs and ascribed to thermal emission from an accretion disk. We found an upper limit to the bolometric flux of a BB component with $kT = 1$ keV of $< 1.4 \times 10^{-11}$ erg s^{-1} cm^{-2} (within the TTM passband this amounts to $< 6 \times 10^{-4}$ times the total measured flux). The lack of a BB component is also observed in two BHCs whose X-ray emissions are persistent: Cyg X-1 and GX339-4 during their 'hard' spectral state (these sources switch from time to time to an 'ultra-soft' spectral state, during which they do show a BB component). As Tanaka (1990) noted, the presence of a BB component is not uniquely given by the mass accretion rate. Whether other parameters are important is not clear; certainly the inclination angle is not, because of the bimodal behavior of Cyg X-1 and GX339-4. For some reason the accretion disk seems to extend less far down to the compact object during the hard state than during the ultra-soft state.

GS2023+338 is exceptional among transient BHCs for yet another reason: its strong N_{H} fluctuation in the first month of the outburst. Such a feature is, among LMXBs, only observed in dipping sources with comparable N_{H} values (see Parmar & White 1988 for a review). Dips in the X-ray flux are presumably caused by irregularities in an accretion disk that occasionally obstruct the line of sight during their orbital motion. Dips have also been seen in Cyg X-1 (see e.g. Bałucińska & Hasinger 1991). A dip-like origin for the low-energy absorption in GS2023+338 does not seem probable because the duration of the absorption relative to the orbital period far exceeds the usual value for dips. A dynamical origin, however, seems likely, given the near-Eddington luminosity in the early stages of the outburst. Such a luminosity may well have provided a rather inhomogeneous environment to the compact object, with a range of different densities. If we interpret the $1\frac{1}{2}$ h time scale as due to Keplerian motion, the dynamical parameters given by Casares *et al.* (1992) yield a lower limit for the distance between the absorbing material and the compact object of $\gtrsim 8 \times 10^{10}$ cm. For comparison, the distance between both binary components is $(1.9 - 2.8) \times 10^{12}$ cm. This result is consistent with the absence of a BB component: the lower limit is far greater than the inner-most radius of a stable accretion disk, i.e. 3 Schwarzschild radii (equivalent to 10^7 cm for a 10 M$_{\odot}$ black hole), where most of the accretion-disk BB radiation within our passband would potentially originate.

The slight correlation between N_{H} and C (cf. Fig. 9.5) suggests that, apart from a dynamical origin, the fluctuation in low-energy absorption on June 8–10 might also be explained in terms of photo ionization (rather than N_{H}, the cross section $\sigma(E)$ fluctuates). We will consider this possibility briefly. Full ionization of all relevant elements up to iron requires the ionization parameter $\xi = L_{\mathrm{x}}/nd^2$ to be at least 10^4 (e.g. Kallman & McCray 1982), where n is the particle density and d the distance to the source. If we assume $n = 1.4 N_{\mathrm{H}}/d$ (for cosmic abundances) with $N_{\mathrm{H}} = 4.5 \times 10^{23}$ cm^{-2} and take for L_{x} the maximum possible value (2×10^{38} erg/s as dictated by the equivalence of the saturated luminosity level, found by Tanaka 1989, to the Eddington luminosity of a 20 M$_{\odot}$ object and the maximum luminosity found from TTM data), we find an upper limit for the radius within which the radiation can fully ionize the environment: $d \lesssim 4 \times 10^{10}$ cm. The longest time scale expected for bremsstrahlung cooling of such a plasma, with $T = 10^7$ K, is ~ 1 minute. This is two orders of magnitude shorter than the time scales observed. In view of the fast variability of the source flux, an explanation of the observed fluctuation in low-energy absorption in terms of photo ionization therefore seems less likely.

Apart from the general decrease in low-energy absorption, the spectral variability of GS2023+338 at time scales of the order of one week to one month is further characterized by a decrease of the reflected component. The question arises whether these tendencies are linked to a single physical process. As was noted previously (e.g. by Sunyaev *et al.* 1991 and Inoue 1989), the X-ray characteristics of both GS2023+338 and Cyg X-1 are reminiscent of those of active galactic nuclei (AGN).

In AGNs, matter is thought to comprise basically two coexisting components that are important in the formation of the X-ray spectrum (see e.g. Lightman & White 1988): cold (thermal, $kT \sim 10$ eV) and hot (non-thermal) matter. Often these two components are envisaged as an accretion disk and a surrounding corona, but theory does not require such a geometry.

The AGN picture may also apply to galactic BHCs, such as GS2023+338 and Cyg X-1 in its 'hard' state, except that the compact object's mass is a factor $\sim 10^7$ smaller, thus the dynamical time scales and the luminosity are accordingly smaller, while the cold matter may be hotter. The sag and the hard tail in the GS2023+338 spectrum is certainly indicative of reflection against cold matter, as indicated by the quality of the spectral fits. It seems conceivable that the low-energy absorbing material represents a cold matter component against which the power-law spectrum is Compton-reflected. This would conveniently explain the coupling in the data between the decrease in the magnitude of the reflected component and the decrease in the general level of low-energy absorption, both potentially arising from a decrease in the amount of cold matter. The general decrease in the observed values of $N_{\rm H}$ indicates a decrease of a factor of ~ 10 in the mass of the circumstellar matter from June to August.

Assuming that all gravitational energy released by the inflow of matter on the compact object was transformed into radiation, we find from the total amount of radiated energy during the whole outburst an equivalent mass of $\sim 2 \times 10^{-9}$ $M_\odot$ $(D/1 \text{ kpc})^2$. If this amount was transferred from the companion during the past quiescent stage of the X-ray transient (since the previous outburst of its optical counterpart 10 to 30 years ago, see introduction) and stored up until the 1989 outburst, the average mass transfer rate during quiescence would have been $(4$–$12) \times 10^{15}$ $(D/1 \text{ kpc})^2$ g s^{-1}. This value is comparable with that observed in other LMXB transient sources (e.g. White *et al.* 1984), as long as $D < 3$ kpc.

We also observed Compton-reflection in the spectrum of Cyg X-1, which was simultaneously measured with GS2023+338. This confirms results obtained with *Ginga* (Tanaka 1990) and represents yet another aspect of the similarity between both sources. The difference between Cyg X-1 and GS2023+338 could be that in Cyg X-1 the Compton-reflection takes place against a stable accretion disk, while in GS2023+338 it predominantly takes place against cold clumpy material, expelled earlier during a near-Eddington luminosity phase.

Finally, we note that the variability in the Compton-reflected component causes apparent changes in the power-law index if Compton-reflection is not taken into account during the spectral modelling of the data. This is clear from Fig. 9.6: the power-law spectrum of June appears to be harder than that of the other two months. However, the full spectral modelling is consistent with a constant power-law index. We suggest that this effect may partly be responsible for the strong index changes seen in early *Ginga*-ASM data (Kitamoto *et al.* 1989).

9.6   Conclusion

In this study we have investigated the spectral variability of the X-ray transient and BHC GS2023+338 on time scales > 250 s during June-August 1989. The spectral signatures of this variability include a fluctuating low-energy absorption with a time scale of $\sim 1\frac{1}{2}$ h and a slowly decreasing Compton-reflected component, on top of a power-law spectrum with essentially a constant index, but a variable intensity. The data can be satisfactory modeled by assuming a clumpy environment around the compact object, which gets progressively more transparent during our observations, probably by accretion of the circumstellar matter onto the compact object. The $1\frac{1}{2}$ h time scale seems to exclude photo ionization as the cause of the fluctuating low-energy absorption.

In many respects GS2023+338 resembles the BHC Cyg X-1 during its 'hard' state. Apart from the rapid intensity variability as seen with another *Röntgen* instrument (*HEXE*, Sunyaev *et al.* 1991), this also applies to spectral characteristics, such as power-law index, the presence of a Compton-reflected component and even, to some extent, low-energy absorption. The main difference between

both BHCs, i.e. persistent versus transient behavior, may result from the different types of companion stars (an early spectral type super-giant for Cyg X-1 and a late type star for GS2023+338), because of the physical processes involved in the mass-loss of these companions.

References

Bałucińska, M., Hasinger, G.: 1991, *Astron. Astrophys.* **241**, 439

Bertin, E.P.: 1975, ""*Principles and Practice of X-ray Spectrometric Analysis*"" (New York: Plenum Press), 2nd ed.

Casares, J., Charles, P.A., Jones, D.H.P., Rutten, R.G.M., Callanan, P.J.: 1991, *Mon. Not. R. Astron. Soc.* **250**, 712

Casares, J., Charles, P.A., Naylor, T.: 1992, *Nature* **355**, 614

Charles, P.A., Casares, J., Jones, D.H.P. *et al.*: 1989, in "*Proc. 23rd ESLAB Symp. on Two Topics in X-Ray Astronomy*", eds. J. Hunt and B. Battrick (Noordwijk: ESA SP-296), p. 103

Gotthelf, E., Patterson, J., Stover, R.J.: 1991, *Astrophys. J.* **374**, 340

Inoue, H.: 1989, in "*Proc. 23rd ESLAB Symp. on Two Topics in X-Ray Astronomy*", eds. J. Hunt and B. Battrick (Noordwijk: ESA SP-296), p. 783

Haswell, C.A., Shafter, A.W.: 1990, IAU Circ. 5074

In 't Zand, J.J.M., Jager, R., Heise, J. *et al.*: 1988, in "*Proc. Workshop on Timing Neutron Stars*", eds. H. Ögelman and E.P.J. van den Heuvel, NATO ASI Series No. C262 (Dordrecht: Kluwer Academic Publishers), p. 317

Kallman, T.R., McCray, R.: 1982, *Astrophys. J. Suppl. Ser.* **50**, 263

Kitamoto, S., Tsunemi, H., Miyamoto, S. *et al.*: 1989, *Nature* **342**, 518

Kitamoto, S.: 1990, in "*Proc. Workshop on Accretion-Powered Compact Binaries*", ed. C.W. Mauche, (Cambridge: Cambridge University Press), 21

Leibowitz, E.M., Ney, A. Drissen, L., Grandchamps, A., Moffat, A.F.J.: 1991, *Mon. Not. R. Astron. Soc.* **250**, 385

Lightman, A.P., White, T.R.: 1988, *Astrophys. J.* **335**, 57

Makino, F., *Ginga* team: 1989, IAU Circ. 4782

Morrison, R., McCammon, D.: 1983, *Astrophys. J.* **270**, 119

Parmar, A.N., White, N.E.: 1988, *Mem. Soc. Astron. Ital.* **59**, 147

Richter, G.A.: 1989, IBVS, No. 3362

Sunyaev, R.A., Kaniovsky, A., Efremov, V. *et al.*: 1987, *Nature* **330**, 227

Sunyaev, R.A., Kaniovsky, A., Efremov, V. *et al.*: 1991, *Sov. Astron. Lett.* **17**, 123

Tanaka, Y.: 1989, in "*Proc. 23rd ESLAB Symp. on Two Topics in X-Ray Astronomy*", eds. J. Hunt and B. Battrick (Noordwijk: ESA SP-296), p. 3

Tanaka, Y.: 1990, in "*Proc. Workshop on Iron Line Diagnostics in X-Ray sources*", eds. A. Treves, G.C. Perola and L. Stella, Lecture Notes in Physics 385 (Berlin: Springer Verlag), p. 98

Udalski, A., Kaluzny, J.: 1991, *Pub. Astron. Soc. Pacific* **103**, 198

Wachman, A.A.: 1948, *Erg. Astron. Nachr.* **11** (5), 42

Wagner, R.M., Starrfield, S.G., Cassatella, A.: 1989a, IAU Circ. 4783

Wagner, R.M., Kreidl, T.J., Howell, S.B., Collins, G.W., Starrfield, S.: 1989b, IAU Circ. 4797

Wagner, R.M., Starrfield, S.G., Howell, S.B. *et al.*: 1991, *Astrophys. J.* **378**, 293

White, N.E., Kaluzienski, J.L., Swank, J.H.: 1984, in "*High Energy Transients in Astrophysics*", ed. S.E. Woosley (New York: American Institute of Physics), p. 31

White, T.R., Lightman, A.P., Zdziarski, A.A.: 1988, *Astrophys. J.* **331**, 939

Appendix A

References to papers concerning *TTM*

References to papers concerning **TTM**

A.1 Papers with the author of this thesis as contributor

Borozdin, K., Gilfanov, M.R., Sunyaev, R.A., Loznikov, V., Yamburenco, N.S., Skinner, G.K., Patterson, T.G., Willmore, A.P., Al-Emam, O., Brinkman, A.C., Heise, J., In 't Zand, J.J.M., Jager, R.: 1990, "*KS1947+300: A New Transient X-Ray Source in Cygnus*", *Sov. Astron. Lett.* **16**, 345

Gilfanov, M.R., Sunyaev, R.A., Churazov, E.M., Loznikov, V., Efremov, V., Kaniovsky, A., Kuznetsov, A., Yamburenco, N.S., Melioransky, A., Skinner, G.K., Al-Emam, O., Patterson, T.G., Willmore, A.P., Brinkman, A.C., Heise, J., In 't Zand, J.J.M., Jager, R., Voges, W., Pietch, W., Döbereiner, S., Englhauser, J., Trümper, J., Reppin, C., Ögelman, H., Kendziorra, E., Mony, B., Maisack, M., Staubert, R., Parmar, A, Smith, A.: 1990, "*Observations of X-Ray Pulsars from the* Kvant *module*", *Sov. Astron. Lett.* **16**, 291

In 't Zand, J.J.M., Jager, R., Heise, J., Brinkman, A.C., Sunyaev, R.A., Gilfanov, M.R., Pappe, N.Yu., Churazov, E.M., Yamburenco, N.S., Skinner, G.K., Al-Emam, O., Patterson, T.G., Willmore, A.P.: 1988, "*X-Ray Observations of SN1987a with a Coded Mask Imaging Spectrometer*", in "*Proc. Workshop on Timing Neutron Stars*", eds. H. Ögelman and E.P.J. van den Heuvel, NATO ASI Series No. C262 (Dordrecht: Kluwer Academic Publishers), 317

In 't Zand, J.J.M., Patterson, T.G., Brinkman, A.C., Heise, J., Jager, R., Skinner, G.K., Willmore, A.P., Al-Emam, O., Sunyaev, R.A., Churazov, E.M., Gilfanov, M.R., Yamburenco, N.S.: 1989, "TTM-Kvant *Observations of the Galactic Plane*", in "*Proc. 23rd ESLAB Symp. on Two Topics in X-Ray Astronomy*", eds. J. Hunt and B. Battrick (Noordwijk: ESA SP-296), 693

In 't Zand, J.J.M., Heise, J., Brinkman, A.C., Jager, R., Skinner, G.K., Patterson, T.G., Pan, H.-C., Nottingham, M.R., Willmore, A.P., Al-Emam, O., Sunyaev, R.A., Churazov, E.M., Gilfanov, M.R., Yamburenco, N.S.: 1991, "*Two New X-Ray Transients near the Galactic Centre*", *Adv. Sp. Res.* **11**, (8)187

In 't Zand, J.J.M., Pan, H.-C., Bleeker, J.A.M., Skinner, G.K., Gilfanov, M.R., Sunyaev, R.A.: 1992, "*The Spectral Variability of GS2023+338 During Its 1989 Outburst*", *Astron. Astrophys.*, in press

Pan, H.-C., In 't Zand, J.J.M., Skinner, G.K., Borozdin, K., Sunyaev, R.A., "*Observations of the X-ray Transient Source GS2023+338 With the* TTM *Coded Mask Telescope*", in "*Proc. Recent Advances in High-Energy Astronomy*", Toulouse, France, March 1992, in press

Patterson, T.G., Skinner, G.K., Willmore, A.P., Al-Emam, O., Brinkman, A.C., Heise, J., In 't Zand, J.J.M., Jager, R., Sunyaev, R.A., Churazov, E.M., Gilfanov, M.R., Yamburenco, N.S.: 1989, "*Identification of Galactic Bulge X-Ray Bursts with Persistent X-Ray Counterparts*", in "*Proc. 23rd ESLAB Symp. on Two Topics in X-Ray Astronomy*", eds. J. Hunt and B. Battrick (Noordwijk: ESA SP-296), 567

Skinner, G.K., Pan, H.-C., Maisack, M., Staubert, R., Borozdin, K., Brinkman, A.C., Englhauser, J., Gilfanov, M.R., Kaniovsky, A., Pietch, W., Sunyaev, R.A., In 't Zand, J.J.M.: 1991, "*The Spectrum and Position of the Hard Galactic Centre Source 1E1740.7-2942*", *Astron. Astrophys.* **252**, 172

Sunyaev, R.A., Gilfanov, M.R., Churazov, E.M., Yamburenco, N.S., Brinkman, A.C., Heise, J., In 't Zand, J.J.M., Jager, R., Skinner, G.K., Al-Emam, O., Patterson, T.G., Willmore, A.P.: 1988, "*Stabilization of the* Mir-Kvant *Space Station According to X-Ray Data from the* TTM *Instrument*", *Sov. Astron. Lett.* **14**, 296

Sunyaev, R.A., Gilfanov, M.R., Churazov, E.M., Loznikov, V., Yamburenco, N.S., Skinner, G.K., Patterson, T.G., Willmore, A.P., Brinkman, A.C., Heise, J., In 't Zand, J.J.M., Jager, R.: 1990, "*X-Ray Observations of the LMC Field by the* TTM *Telescope on Board the* Kvant *module from November 1988 to June 1989*", *Sov. Astron. Lett.* **16**, 55

Sunyaev, R.A., Churazov, E.M., Efremov, V., Gilfanov, M.R., Grebenev, S., Kaniovsky, A., Stepanov, D., Yunin, S., Kuznetsov, A., Melioransky, A., Yamburenco, N.S., Kiselev, S., Lapshov, I., Pappe, N.Yu., Boyarsky, M., Loznikov, V., Prudkoglyad, A., Terekhov, O, Reppin, C., Pietch, W., Englhauser, J., Trümper, J., Voges, W., Kendziorra, E., Bezler, M., Staubert, R., Brinkman, A.C., Heise, J., In 't Zand, J.J.M., Jager, R., Skinner, G.K., Al-Emam, O., Patterson, T.G., Willmore, A.P., Smith, A., Parmar, A.: 1990, "*Highlights from the* Kvant *Mission*", *Adv. Sp. Res.* **10**, (2)41

Sunyaev, R.A., Gilfanov, M.R., Churazov, E.M., Loznikov, V., Yamburenco, N.S., Skinner, G.K., Patterson, T.G., Willmore, A.P., Al-Emam, O., Brinkman, A.C., Heise, J., In 't Zand, J.J.M., Jager, R.: 1990, "*The New X-Ray Transient Burster KS1731-260*", *Sov. Astron. Lett.* **16**, 59

Sunyaev, R.A., Kaniovsky, A., Efremov, V., Aref'ev, V., Borozdin, K., Gilfanov, M.R., Churazov, E.M., Kuznetsov, A., Melioransky, A., Yamburenco, N.S., Pietch, W., Döbereiner, S., Englhauser, J., Reppin, C., Trümper, J., Voges, W., Kendziorra, E., Maisack, M., Mony, B., Staubert, R., Skinner, G.K., Al-Emam, O., Patterson, T.G., Willmore, A.P., Brinkman, A.C., Heise, J., In 't Zand, J.J.M., Jager, R.: 1991, "*Observations of the X-Ray Nova GS2023+338 by the "Röntgen" Observatory on Board "Kvant" Module*", *Sov. Astron. Lett.* **17**, (291)

Sunyaev, R.A., Churazov, E.M., Gilfanov, M.R., Pavlinsky, M., Grebenev, S., Dekhanov, I., Kuznetsov, A., Yamburenco, N.S., Skinner, G.K., Patterson, T.G., Willmore, A.P., Al-Emam, O., Pan, H.-C., Nottingham, M.R., Brinkman, A.C., Heise, J., In 't Zand, J.J.M., Jager, R., Ballet, J., Laurent, P., Salotti, L., Natalucci, L., Niel, M., Roques, J.P., Mandrou, P.: 1991, "*Imaging of the Galactic Center Field by* Kvant *and* Granat", *Adv. Sp. Res.* **11**, (8)177

Sunyaev, R.A., Kaniovsky, A., Efremov, V., Grebenev, S., Kuznetsov, A., Churazov, E.M., Gilfanov, M.R., Yamburenco, N.S., Englhauser, J., Döbereiner, S., Pietch, W., Reppin, C., Trümper, J., Kendziorra, E., Maisack, M., Mony, B., Staubert, R., Skinner, G.K., Patterson, T.G., Willmore, A.P., Al-Emam, O., Brinkman, A.C., Heise, J., In 't Zand, J.J.M., Jager, R., Parmar, A., Smith, A.: 1991, "*The Results of the* Kvant *Module in 1987-1989*", *Adv. Sp. Res.* **11**, (8)5

Sunyaev, R.A., Borozdin,K., Gilfanov, M.R., Efremov, V., Kaniovsky, A., Churazov, E.M., Skinner, G.K., Al-Emam, O., Patterson, T.G., Willmore, A.P., Brinkman, A.C., Heise, J., In 't Zand, J.J.M., Jager, R., Voges, W., Pietch, W., Döbereiner, S., Englhauser, J., Trümper, J., Reppin, C., Kendziorra, E., Mony, B., Maisack, M., Staubert, R.: 1991, "*The Abnormally Hard Spectrum of the Source 1E1740.7-294 from the Data of the* Röntgen *Observatory on the* Kvant *Module*", *Sov. Astron. Lett.* **17**, 54

A.2   Other papers

Brinkman, A.C., Dam, J., Mels, W.A., Skinner, G.K., Willmore, A.P.: 1985, "*Coded Mask Imaging X-Ray Spectrometer for the Saljut-Mission*", in "*Proc. Non Thermal and Very High Temperature Phenomena in X-Ray Astronomy*", eds. G.C. Perola and M. Salvati (Roma: Università "La Sapienza"), 263

Mels, W.A., Lowes, P., Buurmans, B.A., Brinkman, A.C., Naber, A.P., Rook, A., Zandee, W.: 1988, "*A Large Area Position Sensitive X-Ray Detector for Astrophysical Observations*", *Nuc. Instr. Meth. Phys. Res.* **A273**, 689

Nottingham, M.R., Skinner, G.K., Willmore, A.P., Borozdin, K., Churazov, E.M., Sunyaev, R.A.: 1992, "*Observations of the Galactic Center With the* TTM *Instrument*", in "*Proc. Recent Advances in High-Energy Astronomy*", Toulouse, France, March 1992, in press

Skinner, G.K., Al-Emam, O., Brinkman, A.C., Churazov, E.M., Gilfanov, M.R., Heise, J., Jager, R., Mels, W.A., Pappe, N.Yu., Patterson, T.G., Sunyaev, R.A., Willmore, A.P., Yamburenco, N.S.: 1988, "*Coded Mask X-Ray Observations of SN1987a from* Mir", in "*Proc. of the 4th George Mason Astrophysics Workshop*", eds. M. Kafatos and A.G. Michalitsiansos (Cambridge: Cambridge University Press), 361

Sunyaev, R.A., Kaniovsky, A., Efremov, V., Gilfanov, M.R., Churazov, E.M., Grebenev, S., Kuznetsov, A., Melioransky, A., Yamburenco, N.S., Yunin, S., Stepanov, D., Chulkov, I., Pappe, N.Yu., Boyarsky, M., Gavrilova, E., Loznikov, V., Prudkoglyad, A., Rodin, V., Reppin, C., Pietch, W., Englhauser, J., Trümper, J., Voges, W., Kendziorra, E., Bezler, M., Staubert, R., Brinkman, A.C., Heise, J., Mels, W.A., Jager, R., Skinner, G.K., Al-Emam, O., Patterson, T.G., Willmore, A.P.: 1987, "*Discovery of Hard X-Ray Emission from SN1987a*", *Nature* **330**, 227

Sunyaev, R.A., Gilfanov, M.R., Churazov, E.M., Yamburenco, N.S., Brinkman, A.C., Heise, J., Mels, W.A., Jager, R., Skinner, G.K., Al-Emam, O., Patterson, T.G., Willmore, A.P.: 1988, "*Upper Limits on the 2-32 keV X-Ray Emission from SN1987a June-August 1987*", *Sov. Astron. Lett.* **14**, 252

Status: July 29th, 1992

Inleiding en samenvatting

Röntgen-straling uit het heelal

Er zijn twee belangrijke verschillen tussen de hemel zoals we die 's nachts met het blote oog kunnen zien en die in Röntgen-licht: het hemelpatroon van stralingsbronnen (de 'sterrenbeelden') is in beide gevallen totaal verschillend en de intensiteit van Röntgen-bronnen is in het algemeen veel veranderlijker dan de intensiteit van bronnen van zichtbaar licht. De oorzaak van deze twee verschillen ligt bij de verschillende fysische processen die een rol spelen bij de opwekking van beide soorten electromagnetische straling.

De golflengte van Röntgen-straling is ongeveer duizend maal zo klein dan die van zichtbaar licht, waardoor de energie van deze straling duizend maal zo groot is. Röntgen-straling duidt daarom op veel energierijkere processen, dan de processen die verantwoordelijk zijn voor de opwekking van zichtbaar licht. Objecten die de meeste energie uitstralen in het zichtbare deel van het electromagnetische spectrum hebben een temperatuur in de orde van 10.000 K, terwijl objecten die de meeste energie in het Röntgen-gebied uitzenden een temperatuur hebben van grofweg duizend maal zo hoog, dus ongeveer 10 miljoen K.

De meeste sterren stralen, net zoals de zon, het gros van hun energie uit in zichtbaar licht. Deze straling is afkomstig uit de atmosferen van die sterren, waarvan de temperatuur tussen de 6.000 en 50.000 K is. Zulke atmosferen stralen vaak ook een beetje Röntgen-straling uit, maar de intensiteit hiervan staat in geen verhouding tot die van het zichtbare licht. De intensiteit van de Röntgen-straling van de zon bijv. bedraagt circa 10 miljoen maal zo weinig als die in zichtbaar licht.

In 1962 lanceerde een Amerikaanse groep onderzoekers een raket met de bedoeling metingen te verrichten van Röntgen-straling afkomstig van de maan. Tot hun grote verbazing vonden zij een heldere bron van Röntgen-straling, waarvan de positie niet overeen kwam met die van de maan noch met die van de zon. Al speculerend kwamen ze tot de conclusie, dat, als dit object een ster was, zijn intrinsieke lichtkracht in Röntgen-straling minstens 10 miljoen maal zo hoog was als die van de zon. Deze ontdekking ontketende een grote inspanning van zowel theoretische als experimentele astrofysici om een verklaring voor deze en daaropvolgende ontdekte sterke Röntgen-bronnen te vinden. In 1972 werd een theoretisch model experimenteel bevestigd door de eerste waarnemingen verricht vanuit een satelliet. Het bleek dat men hier te maken had met nauwe dubbelstersystemen, waarvan één component een compact object is (een witte dwerg, neutronenster of zwart gat) en de ander een 'normale' ster. Het compacte object is een ster, die aan het einde van zijn evolutie is gekomen: zijn energiebron is uitgeput, waardoor hij geen straling meer produceert. Door het ontbreken van voldoende tegendruk heeft de zwaartekracht vrij spel gehad, waardoor de ster sterk is ingekrompen. Zo heeft een neutronenster een diameter van slechts enkele tientallen kilometers, terwijl zijn massa ongeveer zo groot is als die van de zon (vergelijk dit met de zonsdiameter van 1,4 miljoen kilometer).

De twee componenten van de nauwe dubbelster staan zo dicht bij elkaar, dat veel van de door de 'normale' ster verloren materie door het compacte object ingevangen wordt. Deze materie valt, i.v.m. de kleine diameter van het compacte object, zo ver naar beneden dat zijn snelheid uitzonderlijk hoog wordt: bij een neutronenster circa 100.000 km/s; dit komt overeen met een bewegingsenergie van

circa 10% van de rustmassa van de invallende materie. Deze enorme hoeveelheid energie wordt grotendeels omgezet in warmte en daarna in Röntgen-straling. Vandaar dat men deze dubbelsterren vaak aanduidt met 'Röntgen-dubbelsterren'. Vaak valt de invallende materie (accretie genoemd) niet rechtstreeks op het compacte object, maar via bepaalde trajecten. De vorm van deze trajecten wordt gedicteerd door de manier waarop de 'normale' ster materie verliest en door de sterkte van het magneetveld van het compacte object. Er zijn ruwweg twee soorten trajecten gevonden: spiraliserend in het baanvlak naar het compacte object of via het magneetveld naar de magnetische polen van het compacte object (deze trajecten kunnen aanleiding geven tot de vorming van respectievelijk accretieschijven en pulsars).

In de sterrenkunde stelt men zich de vraag hoe deze Röntgen-dubbelsterren kunnen ontstaan. Om daarover een theorie te vormen, is het natuurlijk belangrijk te weten, hoe iedere waargenomen Röntgen-dubbelster in elkaar zit, bijvoorbeeld wat de afstand tussen beide sterren is, wat de aard is van beide sterren en hoeveel materie er per jaar overgedragen wordt van de 'normale' ster naar het compacte object. De Röntgen-straling blijkt daartoe belangrijke aanwijzingen te geven. Bij de studie van de Röntgen-straling gebruikt men twee diagnostische hulpmiddelen: de helderheidsvariatie en het spectrum. Het spectrum geeft aanwijzingen over de temperaturen en dichtheden die heersen in de dubbelster, en de helderheidsvariatie geeft aanwijzingen over met name de geometrie van de dubbelster[1] en onregelmatigheden in de massa-overdracht. Om een voorbeeld te noemen: een helderheidsvariatie kan ontstaan door de bedekking van de Röntgen-bron door de 'normale' ster, tijdens zijn baanbeweging. De duur van de bedekking geeft dan aanwijzingen over de groottes van de 'normale' ster en de Röntgen-bron.

Door de stand van de techniek op het gebied van Röntgen-metingen heeft in de voorbijgaande periode vooral de helderheidsvariatie als diagnostiek opgang gemaakt. Het is de verwachting dat in komende jaren een flinke verbetering optreedt in het potentieel van spectrale studies.

De helderste Röntgen-bronnen aan de hemel zijn tot onze melkweg behorende, zgn. GALACTIS-CHE Röntgen-dubbelsterren. Het onderzoek naar de sterkste mate van variabiliteit (d.w.z. 'aan' of 'uit') van deze bronnen, gebruik makend van de nieuwe observationele techniek van schaduwmasker-camera's, is het onderwerp van dit proefschrift.

Het meten van Röntgen-straling

Als meetinstrument voor Röntgen-straling wordt meestal gebruik gemaakt van de zogenaamde proportionele telbuis. Dit is een instrument dat verwant is aan de bekende Geiger-Müller telbuis. Het instrument bestaat uit een tank, gevuld met een edel gas, waar een kale metalen draad doorheen loopt die op spanning is gebracht. Het principe van de proportionele telbuis is eenvoudig: zodra een Röntgen-foton geabsorbeerd wordt door het gas, slaat deze een electron weg uit een gasatoom (zgn. ionisatie), dat vervolgens aangetrokken wordt door de draad. Tijdens zijn versnelde weg door het gas zal het electron andere gasatomen ioniseren en de vrijgekomen electronen doen op hun beurt hetzelfde; kort gezegd treedt er een lawine op van electronen die een electrische lading levert aan de draad. Deze lading wordt gemeten en is een maat voor de energie c.q. golflengte van het geabsorbeerde foton.

Door meerdere draden aan te brengen in de tank, kan men ook de positie van het geabsorbeerde foton bepalen. In hoofdstuk 4 wordt de detector behandeld die voor het onderhavige onderzoek is gebruikt. In deze positiegevoelige proportionele telbuis zijn drie dradenframes aangebracht (zie Fig. 4.5), die elk bestaan uit 96 tot 480 draadjes over een oppervlak van 29×29 cm^2. M.b.v. één frame wordt de fotonenergie gemeten, terwijl de andere twee frames gebruikt worden om de plaats te meten (de zgn. X- en Y-positie).

Van belang voor de gebruiker van zo'n meerdraads teller zijn de nauwkeurigheden waarmee de

---

[1]bedenk, dat het onmogelijk is om gedetailleerde 'plaatjes' te maken van sterren; daarvoor staan ze allemaal TE VER weg

foton-energie en -positie gemeten kunnen worden. Deze nauwkeurigheden worden in een meerdraads telbuis in belangrijke mate beïnvloed door de goede positionering van de dradenframes.

Röntgen-straling uit het heelal dringt niet door de aardatmosfeer. Dit heeft een belangrijke consequentie voor de waarneming ervan: dit dient boven de atmosfeer te gebeuren. Dit kan tijdelijk opgelost worden m.b.v. stratosfeerballonnen of raketten, hetgeen in de jaren zestig tijdens het pre-satelliet tijdperk gebruikelijk was. Echter, een meer permanente oplossing is de plaatsing van het instrument in een satelliet. In het laatste geval moet bij het ontwerp rekening worden gehouden, dat het instrument enige jaren zonder technisch onderhoud moet blijven functioneren.

De afbeelding van Röntgen-straling m.b.v. schaduwmaskercamera's

De klassieke optische onderdelen die gebruikt worden om een afbeelding te maken zijn de lens en spiegel. Het toepassingsgebied van met name de spiegel is groot: van radiostraling, via infra-roodstraling en zichtbaar licht, tot en met UV-straling. Bij de energierijke Röntgen-straling is het gebruik van spiegels niet meer zo gemakkelijk: Röntgen-straling heeft een groot doordringingsver-mogen (waarvan dankbaar gebruik wordt gemaakt in de geneeskunde). Daarom reflecteert deze straling slechts bij een zeer geringe invalshoek op het spiegelend oppervlak (kleiner dan ongeveer één graad). Van de parabolisch gevormde spiegel wordt dan niet de 'kop', maar de flank van de parabool gebruikt. Dit legt nogal beperkingen op aan de toepasbaarheid: het beeldveld kan nooit groter zijn dan circa één graad en het principe werkt alleen voor de 'zachte' Röntgen-straling (d.w.z. voor golflengtes groter dan circa 2 Å)[2]. Bovendien zijn de technische specificaties van de spiegel zo veeleisend, dat zulke spiegels relatief duur in de productie zijn.

Wil men grotere beeldvelden creëren en/of bij hardere Röntgen-straling een afbeelding maken (d.w.z. voor golflengtes kleiner dan 2 Å), dan moet een alternatief afbeeldend concept worden gebruikt. Zo'n concept werd in de jaren zestig ontwikkeld, door Dicke en Ables. Het is gebaseerd op een principe dat reeds in het begin van onze jaartelling door Aristoteles is beschreven: dat van de camera obscura. De camera obscura heeft in plaats van een lens een ondoorzichtige plaat met een klein gaatje erin. Er komt geen reflectie of breking aan te pas in zo'n camera; de bovengenoemde nadelen van spiegels en lenzen zijn dan ook niet van toepassing. De kwaliteit van de afbeelding m.b.v. camera obscura wordt bepaald door de grootte van het gaatje t.o.v. de grootte van de ondoorzichtige plaat: hoe kleiner het gaatje, hoe scherper het beeld. Dit brengt een nadeel voor de camera obscura met zich mee, dat vooral in astronomische toepassingen groot is: een verhoging van de scherpte gaat ten koste van het lichtverzamelend vermogen. Welnu, Dicke en Ables bedachten dat dit nadeel ondervangen kan worden door niet één, maar meerdere gaatjes in de ondoorzichtige plaat aan te brengen. De scherpte blijft dan hetzelfde, terwijl de lichtopbrengst stijgt. De plaat met gaatjes noemt men een MASKER.

Het plaatsen van meerdere gaatjes blijft niet ongestraft: men verkrijgt niet meer één DIRECTE afbeelding van het voorwerp, maar net zoveel als er gaatjes zijn, die allemaal over elkaar heen liggen. Als het aantal gaatjes groot is, wordt de afbeelding onherkenbaar. Dit wil echter niet zeggen, dat het plaatsen van meerdere gaatjes het principe onbruikbaar maakt: het is immers bekend wáár de gaatjes geplaatst zijn, zodat in principe bekend is hoe de afbeelding van een willekeurig voorwerp in zijn werk gaat. Daarom is het mogelijk om uit de onherkenbare afbeelding het voorwerp te RECONSTRUEREN. Dit is een bewerkelijke opgave, die met behulp van een computer uitgevoerd wordt. Aldus het principe van de SCHADUWMASKERCAMERA, die samenvattend luidt dat men een gecodeerde afbeelding van het voorwerp 'filmt', die vervolgens met behulp van een computer wordt gedecodeerd.

In hoofdstuk 3 van dit proefschrift wordt een overzicht gegeven van de eisen, die aan verschil-lende componenten van een schaduwmaskercamera gesteld moeten worden om tot een optimale reconstructie te komen. Belangrijk in dit opzicht zijn de afbeeldende kwaliteit van de detector,

---

[2]1 Å is één tienmiljardste meter

het patroon van de gaatjes in het masker en het reconstructie-algoritme. Bovendien worden twee verschillende types van schaduwmaskercamera's onderzocht, waarbij de voordelen en nadelen van elk type aan bod komen.

De doelstelling en het ontwerp van *COMIS*

Begin jaren tachtig aanvaardde de Stichting Ruimteonderzoek Nederland (SRON, toen nog GROC) een uitnodiging van het Ruimteonderzoeksinstituut (IKI) te Moskou om een Röntgen-instrument te ontwikkelen dat deel zou uitmaken van een Röntgen-observatorium welk gekoppeld zou worden aan een bemand ruimtestation. In dit project, *COMIS* genaamd (afkorting van *COded Mask Imaging Spectrometer*, dat vrij vertaald kan worden met 'afbeeldende spectrometer met gebruik van een gecodeerd masker'), werd een derde partner gevonden in de Universiteit van Birmingham (Engeland). De Nederlandse en Engelse partners werden verantwoordelijk gesteld voor de bouw van het instrument en de Russische partner voor de lancering en het operationele gedeelte.

De doelstelling van het *COMIS* project is tweeledig: enerzijds richt het project zich op de studie van die heldere Röntgen-bronnen, die de sterkste mate van variabiliteit vertonen, d.w.z. die bronnen die gedurende slechts een bepaalde tijd Röntgen-straling uitzenden. De tijd dat zo'n bron 'aan' is varieert tussen enkele seconden (dit zijn de zgn. 'bursts', uitgezonden door 'bursters') en weken (deze bronnen heten 'transients'). Het is met name de bedoeling deze bronnen te bewaken, m.a.w. te bepalen waar zulke bronnen staan en wanneer ze 'aan' zijn. Anderzijds is *COMIS* een proefproject voor twee soortgelijke camera's, die in ontwikkeling zijn bij SRON-Utrecht en geplaatst zullen worden in de *Satellite per Astronomia a raggi X* (*SAX*), een samenwerkingsproject tussen Italië en Nederland. De ervaring opgedaan bij de ontwikkeling van de hardware en software voor *COMIS* wordt gebruikt bij die van de *SAX* camera's.

Het moge duidelijk zijn, dat, voor een bewakingstoestel, een groot beeldveld cruciaal is: de kans op detectie van een kortstondige Röntgen-bron is dan het grootst. Bovendien verdient het aanbeveling geselecteerde hemelgebieden te bewaken, specifiek het galactisch vlak (de 'melkweg'), omdat daar in het verleden de meeste kortstondige Röntgen-bronnen zijn gevonden.

Gekoppeld aan een groot beeldveld moet het scheidend vermogen van de camera voldoende zijn om een eenduidige identificatie met een tegenhanger in een ander golflengtegebied mogelijk te maken. Dit houdt in dat een Röntgen-bron met een nauwkeurigheid van minstens 1′ gelokaliseerd dient te worden.

Deze specificaties hebben het ontwerp van *COMIS* gedicteerd. De invulling van het ontwerp wordt behandeld in hoofdstuk 4. Het beeldveld van *COMIS* is ruwweg 16×16 vierkante graden en de hoekresolutie 2 boogminuten (de lokalisatienauwkeurigheid kan tot zo'n 10 maal zo goed zijn). Een aantal van 32,768 gaatjes van 1×1 mm^2 is geëtst in een 0.1 mm dikke roestvrij stalen plaat volgens het patroon zoals getoond in Fig. 4.3. De gevoeligheid als functie van fotonenergie is getoond in Fig. 6.2.b; het maximum ligt tussen golflengtes van ruwweg 1 en 2 Å, waar de te onderzoeken objecten de meeste straling uitzenden.

Een essentieel onderdeel van het instrument is het reconstructie-algoritme, waaraan hoofdstuk 5 gewijd is. In de praktijk blijkt dat de keuze van het algoritme in belangrijke mate bepaald wordt door een afweging tussen de optimale ruisonderdrukking en de minimale hoeveelheid benodigde rekentijd. Enkele ruisonderdrukkings-algoritmen worden geïntroduceerd, die voldoen aan deze afweging, waarbij de correlatie tussen detectorbeeld en maskerpatroon als basis wordt gebruikt voor de reconstructie. Voor de overzichtelijkheid wordt het reconstructie-algoritme geïllustreerd met een gesimuleerde waarneming in een appendix.

COMIS werd, als deel van het 'Röntgen'-observatorium in de 'Kvant'-module, in april 1987 gekoppeld aan het ruimtestation 'Mir'. Helaas bleek al snel dat de detector niet optimaal functioneerde; na augustus moesten de waarnemingen gestopt worden. Echter, mede dankzij de grote inspanningen van de Russische kosmonauten aan boord van *Mir*, kon in oktober 1988 de detector

vervangen worden door een reserve exemplaar en werd het project gered.

In hoofdstuk 6 worden facetten van de calibratie van het instrument behandeld, die door de auteur zijn uitgevoerd. Het moeilijkste onderdeel van deze calibratie is dat van de zgn. puntuitsmeerfunctie, die aangeeft hoe een puntbron wordt afgebeeld. Deze functie wordt in sterke mate beïnvloed door tamelijk onvoorspelbare bewegingen van het ruimtestation, welke niet op een onafhankelijke manier gemeten kunnen worden. Bij de bepaling van intensiteiten van Röntgen-bronnen dient derhalve veel aandacht (c.q. rekenwerk) besteed te worden aan dit gegeven.

Wetenschappelijke resultaten van *COMIS*

In deel II van dit proefschrift wordt ingegaan op de wetenschappelijke uitkomsten van het *COMIS*-project. Allereerst wordt in hoofdstuk 7 een overzicht gegeven van de waarnemingen. Gedurende de eerste $3\frac{1}{2}$ jaar na oktober 1988 heeft *COMIS* 12% van de hemel waargenomen, voornamelijk in de richting van het galactisch centrum. 80% van deze waarnemingen zijn verricht in 1989. Vijfenzestig Röntgen-bronnen werden gedetecteerd. Dit zijn bijna allen Röntgen-dubbelsterren. Ze tonen een verscheidenheid aan variabiliteit (variërend van pulsvormige tot constante intensiteit) en spectra.

Vier van deze bronnen waren nog niet eerder bekend. Het zijn objecten die slechts gedurende een aantal dagen detecteerbaar waren (zgn. 'transients') en dus precies objecten waar *COMIS* naar op zoek is.

COMIS heeft 14 bursts gedetecteerd. Dit zijn kortstondige opvlammingen, die voor het eerst ontdekt zijn m.b.v. de *Astronomische Nederlandse Satelliet* (*ANS*), slechts zo'n 10 seconden duren en te wijten zijn aan nucleaire explosies op neutronensterren. Zes van deze bursts waren afkomstig van twee van de nieuw ontdekte bronnen.

Een archief werd aangelegd van het gedrag van de 65 bronnen, waarvan in hoofdstuk 7 een korte indruk wordt gegeven.

In hoofdstuk 8 wordt een gebied van 6×6 vierkante graden rondom het galactisch centrum nader bekeken. Dit gebied omhelst om zijn minst zo'n 20 Röntgen-bronnen, waarvan tot enkele jaren geleden relatief weinig bekend was, omdat de dichte bevolking en hun vaak sterke variabiliteit voor veel instrumenten een belemmering vormde voor nadere studies. Schaduwmaskercamera's hebben geen probleem met de dichte bevolking en zijn derhalve uitermate geschikt voor de studie van hun variabiliteit. In dit gebied bevinden zich 2 van de 4 door *COMIS* nieuw ontdekte bronnen, welke beide transient zijn. Eén van de bronnen staat op minder dan een graad van het galactisch centrum en vertoonde bovendien tweemaal een burst. De bron is mogelijk dezelfde als één van twee burst bronnen, die in de jaren zeventig met de Amerikaanse *SAS-3* satelliet gedetecteerd werden.

In hoofdstuk 9 wordt een andere transient onder de loep genomen. Dit object is uitermate interessant, omdat het afgelopen jaar is aangetoond dat hij de sterkste kandidaat voor een galactisch zwart gat is: via optische metingen is gebleken, dat het compacte object in deze Röntgen-dubbelster een massa van op zijn minst 6 zonnemassa's heeft. De bron was in het Röntgen-gebied actief gedurende de periode mei tot september 1989. Het bijzondere van de bron is, dat hij een hard Röntgen-spectrum heeft, dat bovendien sterk veranderlijk is op tijdschalen van minder dan één dag. Dit is ongewoon bij heldere transients. *COMIS* heeft ruim vijftig waarnemingen verricht aan de bron. Een spectrale analyse van de resulterende data wijst erop dat de sterke variabiliteit van het Röntgen-spectrum voor het grootste deel toe te schrijven is aan een variabele absorbtie door circumstellair materiaal. Het spectrum van de bron is, voor zover meetbaar, constant in vorm en neemt af in helderheid. Er wordt gesuggereerd dat door de hoge (super-Eddington) lichtkracht de materie in de omgeving van het compacte object sterk inhomogeen is geworden, waardoor variabiliteit in de absorbtie optreedt. Deze variabiliteit neemt in de loop van de tijd af, waarschijnlijk doordat de omgeving van het compacte object door accretie 'schoon geveegd' wordt.

Toekomst verwachtingen

Vooralsnog zijn er geen indicaties dat binnen korte tijd het *COMIS* project eindigt. Er worden nog, weliswaar op onregelmatige basis, waarnemingen uitgevoerd. Het instrument functioneert nog als verwacht.

Voor wat betreft reconstructie-algoritmen, is er een gunstige ontwikkeling gaande in de snelheid van computers. Bij het ontwerp van het algoritme voor de decodering van *COMIS* data speelde de snelheid van de gebruikte computer een grote rol en moest ervoor gewaakt worden, dat het analyseren van de data niet vele malen langer zou duren dan de meting op zichzelf. Deze beperking zal in de toekomst van minder belang zijn, dankzij de introductie van relatief goedkope maar snelle rekenapparatuur.

Met *COMIS* is aangetoond dat het gebruik van schaduwmaskercamera's als bewakingsinstrumenten van de fluctuerende Röntgen-hemel wetenschappelijk nut heeft. De verwachtingen van de twee groothoekcamera's voor de *SAX*-satelliet zijn hoog, omdat, in vergelijking tot *COMIS*, het beeldveld per camera ruim zes keer zo groot is en de waarneemfrequentie velen malen hoger zal zijn.

Populaire literatuur

J.J.M. in 't Zand, R. Jager en F.H.P. Spaan: 1988, "*COMIS, een Röntgencamera aan boord van Mir*", Zenit, december 1988, p. 414

G.K. Skinner: 1988, "*Imaging with coded masks*", Scientific American, augustus 1988, p. 66

Curriculum Vitae

Ik ben geboren op 13 oktober 1960 in Bunde, een dorp enkele kilometers ten noorden van Maastricht. Van 1973 tot 1979 bezocht ik het Henric van Veldeke College in Maastricht. Aldaar werd door mij in 1978 het eindexamen HAVO-b en in 1979 het eindexamen Atheneum-b met goed gevolg afgelegd. Daarna studeerde ik aan de Rijksuniversiteit Utrecht. In juni 1983 behaalde ik het kandidaats-examen sterrenkunde. In de daarop volgende doctoraal-fase verrichtte ik onder andere twee onderzoeken. Het groot onderzoek, op het Sterrekundig Instituut te Utrecht en onder leiding van Dr. J.R.W. Heintze, behelste een studie van de contact-dubbelster AW UMa met behulp van fotometrische waarnemingen verricht vanaf de Nederlandse Sterrewacht Zwitserland; het klein onderzoek, onder leiding van Dr. A.J.F. den Boggende en uitgevoerd op het Laboratorium voor Ruimteonderzoek in Utrecht, betrof voornamelijk een theoretische studie naar het potentieel van spectrale metingen met behulp van reflectie-tralies, zoals die gepland zijn voor de Röntgen-satelliet 'XMM' rond de eeuwwisseling. In juni 1987 sloot ik succesvol de doctoraal studie algemene sterrenkunde af, met bijvakken natuur- en wiskunde en met een onderwijs-aantekening voor natuur- en sterrenkunde. Op 1 augustus 1987 trad ik in dienst bij de Stichting Ruimteonderzoek Nederland (SRON), op het Laboratorium voor Ruimteonderzoek te Utrecht, om onderzoek te verrichten op het gebied van metingen aan hemelse Röntgen-bronnen met behulp van een schaduwmaskercamera, waarvan de weerslag te vinden is in dit proefschrift. Ten bate van dit onderzoek bracht ik werkbezoeken aan het Space Research Institute te Moskou (Rusland) en aan de Universiteit van Birmingham (Engeland). Verder bezocht ik internationale conferenties in Izmir (NATO-workshop 'Timing Neutron Stars', april 1988), Helsinki (COSPAR-symposium 'Advances and Perspectives in X-Ray and Gamma-Ray Astronomy', juli 1988), Bologna ('23rd ESLAB Symposium on Two Topics in X-Ray Astronomy', september 1989) en Den Haag (COSPAR-meeting 'Highlights in X-Ray and Gamma-Ray Astronomy with the Most Recent Missions', juli 1990).

Nawoord

Zo eenvoudig als het principe van de schaduwmaskercamera klinkt, zoveel haken en ogen zitten eraan als het om de praktijk gaat. Dit is DE ervaring van het *COMIS* project. Daarom ontwikkelde mijn onderzoek zich onverwacht in de richting van de instrumentele kant (zowel hard- als software). Daar ben ik niet rouwig om geweest; het was interessant werk (hoewel het niet altijd van een leien dakje ging) en een uitdaging om uit echt 'ruwe' gegevens datgene eruit te halen waarvan je een sterk vermoeden hebt dat het erin zit. Ik hoop dat mijn onderzoek zijn vruchten zal afwerpen bij de ontwikkeling van de hard- en software van de groothoekcamera's voor *SAX* (de betere broertjes van *COMIS*).

Nu is voor mij het hoofdstuk *COMIS* bijna afgesloten. Hoewel het interessant was, stemt mij dat niet helemaal ongelukkig. Het heeft lang genoeg geduurd.

fortuinlijk begin, *COMIS* weer aan de praat te krijgen zodat onder andere dit onderzoek mogelijk was.

Mijn speciale dank gaat verder uit naar de computerafdeling. Niet alleen hebben ze mij, als vreemde eend in de bijt, meer dan een jaar lang gehuisvest, maar ik vond ook altijd grote bereidwilligheid in de vervulling van mijn, soms grote, wensen met betrekking tot het gebruik van de MV.

Iedereen van Integro, met name Rolf Mewe, dank ik voor de belangstelling die zij toonden in mijn werk. Mijn werk lag niet altijd direct in hun richting, maar dat betekende niet dat ik me een buitenstaander voelde.

De laatste jaren deelde ik de kamer met Jos van Geffen. Allebei werkten we aan proefschriften over totaal verschillende onderwerpen. Desalniettemin heerste er een stimulerende sfeer, die we sterk hielden met onze eigen, zeer productieve, koffieautomaat!

Hans Braun dank ik voor de adviezen voor en de hulp bij het illustreren van dit proefschrift, Peter Blom voor de jarenlange verzorging van de dagelijkse gezamenlijke ochtendkoffie en alle niet genoemde collega's op het lab voor de prettige werksfeer.

Pa en Ma, jullie steunden mij bij de, niet helemaal normale, keuze sterrenkunde te gaan studeren. Dat ging toen zo vanzelfsprekend, dat ik me dat pas onlangs realiseerde. Voor die steun, en voor het meeleven wil ik jullie oprecht danken.

Joke, jij hielp mij bij de laatste controle op het gebruik van de Engelse taal. Dank daarvoor. Ik probeer in het vervolg het oneigenlijk gebruik van Engelse komma's te vermijden!

Tot slot, lieve Ria, dat jij het al zolang met me hebt kunnen uithouden, ondanks het 'werk', en me hielp bij het begrijpelijk maken van de Nederlandse samenvatting vind ik ontzettend tof van je! Jouw kameraadschap is me zeer dierbaar.